

A Framework for Flexible Loads Aggregation

Original

A Framework for Flexible Loads Aggregation / DIAZ LONDONO, CESAR EDUARDO. - (2020 Jul 28), pp. 1-190.

Availability:

This version is available at: 11583/2847146 since: 2020-10-01T10:42:24Z

Publisher:

Politecnico di Torino

Published

DOI:

Terms of use:

Altro tipo di accesso

This article is made available under terms and conditions as specified in the corresponding bibliographic description in the repository

Publisher copyright

(Article begins on next page)



PONTIFICIA UNIVERSIDAD
JAVERIANA



POLITECNICO DI
TORINO

DOCTORAL THESIS

A Framework for Flexible Loads Aggregation

Author:

Cesar DIAZ LONDOÑO

Supervisor:

Prof. Fredy RUIZ

Co-supervisor:

Prof. Diego PATIÑO

Supervisor:

Prof. Gianfranco CHICCO

Co-supervisor:

Dr. Andrea MAZZA

Committee in charge:

Prof. Carlos Correa, Pontificia Universidad Javeriana, Bogotá – Colombia

Prof. Andrés Pantoja, Universidad de Nariño, Pasto – Colombia

Prof. Paolo Di Leo, Politecnico di Torino, Turin – Italy

Prof. Marco Merlo, Politecnico di Milano, Milan – Italy

Prof. Carlos Ocampo, Universitat Politècnica de Catalunya, Barcelona – Spain.

A thesis submitted in fulfillment of the requirements for the degrees of:

PhD in Engineering

in the

Departamento de Electrónica

Bogotá, Colombia

**PhD in Electrical, Electronics and
Communications Engineering**

in the

Dipartimento Energia “Galileo Ferraris”

Turin, Italy

2020

Abstract

Cesar DIAZ LONDOÑO

A Framework for Flexible Loads Aggregation

Smart Grids are integrating renewable generation in their electrical supplies. As a consequence, the fluctuations due to solar radiation and wind speed or direction can produce energy unbalances between supply and demand in the grid. Various Demand Response (DR) programs have been proposed to reduce energy unbalances. Moreover, flexible loads management carried out by an aggregator has been proposed to provide ancillary services in DR by applying optimal methods such as Model Predictive Control (MPC). In this dissertation, an aggregator framework is proposed, developing flexible loads models and direct load control structures able to operate in DR plans and provide ancillary services to the system operator. The aggregator framework is presented considering a methodology for loads to provide ancillary services. Then, this methodology is assessed on three flexible loads, Water Booster Pressure Systems (WBPS), ThermoElectric Refrigeration (TER) units, and Electric Vehicle (EV) charging stations. First, a dynamic model of a WBPS is estimated and tuned with real data, and a WBPS aggregator that is capable of offering spinning reserve services is proposed. Second, a TER unit model is estimated and characterized by experimental data, and a TER aggregator able to provide balancing services such as frequency containment reserve is proposed. Third, a dynamic model of an EV charger is developed, and an EV charger aggregator that looks for minimizing costs while maximizing flexibility is proposed. The EV aggregator can offer spinning reserve services and participate in Day-Ahead and Real-Time markets. Moreover, a specific flexibility definition for EV chargers is formulated. As results, the flexible load aggregators have been validated by simulations fulfilling the ancillary service's response time and the power capacity variations requested by the system operator. Finally, a hierarchical architecture (balancing service provider) able to manage the previous flexible load aggregators is proposed in order to provide different European balancing services in a frequency restoration process.

Acknowledgements

I would like to thank my joint Ph.D. supervisors, Prof. Fredy Ruiz, Prof. Gianfranco Chicco, Prof. Diego Patino, and Dr. Andrea Mazza, who guided me in this process by providing the necessary tools in control techniques and electrical energy field. In particular, I would like to express my gratitude to Prof. Ruiz who has served as a mentor and a teacher. His patience, dedication, and excellent advice during these years, kept me constantly engaged with my research. I really appreciate all the time he devoted to supporting me at each stage of this dissertation to get high-quality results.

Thanks to examiners: Prof. Carlos Ocampo, Prof. Andrés Pantoja, Prof. Carlos Correa, Prof. Marco Merlo, Prof. Paolo Di Leo, Prof. Matías Negrete, Prof. Giambattista Gruosso, Prof. Iván Mondragón, and Prof. Carlos Murillo for their insightful comments, feedback, and encouragement during my Ph.D. process.

This journey has been also possible thanks to my family: my parents and sister for supporting me these years and my life in general, as well as my beloved future wife Gabriela who always encouraged me throughout the process. Also, my Javeriana friends: José and Yesid for the interesting discussions on energy efficiency; George, Ricardo, and David for the engaging conversations on different research issues. Likewise, my Polito friends: Francesco G. and Francesco A. for the exciting debates on electric vehicles; Mahmood, Shaghayegh, and Yang for sharing your time teaching me about different cultures; Carlos and Luisa for the time in coffee breaks.

Finally, the financial support of this doctoral thesis has been provided by the program: *“Rodolfo Llinás para la promoción de la formación avanzada y el espíritu científico en Bogotá”* from *Secretaría de Desarrollo Económico de Bogotá* and *Fundación CEIBA*.

Contents

Abstract	iii
Acknowledgements	v
1 Introduction	1
1.1 Flexible Loads and Aggregators	2
1.1.1 Adjustable loads	4
Thermostatically Controlled Loads	4
Water Booster Pressure Systems	7
1.1.2 Deferrable loads	8
Electric Vehicles	8
1.2 Organization and thesis contributions	11
2 Ancillary Services Provision by Load Aggregation	15
2.1 Smart Grid Approach	16
2.2 Ancillary Services	17
2.2.1 North America	18
2.2.2 Europe	19
2.2.3 Colombia	22
2.3 Aggregator Design	22
2.4 Load Aggregation Methodology	24
2.4.1 Flexible load modelling	24
2.4.2 Flexibility analysis	25
2.4.3 Flexible load aggregator design	25
2.4.4 Evaluation of the proposed aggregator by simulation	26
2.5 Remarks	26
3 Modelling and Control of Water Booster Pressure Systems	27
3.1 System model	27
3.1.1 Experimental data acquisition	30

3.1.2	Simulation and experimental validation	31
3.2	Flexibility of the Water Booster Pressure System	34
3.2.1	Evaluating the model	34
3.2.2	Settling time	36
3.2.3	Energy services	37
3.2.4	Capacity and operation conditions	38
3.3	Control system for power reduction	39
3.3.1	Controller Tuning	41
3.3.2	Gain-Scheduled Aggregator	45
3.4	Findings	48
4	Control System for a ThermoElectric Refrigeration Unit	49
4.1	ThermoElectric Refrigeration Unit	50
4.1.1	TER model	51
4.1.2	Experimental data	53
4.1.3	TER parameters characterization	58
Step 1.	Electrical parameters	58
Step 2.	Interior compartment thermal parameters	59
Step 3.	External equivalent model parameters	60
4.1.4	Model validation	60
4.1.5	Experimental TER controller	61
Experimental controller	62
Experimental control results	63
4.2	Flexibility and TER aggregator	66
4.2.1	Flexibility analysis	66
PI-controlled TER flexibility evaluation	67
Modified PI controller	68
Response time analysis	70
4.2.2	TER Aggregator	71
4.3	Remarks	79
5	Optimal Strategy to Manage an Electric Vehicle Charging Station	81
5.1	Electric Vehicle Charging Station Operations	82
5.1.1	Charging Station Operations	83
5.1.2	The Charger Dynamics Model	87
5.2	Flexibility Evaluation	88
5.3	Solution Strategies	92

5.3.1	Minimum Time as a Benchmark	92
5.3.2	Economic Model Predictive Control	93
5.3.3	Optimal Control with Minimum Cost and Maximum Flexibility	97
5.4	Case Study and Results	100
5.4.1	Charger Flexibility Analysis	101
	Deterministic Performance	102
	Results with Uncertainty in Arrival SoC and Arrival Time	105
5.4.2	Savings, Benefits, and Flexibility in the EVCS	106
5.4.3	Monte Carlo Analysis	108
5.5	Findings	111
6	Strategy for EVCS participation in RT and DA Markets	113
6.1	EVCS Operation with RES generation	114
6.2	Bogotá, Colombia Photo-Voltaic generation model	115
	Pre-processing data	116
6.2.1	Profiles based on expected values	117
6.2.2	Non-linear auto-regressive model	119
6.2.3	Residue analysis	122
6.2.4	Solar Power Forecast	123
6.3	Day-Ahead Formulation	123
6.4	Real-Time Formulation	125
6.5	Case study and Day-Ahead and Real-Time strategy results	126
6.6	Remarks	130
7	Hierarchical Architecture Structure for European Balancing Services	131
7.1	Unified Aggregation Framework	131
7.1.1	Hierarchical Coordination	132
7.1.2	Flexible Loads Aggregators	134
	TER-AGG	134
	WBPS-AGG	134
	EVCS-AGG	135
7.2	Balancing Service Provider Operation	136
	Case 1	137
	Case 2.	139
8	Conclusions	143

A Model Predictive Control	145
A.1 MPC strategy	145
A.2 MPC for linear systems	147
A.2.1 Unconstrained case	149
A.2.2 Constrained case	149
Bibliography	152

List of Figures

1.1	Categories of Demand Side Management.	3
1.2	Thesis organization.	11
2.1	Aggregators for flexible loads.	17
2.2	Standard structure of balancing services provision.	20
2.3	Balancing market processes for frequency restoration.	21
2.4	Electricity markets sequence and its participants.	21
3.1	Water Booster Pressure System (WBPS).	28
3.2	Power and Flow Measurement in the pump room.	31
3.3	Experimental measurements in a WBPS.	32
3.4	General block diagram of the WBPS.	33
3.5	Simulated WBPS tank pressure.	33
3.6	Power consumed by the actual and simulated pump.	34
3.7	Power consumption for different pressure limits and output flow.	35
3.8	Switching frequency for different pressure limits and output flow.	36
3.9	Histogram of the time elapsed for cycling again after a set point change.	37
3.10	Block diagram of the aggregator control system.	39
3.11	Plant and Model response to a pulse input with $\beta_{max}=100$	42
3.12	Plant and Model response to a pulse input with $\beta_{max}=50$	42
3.13	Response of the PI aggregator in 3 hours tes for $r=3.90$ kW.	43
3.14	Response of the PI aggregator in 3 hours test for $r=1.95$ kW.	44
3.15	Power consumption during the three hours test for $r=3.90$ kW.	45
3.16	Power consumption during the three hours test for $r=1.95$ kW.	45
3.17	Gain-scheduled aggregator tracking test.	47
4.1	Schematic of the TER unit.	50
4.2	Electrical TEC module scheme.	52
4.3	Equivalent scheme of a TER unit.	53
4.4	Actual TER used in the study.	54

4.5	Current - Voltage curve of the TEC	54
4.6	Current and voltage sensors validation	55
4.7	Block diagram of the implementation.	56
4.8	Hardware implementation.	57
4.9	Measurements for Experiment 1, 2 and 3.	57
4.10	Experimental V_{α}	58
4.11	Temperature validation for the experiments.	61
4.12	Experimental data and Model response in open loop.	62
4.13	TER controllers responses.	65
4.14	Modified TER control strategy.	68
4.15	TER flexibility, with the PI controller and modified PI controller.	69
4.16	Histogram of the time elapsed consuming zero or maximum power after a set point change.	71
4.17	Block diagram of the TER aggregator.	71
4.18	TER Selector sequence.	73
4.19	Models validation.	74
4.20	Aggregator response for the Frequency Containment Reserve (FCR) service.	76
4.21	Aggregator response for the Replacement Reserve (RR) service.	77
5.1	Electric Vehicle Charging Station operation.	84
5.2	Expected and actual time and state of charge for the j th electric vehicle.	85
5.3	SoC area in an EV charger.	90
5.4	Flexibility in an EV charger.	91
5.5	The behaviour of the three charging strategies in charger 1, considering only request parameters.	103
5.6	Flexibility capacity provided by charger 1.	104
5.7	The behaviour of the three charging strategies in charger 1, with arrival SoC and time uncertainties.	105
5.8	The behaviour of the three charging strategies in the EVCS.	107
5.9	EVCS flexibility capacity.	108
5.10	Overall savings for different strategies and remuneration factors based on c_1	110
5.11	Energy price sequence $c_{2,k}$	110
5.12	Overall savings for different strategies and remuneration factors based on c_2	110

6.1	EVCS operation with Photo-Voltaic generation.	115
6.2	Solar radiation <i>Profiles 1, 2 and 3</i> , based on the expected values.	117
6.3	<i>Profile 1</i>	118
6.4	<i>Profile 2</i>	118
6.5	<i>Profile 3</i>	119
6.6	Real data and <i>Profile 2</i> behaviour.	119
6.7	Residue autocorrelation.	120
6.8	Validation between real data and NARX model.	121
6.9	Validation of the estimated model (expected value and NARX model).	122
6.10	Second residue autocorrelation.	122
6.11	Histogram. Gaussian distribution	123
6.12	Solar radiation data at <i>Pontificia Universidad Javeriana</i>	127
6.13	The behavior of the Day-Ahead and Real-Time controllers in charger 3.	128
6.14	EVCS behavior in the Day-Ahead and Real-Time controllers.	129
7.1	Hierarchical Architecture Structure.	133
7.2	Balancing service provider operation.	137
7.3	Hierarchical Architecture Structure perform in balancing services.	137
7.4	TER Aggregator power demand.	138
7.5	Percentage of TER systems changing the set-point.	138
7.6	WBPS Aggregator power demand.	138
7.7	Percentage of WBPS systems changing the set-point.	139
7.8	EVCS Aggregator power demand.	139
7.9	Aggregation system power in balancing services	140
7.10	TER Aggregator power.	140
7.11	TER systems.	140
7.12	WBPS Aggregator power.	141
7.13	WBPS systems.	141
7.14	EVCS Aggregator power.	141
A.1	MPC Strategy.	146
A.2	MPC Structure.	146

List of Tables

3.1	Nomenclature and units of the WBPS system variables.	29
3.2	Parameters of the WBPS employed in the experiments.	31
3.3	Pressure limits evaluated in the flexibility analysis.	35
3.4	Intervals of model parameters for the settling time evaluation.	36
3.5	Defined pressure variables for offering spinning reserve services.	38
3.6	Average power reductions	44
3.7	Power standard deviation.	44
3.8	Gain-scheduled PI Controller parameters.	46
3.9	Performance of the GS aggregator during the tracking test.	47
4.1	Notation of the TER variables.	52
4.2	Experimental values of V_α and ΔT , and computed values for α and R_p	59
4.3	Optimal values for the TER parameters.	60
4.4	Error measures for the TER model.	61
4.5	Consumption comparison between the PI, PID and On/Off strategies.	64
4.6	Temperature comparison between the strategies.	65
4.7	Intervals of model parameters for setting the simulations	67
4.8	Information exchange between the aggregator and the TER units.	72
4.9	Aggregator characteristics during the Frequency Containment Reserve (FCR) service.	76
4.10	Aggregator characteristics during the Replacement Reserve (RR) service.	78
5.1	Notation of the EVCS variables.	83
5.2	Case study simulation parameters.	101
5.3	EV charger schedule.	102
5.4	Three strategies' overall simulation results (three chargers, 11 EV requests)	104
5.5	Strategies' overall simulation results, with uncertainty in the arrival time and initial SoC (three chargers, 11 EV requests).	106

5.6	Three strategies' overall simulation results, considering uncertainties (25 chargers, 110 EV requests)	108
5.7	Mean value and standard deviation of the overall savings with respect to the MT strategy.	111
6.1	Additional variables notation of the EVCS with PV generation.	114
6.2	Lack of data in the solar radiation information.	116
6.3	Similitude of the profiles with the real data	119
6.4	Residues between the original data and each profile statistics.	120
6.5	Similitude of the residue validation with different model orders and prediction steps.	121
6.6	EV Schedule for Charger 3.	128
6.7	Energy and cost for the Day-Ahead schedule and Real-Time controller. .	130

List of Abbreviations

AC	Alternating Current
ADC	Analog Digital Converters
aFRR	automatic Frequency Restoration Reserves
AGC	Automatic Generation Control
ANN	Artificial Neural Network
ARX	AutoRegressive eXogenous
BRP	Balancing Responsible Party
BSP	Balancing Service Provider
COP	Coefficient Of Performance
DA	Day-Ahead
DC	Direct Current
DER	Distributed Energy Resources
DLC	Direct Load Control
DSM	Demand Side Management
DR	Demand Response
DSO	Distribution System Operator
eMPC	economic Model Predictive Control
EV	Electric Vehicle
EVCS	Electric Vehicle Charging Station
FCR	Frequency Containment Reserves
FERC	Federal Energy Regulatory Commission
FRR	Frequency Restoration Reserves
FSA	Food Standards Agency
GC	Generic Charging
GPC	Generalized Predictive Control
GS	Gain-Scheduled
HAS	Hierarchical Architecture Structure
HLC	High Logic Coordinator
HVAC	Heating, Ventilation and Air-Conditioners

IBP	Incentive-Based Programs
ISP	Imbalance Settlement Period
LP	Linear Programming
MAXAE	MAXimum Absolute Error
MBPC	Model-Based Predictive Control
MD	Most Delayed
mFRR	manual Frequency Restoration Reserves
MILP	Mixed-Integer Linear Programming
MPC	Model Predictive Control
MSE	Mean-Squared Error
MT	Minimum Time
NARX	Nonlinear AutoRegressive eXogenous
NOCT	Nominal Operation Cell Temperature
OCCF	Optimal Control with minimum Cost and maximum Flexibility
OOP	Open-loop Optimization Problem
PBP	Priced Based Programs
PDF	Probability Density Function
PI	Proportional-Integral
PID	Proportional-Integral-Derivative
PV	Photo-Voltaic
PWM	Pulse-Width Modulation
RES	Renewable Energy Sources
RHC	Receding Horizon Control
RMSE	Root Mean Squared Error
RR	Replacement Reserves
RT	Real-Time
SO	System Operator
SoC	State of Charge
STC	Standard Test Conditions
TCL	Thermostatically Controlled Load
TEC	ThermoElectric Cooler
TER	ThermoElectric Refrigerator
V2G	Vehicle to Grid
VCR	Vapour-Compression Refrigeration
WBPS	Water Booster Pressure System
WDS	Water Distribution System

Chapter 1

Introduction

The world energy consumption has been increasing over the past few decades and is estimated to increase by 28% between 2015 and 2040, as well as the Renewable Energy Sources (RES) rising by an average of 2.8%/year ([Energy U.S., 2017](#)). The RES uncertainty has a significant impact on the scheduling of conventional generation ([Nghitevelekwa and Bansal, 2018](#)) and storage ([Bakirtzis et al., 2018](#)). The main effects of the uncertainty appear both on power system operation and on the need for procuring sufficient reserve capacity to maintain acceptable levels of reliability and security ([Pandurangan et al., 2012](#)). The System Operator (SO) has the responsibility to ensure the security and reliability of the electrical grid, coordinating the load and supply of electricity. In this context, generation power systems must provide ancillary services, i.e., the balancing services that are delivered to the SO, such as frequency stability and voltage control ([Carreiro et al., 2017](#)). However, a new paradigm where the demand is able to react to different contingencies is raising ([Nijhuis et al., 2016](#)). Indeed, it is needed a transformation to load response instead of generation response in which the customers reduce their consumption, manually or automatically, for decreasing the risk of failure ([Deng et al., 2015](#)). These actions are possible on Demand Response (DR) plans ([Vardakas et al., 2015](#)), managing a trade-off between comfort and reliability. In ([Energy U.S., 2006](#)), DR is defined as *“Changes in electric usage by end-use customers from their normal consumption patterns in response to changes in the price of electricity over time, or to incentive payments designed to induce lower electricity use at times of high wholesale market prices or when system reliability is jeopardized”*.

DR offers several benefits such as the ability to balance RES uncertainties, enhance the implementation of real-time pricing and curtail the generation capacity requirements ([Aghaei and Alizadeh, 2013](#)). These DR plans are adopted due to the predictable and cycling nature of the electricity demand. On this basis, DR can become a

revenue source for agents that aggregate load flexibility. Aggregators offer the opportunity to exploit the flexibility potential of small end-users and promoting their access to the retail electricity market by selling load flexibility and benefiting from rewards or lower energy bills (Carreiro et al., 2017). Then, the demand can be managed by an aggregator using indirect or direct control. Then, aggregators that apply an indirect control structure have limited information, while, on direct control, the communication is individual with each appliance (O'Connell et al., 2014).

In this dissertation, an aggregator framework is proposed, developing flexible loads models and direct control structures able to operate in DR plans and provide ancillary services. This research is addressed in five parts: (i) an aggregator framework is presented considering ancillary services definition, and a methodology for modelling flexible loads and controlling them properly is proposed; then, this methodology is evaluated on three flexible loads; (ii) a dynamic model of a Water Booster Pressure System (WBPS) is estimated and tuned with real data, and a WBPS aggregator has been proposed, capable of offering spinning reserve service; (iii) a ThermoElectric Refrigeration (TER) unit model is estimated and characterized with experimental data, and a TER aggregator able to provide regulation and balancing services is proposed; (iv) a dynamic model of an Electric Vehicle (EV) charger station is developed, an EV charger aggregator is proposed based on an optimal decision maker minimizing costs and maximizing flexibility, it can offer spinning reserve services; (v) day-ahead and real-time strategies are proposed considering RES forecast. A flexibility measure is developed for each flexible load, particularly an EV charger flexibility definition is proposed. Numerical studies and extensive simulations are provided to demonstrate the properties and advantages of these models and aggregators as solutions and tools in smart grids.

This chapter reviews some aspects to be considered in the framework for flexible loads aggregation. A literature review related to flexible loads is presented, oriented on models, flexibility, and aggregators of the three analysed flexible loads (WBPS, TER, and EV). Finally, the thesis contributions and organization are exposed.

1.1 Flexible Loads and Aggregators

In recent years, the participation of the demand in operation scheduling and reserve procurement has increased, also with the definition of demand response programmes that involve manual or automatic variation of the demand to reduce the grid risk (Deng et al., 2015). The current deployment of the generation and demand resources to

improve the power system operation has been represented in the *flexibility* framework (Ma et al., 2013). There is a vast literature about flexibility definitions and applications, however according to (Holttinen et al., 2013), there is no uniform definition of flexibility. Various definitions of flexibility have been proposed for the generation side and the demand side. In (Ulbig and Andersson, 2015), the operational flexibility in power systems is defined as the deviation between the nominal power plant output trajectory and the actual power output trajectory. Interactions between flexibility concepts and the diffusion of RES are discussed in (Holttinen et al., 2013). Various forms of grid-side flexibility are addressed in (Li et al., 2018). The thermal generation flexibility is defined in (Ma et al., 2013) by providing a metric to quantify the technical flexibility for individual generators and for the whole system. On the other hand, there are various viable options to provide flexibility on the demand side.

In order to provide ancillary services in DR programs, the Demand Side Management (DSM) is responsible for the planning, implementation, and monitoring of utility activities that are designed to influence customer's use of electricity, i.e., for handling the flexible loads. The consumers can control their loads by means of DSM policies and strategies or participation in DR programmes focused on controlling and reducing the electricity demand (Palensky and Dietrich, 2011). Then, the DR program can change the time pattern and magnitude of grid load. Usually, the main objective of DSM is to encourage users to consume less power during peak times or to shift energy use to off-peak hours to flatten the demand curve (Gelazanskas and Gamage, 2014). In Figure 1.1, a categorization of the DSM is shown (Gellings, 1985). Note that the load consumption can be rescheduled by reducing or increasing the consumption (Lund et al., 2015).

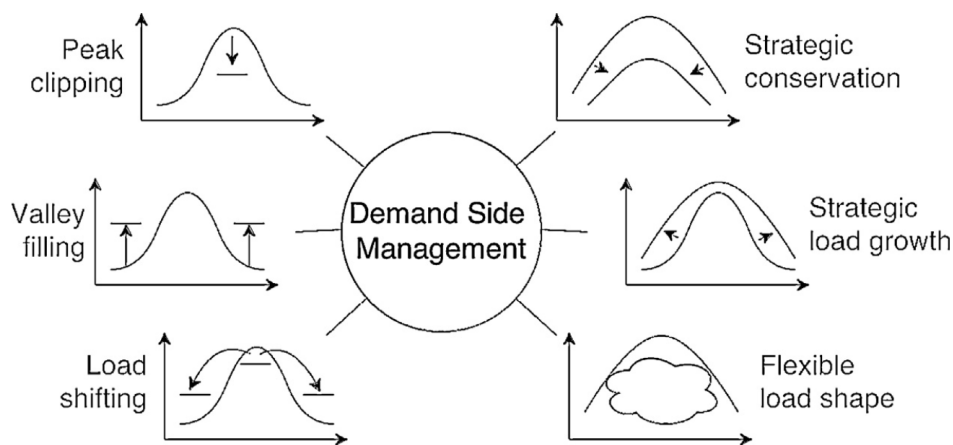


FIGURE 1.1: Categories of Demand Side Management.

Categories of DSM are possible due to the flexible consumption some loads have. Considering these loads, the energy that is not consumed in the service time, must be consumed after or before the service. Then, in this period, the energy consumption will increase generating a *rebound effect* or *payback* (UKERC, 2007; Palensky and Dietrich, 2011; Warren, 2014). Therefore, it must be evaluated in the aggregator, with the purpose of avoiding energy peaks after the service time.

Furthermore, flexible loads can be clustered into two categories: adjustable and deferrable loads (Hao et al., 2015b).

1.1.1 Adjustable loads

An adjustable load is an electric load whose energy requirement is flexible during its service time, i.e., it is flexible for all time service. For example, Thermostatically Controlled Loads (TCLs) are adjusted by modifying the temperature set-point fixed by the user, or WBPS are adjusted by altering the normal operating pressure set-point.

Thermostatically Controlled Loads

Usually, a hybrid model for TCLs is presented in literature, in which the power input of each unit has On-Off switching behaviour. Several authors consider a continuous TCL thermal model (Perfumo et al., 2014; Hao et al., 2015a; Mai et al., 2015; Luo et al., 2017; Hu et al., 2017a); while, others take into account discrete models (Du and Lu, 2011; Mathieu et al., 2012; Lu et al., 2013; Kara et al., 2015; Liu et al., 2016; Zhou et al., 2017). These models are expressed as a first-order ordinary differential equation. For example, continuous models can be written as,

$$\dot{\theta}^k(t) = a^k(\theta_a - \theta^k(t)) - m^k(t)b^kP^k + w^k(t) \quad (1.1)$$

where $\theta^k(t)$ is the internal k TCL temperature, a^k and b^k are constants defined in Eq. (1.2) and are expressed in terms of the thermal resistance R^k , thermal capacitance C^k , and coefficient of performance η^k . Additionally, θ_a is the ambient temperature, and $m^k(t)$ is a dimensionless binary variable that indicates the operating state of each TCL, i.e., 1 when it is On and 0 when it is Off. P^k is the TCL's rated power, it is positive for cooling mode and negative for heating mode. However, $m^k(t)P^k$ is generally considered continuous between 0 and a nominal power P^k , instead of a binary value. Moreover, $w^k(t)$ is the external disturbance such as occupancy and solar radiation,

which is normally disregarded.

$$a^k = \frac{1}{R^k C^k}, \quad b^k = \frac{\eta^k}{C^k} \quad (1.2)$$

For instance, household appliances such as water boilers/heaters, refrigerators, Heating, Ventilation and Air-Conditioners (HVAC) are referred to as TCL (Hu et al., 2017b). The model presented in Eq. 1.1 is a general formulation; however, there is no specific model for TERs as a flexible load.

The aggregate flexibility of a collection of TCL is defined in (Hao et al., 2015a). In (Zhao and Zhang, 2017), TCL flexibility is defined considering a geometric approach. A mathematical definition of flexibility for residential demand aggregation is presented in (Sajjad et al., 2016), formulated through two demand flexibility indicators by using the binomial probability model.

Regarding the buildings sector, there are several flexible loads that can provide regulation services, such as lighting, HVAC, computers and other electrical appliances that can increase or decrease the building consumption, see e.g. (Paschalidis et al., 2012). In (Bilgin et al., 2016), a smart building operator that is capable of modulating the aggregated energy consumption is considered with the purpose of providing regulation services. In (Ogunjuyigbe et al., 2017), a demand side load management technique is developed in order to maximize the user satisfaction and minimize the cost through a residential building load control. In (Blum and Norford, 2014), a dynamic model of a variable air volume system is developed and simulated. It is investigated the response of the system to four common demand response strategies over a range of cooling loads and implementation intensities. Also, it is demonstrated the use of the model to simulate a 10-min spinning reserve provision.

TCLs have been employed to provide regulation services by varying the temperature set point, see e.g. (Hao et al., 2015a; Mai et al., 2015). Model predictive control (MPC) strategies are developed in (Liu and Shi, 2015; Zhou et al., 2017), while in (Liu et al., 2016) is analyzed a distributed MPC. In (Hao et al., 2015a) a priority control is proposed. In addition, in (Yin et al., 2016) commercial and residential TCLs are modeled to quantify their flexibility. Regulation frequency can be operated by centralized controllers with a sample time of 4 seconds (Hao et al., 2015a), or with decentralized controllers capable of providing short duration services (Tindemans et al., 2015). Moreover, several TCL applications have been developed with optimal control systems for providing short duration services. For instance, in (Hao et al., 2012) an linear-quadratic regulator controller is capable of regulating the consumption every 2

minutes; or in (Liu and Shi, 2015; Mai et al., 2015) that regulates the power consumption of a heating and cooling system with an MPC strategy.

Regarding the TER unit, it is composed of a thermally insulated cabinet, in which the temperature has to be lower than the ambient temperature, the ThermoElectric Cooler (TEC) device, the heat exchangers at each side of the TEC device, and one or more electric fans powered by the same external power supply that powers the TEC. Usually, the TEC model is presented in an electro-thermal model that use analogies between thermal and electrical domains. In (Mitrani et al., 2005; Tsai and Lin, 2010; Hsiao et al., 2010) the model is expressed as,

$$Q_c = \alpha T_c I_p - \frac{1}{2} I_p^2 R_p - K_p (T_h - T_c), \quad (1.3)$$

$$Q_h = \alpha T_h I_p + \frac{1}{2} I_p^2 R_p - K_p (T_h - T_c). \quad (1.4)$$

where, Q_c and Q_h are the heat flow absorbed and rejected by the TEC, α is the Seebeck coefficient, K_p is the TEC thermal conductance, R_p is the TEC electrical resistance, T_c and T_h are the cold side and hot side temperatures of the TEC, and I_p is the TEC electric current. In (Arjun et al., 2017) and (Moria et al., 2019), the TEC model is used to test a portable TER feed with solar energy. In (Rahman and Wagner, 2016) a TER is experimentally compared with a vapour compression unit achieving a lower consumption in the TER unit. Moreover, physical properties such as the thermal conductivity of the material, the cooling capacity, and the temperature difference are the most sensitive parameters in the TER (Shen et al., 2020).

The usual marketable TERs contain a on/off temperature controller, which is cheaper and easier to be installed and sets the interior temperature of the thermoelectric compartment. Other control methodologies of a TER unit are Proportional-Integral (PI) control system, PI-Derivative (PID) control system (Astrain et al., 2012), and idling voltage control system (Martínez et al., 2013b). In (Rahman and Wagner, 2016), an amplitude modulation, and a pulse width modulation controller are tested to control the temperature. Likewise, the PWM controller is used in (Saifizi et al., 2018) to automatically correct the temperature using a feedback loop. A temperature-controlled voltage regulated boost converter is presented in (Azad, 2019). Actually, these controllers are for regulating the temperature set-point. However, from the best of the authors' knowledge, there is no reported flexibility analysis or aggregator for TER systems.

Water Booster Pressure Systems

A Water Booster Pressure System (WBPS) is responsible for supplying water and maintaining pressure in a building pipeline. The operation of the pump and tank are directly related to the building water consumption, thereby, a control system is required to satisfy the variable water demand. When the operating pressure is decreased, it generates a reduction in power consumption and in water pressure for the users, especially on the higher floors of the building.

Water pump systems are mathematically modelled in (Janevska, 2013) and simulated in (García et al., 2013; Ghafouri and Khayatzadeh, 2012). In (Latchoomun et al., 2019), a WBPS is designed with a modified storage able to control the pressure at the discharge of the tank. However, as far as the authors know, there are no studies modelling the WBPS as a flexible load. Existing models are based on basic laws of physics and fluid mechanics. These models develop each system element as,

$$J \frac{d\omega}{dt} = M_{MT} - (M_p + M_\zeta) \quad (1.5)$$

$$H = Aw^2 + Bwq_v + Cq_v^2 \quad (1.6)$$

$$\frac{dm(t)}{dt} = Q_{m1} - Q_{m2} \quad (1.7)$$

where Eq. (1.5) shows the motion for the motor-pump, therein, J is the moment of inertia (in specific cases, J is constant), ω is the angular velocity of the pump, M_{MT} is the active torque from the asynchronous motor, M_p is the passive/resistive torque of the pump, and M_ζ is the viscous torque. Moreover, Eq. (1.6) describes the characteristic behaviour of a centrifugal pump, where, A , B , and C are characteristic constants for the pump, and q_v is the pump flow. Eq. (1.7) expresses the change in mass in the tank $m(t)$, which is equal to the mass flow that enters the tank Q_{m1} minus the mass flow that leaves the tank Q_{m2} .

Buildings of considerable height present important challenges in pumping water to the upper floors (Brickey and Sanchez, 2005). Water Distribution Systems (WDS) can provide balancing services with demand response through pump scheduling. In (Menke et al., 2016), a branch and bound algorithm is proposed in order to offer financial benefits to the system operator. It is clarified that a large amount of water distribution systems would provide a short-term operational reserve, also a power reserve of 3 MW is estimated for the UK. Whereas in (Nguyen et al., 2014), a commercial building pumping system with a tank on the top is used as an energy storage component to respond to the market price and provide demand response services. This

approach is carried out by dynamic programming methods and a 30.9% saving in the electricity cost is achieved. Moreover, a WDS framework able to provide frequency regulation is proposed in (Oikonomou et al., 2018), in which the WDS can participate in DR by solving a Mixed-Integer Linear Programming (MILP) problem.

Pump systems can also be controlled as flexible loads by an aggregator. Then, pump system controls are based on two position controllers or variable frequency drives (Cabrera et al., 2015; Arun Shankar et al., 2016). Different techniques are used to control the input speed of the pump. For example, in (Ghafouri and Khayatzadeh, 2012; Xu et al., 2016) a PID controller is designed and evaluated in simulation, while in (Gevorkov et al., 2016) a Hardware-in-the-Loop simulator is carried out, where the variable speed driver is connected via a programmable logical controller. In (Coccia et al., 2019), a water loop heat pump of a supermarket is used in a DSM strategy to minimize the yearly energy cost, by shifting the electricity demand; whereas, in (Arteconi and Polonara, 2018), the heat pump flexibility of a building is used in off-peak hours by DR programs. However, no flexibility evaluation nor aggregator for WBPS systems is reported.

1.1.2 Deferrable loads

A deferrable load has a fixed energy requirement at the end of the service (Hao and Chen, 2014). For example, a pool pump must be switched on a determined amount of time by the end of the day and can provide regulation services by turning it on and off (Meyn et al., 2015); or an Electric Vehicle (EV) state of charge should be above a certain level at the departure time (Zhou et al., 2016).

Electric Vehicles

One of the most important flexible loads in terms of emissions reduction, variable power capacity, and promising useful green transport are the EVs. This technology is a sustainable alternative for private and public road transport. Therefore, countries such as Germany, Australia, Canada, U.S.A, among others, offer benefits in terms of subsidized, finance or facilities constructions to the customers (García-Villalobos et al., 2014).

The most common model reported in the literature can be applied for charging and discharging strategies. It can be modelled in continuous time (Diaz et al., 2015) or

discrete time ([Hao et al., 2015b](#); [You et al., 2016](#)). Then, the model in discrete form is,

$$x_{k+1}^i = x_k^i + P_k^i \delta \quad (1.8)$$

where x_k^i is the State of Charge (SoC) of EV i at time slot k , P_k^i is the injected power and δ is the discretisation step. This model consider an initial condition $x_0^i \geq 0$ for each EV i . Moreover, it must fulfil a final SoC which is selected by the EV owner, i.e.,

$$x_{d^i}^i \geq E_-^i \quad (1.9)$$

where d^i is the EV departure time and E_-^i is the minimum SoC at the departure.

In addition, specific models have been developed, for instance, in ([Papadaskalopoulos et al., 2013](#)), charging losses and self-discharging energy losses are considered; in ([Khemakhem et al., 2017](#)), the SoC is based on Coulomb counting, taking into account a lithium-ion battery; in ([González Vayá and Andersson, 2016](#)), an EV fleet model is considered as a virtual battery. However, to the best of our knowledge, an EV charger model as a flexible load is not reported in the literature.

EVs are among the most important deferrable loads, in terms of improving the RES integration in the grid ([Borba et al., 2012](#)), smoothing the demand curves ([Khemakhem et al., 2017](#)), providing frequency regulation services ([Wenzel et al., 2018](#); [Sortomme and El-Sharkawi, 2011](#)) and spinning reserve services ([Pavić et al., 2015](#)), incrementing self-consumption ([Giordano et al., 2018](#)), reducing emissions, and supporting green transport ([Noel et al., 2018](#)). In the last few years, EVs are becoming more and more a sustainable alternative for private and public road transport ([Cao et al., 2018](#)). Besides, national governments such as Germany, Australia, Canada, and U.S.A, offer benefits to the customers, in terms of subsidies, financing, or facilities constructions ([García-Villalobos et al., 2014](#)).

The charging of EVs can be managed in a context where the EVs are not allowed to inject power in the grid, or in the Vehicle-to-grid (V2G) context, where the EVs can inject power into the grid to support grid operation needs ([Quirós-Tortós et al., 2018](#)). In both cases, appropriate coordination strategies for EVs charging have to be defined to avoid that inappropriate EV dispatch gives unfavourable impacts to the power networks ([Haidar et al., 2015](#)), e.g., with over-currents in network branches or over-voltages at network nodes ([Sundström and Binding, 2012](#)). This dissertation addresses appropriate dispatching strategies for EV charging, excluding V2G operation. As such, there is no specific discussion on the aspects concerning V2G and its literature references.

Moreover, given the huge potential for EVs integration, it becomes necessary to assess not only the strategy to streamline the EVs battery charging process, but also the possibilities for the electrical grid to take advantage of the charging process. Typically, an aggregator coordinates EVs battery charging. A review of the EV fleets aggregator strategies is presented in (Hu et al., 2016), assessing the potential approaches to provide services to electrical grid operators. The challenge is to define how to manage the EV charging profiles with the purpose of fulfilling the users' requirements and offering a power flexibility capacity to the system operator for maintaining the energy balance in the grid. Specifically, the EVs flexibility to reduce the RES power fluctuations is quantified in (Schuller et al., 2015). The flexibility characterisation of EVs charging sessions is addressed in (Sadeghianpourhamami et al., 2018), with the introduction of two measures based on flexibility utilization in terms of energy and duration. A discussion on how the EV batteries management can unlock the potential of using Distributed Energy Resources (DER) is presented in (Mills and Macgill, 2018). A definition of EV flexibility is proposed in (Munshi and Mohamed, 2018) by adapting to case of EVs the framework introduced in (Sajjad et al., 2016) for the flexibility of aggregate residential demand. EV flexibility is described in (Wenzel et al., 2018) in terms of *laxity*, that is, the amount of time left until an EV must charge at its maximum charge rate to reach its minimum scheduled state of charge at the departure time. In (Grahm et al., 2014) the EV recharging flexibility is included in the EV utilization model together with the type of trip and the possible use of a secondary fuel.

For the EVs flexibility assessment, the EV dispatch problem has to be evaluated, also by considering different charging preferences for the EV owners (Clairand et al., 2018). For instance, a distributed control strategy is proposed in (Qi et al., 2014) based on the Lagrangian relaxation method to achieve charging coordination between multiple EV parking decks. In (Yang et al., 2014), risk-aware day-ahead scheduling and real-time charging dispatch for EVs are studied. The maximization of the revenues offering secondary regulation and the maximization of an EV fleet charging station efficiency are simultaneously addressed in (Janjic et al., 2017). The charging scheduling of a large number of EVs at a charging station is proposed in (Wang et al., 2017). A time-variant storage model for aggregated EVs has been proposed in (Pertl et al., 2019).

Other studies, also consider the minimization of the operating energy cost, in combination with the dispatching problem. To this aim, in (Esmaili and Goldoust, 2015), a multi-objective optimization framework is proposed, where the objectives include the

minimization of both the energy cost purchased by the aggregator and the grid energy losses. Conversely, (Škugor and Deur, 2015) focuses on a dynamic programming-based optimization to provide optimal solutions to charge an EV fleet. In (González Vayá and Andersson, 2016), it is proposed a co-optimization trade off between the cost of a day-ahead market and the revenues from providing balancing services.

The identification of energy-flexibility and deadline-flexibility referring to EV co-ordinated charging is carried out in (Sun et al., 2018) by first formulating a social welfare maximization problem, followed by an on-line auction. The coordination can include either the EV owner participation to decide adjustable limits for the EV charging demand (Zhou et al., 2016), or the incorporation of vehicle-originated signals that incorporate various information into two synthetic variables to make the information exchange with the aggregator more effective (del Razo et al., 2015).

1.2 Organization and thesis contributions

The dissertation is organized in chapters and each one can be read independently. Figure 1.2 depicts the organization of the thesis, numbered by the respective chapter and their roles in the aggregator framework.

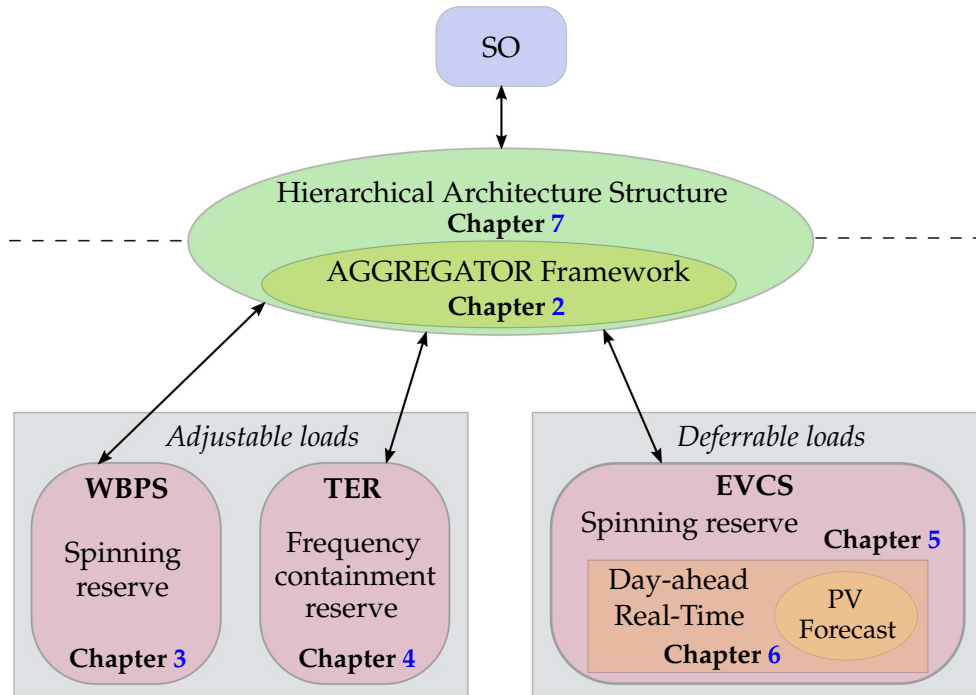


FIGURE 1.2: Thesis organization.

First, in Chapter 2, a methodology for loads aggregation is proposed. The aim is to provide ancillary services to the system operator by controlling the power consumption in the loads. Then, ancillary services are explained by defining the response time of each service. Moreover, the methodology considers the exchange signals between the aggregator and flexible loads. Finally, the main contribution of this Chapter is a framework for loads to provide ancillary services.

In Chapter 3, WBPS dynamics are modelled by first-principles and tuned by experimental data of a 6-floor university building with a single WBPS. Then, it is shown that the WBPS can provide spinning reserve services to the grid, by evaluating its flexibility through set point changes. In order to evaluate flexibility, the effect of parameters such as minimum and maximum consumption levels, the amount of required energy, limitations in commutation frequency and turn-on time, on power consumption are evaluated. Finally, an aggregation strategy, which responds when the system operator requires a power reduction service, is proposed. Thus, the main contributions of this Chapter are: 1) a model of WBPSs as flexible loads validated with experimental data; 2) the definition of the energy service that the system can provide to the grid; and 3) the design of a control architecture that leads to providing the energy service with a set of WBPSs. The results of this Chapter were derived in the publications (Diaz et al., 2017a,b).

In Chapter 4, a TER dynamic model is developed and characterized by experimental data. Then, it is shown that modifying the TER temperature controller, this system can provide balancing services such as frequency containment reserve, through changing the temperature set-point. A flexibility analysis is carried out in a set of TERs considering different TER capacities, TER normal operation set-points, and variations on ambient temperature and thermal disturbances. Finally, an aggregator controller is proposed. It is able to reduce or increase the power consumption in a set of TERs when the system operator requires the service. Therefore, the main contributions of this Chapter are: 1) the TER model as a flexible load characterized by experimental data; 2) a flexibility analysis based on the modification of a tested PI controller; 3) the definition of the frequency containment reserve (it can provide more balancing services) as the energy services a set of TERs can provide to the electrical grid.; and 4) the design of an aggregator able to provide the energy services. The results of this Chapter were derived in the publications (Enescu et al., 2018; Diaz-Londono et al., 2019b, 2020a).

Chapter 5 presents the evaluation and the maximization of the EV flexibility degree to provide flexibility, together with a dispatch that minimizes the operation costs. An

Electric Vehicle Charging Station (EVCS) and its chargers are modelled and controlled as flexible loads. Then, it is shown that EV chargers can provide spinning reserve services to the grid. The EVCS is entrusted with charging all the incoming EVs, whose State of Charge (SoC) must reach at least the minimum amount desired by the EV owners at the departure time. From this perspective, two EV charging strategies are formulated taking into account the EV users preferences. First, a novel formulation that minimizes the EVCS operation cost is presented. Second, a strategy that maximizes the flexibility capacity, while minimizes the EVCS operation cost is proposed. These strategies are compared with a typical minimum time strategy as a benchmark, to adjust the trajectories of the charging power delivered to the EVs through the chargers. Thus, the main contributions of this Chapter are: 1) a dynamic model of an EV charger as a flexible load; 2) a specific flexibility definition for EV chargers; 3) a novel formulation for minimizing the EVCS operation cost; and 4) a novel optimal strategy that maximizes the EV charges flexibility capacity while minimizes the EVCS operation cost that leads to providing spinning reserve services. The results of this Chapter were derived in the publications ([Diaz et al., 2018a,b](#); [Diaz-Londono et al., 2019a](#)).

Chapter 6 presents strategies for an EVCS to participate in Day-Ahead (DA) and Real-Time (RT) markets considering distributed renewable sources. Thus, the main contributions of this Chapter are: 1) a Photo-Voltaic (PV) generation model for *Bogotá, Colombia*; 2) an EVCS DA strategy that minimizes the operation cost; and 3) a RT controller strategy that aims to follow a DA power schedule. The results of this Chapter were derived in the publications ([Diaz-Londono et al., 2020b](#); [Giordano et al., 2020](#)).

In Chapter 7, a Hierarchical Architecture Structure (HAS) is presented with the purpose of providing the European Balancing Services with the flexible loads studied in this dissertation. The structure coordinates the power demand of all the aggregators and works as a balancing service provider. Then, the main contributions of this Chapter are: 1) the proposal of a two hierarchical level control, considering the flexible loads' aggregators, and 2) a logic coordinator able to manage the sequence of the balancing services provided.

Finally, it is highlighted that the mathematical notation is independent of the chapters. However, some variables are maintained such as power P .

Chapter 2

Ancillary Services Provision by Load Aggregation

In this chapter, a framework for flexible loads aggregation is proposed, developing aggregators able to provide Demand Response (DR) services in Smart Grids. DR programs can be classified into two main categories: Incentive-Based Programs (IBP) and Priced Based Programs (PBP) ([Albadi and El-Saadany, 2008](#)). In this aggregation framework, the IBP is considered, avoiding dynamic pricing rates and the strategic behavior of the aggregator or the customers ([Vuelvas and Ruiz, 2017](#)), which are analysed in PBP. In IBP, participating customers receive participation payments usually as a bill credit or discount rate for their participation in the programs, depending on the amount of load reduction during critical conditions. Direct Load Control (DLC) programs are included in IBP, where the utilities have the ability to remotely shut down participant equipment on short notice. Moreover, it is assumed that customers voluntarily participate in DLC.

Therefore, in this dissertation, DLC strategies are performed by aggregators in order to offer ancillary services and participate in day-ahead and real-time markets. Indeed, an aggregator faces a two-level challenge, a customer level, and a wholesale market level ([Mahmoudi et al., 2017](#)). At the customer level, the aggregator looks for performing RD programs with the lowest cost, by modelling technical constraints in both users preference and the loads' operation. On the other hand, in the wholesale market level, the aggregator aims to determine the optimal trading options in the market, which is not the aim of this framework. This dissertation seeks for developing aggregators taking into account the customer level, where the problem is how to control loads with the purpose of offering different ancillary services to the electrical grid.

The chapter is organized as follows. Section [2.1](#) introduces the Smart Grid scheme

where the aggregators are considered, presenting the hypotheses of this framework. In Section 2.2, ancillary services are explained based on its time response. Section 2.3 presents the aggregator design criteria that can be applied to flexible loads. Finally, Section 2.4 formulates the proposed methodology for loads aggregation.

2.1 Smart Grid Approach

A general Smart Grid scheme with power generation and demand is shown in Figure 2.1. This Smart Grid can be evaluated in three elements: Generation, Demand, and an Aggregation system. First, on the generation side, conventional and renewable energies are included. It is assumed the energy networks and its communications are ideal, i.e., there are no energy losses in the distribution system nor problems from latency or distance in the communication. Indeed, these issues can be minimized for example by considering that generation and demand are close to each other. Therefore, both sources send their available energy generation to a System Operator (SO), particularly to a Distribution System Operator (DSO), which tries to maintain the energy balance in the electrical grid. Moreover, this system is not only in charge of collecting the total generation information but also the inflexible demand requirements. Second, on the demand side, flexible and inflexible loads are located. Third, the Aggregation system aims to control the demand consumption of the flexible loads, with the purpose of providing ancillary services and fulfilling the SO requirements. This system has a Hierarchical Architecture Structure (HAS), in which there is a central allocator (High Logic Coordinator - HLC) entrusted of assigning energy services to the different linked aggregators (see Chapter 7). Therefore, the Aggregation system is located in the middle of generation and demand.

In this dissertation, Photo-Voltaic (PV) integration is taken into account as a renewable source, but, with the possibility to extend later the results to wind energy or another green source. Moreover, several flexible loads studied in section 1.1 such as Water Booster Pressure Systems (WBPS) (see Chapter 3), ThermoElectric Refrigeration (TER) units (see Chapter 4), and Electric Vehicles (EV) chargers (see Chapter 5) are evaluated. Flexible loads can be controlled by smart meters that are associated with them (Siano, 2014). This framework considers devices like power, temperature, pressure and radiation meters, EV chargers, among others. It is assumed that these monitoring systems have no operating nor communication problems. Then, Aggregators take advantage of these smart meters to control and monitor each flexible load consumption, according to the SO requirements and the variability reported from the

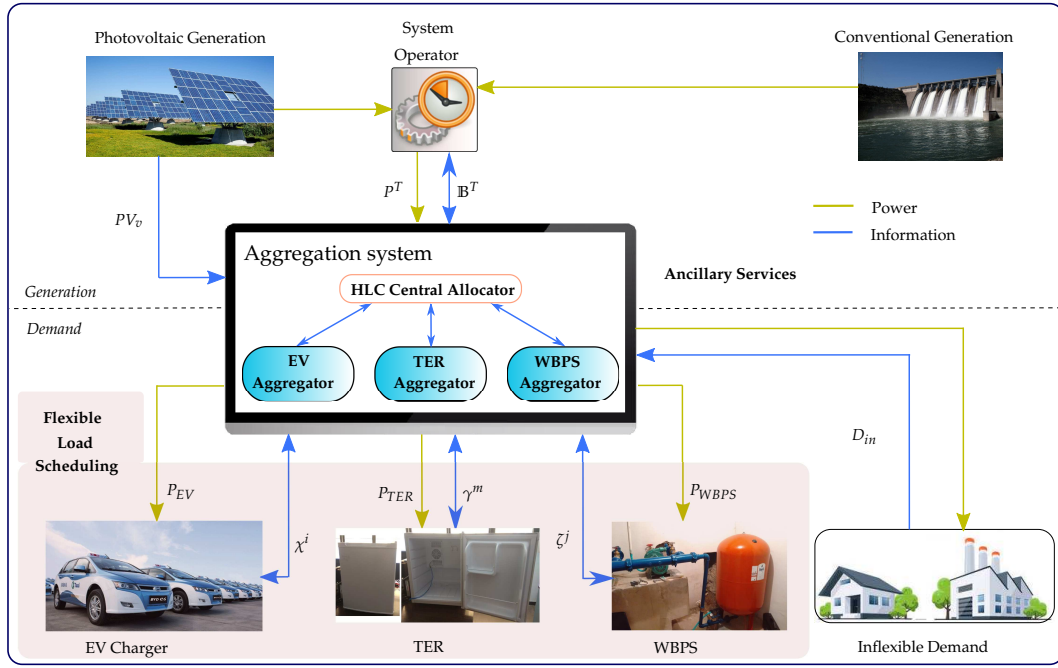


FIGURE 2.1: Aggregators for flexible loads.

PV generation. In addition, it is assumed that the operational decisions of the Aggregation system are purely technical. The economic variables, such as energy prices or market biddings, are given as inputs.

Besides, on account of the particularities on flexible loads such as dynamics, communications protocols, and hardware, the response times scales between them are different, leading each load to offer a specific energy service. For example, WBPSs are able to respond in less than 10 min (see subsection 3.2.2), TERs can respond in seconds (see subsection 4.2.1), and EV chargers have a few-minute response (see Section 5.2). Therefore, each Aggregator is capable of providing an ancillary service to the grid, given the possibility to define different consumption schedules in the flexible loads. The following section explains ancillary services.

2.2 Ancillary Services

Security problems emerge due to the imbalance between load and generation in power systems, for example, large frequency deviations can make the system collapse. Hence, in order to avoid system instabilities, DR programs can deliver ancillary services for the SO (Siano, 2014). SO and regulatory authorities of different countries have defined diverse specifications and standards for the energy services required in their systems.

Nevertheless, the aim is always the same: the safe, secure and reliable operation of the power grid (Pandurangan et al., 2012). These services are provided depending on the component that unbalances the system (Hao et al., 2015a). In consideration of the system needs in terms of operating requirements, ancillary services can be divided into four main categories: stability control, voltage control, system restart, and frequency control. However, load flexibility is only suitable for providing frequency control (Carreiro et al., 2017). In (Lund et al., 2015), grid ancillary services are divided into four categories based on their response time, as,

- *Very short duration*: milliseconds to 5 min.
- *Short duration*: 5 min to 1 h.
- *Intermediate duration*: 1 h to 3 days.
- *Long duration*: several months.

2.2.1 North America

Ancillary services are usually classified according to the time-scale in which they respond, controlling mechanisms that rule their coordination, and type of event they must respond to. According to (González et al., 2014), the Federal Energy Regulatory Commission (FERC) definitions of reserves applied in North America are:

- *Regulation*: This service can be provided by units that respond, varying their power production, within 15 - 30 seconds for fast changes in frequency (Baccino et al., 2014). Regulation services can be provided only by on-line units (Kirschen and Strbac, 2004). They are controlled by an Automatic Generation Control (AGC). In North America, markets like PJM (Forward Market Operations, 2017) and New-England (ISO New England Inc, 2006) call this service Frequency Regulation. Power delivery in this service should last between 10 and 15 minutes (Kirby, 2004).
- *Spinning reserve*: This service is any backup energy production capacity, synchronized to the grid, that can be made available to a transmission system immediately in order to restore the generation and load balance in the event of a contingency, and once on-line, can operate continuously for a period of time established by the local system operator (Kirby et al., 2008). Units must be fully on-line within 10 minutes to provide this service. Besides, this service should be maintained for at least 105 minutes.

- *Non-spinning reserve*: It is any backup energy production capacity that can be made available to a transmission system in the event of a contingency, similar to spinning reserve. The difference is that non-spinning reserve does not require the permanent synchronization of the unit to the grid, but rapid start up and total availability must be guaranteed within 10 min. Moreover, spinning reserve is more valuable economically for the SO, because it is usually worth 2 to 8 times as much as a non-spinning reserve on an annual average basis (Kirby et al., 2008). Besides, this service should be maintained for at least 105 minutes (Kirby, 2004).
- *Replacement reserve*: This service is used to substitute the faster and more expensive reserves so as to reduce regulating cost, it must be supplied within 30 min at the latest. Besides, this service should be maintained for four hours (Kara et al., 2014).

Balance problems can be handled by DR initiatives in the energy consuming sectors. In (Haeri et al., 2014), winter DR achievable potential is estimated for each sector during peak periods, obtaining 130 MW for the residential, 78 MW for the commercial and 4 MW for the industrial sector in the Puget Sound region of the Northwest United States. Moreover, in order to solve balance problems, these sectors take advantage of several flexible loads that can provide energy services to the grid.

2.2.2 Europe

The SOs in Europe use different processes and products to balance the system and restore the frequency. In this sense, the Commission Regulation (EU) 2017/2195 of 23 November 2017 (The European Commission, 2017) sets up the requirements for the technical parameters of standard products in order to facilitate the exchange of balancing energy across borders.

The standard structure is presented in Figure 2.2. The preparation period is the time required to receive the signal and activate the service. Then, there is a ramp-up period, followed by the delivery period, and finally the ramp-down period. The request for the ramp-down period is not specified in the current versions of the rules. Indicatively, the ramp-down period can be similar to the full activation time. The technical parameters of the standard structure are aligned with operational flexibility indicators presented in studies such as (Makarov et al., 2009) and (Ulbig and Andersson, 2015), where the defined metrics are the power provision capacity, power ramp-rate capacity, and ramp duration. Notice that these indicators can be obtained with the information in Figure 2.2.

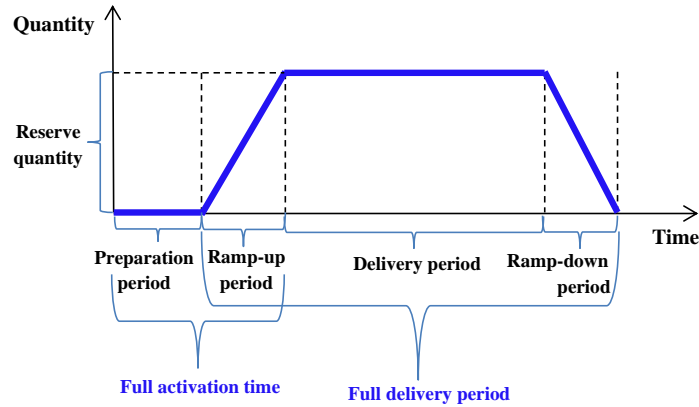


FIGURE 2.2: Standard structure of balancing services provision.

Considering the guideline on electricity balancing, presented by the Commission Regulation ([The European Commission, 2017](#)), the balancing energy services in Europe are organised as:

- *Frequency Containment Reserves (FCR)*: The active power reserves available to contain system frequency after the occurrence of an imbalance. During the ramp-up period, it requires the delivery of 50% of the reserve within 15 s, and 100% within 30 s. The FCR rules also specify that this delivery should be sustained for 15 min. In addition, the FCR must have automatic activation ([European Commission, 2017](#)).
- *Frequency Restoration Reserves (FRR)*: The active power reserves available to restore system frequency to the set point and, for a synchronous area consisting of more than one load-frequency control area, to restore power balance to the scheduled value. The standard FRR can be activated manually ([ENTSO-E, 2018a](#))¹ or automatically ([ENTSO-E, 2018b](#))¹; the full activation time for the first one shall be 12.5 min, while for the second is 5 min. Moreover, for both FRR services, the delivery should be for 15 min.
- *Replacement Reserves (RR)*: The active power reserves available to restore or support the required level of FRR to be prepared for possible additional system imbalances. The full activation time of the RR service is 30 min, considering the preparation and the ramp-up periods from 0 to 30 min. Moreover, the duration of the delivery period is between 15 min and 60 min; whereas, the activation of the service is scheduled with manual activation ([ENTSO-E, 2018c](#))¹.

¹At the current stage, the specifications referring to FRR and RR are still under development. Technical characteristics have to be considered as the ones currently available on the official ENTSO-E website.

Figure 2.3 depicts how the balancing services are deployed in case of a grid imbalance. Then, the use of these services is divided into four steps, i.e., the services FCR, aFRR, mFRR, and RR. The figure presents the idealized case, where all the services are synchronized for providing a constant energy consumption. Besides, it is shown the timings of the services after a disturbance in the frequency. Then, the first response is given automatically by the FCR; to release the FCR, aFRR is activated (when necessary). Later, to release the aFRR, mFRR is activated; finally, RR activation is performed.

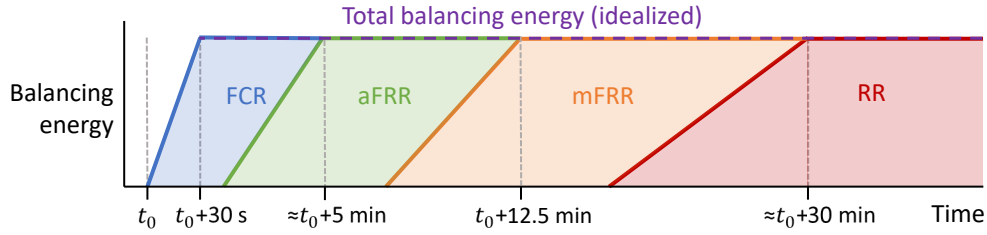


FIGURE 2.3: Balancing market processes for frequency restoration.

These balancing services are actions that the SO continuously takes to ensure the system frequency as well as the compliance with the reserve amount needed. Therefore, the SO function is to ensure that demand and supply remain balanced by operating the system close to real-time. Figure 2.4 presents the electricity market sequence. Then, the balancing market considers three main actors, i) the SO, ii) the Balancing Service Provider (BSP), and iii) the Balancing Responsible Party (BRP). The BRP submit the energy schedule to the SO, reporting the planned generation and consumption, as well as the computation of the Imbalance Settlement Period (ISP). Moreover, the BSP (i.e., the aggregator), submits the balancing service to the SO; whereas, the SO is responsible for resolving the power imbalances within the ISP by activating the BSP service. The ISP time frame is generally 15 min.

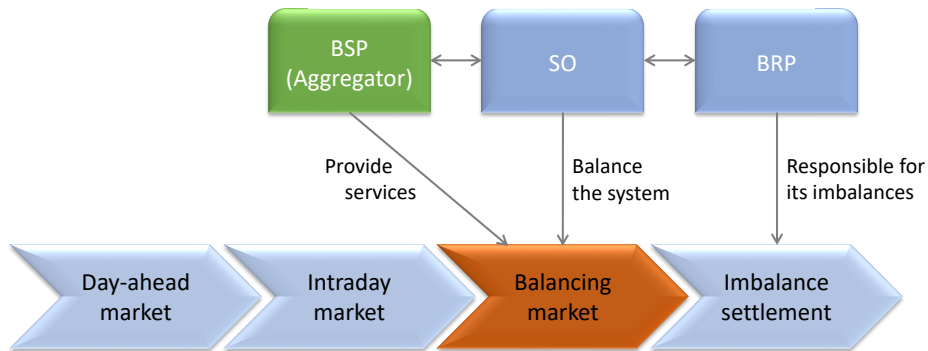


FIGURE 2.4: Electricity markets sequence and its participants.

2.2.3 Colombia

According to (CREG, 2018) the current Colombian ancillary services are:

- *Primary regulation reserve*: It is provided by the generators capable to have an immediate response; then, the full activation time is up to 10 s, and the duration of the delivery period should be at least 30 s.
- *Secondary regulation reserve*: It is provided by the spinning reserve of generators able to respond in 30 s (full activation time). The duration of the delivery period should be at least 30 min. This reserve is used by the Automatic Generation Control (AGC) for injecting or reducing power to arrive at the nominal frequency.
- *Additional reserves*: In normal conditions, they are used to restore the secondary reserve. These reserves can be classified in sub-reserves such as hot reserve, operative reserve, or cold reserve.

Moreover, the energy Colombian market is moving into a more international approach, considering the following categories in the ancillary services:

- *Primary regulation reserve*: The full activation time is 10 s and must start before 5 s. The duration of the delivery period should be 5 min. The service activation is automatic.
- *Secondary regulation reserve*: The full activation time is 5 min and should start before 10 s. The duration of the delivery period is 15 min. The service activation could be automatic or manual.
- *Tertiary regulation reserve*: The full activation time is 5 min. The duration of the delivery period is 2 h. The service activation could be automatic or manual. Moreover, the *Additional reserves* such as spinning reserve, operative reserves, and cold reserves (activation time is 15 min) are managed in the tertiary regulation reserve.

2.3 Aggregator Design

The Aggregation system (i.e, the HAS) in Figure 2.1 is in constant communication with the SO through a Central Allocator that receives the generated power information \mathbb{B}^T . Additionally, this Aggregation system gets information on the PV generation uncertainty PV_v . The Aggregation system includes the aggregators, i.e., the flexible load aggregators. They are designed to manage the consumption of each flexible load (cases

of study). Then, the Central Allocator seeks to distribute the ancillary services into the flexible loads' aggregators, depending on each response time scale of the loads. For instance, the allocator assigns the frequency containment reserve and frequency restoration reserve (very short duration) as well as replacement reserves (intermediate duration) services to the TERs aggregator (see subsection 4.2.2), and the spinning reserve service (short duration) to the WBPSs (see Section 3.3) and EV chargers (see subsections 5.3.2 and 5.3.3) aggregators. Thus, depending on the SO request, the central allocator sends the request to the suitable flexible load aggregator. Furthermore, the Aggregation system can participate in Day-Ahead (DA) (see Section 6.3) and Real-Time (RT) (see Section 6.4) markets.

Aggregator plays fundamental role in taking advantage of the end-consumption, by creating customized, automated controls for consumer loads and appliances that enable remote access, while taking into consideration preferences and behavioural patterns. In (Ikäheimo et al., 2010), an aggregator is defined as *"a company who acts as an intermediary between electricity end-users, who provide distributed energy resources, and those power system participants who wish to exploit these services"*. There are other definitions that can be restricted or expanded depending on regulations that define the roles and activities that aggregators can perform.

In order to develop the Aggregation system, each flexible load aggregator is carried out independently. Note that each one is built in a centralized structure, but, the loads are distributed. Moreover, aggregators look to guarantee the service time, avoiding the rebound effect, minimize the exchangeable information with the loads, among others. Then, the Aggregator design process considers:

Signal to be controlled. It depends on the model dynamics. Then, a control signal identification in the flexible load that allows manipulating the power consumption is necessary, without affecting significantly the load operation.

Service to be provided. The aim is to provide an ancillary service to the SO. The service type is determined by the load response time and is delivered when the SO requires it.

Bilateral communication with the SO. The Aggregator not only offers the flexibility capacity the load has over a period of time, but also the required demand power prediction. Then, the SO informs on generation capacity limits, and guidelines to perform the ancillary service.

Bilateral communication with the flexible load. The Aggregator is entrusted with loads consumption management, i.e., each load consumes at every time slot as the controller decides. Therefore, each load provides its state information to the Aggregator with the purpose of delivering the correct control action.

Market Information. For example, the time-variant energy prices.

This aggregator design process can be applied to several flexible loads and can be developed through classical and optimal control strategies. For instance, first, a WBPS aggregator that modifies the amount of energy consumed by a set of WBPSs is studied in order to follow a SO reference power signal. It can be developed by modifying the pressure set-point, which is performed in each system with a binary signal (see Chapter 3). Second, a TER aggregator able to reduce and increase the power consumption of a set of TERs is assessed. The power consumption can be managed by changing the temperature set-point state, which considers three-states (see Chapter 4). Third, an EV charger controller is evaluated by considering different charging power trajectories for the EVs connected to the station. It can be carried out with an optimal control strategy that maximizes the flexibility capacity and minimizes the station operating costs (see chapters 5 and 6).

2.4 Load Aggregation Methodology

The proposed methodology is developed in four phases, going from an individual load analysis to a complex system of aggregators assessment.

2.4.1 Flexible load modelling

In order to develop models of flexible loads, some general characteristics should be evaluated:

1. A state of the art review of the currently proposed load models.
2. An identification of a manipulable variable that has the possibility to modify the power consumption of the load is required.
3. A setup of the modification limits that the variable can reach, with the aim of not modifying significantly the load operation.
4. An evaluation for understanding if the load can increase and decrease its electrical demand.

Therefore, case studies of flexible loads are evaluated. First, WBPSs are modelled considering the pressure in the tank and the centrifugal pump switching (see the model in Section 3.1). Second, the TER model takes into account the internal temperature (see the model in subsection 4.1.1). Third, taking into consideration an EV charging station, EV chargers dynamics are modelled (see the model in subsection 5.1.2).

2.4.2 Flexibility analysis

Once the flexible load model is developed, the following features should be analysed for defining the ancillary service.

1. The load response time in front of modifications in the variable parameter.
2. The time the load can keep the modification of power consumption.
3. The power capacity and periods of time the load can modify its consumption.

Therefore, WBPSs and EV chargers are able to provide the spinning reserve service, and TERs can offer the frequency containment reserve and balancing services.

2.4.3 Flexible load aggregator design

Note that, due to the different types of flexible loads dynamics, different control strategies are needed. They are developed considering classical and optimal controller techniques. Then, with the purpose of designing each aggregator, considerations of Section 2.3 are followed.

Regarding the case study, several flexible load aggregators are taken into account. For example, the WBPS power consumption can be controlled by changing the normal operating tank pressure set-point. Therefore, a Gain-scheduled Proportional Integral (PI) controller is developed for following a reference signal provided by the SO (see subsection 3.3.2). Moreover, TER power consumption can be controlled by modifying the operating internal temperature set-point. Hence, a PI and sequential controller are proposed for fulfilling the power SO requirements (see subsection 4.2.2). Another instance, EV chargers can be controlled by applying optimal control techniques. Then, an Model Predictive Control (MPC) strategy can handle the power delivered by chargers of a station to the connected EVs, compensating uncertainties originating from PV generation fluctuations (see Section 6.4) and price variations (see subsections 5.3.2 and 5.3.3).

2.4.4 Evaluation of the proposed aggregator by simulation

With the purpose of assessing and validating the flexible loads controllers, simulations of each one are developed in MATLAB® software and Simulink tool.

The application of this methodology is aimed at the Bogotá, Colombia conditions. Then, the EV taxis, buildings and weather characteristics of Bogotá are considered, analysing the solar variability based on historical data (see section 6.2).

In addition, the WBPSs aggregator considers water flow measures as an input acquired in a Bogotá university building (see subsection 3.1.1). The aggregator simulation is carried out by considering a set of WBPSs with different parameters of tank volume, pump capacity and water flow demanded. Moreover, the TERs aggregator considers disturbances that were characterized by an experimental test. The simulated PI controller used for managing the temperature in each TER is validated in a real TER (see subsection 4.1.5). The TER aggregator simulation is developed by taking into account a set of TERs with different thermal resistances and capacities, ambient temperature, and disturbances. Besides, in the EV chargers aggregator, the EV arrival state of charge uncertainty is analysed (see subsection 5.4.1), and a Monte Carlo analysis is performed to evaluate operation costs and savings (see subsection 5.4.3).

Finally, aggregators are validated by simulations fulfilling the response time and the power capacity variation requested by the SO.

2.5 Remarks

In this Chapter, a framework for flexible loads has been proposed, allowing to develop aggregators for diverse types of loads. Then, the aggregator design parameters are presented.

Moreover, a load aggregation methodology is proposed, assessing the load characteristics and the load flexibility for defining the ancillary service, the flexible load can provide. The application of this methodology is presented in the following chapters.

Notice that the Aggregation system or hierarchical architecture structure can add flexible load aggregators without affecting the operation of the other aggregators. As future work, this structure can be improved by developing strategies not only for bidding in the ancillary services market but also for defining the services remuneration.

This approach leads to a new perspective for aggregating loads with a clearly defined structure, as well as the research in aggregating aggregators with low communication parameters.

Chapter 3

Modelling and Control of Water Booster Pressure Systems

In this chapter, a Water Booster Pressure System (WBPS) is modelled and controlled as a flexible load. This system is responsible of supplying water and maintaining pressure in a building pipeline. The operation of the pump and tank are directly related to the building water consumption, thereby, a control system is required to satisfy the variable water demand. When the operating pressure is decreased, it generates a reduction in power consumption and in water pressure for the users, especially on the higher floors of the building. This work aims at modifying the system operating pressure, not cutting the water supply in the building or stopping the WBPS operation, limiting the discomfort caused to the consumers.

The chapter is organized as follows. Section 3.1 describes the model of the system, taking into account the centrifugal pump and the pressure tank, for later being implemented in a simulation. Section 3.2 explains the flexibility that a WBPS can have in power consumption and also defines the energy service that the system can provide. Section 3.3 shows the proposed aggregation architecture, its aim is to respond to a request of power consumption reduction, sent by the SO. The results of this Chapter were derived in the publications ([Diaz et al., 2017a,b](#)).

3.1 System model

In order to determine the potential of a Water Booster Pressure System (WBPS) for use as flexible load, a model that can reproduce its dynamics is built. This section presents a model of a WBPS settled and validated with experimental data. It begins explaining the general operation of the system, then the model is proposed and compared with

experimental data. Table 3.1 summarizes the nomenclature and units of the system variables.

Figure 3.1 shows a WBPS. The system stores energy in the tank as compressed air with the purpose of guaranteeing a minimal pressure in all the pipelines and taps of the building. The system acts supplying water from the reservoir to the tank by the centrifugal pump, compressing the air and increasing the pressure. Then, water with high pressure flows to the hydraulic network.

The model of a WBPS can be split into two sub-systems. These elements are the pressure tank and the centrifugal pump, the actuator driving the pump is an asynchronous motor. In the model development, electric transients generated during the motor start and stop are not considered due to their reduced duration and energy consumption.

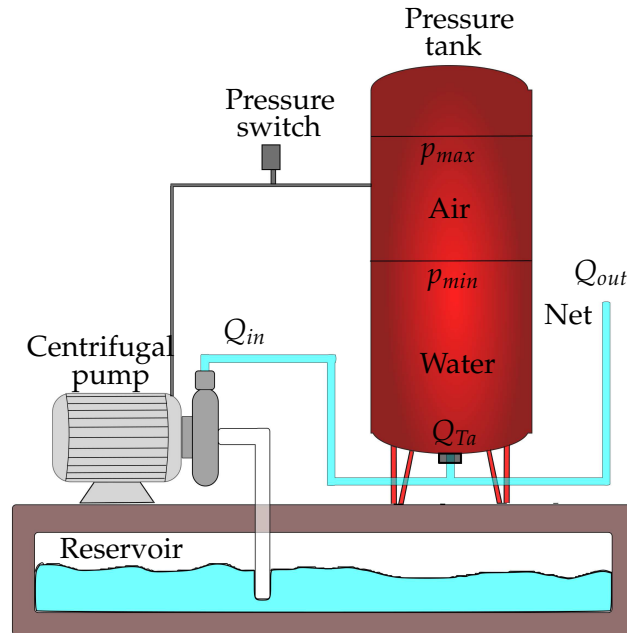


FIGURE 3.1: Water Booster Pressure System (WBPS).

The following equations describe the dynamics of the WBPS:

$$\dot{V}_f(t) = Q_{Ta}(t) = Q_{in}(t) - Q_{out}(t) \quad (3.1)$$

$$p_{air}(t) = (p_{pr} + p_a) \frac{V_T}{V_T - V_f(t)} - p_a \quad (3.2)$$

$$P_{Cp}(t) = \frac{(p_{air}(t) - p_a) * Q_{in}(t)}{c_u \eta} \quad (3.3)$$

TABLE 3.1: Nomenclature and units of the WBPS system variables.

Symbol	Variable	Units
V_T	Tank volume	l
V_f	Water volume in the tank	l
p_{air}	Tank air pressure	bar
p_{min}	Lower pressure limit	bar
p_{max}	Upper pressure limit	bar
p_{pr}	Pre-load pressure in the tank	bar
p_a	Atmospheric pressure	bar
p_{tap}	Minimum pressure in the tap	bar
Q_{in}	Centrifugal pump actual flow	l/s
Q_{Cp}	Centrifugal pump nominal flow	l/s
Q_{Ta}	Pressure tank flow	l/s
Q_{out}	Hydraulic network flow	l/s
P_{Cp}	Power consumed by the pump	kW
η	Electric pump efficiency	%
c_u	Scaling factor	-
Δt	Controller sampling time	s
T_s	Registered sample time	s
T	Controller sample time	min
AQ_{Cp}	Activates the water flow rate	-
ρ	Water density	kg/m ³
g	Gravity	m/s ²
h	Building height	m
r	Reference signal	kW
e	Error signal	kWh
β	Number of systems that should enable the flexibility	-
E_T	Total energy demand	kWh
P_T	Total power	kW
P_{a_i}	Power in the WBPS i	kW
y	Power reduction of the set of WBPSs	kW
n	Amount of systems	-
C_{PI}	Control action	-
k_p	Proportional controller constant	-
k_i	Integral controller constant	-
α_0, α_1	First-order constants	-
γ_0, γ_1	First-order constants	-

Eq. (3.1) follows from water mass conservation in the tank. Eq. (3.2) is given by the Ideal Gas Law, assuming constant air temperature and mass. Eq. (3.3) is the power delivered by the pump, assuming zero head and no pressure drop in the pipes. c_u is a scaling factor for obtaining $P_{Cp}(t)$ in kW.

Flow Q_{in} depends on the system state and, in most existing systems, it is regulated by an ON/OFF control law with hysteresis, following Eq. (3.4), where Δt is the controller sampling time and $k \in \mathbb{Z}$ is the discrete time variable.

$$Q_{in}(k\Delta t) = \begin{cases} Q_{Cp} & \text{if } p_{air}(k\Delta t) \leq p_{min} \\ Q_{in}((k-1)\Delta t) & \text{if } p_{min} < p_{air}(k\Delta t) < p_{max} \\ 0 & \text{if } p_{air}(k\Delta t) \geq p_{max} \end{cases} \quad (3.4)$$

The upper limit p_{max} is bounded by the safe operating conditions of the piping system, while p_{min} must allow to serve the highest points in the building, i.e.,

$$p_{min} > \rho gh + p_{tap} \quad (3.5)$$

where p_{tap} is the minimum pressure in the tap, h is the height of the building, g is the gravitational constant and ρ is the water density.

3.1.1 Experimental data acquisition

In order to adjust and validate the WBPS model described in the previous subsection, experimental measurements were recorded in a 6-floor building with a single WBPS, with a tank of 200 l fed by a 1.5 kW centrifugal pump. This is a university building of labs and offices that is open to the public twenty-four hours a day. There are around 200 people staying in it at working hours, i.e., arriving between 7:00 and 9:00, and departing between 16:00 and 18:00. Additionally, there is a variable number of students (around 600 people at any moment) going in and out through a day. The main end-uses of water are toilets, kitchens, and laboratories.

With the purpose of knowing the WBPS behaviour on a normal day, P_{Cp} was measured as the electric power absorbed by the centrifugal pump, Q_{out} was registered by an ultrasonic flow sensor, p_{min} and p_{max} were extracted from the ON/OFF controller. The sample time is $T_s = 10$ s. Table 3.2 shows the parameters of the system. Figure 3.2 shows equipments installation for the data acquisition, in which the red boxes exhibit

how P_{Cp} was measured, and in the yellow ones Q_{out} . Experimental data were measured on February 26 of 2015.

TABLE 3.2: Parameters of the WBPS employed in the experiments.

Symbol	Value	Units
V_T	200	l
p_{min}	1.52	bar
p_{max}	2.90	bar
p_a	0.75	bar

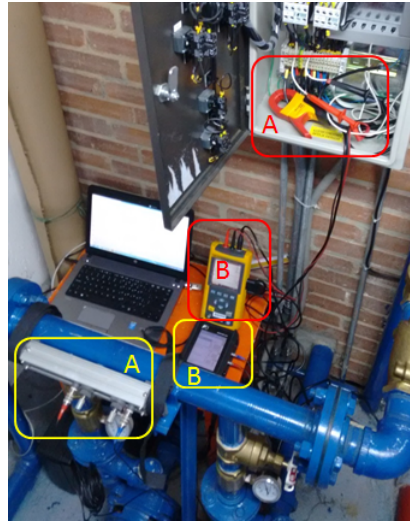


FIGURE 3.2: Power and Flow Measurement in the pump room.

In Figure 3.3a, the measured water flow Q_{out} is shown. It is noted that the highest water consumption occurs between 9:00 and 12:30, and between 15:30 and 21:00. Besides, the total daily water consumption was 4.812 l. Figure 3.3b, shows the measured P_{Cp} , where the energy consumed during the day was 1,086 kWh. Note that power consumption is synchronized with water demand. For this system, the potential energy service could be performed in those periods of high consumption, being particularly useful between hours 15:30 and 21:00, where the electric system has the peak demand.

3.1.2 Simulation and experimental validation

The model parameters η and p_{pr} are estimated by minimizing the mean squared error between measured and simulated power consumption. The system simulation is performed in MATLAB® R2019a using *Simulink* on a computer with a Intel® Core i7-7700HQ, CPU 2.80 GHz, 16 GB of RAM, and running Windows® 10 64-bit operating

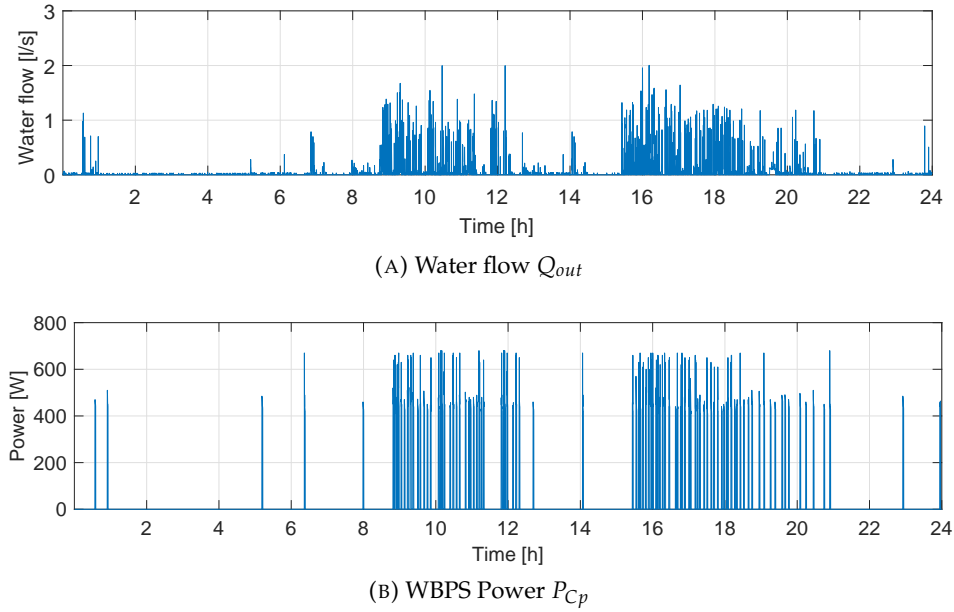


FIGURE 3.3: Experimental measurements in a WBPS.

system. In Figure 3.4, it is shown the general block diagram of the WBPS. The Centrifugal Pump block is simulated by using the *SimHydraulics* toolbox. Water is supplied by a reservoir. It has a Pressurized Tank that fulfils Eq. (3.2), simulated with a *Gas-Charged Accumulator* model. The power demanded by the pump is computed in the olive-coloured block following Eq. (3.3). It has an ON/OFF controller that fulfils Eq. (3.4). The Flow Supply block is in charge of activating the water flow rate (AQ_{Cp}). In the diagram, blue signals refer to water flow and black signals refer to electric signals. In the simulation P_{Cp} is the output, Q_{out} is the input, and p_{min} and p_{max} are parameters. The experimental data measured from hours 15:30 to 17:00 are used for parameter tuning. This time interval is selected because it shows high activity in power consumption. The water consumption in this interval is 1.197 l, that is 26% of the daily demand.

The power consumed by the actual pump and by the simulated model are compared as validation criterion. Figure 3.5 shows the tank pressure behaviour. It is observed that the pressure keeps under p_{max} . However, there are some intervals where the pressure drops below p_{min} . This results from the fact that at some points the water feed is not enough to supply both the demand and the pressurized tank. Figure 3.6 shows the power consumed by the actual pump in blue and power predicted by the simulated model in red. In the figure, it can be seen that in the actual data, the pump switches 19 times while in the model it commutes 20 times. Likewise, it can be seen

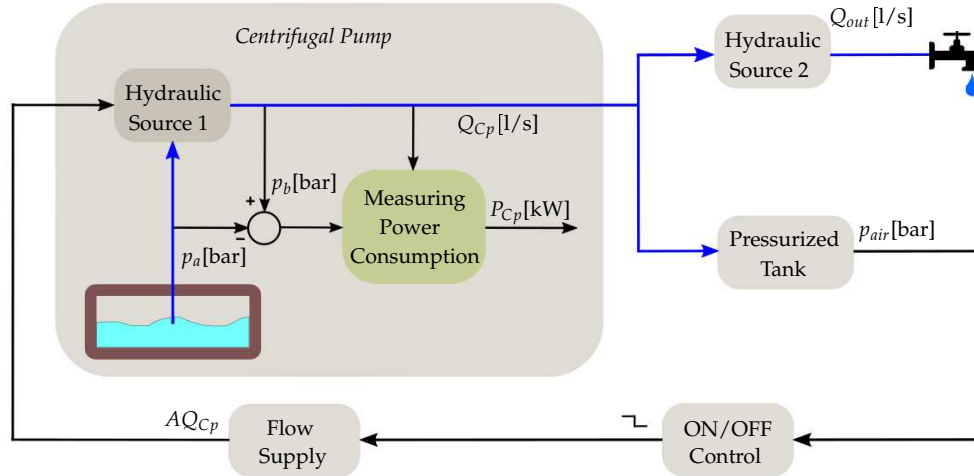


FIGURE 3.4: General block diagram of the WBPS.

that there is a match in many switching moments between the model and the experimental data. The shift between the signals can be caused by differences in the initial conditions in the pressurized tank. Moreover, energy consumption on the interval is 148.6 Wh, in which the pump is ON 29 minutes 20 seconds, while in the simulation the consumption is 145 Wh, with the pump ON during 30 minutes. In this case, energy error is 2.42%. The difference in the power consumption can be explained by considering that the model does not take into account losses on pipes, electric transients, wear of equipment, among other factors.

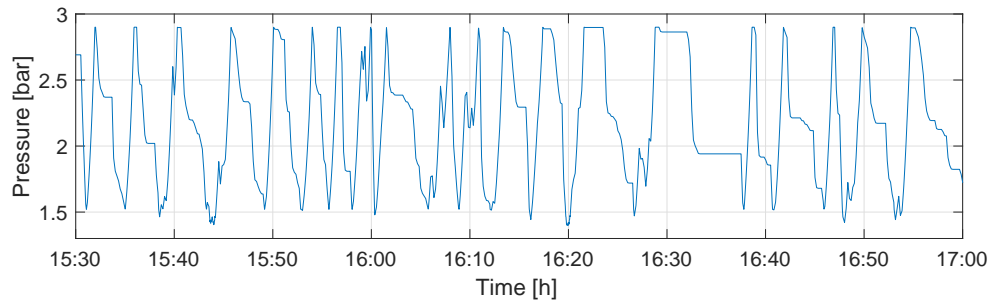


FIGURE 3.5: Simulated WBPS tank pressure.

Finally, the WBPS is simulated for a twenty-four hours interval, obtaining an energy demand of 1.072 kWh, in which the pump is ON 2 hours 13 minutes 40 seconds, while the actual system presented a requirement of 1.086 kWh consumed in 2 hours 18 minutes 10 seconds. Thus, the energy consumption error is 1.11%. It can be concluded that the model is suitable to represent the system.

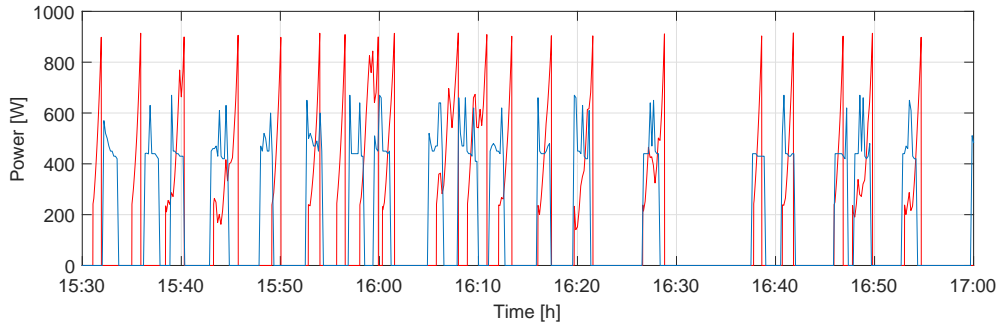


FIGURE 3.6: Power consumed by the actual and simulated pump.

3.2 Flexibility of the Water Booster Pressure System

In this section the flexibility of WBPSs is evaluated. The aim is to reduce power consumption while keeping the system running all the time. Water pressure is reduced, affecting the users comfort, but it is guaranteed that the flow is never stopped. Given that water consumption is variable, different levels of water demand are analysed. The next questions explore the flexibility problem.

- How would the power consumption be altered by varying pressure limits p_{min} and p_{max} ?
- How much time does the system require to achieve equilibrium after a pressure set point change?
- According to the energy services usually employed by power systems operators, which service can a WBPS provide?

In order to address these questions, the average stored energy in the tank is altered by changing the pressure set point. Two sets of simulations are performed. The first one seeks to evaluate the model performance and flexibility in terms of power consumption. The second one seeks to define the kind of ancillary service that the WBPS can provide, analysing distinct energy services and their characteristics.

3.2.1 Evaluating the model

In the first set of simulations, power consumption and commutation frequency are evaluated for different combinations of the parameters p_{min} and p_{max} . Table 3.3 shows the evaluated pressure limits, where normal and max values are the most common typical pressure ranges used in the tanks (IHM S.A., 2002), the min values are the

minimum supported in commercial systems, and medium A and B are medium values. Then, twenty-five conditions are evaluated considering all the possible combinations between the values of p_{min} and p_{max} presented in Table 3.3. For each combination, scenarios with constant consumption flow Q_{out} are analysed. Then, high (1.8 l/s), medium (0.7 l/s) or low (0.2 l/s) consumption is considered for residential buildings (Bastidas, 2009).

TABLE 3.3: Pressure limits evaluated in the flexibility analysis.

Variable	Pressure (bar)				
	Min	Medium A	Normal	Medium B	Max
p_{min}	1.31	1.41	1.52	1.85	2.21
p_{max}	2.41	2.65	2.90	3.25	3.59

Figure 3.7 shows three surfaces of average power consumption for constant output flow, corresponding to the considered values of Q_{out} (high, medium and low), these are seen from top to bottom, respectively. The different operating points are obtained combining the pressure limits shown in Table 3.3. It is concluded that if both p_{min} and p_{max} are reduced, the power consumption also reduces. Furthermore, it can be seen that the system is more sensitive to p_{min} variations. Likewise, slopes are greater for the curves between $p_{min}=1.31$ bar and $p_{min}=1.52$ bar. On the other hand, slopes are higher for the curve between $p_{max}=3.25$ bar and $p_{max}=3.59$ bar when Q_{out} is high.

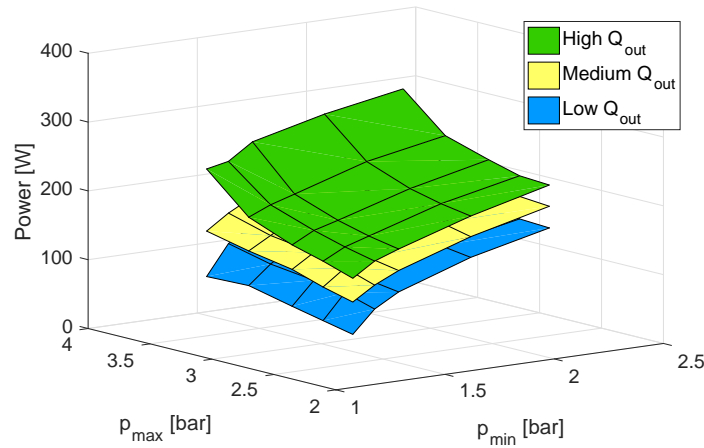


FIGURE 3.7: Power consumption for different pressure limits and output flow.

Figure 3.8 shows the centrifugal pump switching frequency. It is noted that when the difference between the limits is higher than 1 bar, the changes in switching frequency are negligible. Otherwise, when the gap is lower than 1 bar the switching

frequency rises abruptly. This observation sets a limit to the possible set point variations. High switching frequencies reduce lifetime and can damage the system.

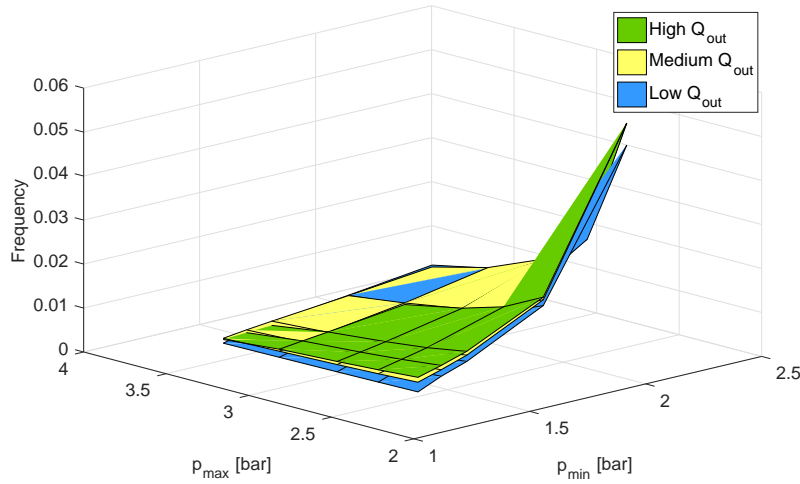


FIGURE 3.8: Switching frequency for different pressure limits and output flow.

3.2.2 Settling time

The second set of simulations seeks to evaluate the response time to a change in the pressure set point. A total of 125 simulations are performed for different values of the parameters V_T , Q_{Cp} and Q_{out} , selected randomly within the intervals shown in Table 3.4. Those intervals for V_T and Q_{Cp} have been defined based on a review of existing system specifications; while, Q_{out} values are taken according to (Bastidas, 2009), the selected values are for medium and high water consumption demands. Notice that the selected values for V_T , Q_{Cp} and Q_{out} remain constant in each simulation. The difference between p_{min} and p_{max} is kept fixed at 1 bar and the pressure set point is reduced from 2.7 bar (i.e., $p_{min}=2.2$ bar and $p_{max}=3.2$ bar) to 1.8 bar (i.e., $p_{min}=1.3$ bar and $p_{max}=2.3$ bar). The simulation evaluates the time taken for each WBPS to start cycling again after the set point change.

TABLE 3.4: Intervals of model parameters for the settling time evaluation.

Variable	Minimum	Maximum	Units
V_T	200	500	l
Q_{Cp}	2.52	5.68	l/s
Q_{out}	0.7	1.8	l/s

Results are summarized in Figure 3.9. It shows a histogram of the number of systems that start cycling again when a given time interval after the set point change has elapsed. It can be observed that approximately 70% of the systems are delayed less than 540 seconds (9 minutes) for cycling again, while a 20% lasts more than 1500 seconds (25 minutes).

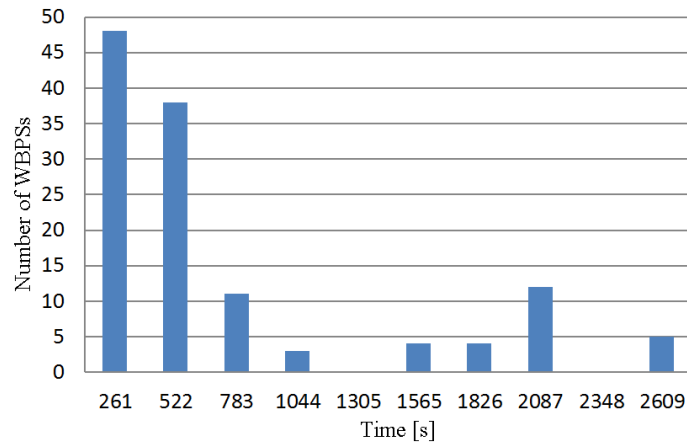


FIGURE 3.9: Histogram of the time elapsed for cycling again after a set point change.

3.2.3 Energy services

In Subsection 2.2, demand response and ancillary services are presented. This subsection shows that WBPSs can provide spinning reserve services, given the flexibility evaluation exposed in the previous subsection. Likewise, regarding Colombian ancillary services, the WBPS can provide a tertiary regulation reserve.

Taking into account the WBPSs response time in Figure 3.9, it is not possible to locate the WBPSs in a fast regulation service, due to the impossibility to change power consumption within seconds. However, WBPSs can provide Spinning reserve services, considering that, in front of a set-point change, 70% of the systems stabilize in less than 10 minutes and the power consumption is reduced while the set-point is kept low, see Figure 3.9. Moreover, WBPSs might provide Non-spinning reserve services; nevertheless, spinning reserve is more valuable economically for the SO, because it is usually worth 2 to 8 times as much as a non-spinning reserve on an annual average basis (Kirby et al., 2008). Then, in this work spinning reserve is selected for the remaining results. Finally, WBPSs might provide replacement reserve services; nevertheless, spinning reserve is more valuable economically for the SO, because it is usually worth

2 to 20 times as much as a replacement reserve on an annual average basis (Kirby et al., 2008). Then, in this work *Spinning reserve* is selected for the remaining results.

3.2.4 Capacity and operation conditions

After selecting Spinning Reserve as the service to be provided by the WBPSs, it is shown how the operating conditions of the WBPSs are managed to offer the selected energy service, guaranteeing a minimum quality of service and avoiding system damage. Also, the average reduction in power consumption is evaluated.

It is required to define adequate pressure limits ($p_{min,CP}$ and $p_{max,CP}$) for the set point change applied to the system when the SO calls for a reserve service. Normal operation pressures $p_{min,ON}$ and $p_{max,ON}$ are standard levels for a 6-floor building, as shown in Table 3.5.

The lower limit $p_{min,CP}$ is selected satisfying Eq. (3.5), where the height of the building is $h=18$ m, and considering $p_{tap}=0.55$ bar, according to (International Code Council, 2008), thus $p_{min,CP} > 2.32$ bar. A pressure limit $p_{min,CP}=2.52$ bar is selected, guaranteeing $p_{tap,CP}=0.75$ bar in static conditions, i.e., a reduction of 25% with respect to the normal operation pressure $p_{tap,ON}=0.99$ bar. This pressure reduction impacts the users comfort in the higher floors. However, the water supply does not stop in any moment. The selection of $p_{max,CP}$ is done by limiting the pump switching frequency to 52 cycles per hour, i.e., doubling the normal operation frequency when the highest water flow demand remains constant in an hour. Higher frequencies can cause heating and deterioration of the insulation of the motor, reducing its lifespan (Venkataraman et al., 2005). Moreover, the time the centrifugal pump motor will stay on will be lower after the set-point change; and, the time the motor will stay off will be higher than the time staying on. Then, it is supposed there will be no overheating in the motor. Notice that the set-point change will last 1 hour maximum (spinning reserve full delivery period). Table 3.5 summarizes the selected pressure limits.

TABLE 3.5: Defined pressure variables for offering spinning reserve services.

Parameter	Value [bar]
$p_{min,ON}$	2.76
$p_{min,CP}$	2.52
$p_{max,ON}$	4.14
$p_{max,CP}$	3.02

Finally, the average reduction in power consumption when the pressure limits are modified according to Table 3.5 is evaluated. It is calculated the average power consumption during one hour with the standard limits ($p_{min,ON}$ and $p_{max,ON}$). Then, it is calculated the average power for the next hour, when the set point changes to $p_{min,CP}$ and $p_{max,CP}$. Finally, the difference is calculated. In this test, the average power reduction is 27%.

3.3 Control system for power reduction

This section proposes an architecture to offer Spinning Reserve services with a set of WBPS, through an aggregator that synchronizes the pressure set-point variations among the systems.

In order to reduce the power consumption in a set of WBPSs, taking advantage of the flexibility found in the previous section, an automatic control strategy is proposed. The aggregator (Controller) is designed to respond to a SO requirement, assuming there is a signed contract with defined prices between the SO and the aggregator in order to provide spinning reserve service. Also, the amount and characteristics of the WBPS enrolled in the demand response program are fixed and known in advance. Figure 3.10 shows the block diagram of the system.

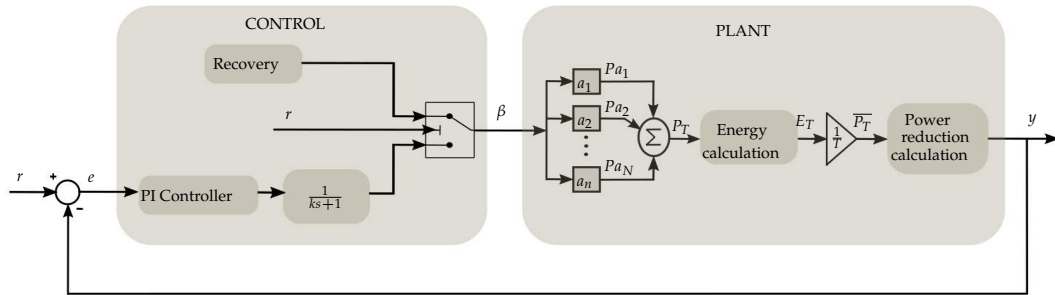


FIGURE 3.10: Block diagram of the aggregator control system.

For this strategy, the SO sends a reduction signal r in kW to the aggregator. Also, the time to carry out the reduction and the time to restore the system to normal operation are informed, i.e., the schedule of the DR plan is notified. The aggregator follows a feedback control action every sampling time, that allows to follow the SO command and handle the uncertainty caused by the random behaviour of each system, e.g., consumption level or model parameters. The blocks of Figure 3.10 are explained below.

The PLANT block models the power reduction achieved by all the systems participating in the DR plan. The CONTROL block decides how many systems should

perform a pressure set-point reduction to accomplish the power curtailment requested by the SO. The control signal β represents the number of systems whose flexibility is activated and is determined by the CONTROL block, according to the evolution of the error e between the SO command r and the measured power reduction y . For this control loop, the variables are:

- Controlled variable: y , power reduction of the set of WBPSs.
- Manipulated variable: β , number of systems that should enable or disable the flexibility to maintain power reduction. It is a number between 0 and N , where N is the number of systems participating in the DR program.
- Reference signal: r , power reduction sent by the system operator.

The CONTROL block is formed by two control actions. The first one is a discrete-time Proportional-Integral (PI) Controller with a low-pass filter. It is operated when the DR plan is active. It is responsible for enabling and maintaining flexibility to meet the requested power reduction. It is designed to respond in an appropriate time for spinning reserve services. This discrete control action has a sampling time of $T=3$ minutes because a faster control is unnecessary given the response characteristics of the WBPS. The second control action, Recovery, is responsible for disabling flexibility at the time when the DR plan finishes. This control action is designed to avoid overshoots when the pressure set-points are restored to the original settings.

In the PLANT block each WBPS a_i is commanded by a binary input signal that enables or disables the DR plan. Furthermore, each subsystem delivers as output the power Pa_i that is being consumed. Hence, the total power P_T is given by:

$$P_T = \sum_{i=1}^N Pa_i \quad (3.6)$$

which is used to calculate the energy demand E_T for each interval of length T . The average power $\overline{P_T}$ in the interval is:

$$\overline{P_T} = \frac{E_T}{T} \quad (3.7)$$

Thus, $\overline{P_T}$ goes into the sub-block Power reduction calculation and, if the DR plan is active, the average power of the last 3 minutes is subtracted from the average power consumed before activating the DR plan. The resulting power reduction is the controlled variable y .

3.3.1 Controller Tuning

In this subsection, a simulation is performed with a set of $N=100$ WBPSs representing 100 buildings. This amount of WBPSs is selected considering a trade-off between the computational effort and a reasonable systems aggregation, i.e., a feasible simulation with a number of systems that are able to reduce the individual effect in the complete aggregation performance. In these buildings, V_T , Q_{Cp} and Q_{out} are variables generated randomly within the intervals shown in Table 3.4; furthermore, these generated values remain constant at each building along the entire simulation horizon. The sample time is 1 s. Then, plant models are estimated and a controllers are derived. In order to assess the automatic control behaviour, two simulations are performed for different r .

In order to tune the controller parameters, it is analysed how the plant reacts to an open loop step command, activating 100 or 50 WBPSs. Simulations are performed for a 3-hour interval. β is formed as a pulse signal. First, it remains at $\beta=0$ for one hour (it allows to establish the power consumption before activating the DR plan), then it rises to $\beta_{max}=100$ or $\beta_{max}=50$ (here the power reduction is carried out). Finally, during the last hour, the DR plan is deactivated ($\beta=0$) and the WBPSs return to normal operation.

Figure 3.11 and Figure 3.12 shows in blue the power reduction response with $\beta_{max}=100$ or $\beta_{max}=50$, respectively. Recall that this simulation is performed in open loop, without control. Two transfer functions are estimated to model the dynamics of the plant, i.e., to explain the behaviour of P_T . These are first-order, minimum phase systems are considered as:

$$G_{100}(s) = \frac{10.21s + 0.039}{45s + 1} \quad (3.8)$$

$$G_{50}(s) = \frac{24.8s + 0.039}{18.3s + 1} \quad (3.9)$$

Their response are shown as red lines in Figure 3.11 and Figure 3.12. It is observed that the estimated models share the same DC gain, while the transient behaviour changes, the response for $\beta_{max}=50$ is faster than for $\beta_{max}=100$.

A controller is designed to eliminate the overshoot effect of the plant and to stabilize the system in less than 9 minutes. A PI controller is selected as a common but effective solution. The controller is designed with the criteria of eliminating the overshoot and guaranteeing an settling time of less than 8 minutes. The controllers are discretised with a sample rate of 3 minutes. Eq. (3.10) and Eq. (3.11) show the transfer

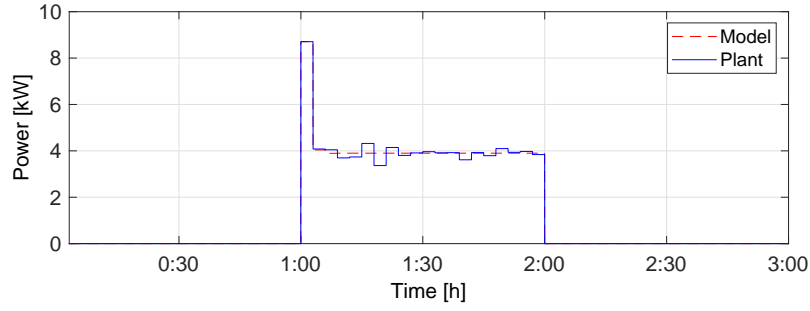


FIGURE 3.11: Plant and Model response to a pulse input with $\beta_{max}=100$.

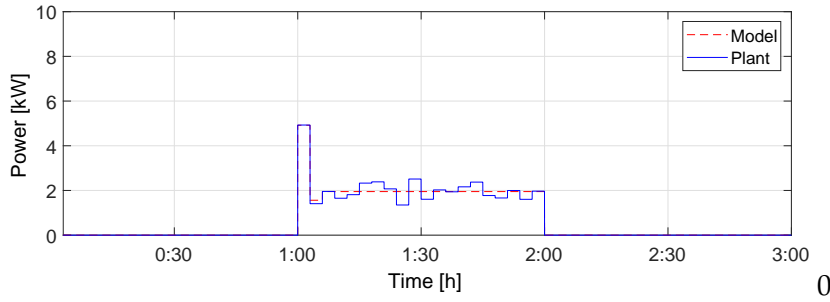


FIGURE 3.12: Plant and Model response to a pulse input with $\beta_{max}=50$.

function of the designed controllers.

$$C_{100}(z) = 1.948 + 0.224 * \frac{2z + 1}{Tz - 1} \quad (3.10)$$

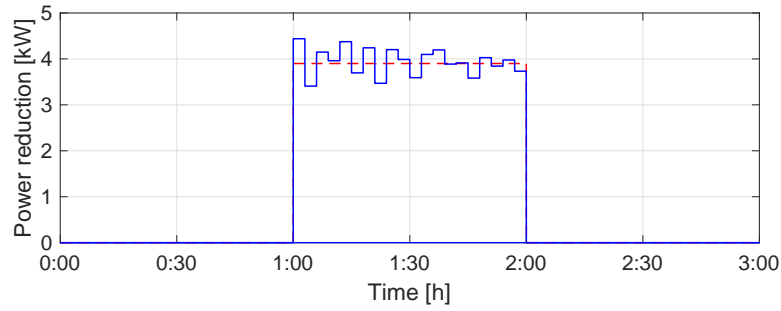
$$C_{50}(z) = 14.341 + 0.085 * \frac{2z + 1}{Tz - 1} \quad (3.11)$$

The closed-loop behaviour of the system is evaluated with the following experiment: a reduction schedule is sent to the controller with a DR plan defined by a start time after one hour of operation, finish time after two hours and a reduction signal r .

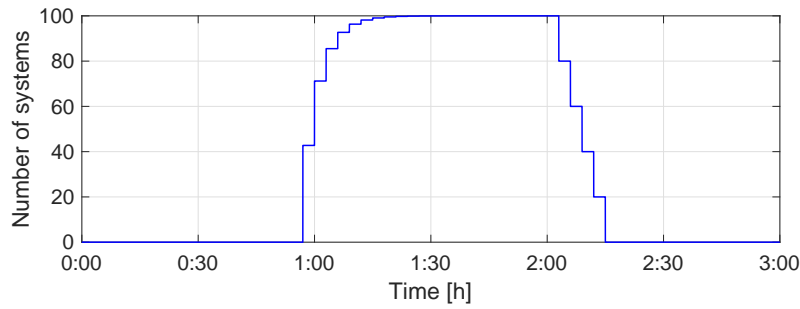
Figure 3.13a shows the power reduction response with $r=3.90$ kW. It is shown that the controlled variable y reaches the set-point in three sample times (9 minutes) and oscillates around r , between 3.41 kW and 4.44 kW, with standard deviation $\sigma=0.304$ kW. Note that the signal does not exhibit overshoot either at the beginning or finishing the service. However, fluctuations are inevitable because WBPSs are regulated by ON/OFF controllers. Finally, the average consumed power is 3.93 kW, quite similar to r .

Figure 3.13b shows the number of systems that are called to active flexibility in the DR plan. It is shown that the controller enables the flexibility of 85 WBPSs in 9 minutes and disables the flexibility of all WBPSs 15 minutes after ending the service

time. Additionally, the aggregator does not enable all WBPSs in the first sample time, but it increases the number of active systems smoothly, in order to avoid an overshoot in power reduction. Note also that the aggregator knows in advance the beginning of the service period one sample time before it starts. Then, the time elapsed between the call of the SO and the stabilization of the power reduction is 12 minutes, complying with the requirements of a spinning reserve service.



(A) Power reduction achieved by the WBPSs.

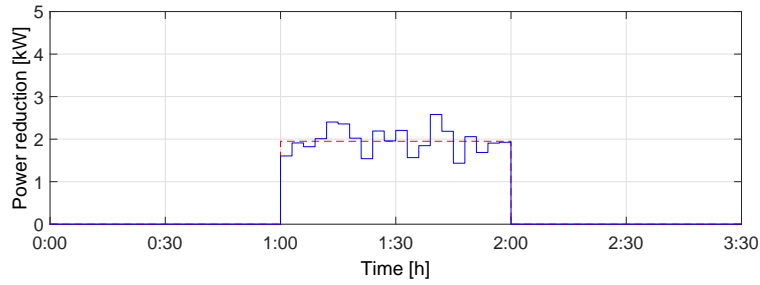


(B) Number of systems activated for demand response.

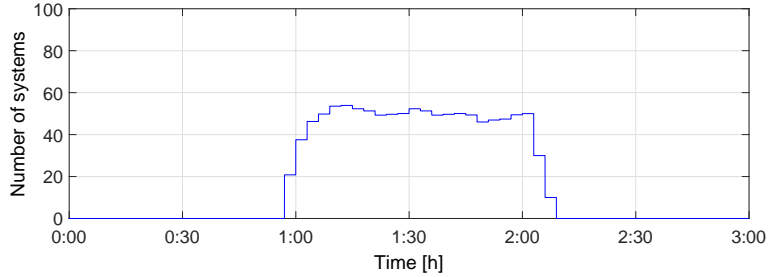
FIGURE 3.13: Response of the PI aggregator in 3 hours tes for $r=3.90$ kW.

In Figure 3.14a, it is shown the power reduction response with $r = 1.95$ kW. It is shown that the controlled signal y reaches the set-point in two sample times and shows a standard deviation of $\sigma = 0.305$ kW that varies between 2.58 kW and 1.43 kW. In Figure 3.14b, it is shown the number of systems that are called to activate flexibility in the DR plan, and those who are disabled after the plan. It is shown that the controller enables the flexibility of 38 WBPSs in 6 minutes and varies between 46 and 54 active systems.

Figure 3.15 and Figure 3.16 show the power consumption of the set of WBPSs throughout the test with $r = 3.90$ kW and $r = 1.95$ kW, respectively. In both figures, it is observed that the power reduction meets the spinning reserve service requirements. Besides, for $r = 3.90$ kW it is shown that in 3 minutes the power consumption



(A) Power reduction achieved by the WBPSs.



(B) Number of systems activated for demand response.

FIGURE 3.14: Response of the PI aggregator in 3 hours test for $r=1.95$ kW.

is reduced to 4.44 kW, while for $r = 1.95$ kW in 6 minutes the power consumption is reduced to 1.88 kW. Table 3.6 reports the average power consumption per hour. The tracking error of the aggregator strategy is adequate to offer spinning reserve services. Table 3.7 shows the standard deviation of the consumption around the average power. Note that the variability is lower during the second hour when the DR service is active. Finally, it can be seen that the time taken in the recuperation, i.e., at the beginning of the third hour, is 9 minutes for $r = 3.90$ kW and 3 minutes for $r = 1.95$ kW.

TABLE 3.6: Average power reductions

r	First hour average	Second hour average	Error
3.90 kW	15.47 kW	11.54 kW	0.77 %
1.95 kW	15.47 kW	13.54 kW	1.03 %

TABLE 3.7: Power standard deviation.

r	First hour σ	Second hour σ	Third hour σ
3.90 kW	0.559 kW	0.294 kW	0.777 kW
1.95 kW	0.581 kW	0.304 kW	0.408 kW

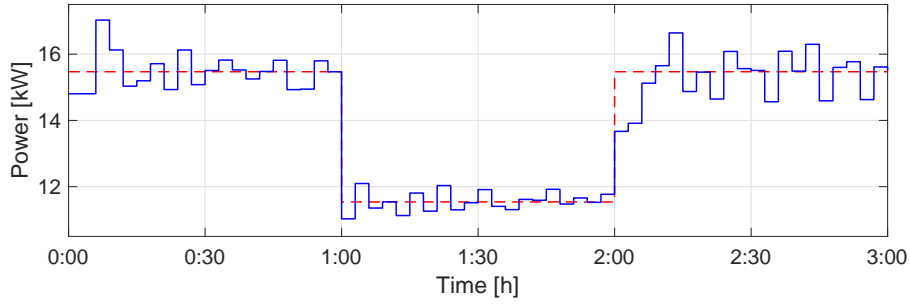


FIGURE 3.15: Power consumption during the three hours test for $r=3.90$ kW.

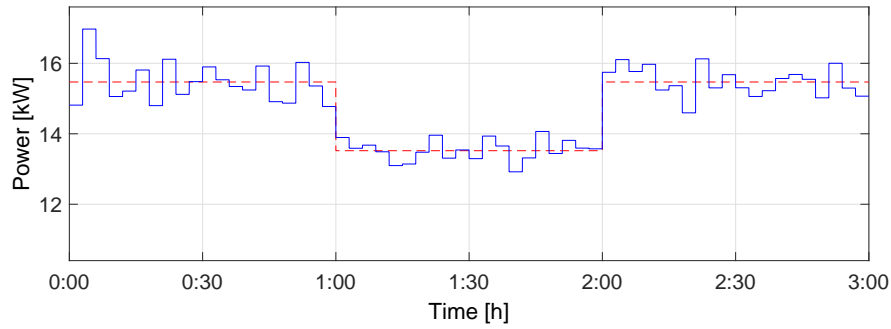


FIGURE 3.16: Power consumption during the three hours test for $r=1.95$ kW.

3.3.2 Gain-Scheduled Aggregator

In this Subsection, a Gain-Scheduled (GS) controller is proposed allowing the aggregator to follow time-varying reduction signals requested by the SO. Simulations are performed with the same setting and parameters of the previous subsection 3.3.1.

The controllers obtained in the previous subsection were tuned to maintain a reduction of $r=3.90$ kW or $r=1.95$ kW. However, when the reduction signal has different amplitudes, the response of the plant varies. Then, for each power reduction level, it is required to estimate a new process model (see Eq. (3.8) and Eq. (3.9)) and a new PI controller (see Eq. (3.10) and Eq. (3.11)). Therefore, a GS PI controller is designed with the purpose of obtaining time-varying controller parameters. A GS control strategy is formed by multiple locally tuned generalized PI algorithms (Vesely and Ilka, 2013; Rodriguez Martinez et al., 2011). In this case, $r=1,0$ kW, $r=2,0$ kW, $r=3.0$ kW and $r=3.9$ kW were used, obtaining the parameters shown in Table 3.8.

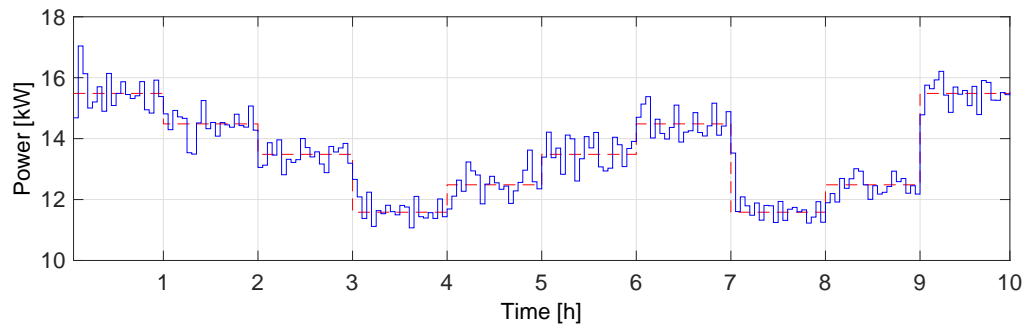
TABLE 3.8: Gain-scheduled PI Controller parameters.

r	k_p	k_i
1.0 kW	19.002	0.071
2.0 kW	14.041	0.085
3.0 kW	11.978	0.092
3.9 kW	1.948	0.224

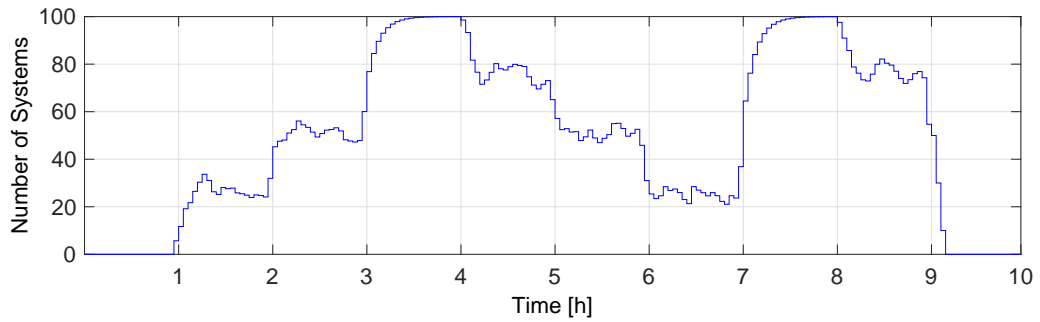
The GS aggregator is evaluated in a 10 hours test, with a reduction signal changing every hour as reported in the first column of Table 3.9. The simulation run time is 1 h 25 min per tested hour, this is owing to the dynamics of all WBPSs (the GS aggregator solution for each tested hour is developed in few run time seconds). Figure 3.17a shows in red the requested reduction send by the SO and the consumed power in blue. Figure 3.17b shows the number of systems that are called to active flexibility in the DR plan. It is shown how the GS controller responds to the SO request, sending a proper enabling signal to a subset of WBPSs and reaching the power reduction in less than 9 minutes for all the set-point changes, meeting the spinning reserve requirements.

Table 3.9 summarizes the results. Note that the average power consumption deviates less than 1% for any reduction level. The standard deviation σ of the reduced power is lower than the oscillation exhibited by the set of WBPSs in normal operation, reported in Table 3.7. The last column of Table 3.9 shows the ratio between σ and the requested reduction. It can be concluded that when enabling a higher number of buildings in the DR plan the tracking error decreases. Moreover, for a small r the ratio is higher than 40%. Therefore, if more buildings join in the DR plan, the variability in the tracking would be reduced.

Finally, notice that this WBPS aggregator can operate with any number of WBPSs (with any centrifugal pump and tank configuration). The pressure set-point change in the tank can be different among the systems, because the aggregator only considers a flexibility activation/deactivation parameter. Moreover, the GS controller only needs a recalculation of the PI controller parameters. Then, a technical resource such as smart meters is needed in order to acquire the aggregated power behaviour. This information will lead to identifying the new WBPS set response for computing the new parameter of the PI controller (with a step response). The identification and parameters computation can be developed by an adaptive controller. The number of systems N in the service is needed for knowing the controller saturation.



(A) Power reduction achieved by the WBPSs.



(B) Number of systems activated for demand response.

FIGURE 3.17: Gain-scheduled aggregator tracking test.

TABLE 3.9: Performance of the GS aggregator during the tracking test.

r	Power set-point	Average Power	Error	σ	σ/r
0.0 kW	15.48 kW	15.48 kW	0.00 %	0.591 kW	-
1.0 kW	14.48 kW	14.47 kW	0.08 %	0.435 kW	43.5 %
2.0 kW	13.48 kW	13.44 kW	0.29 %	0.352 kW	17.6 %
3.9 kW	11.58 kW	11.67 kW	-0.78 %	0.382 kW	9.8 %
3.0 kW	12.48 kW	12.52 kW	-0.28 %	0.468 kW	9.3 %
2.0 kW	13.48 kW	13.55 kW	-0.51 %	0.499 kW	25.0 %
1.0 kW	14.48 kW	14.50 kW	0.11 %	0.451 kW	45.1 %
3.9 kW	11.58 kW	11.68 kW	-0.86 %	0.498 kW	12.7 %
3.0 kW	12.48 kW	12.43 kW	0.46 %	0.330 kW	11.0 %
0.0 kW	15.48 kW	15.48 kW	0.00 %	0.388 kW	-

3.4 Findings

In this chapter, an aggregator for WBPSs has been proposed, capable of offering spinning reserve services in a demand response plan. An automatic control system performs the demand response decisions with the aim of tracking a reduction signal sent by the system operator. The strategy showed an error lower than 1% in the average power reduction.

A dynamic model of the WBPS was estimated. The model was developed from first-principle laws and tuned with real data. The energy consumption error between the experimental data and the model was 1.11% for a twenty-four hours data set.

The system flexibility in power consumption was evaluated by changing the operation pressure set-point. The analysis evidenced that a pressure set point change can reduce a 27% of the normal power consumption of the system. Besides, from the evaluation of the response time, it was found that a set of WBPS can provide spinning reserve services.

The WBPSs are low energy consumption systems able to provide a slight power reduction in an electrical grid. However, this power deviation is useful for a balancing service provider that can apply reserves from different aggregators.

Future work will be addressed in the experimental implementation evaluation considering synchronization and communication requirements. Besides, quantifying the discomfort caused to the users could improve the aggregator performance. Last but not least collect real data for understanding the energy needed over a day and design a strategy to bid in the ancillary service market, as well as the creation of proper contracts to motivate customers to participate in the balancing service.

This WBPS research leads to assess different water pumping systems as flexible loads, e.g., by considering hot water in the systems. In addition, the viability of the real power deviation that a smart city can provide can be analysed considering different WBPS settings.

Chapter 4

Control System for a ThermoElectric Refrigeration Unit

This chapter addresses the ThermoElectric Refrigerator (TER) unit, as a very flexible load included in an electrical demand management system. The TER is a solid-state energy conversion technology that exploits the Peltier effect to convert electricity into thermal energy for heating or cooling, commonly used in commercial and residential sectors ([Ponds et al., 2018](#)). This chapter proposes an aggregation strategy for TER loads that could provide balancing services such as frequency containment reserve, frequency restoration reserve or replacement reserve to the electrical grid. First, a detailed model of the energy consumption dynamics of a TER is presented. The model is able to reproduce experimental temperature data with an error lower than 1°C also in transient conditions. Then, based on the evaluation of the power demand response of a set of heterogeneous TERs under temperature set-point changes, a modified PID temperature controller is proposed and it is determined that the TERs can offer balancing services to the grid, responding in less than 30 seconds to any power deviation command and sustaining the modified consumption for up to 15 minutes in the frequency containment and restoration reserves services, and up to 1 hour in the replacement reserve service, without overshoots, rebounds, or synchronization problems. Finally, an aggregation strategy with reduced communication requirements is formulated and the capability of following power requests from the system operator is verified by extensive simulations.

The sections of this chapter are organized as follows. Section [4.1](#) presents the structure, the proposed model and its validation through experimental data as well as an experimental evaluation of classical control strategies applied to a small size TER is analysed. In Section [4.2](#), a TERs aggregator is proposed, considering the flexibility

a set of TERs can provide. The results of this Chapter were derived in the publications (Enescu et al., 2018; Diaz-Londono et al., 2019b, 2020a).

4.1 ThermoElectric Refrigeration Unit

A TER unit is composed of the ThermoElectric Cooler (TEC) device (an insulated cabinet with temperature lower than the ambient temperature), the heat exchangers at each side of the TEC device, and one or more electric fans. The fans force the air-flow over the dissipator inside and outside the cabinet, as shown in Figure 4.1.

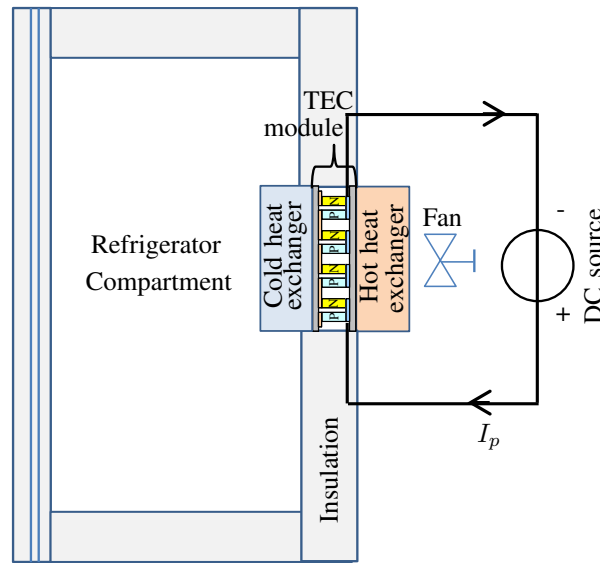


FIGURE 4.1: Schematic of the TER unit.

The TEC module is composed of the union of some thermoelectric elements of N- and P-type. The thermoelectric elements are thermally connected in parallel, to ensure that one side of the TEC is hot while the other is cold when the TEC is supplied. The thermoelectric elements are electrically connected in series through copper strips, to enable the electric current flowing through their legs. Furthermore, the thermoelectric elements are sandwiched between two ceramic plates of aluminium oxide, which isolate the TEC electrically from both heat exchangers.

The cold side of the TEC is located within the interior compartment, while the hot side is located on the outer part of the TER. The thermoelectric compartment is insulated, with insulation having a variable thickness depending on the TER capacity. The interior heat exchanger, made of aluminium finned heat sink, is attached to the cold side of the TEC. This heat exchanger is useful to transfer the cooling effect from

the cold side of the TEC to the thermoelectric compartment (Astrain et al., 2012). The electric fan installed on the cold heat sink is useful to provide forced convection for circulating cold air inside the compartment. This fan makes the temperature decreasing within the selected range (Söylemez et al., 2018).

The heat exchanger outside the TER is installed on the hot side of the TEC module being useful to dissipate the heat from the hot side of TEC into the environment. The finned heat sink is the most conventional heat exchanger, but sometimes it is not powerful enough to obtain the desired performance. Other types of heat exchangers used at the hot side of TEC are heat pipe and water–air (Astrain et al., 2016). A fan is installed at the hot side, it is useful to control the air flowing through the fins of this heat dissipator. During the TER operation, an external DC power source supplies the TEC system. Heat is pumped from one side of the TEC to the other side through charge carriers (electrons or holes) when a DC electric current supplies the TEC. In this time, the hot heat exchanger warms up, and the cold heat exchanger cools down, and the heat is transferred against the temperature gradient with consumption of electrical energy.

4.1.1 TER model

In order to determine the TER potential as a flexible load, a model that can reproduce its dynamics is built. This subsection presents a model of a TER which afterwards is used in the characterization methodology for evaluating the TER parameters through experimental data. Table 5.1 summarizes the nomenclature and units of the system variables.

Regarding the TEC module, the thermal operation model considered is presented in Eq. (4.1) and Eq. (4.2). This model has been used previously in (Jugsujinda et al., 2011; Zhao and Tan, 2014; He et al., 2017). A heat flow rate \dot{Q}_c is absorbed by the TEC, as shown in Eq. (4.1), whereas a heat flow rate \dot{Q}_h is delivered from the TEC module to the hot side sink, with magnitude given by Eq. (4.2).

$$\dot{Q}_c = \alpha T_c I_p - \frac{1}{2} I_p^2 R_p - K_p \Delta T, \quad (4.1)$$

$$\dot{Q}_h = \alpha T_h I_p + \frac{1}{2} I_p^2 R_p - K_p \Delta T, \quad (4.2)$$

where $\Delta T = T_h - T_c$.

Note that the heat flows depend on the electric current I_p , flowing through the module and the temperature of both plates, T_c and T_h .

TABLE 4.1: Notation of the TER variables.

Variable	Symbol	Units
Electric power of the TER	P	W
TEC module electric current	I_p	A
Seebeck coefficient	α	V/K
TEC module thermal conductance	K_p	W/K
TEC module electrical resistance	R_p	Ω
Outer thermal resistance	R_{out}	W/K
Thermal TER resistance	R_{TR}	W/K
Thermal disturbance resistance	R_d	W/K
Heat flow rate rejected by the TEC	\dot{Q}_h	W
Heat flow rate absorbed by the TEC	\dot{Q}_c	W
Hot side temperature of TEC	T_h	$^{\circ}\text{C}$
Cold side temperature of TEC	T_c	$^{\circ}\text{C}$
Ambient temperature	T_{amb}	$^{\circ}\text{C}$
Outer thermal capacity	C_{out}	J/K
Thermal TER capacitance	C_{TR}	J/K
Voltage supply	V_{in}	V
Downward time constant	τ_c	s
Upward time constant	τ_h	s

Figure 4.2 shows a scheme of the electrical behaviour of the TEC module. Note that the consumed electric power is:

$$P = V_{in} I_p, \quad (4.3)$$

while the current I_p is determined by the difference between the input voltage V_{in} and the Seebeck effect voltage V_α by considering the Peltier electrical resistance R_p :

$$V_{in} - V_\alpha = I_p R_p. \quad (4.4)$$

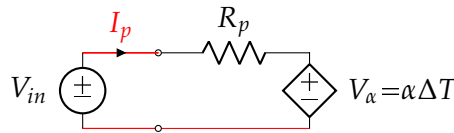


FIGURE 4.2: Electrical TEC module scheme.

The equivalent scheme of a TER is shown in Figure 4.3. In the scheme, the ambient temperature T_{amb} is a (possibly time-variant) parameter. The TER considers the

internal compartment as a volume with temperature T_c and capacitance C_{TR} , isolated from the ambient temperature through a resistance R_{TR} , which represents the equivalent quantities for the internal parts of the TER (e.g. cold heat sink, cold extender, and insulated walls). The TEC module extracts heat from it at a rate \dot{Q}_c . Capacitance C_d and resistance R_d model the loads inside the TER (e.g. bottles of water or food stored), which are controlled by the switch s . The outer environment of the TER, formed by the external plate and the heat sink is modelled as a mass with temperature T_h and capacitance C_{out} . It receives a heat flow \dot{Q}_h from the TEC module while dissipates heat to the ambient through a thermal resistance R_{out} .

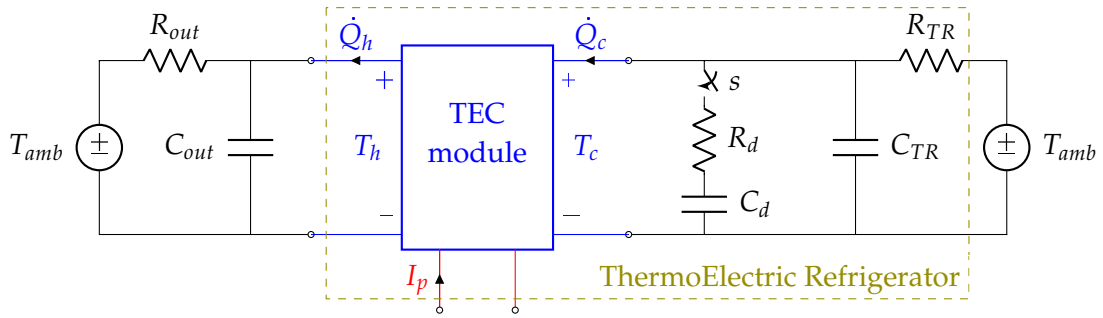


FIGURE 4.3: Equivalent scheme of a TER unit.

The dynamics of the cold $T_c(k)$ and hot $T_h(k)$ temperatures of the TER are given by Eq. (4.5) and Eq. (4.6), respectively, where k is the discrete time slot. Notice that the switch s is assumed open in these energy balances.

$$T_c(k) = \frac{T_{amb}(k-1) - T_c(k-1)}{C_{TR}R_{TR}} - \frac{\dot{Q}_c(k-1)}{C_{TR}} \quad (4.5)$$

$$T_h(k) = \frac{T_{amb}(k-1) - T_h(k-1)}{C_{out}R_{out}} + \frac{\dot{Q}_h(k-1)}{C_{out}} \quad (4.6)$$

4.1.2 Experimental data

In order to estimate the parameters of the TER model described previously (see Figure 4.3), experimental measures were recorded in a commercial TER. Figure 4.4 presents the actual TER unit used in this work.

A TER, originally supplied by the AC grid, has been tested. The TER has a width of 0.42 m, a length of 0.42 m, and a height of 0.50 m. The internal capacity of the device is 42 l, and contains an insulation compartment with the bottom and upper thickness of 0.06 m, while the lateral thickness is 0.04 m. The device has two air fans:



FIGURE 4.4: Actual TER used in the study.

the first is inside, while the external one is mounted on the rear side of the appliance on the heat sink. The unit has a rated power of 50 W at a rated voltage of 230 V (50 Hz) (Enescu et al., 2017). The original internal electronic board, containing the AC/DC converter and the control system is disconnected and the TER is supplied by a controllable AC/DC supply.

In Figure 4.5, the current-voltage characteristic of the TER load is shown. The curve is obtained varying the supply voltage and measuring by using two calibrated Fluke 189 multimeter (red line) for voltage and current, respectively; and also by the data acquisition system (dashed-blue line) inside the control system. Current and voltage measurements obtained from the data acquisition system are validated by comparing them with measurements delivered by the commercial multimeters. The Fluke has a 0.025% accuracy in the voltage measurement, while it has 1.5% for the current.

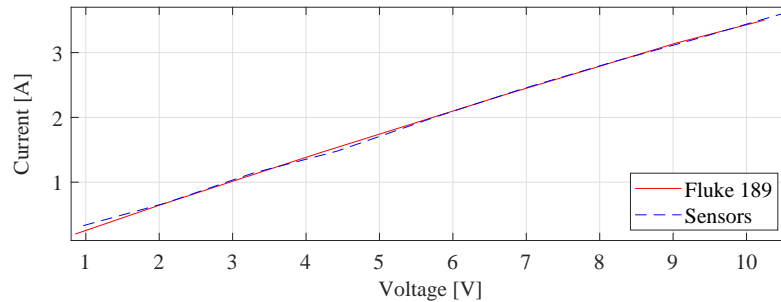


FIGURE 4.5: Current - Voltage curve of the TEC

In Figure 4.6, both voltage and current measures are shown with the multimeter and the sensors implemented. Then, it is calculated the Mean-Squared Error (MSE) for the current (MSEc) and voltage (MSEv) measures, obtaining MSEc=0.0073 and MSEv=0.0477, which are acceptable errors for our purpose.

Figure 4.7 shows the block diagram of the hardware implementation and its components for measuring and controlling the TER. In the block diagram, it is shown that

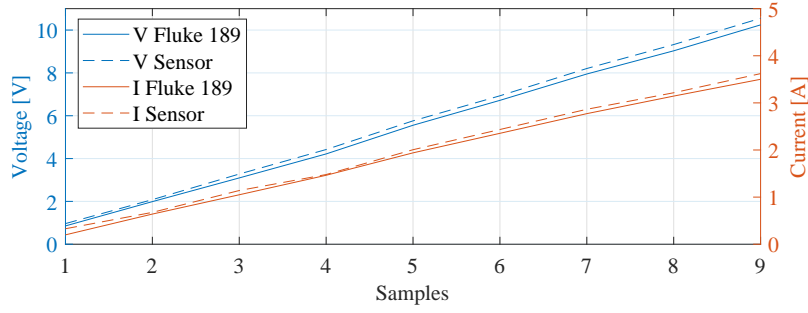


FIGURE 4.6: Current and voltage sensors validation

the electrical grid delivers power to an AC/DC converter, which is implemented by an adjustable DC power supply that can deliver 5 A and 30 V. However, it is fixed in 12 V and feeds an adjustable analog DC/DC converter. The DC/DC converter is the actuator capable of regulating the voltage delivered to the TER. The converter can operate maximum at 5 A and regulate the output voltage between 0 V and 32 V. Moreover, a current sensor S_C is installed to measure the TER power consumption. The S_C is a Hall-effect current sensor ACS714, its maximum current flow is 5 A which corresponds to 5 V in the output, and has a sensitivity of 185 mV/A. Furthermore, a resistor divider S_V is used for measuring the voltage delivered to the TER. Both measures S_C and S_V are sent to Analog Digital Converters (ADC) of a Data logger. In addition, T_c and T_h temperatures of the TER are measured with DHT22 sensors, S_{T_c} and S_{T_h} , respectively. Both measures are sent to Digital inputs of the controller. All the information arriving at the controller is sent to a computer with Simulink by serial communication. Depending on the measures and on the control action implemented in Simulink, a different Pulse-Width Modulation (PWM) signal is delivered to the PWM driver. Finally, the driver delivers an analog voltage to the DC/DC converter.

Figure 4.8 shows the implementation. It can be seen the back side of the TER, the computer with Simulink, and two power supplies, one as the AC/DC converter and the other for supplying the fans (internal and external).

Moreover, the letters in the figure depict the elements as:

- A. DC/DC converter.
- B. Current sensor S_C .
- C. Data logger.
- D. PWM Driver.
- E. Resistor divider S_V .

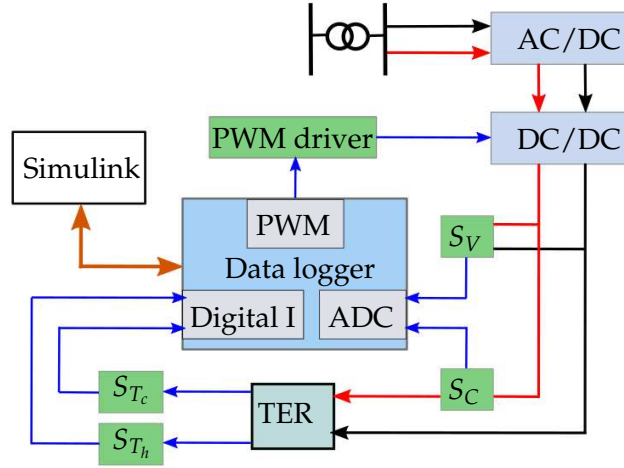


FIGURE 4.7: Block diagram of the implementation.

F. External temperature sensor S_{T_h} .

G. Internal temperature sensor S_{T_c} .

With the purpose to characterize the TER response, V_{in} and I_p were measured for computing the electric power P absorbed by the TER. Moreover, temperatures T_c , T_h and T_{amb} were registered with thermistor-type temperature sensors. The sample time is 1 s. It is highlighted that the measurements were carried out in a temperature controlled chamber. Then, T_{amb} is the same in all measurement time. There were acquired three different measurements with different input conditions i.e., three experiments, where:

- Experiment 1: by applying 10.68 V;
- Experiment 2, by applying 8.64 V;
- Experiment 3, by applying 6.56 V.

For each experiment, the test started when $T_c = T_h = T_{amb}$, and $V_{in} = 0$ (hence, $I_p = 0$). Then, after one minute, V_{in} was set to the voltage defined in the experiment (1, 2, or 3). This voltage was kept for 4 h, that is the time required for T_c to reach equilibrium; after that, the voltage supply is turned off and the data acquisition continued for 5 more hours, enough time for achieving $T_c = T_{amb}$ again. Figure 4.9a shows the behaviour of T_c , T_h , and T_{amb} for the three experiments. In Figure 4.9b, current I_p and voltage V_{in} are reported.

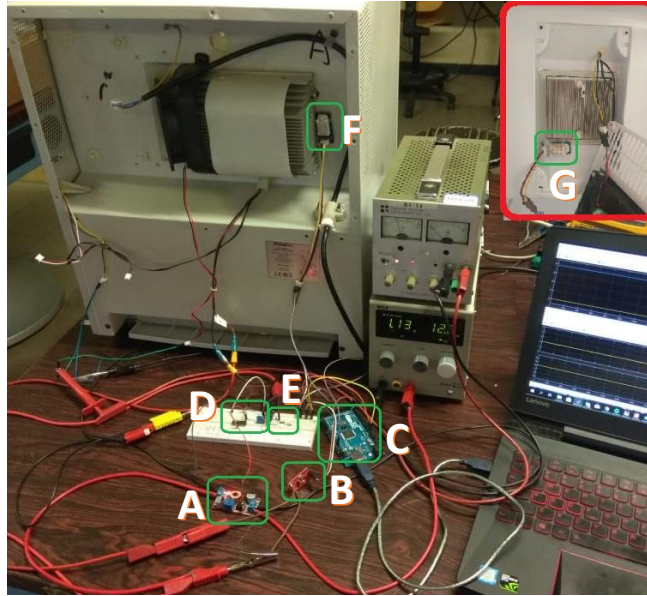


FIGURE 4.8: Hardware implementation.

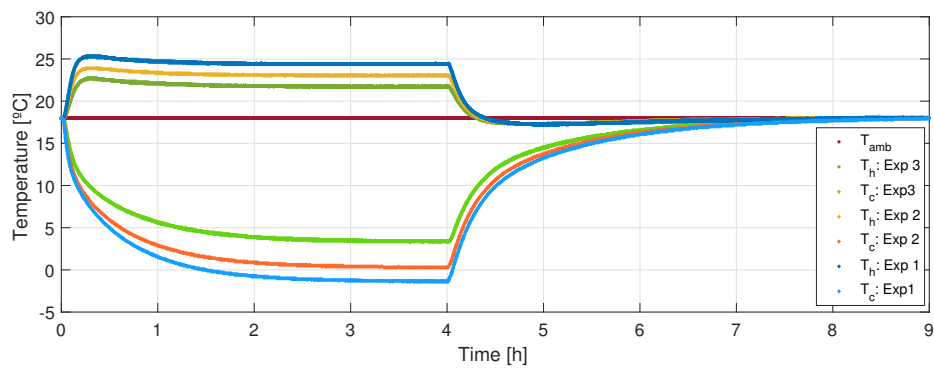
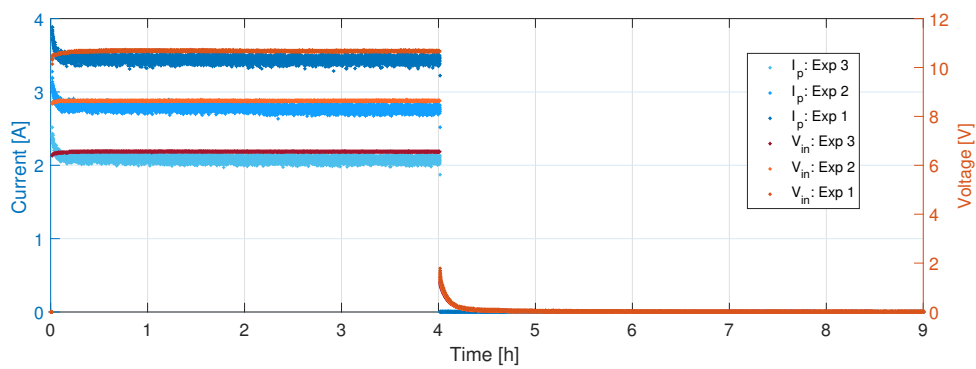
(A) Measurements of temperatures T_c , T_h , and T_{amb} during the 3 experiments.(B) Measurements of current I_p and voltage V_{in} during the 3 experiments.

FIGURE 4.9: Measurements for Experiment 1, 2 and 3.

4.1.3 TER parameters characterization

This subsection shows the methodology employed to obtain the TER parameters α , K_p , R_p , R_{TR} , C_{TR} , R_{out} , and C_{out} (see Figures 4.2 and 4.3). It is worth noting that the values of the parameters change depending on the TER under test; however, the procedure presented below can be applied as it is to any other TER. The parameters are calculated in three steps, as detailed in the following.

Step 1. Electrical parameters

The first step aims to obtain α and R_p from the experimental data of the three experiments. The Seebeck voltage can be obtained by cutting off the current I_p and measuring instantaneously the residual voltage, i.e.:

$$V_\alpha = V_{in} |_{I_p=0} . \quad (4.7)$$

Then, the Seebeck parameter α is determined as:

$$\alpha = \frac{V_\alpha}{\Delta T} . \quad (4.8)$$

Finally, considering only the electrical part of the TEC module, the module electrical resistance can be computed as:

$$R_p = \frac{V_{in} - \alpha \Delta T}{I_p} \quad (4.9)$$

Figure 4.10 shows the Seebeck voltages V_α for the experiments when V_{in} is turned off (after 4 h in Figure 4.9b). The purple asterisks (*) plotted on the curves represent the TEC voltage measurements one step after switching V_{in} off.

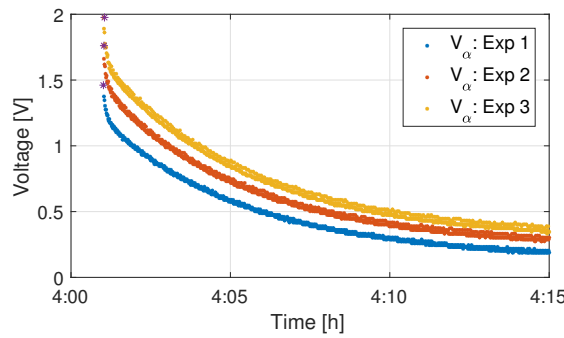


FIGURE 4.10: Experimental V_α .

Table 4.2 presents the resulting values for V_α and ΔT , aiming to compute α in each experiment; while the computed R_p takes into account V_{in} , I_p , and ΔT and is obtained as a mean value. It is noticed that R_p and α are consistent for the three experiments.

TABLE 4.2: Experimental values of V_α and ΔT , and computed values for α and R_p .

Experiment	V_α [V]	ΔT [°C]	α [V/K]	R_p [Ω]
1	1.98	25.8	0.0766	2.55
2	1.76	22.8	0.0773	2.54
3	1.46	18.3	0.0798	2.50
Mean value			0.0779	2.53

Step 2. Interior compartment thermal parameters

The second step aims to calculate the parameter K_p , C_{TR} , and R_{TR} through an optimization problem minimizing the Root Mean Squared Error (RMSE) between the measured temperature \tilde{T}_c and the temperature T_c predicted by the model for the given voltage V_{in} and external plate temperature T_h .

The following equation reports the proposed optimization problem formulated to estimate the set of parameters:

$$\min_{K_p, C_{TR}, R_{TR}} \sum_{j=1}^J \sum_{k=1}^N (T_{c,j}(k) - \tilde{T}_{c,j}(k))^2 \quad (4.10a)$$

$$\text{s.t.} \quad T_{c,j}(k) = f(T_{c,j}(k-1), T_{amb}(k-1), \dot{Q}_{c,j}(k-1); K_p, C_{TR}, R_{TR}) \quad (4.10b)$$

$$\tau_{c,min} \leq C_{TR} R_{TR} \leq \tau_{c,max} \quad (4.10c)$$

$$0 < K_p, C_{TR}, R_{TR} \quad (4.10d)$$

where $J=3$ is the number of the experiments, j refers to the considered experiment (i.e., $j=\{1, 2, 3\}$), and N refers to the experiment data length (i.e., $N=32,400$ s equivalent to 9 h, as shown in Figure 4.9).

The dynamic constraint in Eq. (4.10b) corresponds to the dynamic behaviour of T_c , where $f(\cdot)$ is defined as the right hand side of Eq. (4.5), evaluated using the measurements of I_p , T_h and T_{amb} for each experiment, while R_p and α are the mean values of the estimates for the 3 experiments in Table 4.2. The lower and upper bounds of the non-linear constraint (Eq. (4.10c)) are the minimum and maximum expected time constants of T_c when the system is cooling down, i.e., $\tau_{c,min}=1179$ s and $\tau_{c,max}=2506$ s. The optimization problem is solved in MATLAB[®], by using the Sequential Quadratic

Programming solver *fmincon* function. The optimal parameters are shown in Table 4.3. Note that the non-linear constraint is fulfilled, obtaining $\tau_c = C_{TR}R_{TR} = 2282$ s.

TABLE 4.3: Optimal values for the TER parameters.

Parameter	Value	Units
K_p	0.134	W/K
C_{TR}	6300	J/K
R_{TR}	0.362	W/K
C_{out}	4500	J/K
R_{out}	0.072	W/K

Step 3. External equivalent model parameters

In order to calculate the outer plate thermal parameters C_{out} and R_{out} , the following optimization problem is formulated:

$$\min_{C_{out}, R_{out}} \sum_{j=1}^J \sum_{k=1}^N (T_{h,j}(k) - \tilde{T}_{h,j}(k))^2 \quad (4.11a)$$

$$\text{s.t.} \quad T_{h,j}(k) = f(T_{h,j}(k-1), T_{amb}(k-1), \dot{Q}_{h,j}(k-1); C_{out}, R_{out}) \quad (4.11b)$$

$$\tau_{h,min} \leq C_{out}R_{out} \leq \tau_{h,max} \quad (4.11c)$$

$$0 < C_{out}, R_{out} \quad (4.11d)$$

The aim is to obtain the values of C_{out} and R_{out} that minimize the RMSE between the modelled T_h and the experimental \tilde{T}_h temperatures. This problem is developed with the same structure of the problem in Eq. (4.10). Constraint Eq. (4.11b) corresponds to the dynamic behaviour of T_h , where $f(\cdot)$ is defined as the right hand side of Eq. (4.6). However, K_p is a known parameter and T_c is taken from the TER experimental measurements. Moreover, $\tau_{h,min} = 267$ s and $\tau_{h,max} = 564$ s. the resulting parameters are shown in Table 4.3. The non-linear constraint is fulfilled, obtaining $\tau_h = C_{out}R_{out} = 323$ s.

4.1.4 Model validation

In order to validate the proposed model, simulations with all the obtained parameters are developed and compared with the experimental data. Figure 4.11 shows the T_c and T_h responses of the model for the three experiments.

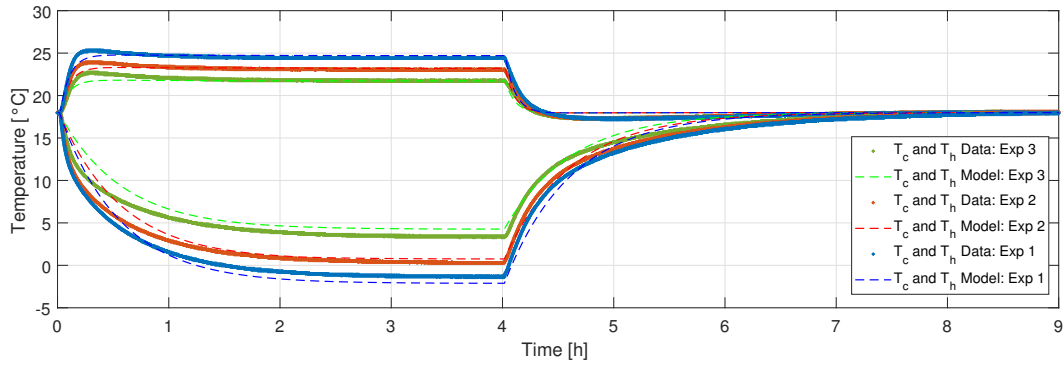


FIGURE 4.11: Temperature validation for the experiments.

Table 4.4 reports the characterization of the error of the estimated model for T_c and T_h . The RMSE and Maximum Absolute Error (MAXAE) are reported. Notice that the RMSE is lower than 1°C , also considering transient conditions for the inner temperature and lower than 0.4°C for the external temperature. The maximum deviation is observed for T_c at the beginning of the tests, when T_c is above 10°C , out of the operation range. It can be seen from Figure 4.11 that there is no systematic bias in the model output along all the experiments. It can be concluded that the model is suitable to properly represent the system for consumption analysis and control design.

TABLE 4.4: Error measures for the TER model.

Exp	T_c		T_h	
	RMSE [$^\circ\text{C}$]	MAXAE [$^\circ\text{C}$]	RMSE [$^\circ\text{C}$]	MAXAE [$^\circ\text{C}$]
1	0.92	3.3	0.38	0.8
2	0.86	3.4	0.33	0.7
3	0.94	2.9	0.36	0.7
<i>Mean</i>	0.91	-	0.35	-

4.1.5 Experimental TER controller

This subsection presents an experimental evaluation of a Proportional-Integral (PI) and Proportional-Integral-Derivative (PID) control strategies applied to the TER presented in the previous section. In these control strategies, the power consumption is continuous, offering the possibility to have the flexibility for increasing or reducing the energy consumption, which is an aim of flexible loads in DR plans. Results in this section are compared with benchmark On/Off strategy and have been published in (Enescu et al., 2018).

Experimental controller

To determine the PI and PID controllers, the TEC model is readjusted with temperature updated data. First, it is analysed how the plant reacts to an open-loop (without control) input signal by applying a constant voltage of 10 V by 2 hours and 20 minutes (equivalent to 8400 s). This is the time required for achieving the 6°C stabilization temperature after an initial temperature of 26°C (as shown in Figure 4.12). However, the settling time is 6290 s. Therefore, with the purpose of identifying the model, the *System Identification* Toolbox of MATLAB® is used. The internal temperature T_c is treated as the system output and the injected voltage as the input. In particular, the data is pre-processed by removing means, and taking into account the *Polynomial Models* tool, an ARX (autoregressive exogenous) model is obtained. A first-order model with delay characterizes the TER as following:

$$G(s) = \frac{-1.881}{1045.4s + 1} e^{-12s} \quad (4.12)$$

Figure 4.12 depicts the internal temperature of the TER obtained by the experimental data (red line) and the identified model (dashed blue line). The model is validated with a $FIT=79.23\%$, which represents the similitude of the model regarding the real data. This fit is accurate enough to design the controllers. The parameter FIT is defined as,

$$FIT = 100 - \frac{\|x - x_{ref}\|}{N_s} 100(\%) \quad (4.13)$$

where x is the test data (i.e., the identified model), x_{ref} is the reference data (i.e., the experimental data), and N_s is the number of samples.

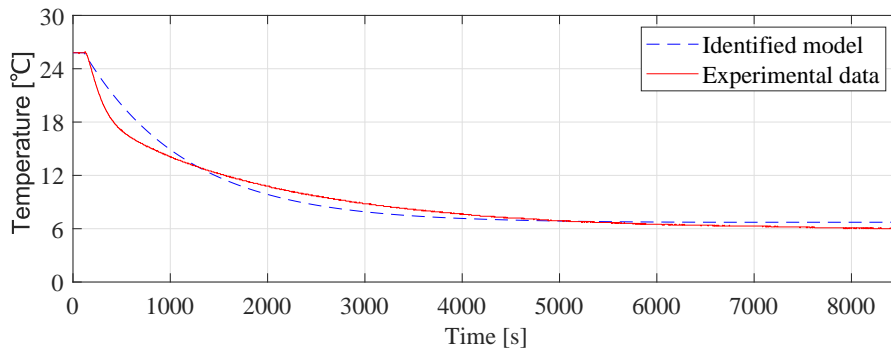


FIGURE 4.12: Experimental data and Model response in open loop.

Considering the identified model, the next step is to calculate the PI and PID controller that satisfy the following requirements:

- An overshoot effect must be lower than 5%, i.e., $M_p \leq 5\%$, because the idea is to keep the internal temperature inside a $\pm 1^\circ\text{C}$ hysteresis gap.
- A settling time of 3145 s, i.e., $t_s \leq 3145$ s, which is the 50% of the open-loop settling time. It is calculated with an acceptable error of 2%.
- The control signal dynamic range must not exceed 2 V with a temperature change of 1°C .

Hence, using the *Control System* Toolbox of MATLAB[®], the PI and PID controllers obtained for the identified model are:

$$C_{PI}(s) = -1.804 + \frac{-0.00173}{s} \quad (4.14)$$

$$C_{PID}(s) = -0.841 + \frac{-0.01498}{s} - 32.62s \quad (4.15)$$

Finally, the expected closed-loop behaviour with the controller is simulated, obtaining for the PI controller the following parameters: $M_p=0\%$, $t_s = 1210$ s, and a control effort of 1.8 V; while in the PID controller the parameters are $M_p=4.5\%$, $t_s=1290$ s, and a control effort of 1.2 V.

Experimental control results

In this subsection, the experimental results of the control strategies are assessed and compared with a traditional On/Off controller. The aim is to maintain the internal temperature set-point of the TER at 10°C .

A test of 10 hours (36000 s) per each control strategy is developed. The initial internal and external temperatures are almost the same $T_c \approx T_h \approx T_{amb} \approx 24^\circ\text{C}$, besides, the TER door is closed. The AC/DC supply is turned on when the test begins, likewise, the control action starts working. The system conditions do not change for 3 hours to achieve temperature and power stability. Then, the system is perturbed by introducing a 500 ml bottle of water at ambient temperature (24°C) inside the TER. The process is evaluated also for the next 7 hours. The sample time of the controllers is 10 s. It is worth highlighting that in this test the ambient temperature T_{amb} is not controlled but the actual one, i.e., T_{amb} varies in time.

In this test, energy consumption, power P , and, T_c and T_h temperatures are measured. Figure 4.13a shows the power consumed by the TER with the three strategies. Notice that the On/Off controller is constantly switching, but, after the perturbation, the following switchings remains longer, it means a longer power settling time. In this

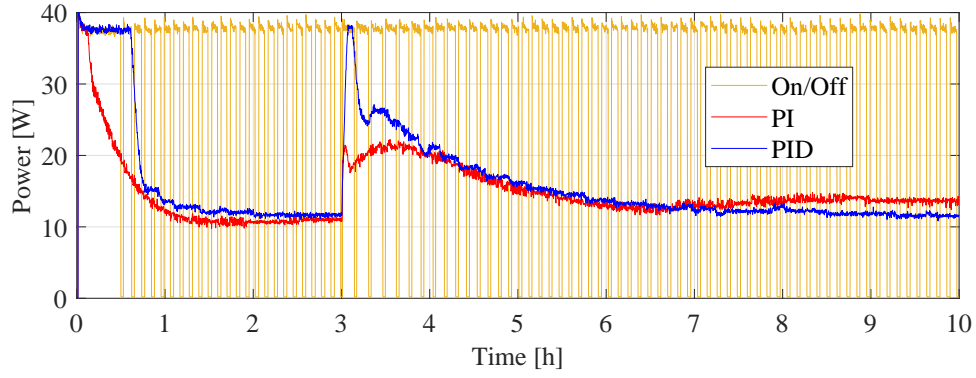
strategy the maximum power slew rate is 39.61 W achieved with current and voltage changes of 3.88 A and 10.26 V, respectively. However, this slew rate is almost the same in all the switching moments. In spite of the switching power of the On/Off controller, the PI and PID controllers are significantly smoother; where the maximum power slew rates are 4.30 W and 2.51 W, respectively, and occurs at 10830 s (3 h and 30 s), i.e., 30 s after the perturbation. This result fulfils the design voltage control effort. According to the closed-loop simulation, it is expected to have a higher slew rate in the PI. Table 4.5 summarizes the results, comparing energy consumption, energy savings of the PI and PID strategies with regard to the On/Off strategy, and the maximum slew rate of power, current and voltage.

In this test, both controllers PI and PID present a smooth and constant power consumption, leading to a suitable performance when following renewable sources or system operator request, given that the power profile can be modified (upper or lower) without affecting significantly the internal temperature T_c , i.e., it can be treated as a flexible load. Note that, with the On/Off controller this is not possible because it can only offer upper or lower flexibility at each step, depending on the switching behaviour. Moreover, the PI and PID strategies save energy regarding the On/Off strategy. In addition, the TER with the PI controller consumes lower energy and achieves the highest savings.

TABLE 4.5: Consumption comparison between the PI, PID and On/Off strategies.

Control Action	Energy consumed	Energy savings	Maximum slew rate		
			ΔP	ΔV	ΔI
On/Off	263 Wh	-	39.6 W	10.3 V	3.88 A
PI	148 Wh	43%	4.30 W	0.92 V	0.36 A
PID	161 Wh	38%	2.51 W	0.55 V	0.20 A

On the other hand, Figure 4.13b shows the T_c and T_h temperatures of the TEC during the test for each controller. As in case of power, it is shown that the On/Off controller leads to oscillations in the temperature, achieving the lower limit 9°C but exceeding the upper limit 11°C. To analyse the transient in the strategies, it is required to evaluate when is achieved a constant switching frequency. Furthermore, the PI controller, before achieving temperature stability has a lower overshoot than the PID; it happens for both initial transient and disturbance response. While, the PID controller, for both periods, achieves lowers settling times; this is due to the derivative action in the controller. Likewise, for both controllers, overshoots are fulfilled considering



(A) Power consumed in the test by the controllers.

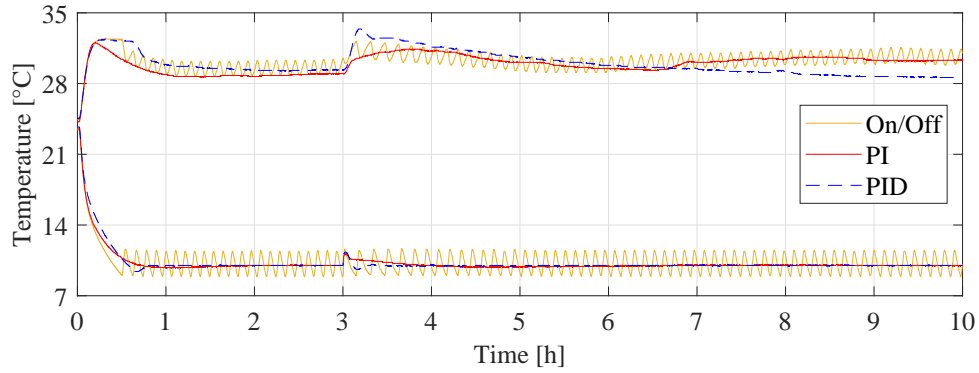
(B) Internal T_c and external T_h TER temperatures.

FIGURE 4.13: TER controllers responses.

the design parameter. Table 4.6 summarizes the temperature settling times and the overshoot of the controllers.

TABLE 4.6: Temperature comparison between the strategies.

Control Action	Temperature settling time		Overshoot	
	Initial	Disturbance	Initial	Disturbance
On/Off	4360 s	7380 s (18180 s)	Not defined	Not defined
PI	4210 s	2020 s (12820 s)	2.19% (9.7°C)	1.46% (9.8°C)
PID	2720 s	770 s (1157 s)	4.38% (9.4°C)	2.92% (9.6°C)

Finally, the PI and PID controllers allow modifying the power upward and downward for controlling it as a flexible load. However, the PI presents lower energy consumption, higher energy savings, and lower overshoot for initial transient and disturbance response. Therefore, the PI controller is considered for the flexibility analysis presented in the next section.

4.2 Flexibility and TER aggregator

Once the TER has been characterized and the PI controller has been tested in the real device, it is shown the potential of TERs to provide ancillary services to the grid.

In this section, the flexibility in energy consumption of a set of TERs is evaluated. Then, an aggregation strategy is proposed in order to provide balance services to the electrical grid. It is shown that power demand of TERs can deviate from nominal values while keeping the system in normal working conditions, by modifying the internal set-point temperature (the set-point temperature is the target value of the controlled temperature that has to be maintained by the control strategy). Moreover, it is proposed an aggregator that manipulates the set-points of a set of TERs to follow up/down power requirements from the System Operator (SO).

4.2.1 Flexibility analysis

The analysis of the flexibility in energy consumption of a set of TERs set is performed evaluating the following characteristics:

1. The power modification when there is a temperature set-point change.
2. The time required for the TER to achieve equilibrium after a temperature set-point change.
3. The service that a set of TERs can provide to the electrical grid.

Hence, a set of simulations have been developed with the purpose of evaluating these three characteristics. Power demand P , cold temperature T_c and stabilization times are thus assessed. The simulation is performed in MATLAB® R2019a using *Simulink* on a computer with a Intel® Core i7-7700HQ, CPU 2.80 GHz, 16 GB of RAM, and running Windows® 10 64-bit operating system.

Considering the TER controlled temperature, the standard temperature set-point used for domestic thermoelectric refrigerators is 5°C (Bansal and Martin, 2000; Min and Rowe, 2006; Saidur et al., 2008). It must not fall below 0°C to avoid the presence of frost inside the cabinet (Martínez et al., 2013a); and according to common standards such as the EC Regulation 852/2004 (The European Parliament and the Council of the European Union, 2004), the regulation of the Food Standards Agency (FSA) in the UK (Food Standards Agency (FSA), 2016), and the Essential food safety practices of the Food Standards Australia New Zealand (FSANZ) (Food Standards Australia New Zealand (FSANZ), 2017), the chilled food storage inside the cabinet must not

exceed 8°C ; therefore, the TER set-point is modified to $T_{sp,down}=2^{\circ}\text{C}$ when a power demand increment is required, and to $T_{sp,up}=8^{\circ}\text{C}$ when a power demand reduction is requested, in order to evaluate the power modification when there is a temperature set-point change.

The behaviour of 50 TERs is evaluated for different conditions of cold temperature set-point $T_{c,sp}$, capacitance C_{TR} , ambient temperature T_{amb} , and disturbances (parametrized by s , C_d and R_d , see Figure 4.3). Each test lasts 5 h and starts with the TER controlled in equilibrium, i.e., $T_c=T_{sp}$. In particular, $T_{c,sp}$ is randomly selected from the set $\{3,4,5,6,7\}^{\circ}\text{C}$ with uniform probability. T_{amb} is selected randomly for each TER and for each T_{amb} a random walk strategy is performed by varying it within $\pm 1^{\circ}\text{C}$ each hour. For C_{TR} , three TER sizes are analysed, 42 l (which was previously assessed), 30 l and 60 l; with associated thermal capacitance of 6300 J/K, 4600 J/K, and 9300 J/K, respectively.

Regarding the disturbances, during the test each TER is perturbed with masses (representing food) at ambient temperature. C_d and R_d are tuned to represent bottles of water containing 0.5-1 l that can be introduced/removed from the TER up to 10 times during the simulation. Table 4.7 summarizes the range of variation for each parameter.

TABLE 4.7: Intervals of model parameters for setting the simulations

Parameter	Minimum	Maximum	Units
$T_{c,sp}$	3	7	$^{\circ}\text{C}$
T_{amb}	18	26	$^{\circ}\text{C}$
C_d	8000	58400	J/K
R_d	0.35	0.75	W/K

PI-controlled TER flexibility evaluation

In the first set of simulations, a temperature set-point change is executed for the 50 TERs considering the PI controller presented in the subsection 4.1.5. For example, one TER temperature response is shown in Figure 4.15. This simulation is run two times:

- the first time it is made by changing the set-point to $T_{sp,down}$ (see Figure 4.15a green line).
- the second time it is made by changing the set-point to $T_{sp,up}$ (see Figure 4.15a blue line).

Figure 4.15b depicts the TER power demand, for the set point changes $T_{sp,up}$ and $T_{sp,down}$. Before a set-point variation, this TER is consuming on average 16.86 W. Then, when $T_{sp,up}$ is applied, the power (blue line) reduces to 1.10 W instantaneously (i.e., 93.5% reduction); further on, the power stabilizes after 2580 s (43 min) consuming on average 9.89 W (i.e., 58.7% reduction). Likewise, when $T_{sp,down}$ is applied, the power (green line) increases to $P_{max}=38.90$ W instantaneously (i.e., 230.7% increment) and remains there for a few seconds; further on, the power stabilizes after 2640 s (44 min) consuming on average 26.40 W (i.e., 156.6% increment). Small oscillations are observed when perturbations increase/decrease the thermal capacitance of the system.

Therefore, it is noticed that changing the temperature set-point, the system can either reduce or increase its demand instantaneously and could provide balancing services such as FCR, FRR and RR. Likewise, regarding Colombian ancillary services, the TER can provide primary, secondary and tertiary regulation reserves (see Section 2.2). However, considering the results with PI controller, the duration for which the TER maintains the power at zero or P_{max} is not enough to comply with the required delivery time. Then, a modified controller is proposed to provide a reliable energy service.

Modified PI controller

The PI controller has been thus modified with the purpose of increasing the interval length when $P=0$ or $P=P_{max}$ after a set-point change. Figure 4.14 shows the block diagram of the proposed modified control strategy. A new variable β is defined to change the set-point. It only considers three possible states for each TER:

- 0: Nominal operating set-point, i.e., $T_{sp,nor}$ which is defined from the set $\{3, 4, 5, 6, 7\}^{\circ}\text{C}$;
- 1: High set-point, i.e., $T_{sp,up}=8^{\circ}\text{C}$;
- -1: Low set-point, i.e., $T_{sp,down}=2^{\circ}\text{C}$.

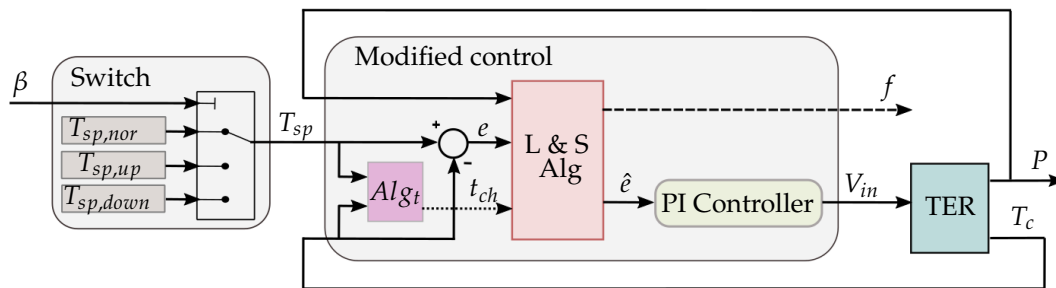
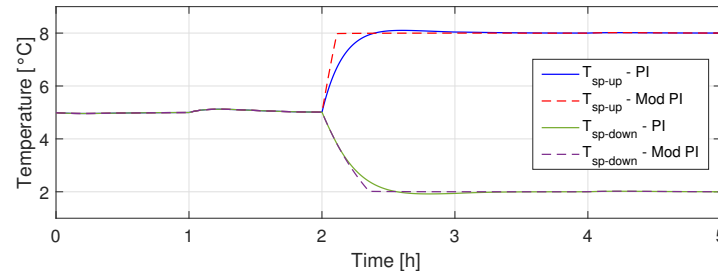


FIGURE 4.14: Modified TER control strategy.

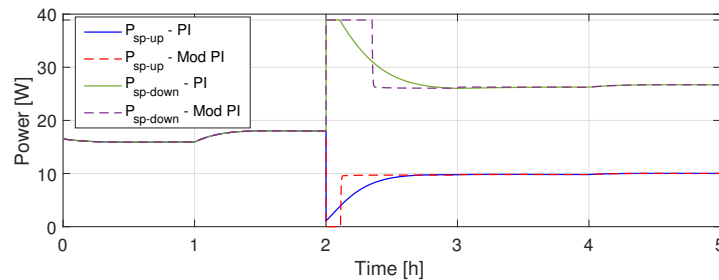
The Modified control block aims to saturate the controller action when a set-point change command arrives. This modification allows the TER to achieve the new set-point faster than with the PI controller and also maintains the power at zero or maximum power for a longer interval.

The algorithm (Alg_t block) identifies when a set-point change is requested, either to reduce (β goes from 0 to 1) or increase (β goes from 0 to -1) the demand, and saturates the controller output ($V_{in}=0$ to increase temperature or $V_{in}=V_{max}$ to reduce it) while the TER reaches the new temperature set-point. The algorithm (L & S Alg block) also reports if the TER already achieved the new temperature. The variable f indicates the TER flexibility; $f=1$ signals to the aggregator that the system is not saturated and has the possibility to vary power demand, while $f=0$ signals a saturated controller without capacity to vary power demand. In fact, the aggregator needs f in order to select which TERs are able to modify their temperature set-points.

A second set of simulations evaluates the flexibility of TERs with the modified controller. The same conditions of the simulation campaign in subsection 4.2.1 are maintained, using the modified controller architecture instead of the PI controller. Figure 4.15a depicts the TER temperature when high (see red dashed lines) and low (see purple dashed lines) set-point changes are applied, while Figure 4.15b shows the power demand (see red and purple dashed lines).



(A) TER temperature.



(B) TER power.

FIGURE 4.15: TER flexibility, with the PI controller and modified PI controller.

Response time analysis

The modified PI controller allows achieving $P=0$, as well as $P=P_{max}$ for a longer time interval than the one related to the PI controller. By considering the power reduction to $P=0$, the system can instantaneously reduce the demand by 100% and keeps this condition for 7 min; after that, the power stabilizes at the same value obtained when using the PI controller. This time does not fulfil the requirements for FCR provision. Considering a power rise to $P=P_{max}$, the system increases its demand instantaneously by 230.7%, and keeps it for 21 min. It is worth noting that this time matches with the requirements related to FCR and FRR service provision but not the RR service. In order to guarantee a proper compliance of the technical requirements of the balancing services, an aggregation strategy is introduced in section 4.2.2.

Recall that the TERs evaluated in the simulation campaigns have different parameters (see Table 4.7), then, their time response to a set-point change varies. The histograms in Figure 4.16 illustrate this fact by reporting the number of TERs staying at maximum/zero power for given time intervals, for both control strategies. Note that even the same TER subject to different perturbations can stay different periods in saturated condition.

Figure 4.16a depicts the number of TERs that remain in $P=0$. It is noted that with the nominal PI controller, most of the TERs (92%) come back to consume power after 5 min or less and 8% after 5 ÷ 10 min, whereas with the modified controller, on average they stay longer at $P = 0$ but they show more dispersion, 20% of the TERs resume their power after 0 ÷ 5 min, 52% after 5 ÷ 10 min, 24% after 10 ÷ 15 min, and 4% remain more than 15 min. In the same way, Figure 4.16b shows that with the nominal PI controller just 18% of the TERs remains at $P=P_{max}$ for more than 15 min, whereas with the modified controller this number increases to 68%. Notice that not all TERs are reported in Figure 4.16b, because they remain longer than 1800 s (7 TERs for the PI and 17 TERs for the modified PI).

Summarizing, the considered TER systems equipped with the nominal PI controller cannot maintain their power at zero or P_{max} for a time long enough to provide FCR services. While, with the modified PI controller, the systems improve their ability to respond within the time frame specified for the regulation service. However, to properly exploit the above mentioned characteristics, an aggregator is required to synchronize the power deviations of the set by managing the temperature set-point of each TER, providing energy services to the SO.

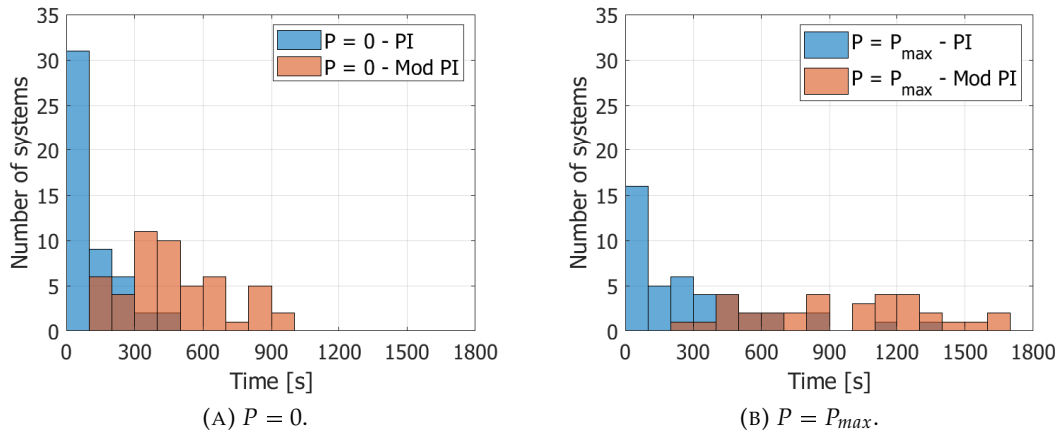


FIGURE 4.16: Histogram of the time elapsed consuming zero or maximum power after a set point change.

4.2.2 TER Aggregator

This subsection proposes an architecture to offer balancing services, such as FCR, FRR and RR, with a set of TERs, through an aggregator that synchronizes the temperature set-point changes of the TERs. An automatic control strategy is proposed in order to reduce or increase the power demand of the set, taking advantage of the flexibility found in the previous sections.

The aggregator is designed to respond to a SO requirement, assuming there is a signed contract with defined prices between the SO and the aggregator in order to provide the service. The number of TERs involved in the demand response program is known in advance. Figure 4.17 shows the block diagram of the system, whereas Table 4.8 presents the information exchange between the aggregator and each TER.

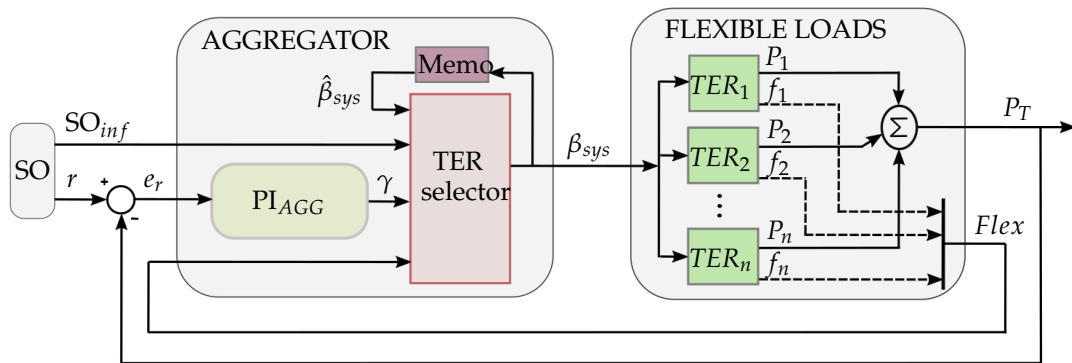


FIGURE 4.17: Block diagram of the TER aggregator.

TABLE 4.8: Information exchange between the aggregator and the TER units.

Message	Aggregator		TER unit	
	Variable	Data type	Variable	Data type
Send	β state	2 bits	Power P	Integer
			f state	Boolean

When the SO makes a power deviation request (signal r), the aggregator must decide how many and which TERs must activate their flexibility to achieve the requested service and it must be performed within the established times. As the power demand and flexibility state of each TER vary with time, it is not a trivial task to select the subset that will offer the service. Then a feedback strategy is proposed.

The AGGREGATOR operates through two control actions, i.e., a PI controller (PI_{AGG}) and a TER selector. Both actions operate when a SO request arrives. The controller has a 1 s sampling time, enough for accomplishing the system time response when providing the energy service (30 s in FCR service).

The output of the PI_{AGG} , signal γ , is the number of TERs that must change the set-point. A positive value indicates increasing the set-point, and a negative number the opposite. Thus, the output is saturated between $-n$ and n , where n is the number of TERs participating in the service provision.

The TER selector block is developed for deciding which TERs must change set-point to comply with the PI_{AGG} command. This selector follows the flow chart sequence presented in Figure 4.18. This sequence has two main logics, one for the power reduction request and another for the power increase. In both cases, the sequence looks for the TERs subset that has flexibility i.e., $f=1$, and can change the set-point to the value desired by the PI_{AGG} . The output β_{sys} contains the temperature set-point state of all the TERs, i.e., $\beta_{sys}=\{\beta_1, \beta_2, \dots \beta_n\}$.

The FLEXIBLE LOADS block represents the set of TERs and provides as output the total electric power P_T of the set. It also collects the flexibility information f of all systems and reports the signal $Flex=\{f_1, f_2, \dots f_n\}$ to the AGGREGATOR. Notice that the TER_i blocks presented in Figure 4.17 are considering not only the TER unit but also the modified PI controller and the switch, as depicted in Figure 4.14.

In order to calculate the PI_{AGG} parameters, a simulation with a set of $n=100$ TERs is developed. The 100 TERs are selected considering a trade-off between the computational effort and a reasonable systems aggregation, i.e., a feasible simulation with a number of systems that are able to reduce the individual effect in the aggregation performance. In this case, cold temperature set-point T_{sp} , capacitance C_{TR} , ambient

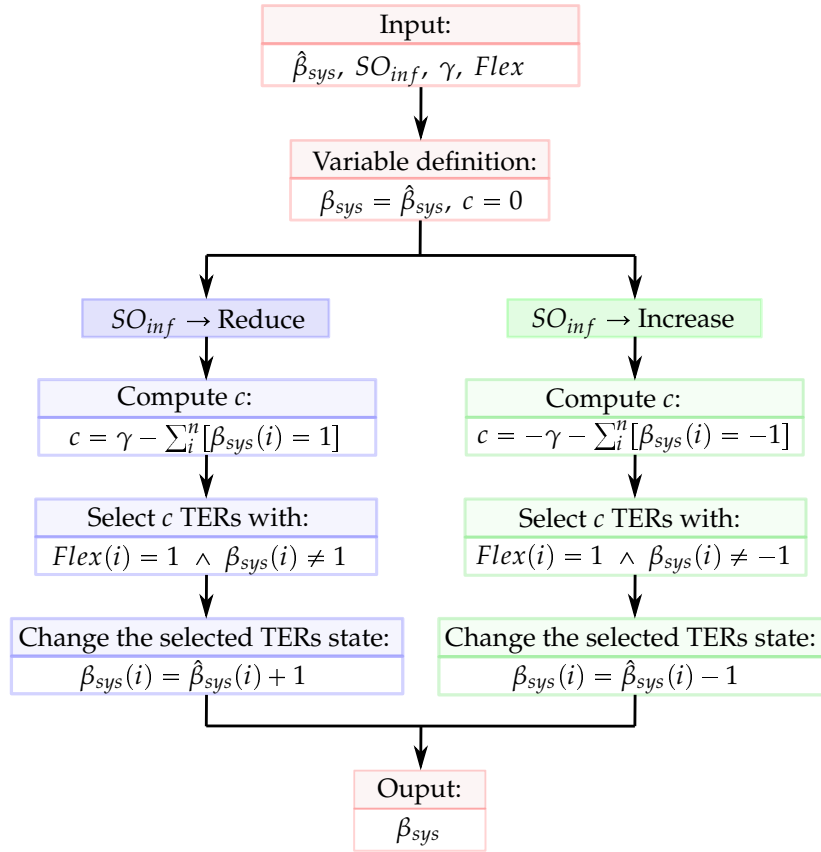


FIGURE 4.18: TER Selector sequence.

temperature T_{amb} , and disturbances C_d and R_d are randomly generated as in the previous section.

First, the power demand of the aggregated set is analysed by modifying simultaneously the 100 TER temperature set-points to 1, i.e., $\beta_{sys} = \{1, 1, \dots, 1\}$ (activating downward flexibility). Secondly, it has been studied the plant (FLEXIBLE LOADS block) behaviour by modifying the 100 TER temperature set-points to -1, i.e., $\beta_{sys} = \{-1, -1, \dots, -1\}$ (activating upward flexibility). Figure 4.19 shows the plant response for both set-point modifications.

Then, two dynamic models of the plant behaviour are estimated to represent the upward and downward dynamics of the systems and a controller is derived. The models are linear and time-invariant in transfer function form, $G_{up}(s)$ and $G_{down}(s)$, expressed as:

$$G_{up}(s) = \frac{25.95s^2 + 0.017s + 9.3e^{-6}}{s^2 + 1.1e^{-3}s + 6.8e^{-7}}, \quad (4.16)$$

$$G_{down}(s) = \frac{-17.35s^2 - 0.018s - 3.6e^{-6}}{s^2 + 2.3e^{-3}s + 3.7e^{-7}}. \quad (4.17)$$

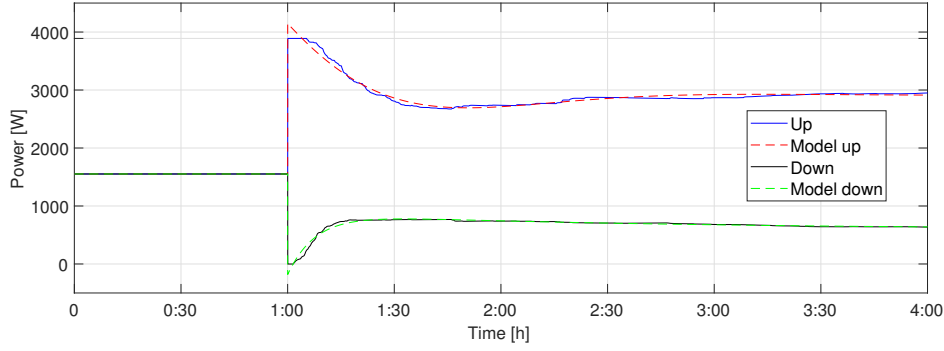


FIGURE 4.19: Models validation.

The quality of the models is measured evaluating the similitude of the models output with the aggregated power obtained in the simulation, i.e., the *FIT*, defined as,

$$FIT = 100 - \frac{\|x - x_{ref}\|}{N_s} 100(\%) \quad (4.18)$$

where x is the test data (i.e., the estimated model output), x_{ref} is the target data (i.e., the simulation response), and N_s is the number of samples.

The estimated models have $FIT_{up}=93\%$ and $FIT_{down}=94\%$, respectively. This is accurate enough to design the controllers.

Considering the MATLAB *Control System* toolbox, a PI controller that works for both models ($G_{up}(s)$ and $G_{down}(s)$) is designed to stabilize the power in less than 25 s. The controller parameters are $k_{pr}=0$ and $k_i = -0.012$.

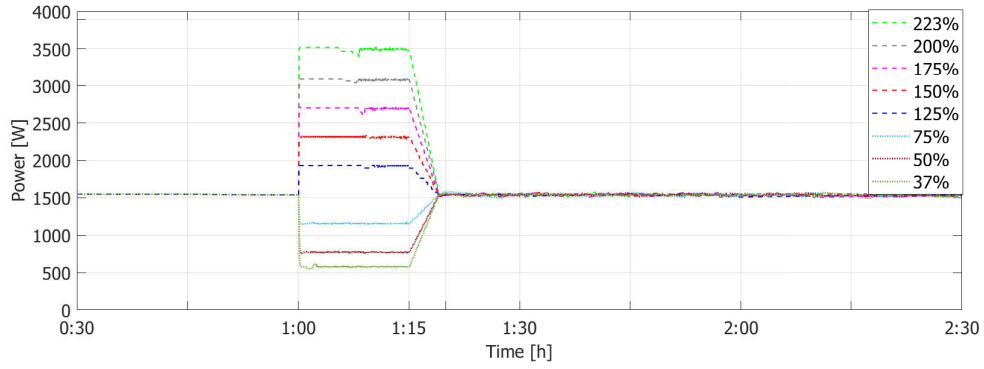
The system is evaluated in several Demand Side Flexibility (DSF) plans for providing FCR, FRR and RR services, following the sequence: the SO sends to the aggregator the power that the set of TERs must consume for the following 15 min (FCR and FRR) or 1 hours (RR), this power can be lower or higher than the one in normal operation. Therefore, two sets of experiments are developed for evaluating these energy services. For all experiments, cold temperature set-point T_{sp} , capacitance C_{TR} , ambient temperature T_{amb} , and disturbances C_d and R_d are generated randomly within the intervals in Table 4.7. The simulation run time is 1 h 21 min per experiment hour, this is owing to the dynamics of all TER models (the PI-selector aggregator solution for each experiment hour is developed in few run time seconds).

First, in the FCR service experiments, 8 different power levels (SO requests) are assessed. Moreover, following the FCR service specifications, the requested power must be delivered within 30 s after the SO request, and 50% of the requested power must be delivered within 15 s of the request arrival; while the ramp-down period must be lower than 5 min.

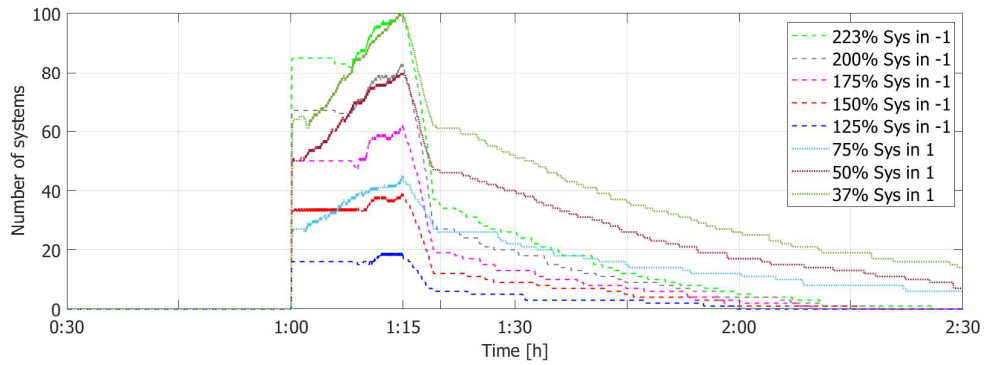
In Figure 4.20, the aggregator response for different power levels is presented. Figure 4.20a shows the deviations in the power demand following the SO requests. These power modifications are based on the nominal operation power i.e., the set of TERs has an average power of $P=1540$ W in nominal operation then, at the hour 1:00, the SO request arrives. This power request is supposed to be 37%, 50%, 75%, 125%, 150%, 175%, 200%, and 223% of the nominal power (i.e., 1540 W being 100%). The minimum and the maximum power requests, i.e., 37% and 223%, are found through repetitive simulations and they are related to the condition where the entire set of TERs has been involved in the FCR service provision (no more devices are available for further regulation). Therefore, the flexibility of the set of TERs allows the SO to request any power demand between 575 W and 3500 W for the next 15 min, i.e., the flexibility band for offering the FCR service is 2925 W. Besides, when the FCR service has finished, the aggregator recovers the power to the nominal one in 4 min avoiding any rebound effect, that is, there is no (positive or negative) peak in power demand at the end of the service, during the ramp-down period or later, see e.g. (Cui et al., 2018). Notice that this aggregator response satisfies also the delivery period of the FRR service, and the activation period can be regulated to a longer ramp-up time in order to fit the specified time of this service.

Figure 4.20b depicts the number of systems that are called to modify their temperature set-point, either upward ($\beta_i=1$) or downward ($\beta_i=-1$), i.e., the variable β_{sys} in each experiment. Then, at each time step, it is reported the number of TERs with temperature state in 1 for the SO requests higher than the nominal power, and in -1 for requests lower than the nominal power. It is shown how the aggregator responds to the SO request, modifying properly the temperature set-points of some TERs, reaching the requested power in less than 30 s and maintaining it during 15 min for all the different power levels, meeting the FCR service requirements.

Table 4.9 summarizes the results. For each SO request (r) are reported the average power effectively consumed during the delivery period (\bar{P}), the resulting percent error (\bar{E}), the standard deviation of the power demand (σ), the ramp-up times to the 50% ($t_{ru,50\%}$) and 100% (t_{ru}) of the capacity, the recovery time required by the 95% of the TERs for returning to the normal temperature set-point after the service ($t_{r,95\%}$), the recovery time required by the complete set of TERs (t_r) and finally the resulting ramp-up (ρ_u) and ramp-down (ρ_{dw}) rates. Note that the worst-case power deviation is 0.53%, all the power requests are achieved in less than 20 s, and half of the requests are fulfilled in less than 10 s. The standard deviation of the service is lower than 1% of the delivered power. The recovery time indicates the interval required to offer again



(A) Power consumed by all the TERs.



(B) Number of TERs changing the set-points.

FIGURE 4.20: Aggregator response for the Frequency Containment Reserve (FCR) service.

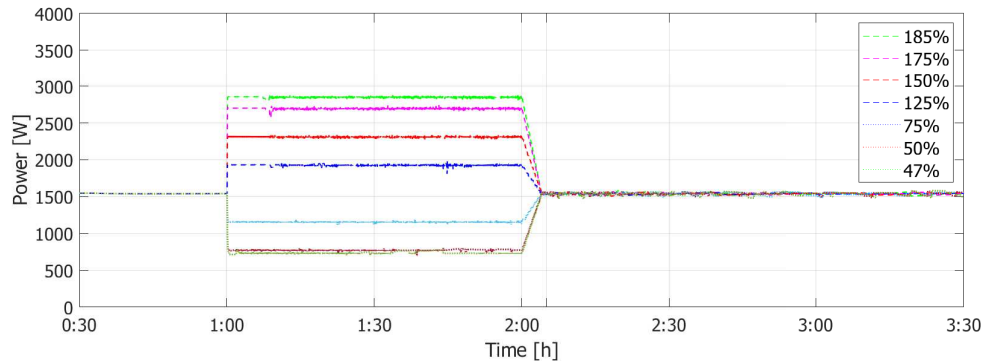
the service. It can be seen that t_r is much longer than the delivery period and it varies widely with the offered power level. However, most of the capacity (i.e., 95%) is available after a shorter time $t_{r,95\%}$. This characteristic can be exploited by the aggregator to modulate its offer in successive time periods.

TABLE 4.9: Aggregator characteristics during the Frequency Containment Reserve (FCR) service.

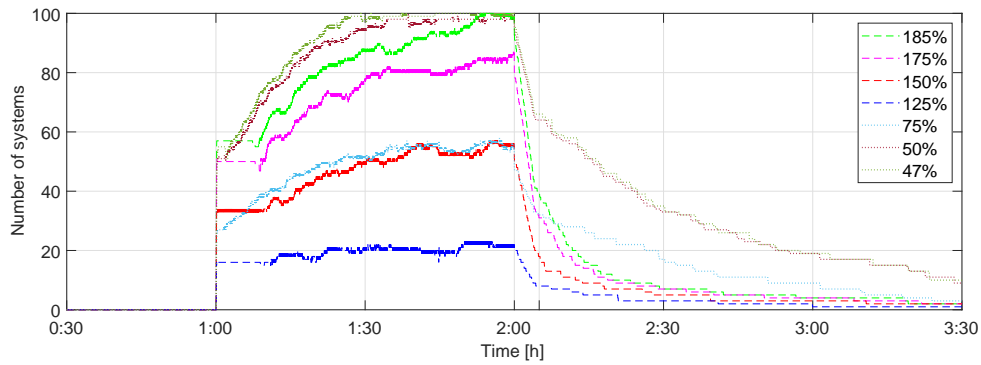
r [W]	\bar{P} [W]	\bar{E} [%]	σ [W]	$t_{ru,50\%}$	t_{ru}	$t_{r,95\%}$	t_r	ρ_u [W/s]	ρ_{dw} [W/s]
3500	3498.0	0.06	23.8	5''	9''	39'44''	1h6'5''	217.8	-2.3
3080	3078.7	0.04	13.3	5''	9''	36'55''	58'48''	171.1	-1.8
2695	2694.0	0.04	17.5	5''	9''	32'57''	49'53''	128.3	-1.4
2310	2309.7	0.02	9.4	5''	9''	24'39''	55'57''	85.6	-0.9
1925	1926.9	-0.10	9.4	5''	8''	3'42''	39'29''	48.1	-0.5
1155	1156.6	-0.13	5.2	7''	18''	1h17'	2h5'	-21.4	0.5
770	772.6	-0.34	5.5	7''	15''	1h22'	2h51'	-51.3	0.9
575	578.1	-0.53	9.5	7''	17''	1h37'	3h24'	-56.8	1.2

Second, in the RR service experiments, 7 different power levels (SO requests) are assessed. Following the RR service specifications, the requested power must be delivered within 30 min after the SO request and must be maintained for 1 h.

In Figure 4.21a, the aggregator response for different power levels is presented. Figure 4.21a shows the deviations in the power demand following the SO requests. The power modifications are based on the nominal operation power. This experiment is carried out for 47%, 50%, 75%, 125%, 150%, 175%, and 185% of the nominal power. Therefore, the flexibility of the set of TERs allows to offer reserve capacities between 730 W and 2850 W for delivery periods of 1 hour, i.e., the flexibility band for offering the RR service is 2120 W. Notice that the capacity for this service is 805 W lower than for the FCR one. Finally, no rebounds are generated at the end of the service.



(A) Power consumed by all the TERs.



(B) Number of TERs changing the set-points.

FIGURE 4.21: Aggregator response for the Replacement Reserve (RR) service.

Figure 4.21b depicts the number of systems that are called to modify their temperature set-point, either upward or downward, for each experiment. It is shown how the aggregator responds to the SO request, modifying properly the temperature set-points of some TERs, maintaining the power deviation during 1 hour for all the

different power levels, meeting the RR service requirements.

Table 4.10 summarizes the results. The same characteristics evaluated in Table 4.9 for the FCR service are considered. It can be seen that the precision in power tracking is similar for both services. Also the ramp-up and recovery times are comparable. In this case, the ramp-up time to the 50% ($t_{ru,50\%}$) is not reported as the full ramp-up time t_{ru} is much lower than the limit of 30 min, defined for the RR service.

Thanks to the proposed control strategy, the aggregation of TERs is able to offer this service according to the specifications. The set of TERs considered in this work covers partially the minimum reserve capacity required by the SO but the strategy can be scaled to manage a larger set of TERs. Thanks to the appropriate control actions, this chapter demonstrates the possibility for the TERs to be compliant with real services defined in existing network code.

TABLE 4.10: Aggregator characteristics during the Replacement Reserve (RR) service.

r [W]	\bar{P} [W]	\bar{E} [%]	σ [W]	t_{ru}	$t_{r,95\%}$	t_r	ρ_u [W/s]	ρ_{dw} [W/s]
2850	2849.7	0.01	10.1	10''	37'2''	3h32'39''	131.0	-1.6
2695	2694.8	0.01	11.1	9''	35'6''	3h19'49''	128.3	-1.4
2310	2310.0	0.00	9.9	9''	22'38'	2h37'45''	85.6	-0.9
1925	1925.4	-0.02	10.5	8''	8'48''	1h33'37''	48.1	-0.5
1155	1155.2	-0.02	5.7	19''	1h5'25''	3h7'1''	-20.3	0.5
770	771.9	-0.24	7.8	15''	1h50'24''	5h54'28''	-51.3	0.9
730	736.5	-0.90	13.2	19''	1h52'23''	5h55'23''	-42.6	1.0

Finally, notice that as in the WBPS aggregator (see Section 3.3), the TER aggregator can operate with any number of TERs. The aggregator only considers if the TER has flexibility on not and defines the temperature set-point state. Moreover, the PI_{AGG} controller only needs a recalculation of the PI controller parameters. Then, a technical resource such as smart meters is needed in order to acquire the aggregated power behaviour. This information will lead to identifying the new TER set response for computing the new parameter of the PI controller (with a step response). The identification and parameters computation can be developed by an adaptive controller. The number of systems n in the service is needed for knowing the controller saturation.

4.3 Remarks

In this chapter, an aggregator for TERs has been proposed. It is capable to offer balancing services such as frequency containment reserve, frequency restoration reserve, or replacement reserve, by reducing and increasing the power of a set of TERs. Based on a three-state signal (0,1, or -1), the aggregator decides the temperature set-point of each TER for following the signal sent by the system operator.

A dynamic model of a TER unit has been estimated from experimental data. The model error is less than 1°C. Then, the system can be treated as a flexible load by changing the temperature set-point.

A modified PI controller strategy is proposed based on a tested PI controller, achieving a longer time interval when the TER power is zero or maximum power after a set-point change, improving the regulation service offer.

The proposed aggregator can follow a requested power trajectory in less than 30 s, arriving at the 50% of the power in less than 15 s. Moreover, the information exchange between each TER and the aggregator is reduced to i) a three-state signal, ii) the power demand, and iii) the flexibility state. This is desired in a fast ancillary service as the frequency containment reserve service, due to it is achieved faster and simple communications between the stakeholders.

By knowing the upward and downward capacity (which depend on the current and predicted usage of the TERs in the aggregation and on the temperature preferences) and the aggregated TER baseline, the quantity offered can be established. However, the determination of the offers implies to establish not only the quantity, but also the price. These aspects, together with additional experimental evaluations considering spatially distributed TERs, will be addressed in future works.

Chapter 5

Optimal Strategy to Manage an Electric Vehicle Charging Station

This Chapter presents a framework to take advantage of EVs flexibility, maximising demand response capacity and minimizing operation costs. An Electric Vehicle Charging Station (EVCS) and its chargers are modelled and controlled as flexible loads. The EVCS is entrusted with charging all the incoming EVs, whose State of Charge (SoC) must reach at least a minimum level desired by the EV owners at the departure time. An cost-minimisation operation strategy and a novel EV charging strategy based on the maximisation of the flexibility for EV chargers are presented, taking into account the preferences of the EV users. These strategies are compared with a typical minimum time strategy as a benchmark, to adjust the trajectories of the charging power delivered to the EVs through the chargers. Meanwhile, a specific definition of flexibility for EV chargers is provided by adapting the operational flexibility in power systems concept used in (Ulbig and Andersson, 2015). This flexibility definition, different from (Ulbig and Andersson, 2015), leverages the ramp rate in kW to describe the variations. Furthermore, considering an analysis with time steps of the order of minutes for the EV chargers it is possible to adjust the power from maximum power to 0 (and vice versa) in one time step. Subsequently, EVs do not require a ramp rate constraint for varying the required amount of power.

The EV charging strategies are based on different optimization criteria of the charging power trajectories, namely:

- minimize the EVCS operation cost, by varying the charging power depending on the energy prices and the charging duration;
- maximise the flexibility capacity (based on Definition 1, section 5.2), while minimizing the EVCS operation cost.

In order to compensate for the uncertainties on the EV initial state of charge and the power generation, a Model Predictive Control (MPC) strategy is adopted within the two proposed solutions. Furthermore, the EV charger flexibility is analysed and tested related to the EV charging time, the specific time slot, and the power delivered by the charger.

The rest of the Chapter is organized as follows: Section 5.1 describes the problem faced by an EVCS, how it operates, the charger dynamics model, how to take into account the uncertainties, and introduces the proposed EV flexibility analysis. In Section 5.3, the charging strategies are illustrated and thoroughly described. In Section 5.4, case study is shown, along with the related numerical results. The results of this Chapter were derived in the publications ([Diaz et al., 2018a,b](#); [Diaz-Londono et al., 2019a](#)).

5.1 Electric Vehicle Charging Station Operations

An Electric Vehicle Charging Station (EVCS) is composed of various chargers, to which EVs connect with the aim of getting charge. The problem faced by a typical EVCS for managing the charge of the connected EVs, is twofold:

1. chargers scheduling, also taking into account the uncertainty of the EV arrival time and initial state of charge of the EV battery; and,
2. EV load profile management.

The first problem refers to the assignment of a charger to each EV approaching the charging station, as well as their charging time. Secondly, the EV load profile, namely, the charging power delivered by each charger at each time slot defined for the analysis, must also be considered.

In this study, the EVCS works with a centralised infrastructure to collect EV information and to deliver power to each vehicle, i.e., EV battery chargers can be considered as flexible loads in the energy consumption. Consequently, an EVCS can be modelled as an aggregator that is capable of modulating the energy delivered by the chargers. The EV owner willing to recharge the EV battery goes to the charging station and takes part in the program managed by the aggregator. At the departure time specified by the EV owner, the battery will be charged according to the agreement between the aggregator and the EV owner. In the time period in which the EV is managed by the aggregator, the aggregator provides flexibility to the system without the direct action of the EV owner.

In this section, the station operation process and then the EVCS problem formulation are presented. Then, a flexibility evaluation is presented, leading to a novel EV battery charger flexibility definition. For the sake of completeness, Table 5.1 summarizes the notation adopted for the system variables.

TABLE 5.1: Notation of the EVCS variables.

Symbol	Variable	Units
k	Time slot	-
$x_{i,k}$	State of Charge in charger i	kWh
$SoC_{j,k}$	State of Charge in EV j	kWh
$P_{T,k}$	Power delivered by the station	kW
F_k	Flexibility capacity of the station	kW
$F_{i,k}$	Flexibility capacity in charger i	kW
$P_{i,k}$	Power delivered to charger i	kW
$U_{i,k}^F$	Upward flexibility capacity in charger i	kW
$L_{i,k}^F$	Downward flexibility capacity in charger i	kW
I	Amount of chargers	-
H	Prediction horizon	h
β	Operation time of the station	h
EV_j	Electric vehicle j	-
C_j	Battery capacity in EV j	kWh
χ_j	Information provided by the EV j	{set}
χ_T	Information provided by all EV	{set}
$\xi_{i,k}$	Schedule of chargers i	[0,1]
$\xi_{T,k}$	Schedule of all chargers in the station	{set}
c_k	Energy Price	\$/kWh
π_k^U	Remuneration Price of the upward flexibility capacity	\$/kWh
π_k^L	Remuneration Price of the downward flexibility capacity	\$/kWh
a_j	EV j arrival time	h
d_j	EV j departure time	h
r_j	EV j charger request time	h
d_m	Time for charging EV j with maximum power	h
\widetilde{SoC}_{j,d_j}	Minimum State of Charge in EV j (at departure)	kWh
γ	SoC information by all EVs	{set}
Δt	Sampling time	min

5.1.1 Charging Station Operations

The EVCS goal is to charge all the EVs connected to the battery chargers, within their own charging time, achieving a SoC between the minimum SoC desired by the owners at the departure time and full charge (100%). To this aim, an aggregator is responsible for scheduling the charging patterns of an EV group (see Figure 5.1).

Given a typical EVCS, let us assume that there are I chargers, whose load patterns have been programmed through the aggregator for the next H hours. Notice that these load patterns are affected by uncertainty in the arrival time and the initial SoC of each EV. Furthermore, the operation time of the station is divided into K discrete time intervals with equal length, each of them being a discrete time slot $k = 1, \dots, K$, lasting a sampling time Δt in minutes. Finally, for each day, it is expected to serve J EVs, where for each EV j , its charging time spans from the arrival time a_j to the departure time d_j .

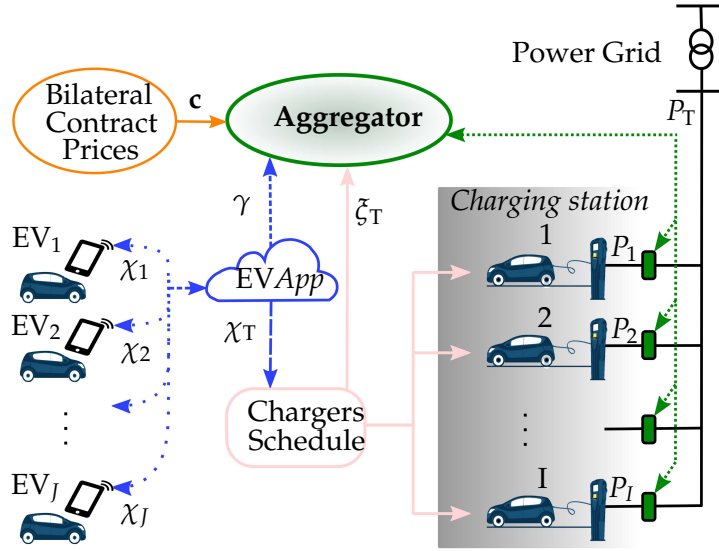


FIGURE 5.1: Electric Vehicle Charging Station operation.

A typical EVCS work-flow starts with the users, i.e., the EV owners, requesting an available charger, possibly through a mobile application (let us say, *EVApp*), at least one hour before arriving at the station. This recharge request includes the EV_j relevant information, collected in χ_j ,

$$\chi_j = \{\tilde{a}_j, d_j, \widehat{SoC}_{j,r_j}, \widehat{SoC}_{j,d_j}\}, \quad \forall j = 1, 2, \dots, J; \quad (5.1)$$

\widehat{SoC}_{j,d_j} being the minimum SoC desired by the EV_j owner at the departure instant d_j , \widehat{SoC}_{j,r_j} the EV_j SoC at the request time r_j , and \tilde{a}_j the reported arrival time. Then, the EV owner looks for booking an EV charger from \tilde{a}_j to d_j . Finally, all the EV information to be sent to the charger scheduling algorithm is collected in χ_T :

$$\chi_T = \{\chi_1, \chi_2, \dots, \chi_J\}. \quad (5.2)$$

For the purpose of this study, it is assumed that the actual arrival SoC is higher than zero, i.e., $SoC_{j,a_j} > 0$. In Figure 5.2, the request time r_j , the expected arrival time \tilde{a}_j , the actual arrival time a_j , and the actual departure time d_j of an EV are presented considering the SoC at the request \widehat{SoC}_{j,r_j} , the expected SoC at the arrival \widetilde{SoC}_{j,a_j} , the actual SoC at the arrival SoC_{j,a_j} , the minimum SoC desired by the owner at the departure \widetilde{SoC}_{j,d_j} , and the actual SoC at the departure SoC_{j,d_j} . Then, notice that the actual arrival SoC and the reported SoC at the request are generally different, i.e., $SoC_{j,a_j} \neq \widehat{SoC}_{j,r_j}$ (see Figure 5.2a).

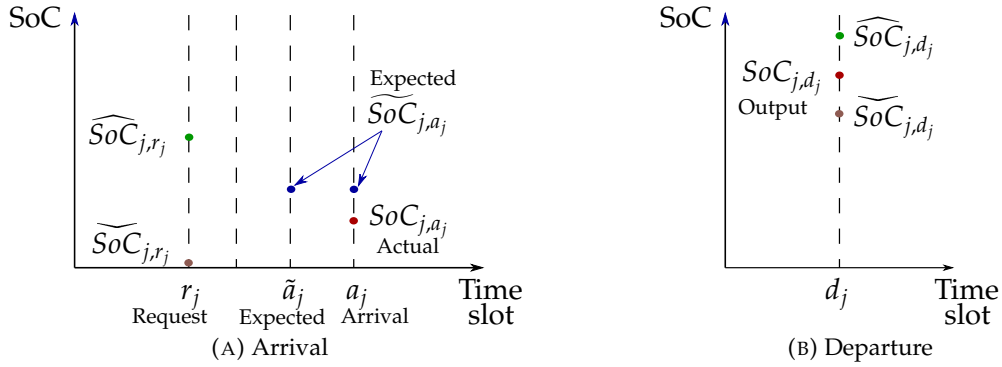


FIGURE 5.2: Expected and actual time and state of charge for the j th electric vehicle.

Then, the EV arrival SoC and the EV arrival time are uncertain variables that must be managed by the aggregator. Then, the mobile app collects and sends the information $\gamma = \{SoC_{1,r_1}, SoC_{2,r_2}, \dots, SoC_{J,r_J}\}$ to the aggregator. The timings are considered by introducing practical assumption for serving the EV:

- in case of early arrival, nothing changes with respect to the scheduled charging starting instant (\tilde{a}_j); the EV will wait until the scheduled time slot;
- in case of late arrival, up to a given delay δ , the charging procedure can be performed guaranteeing a departure SoC within the requested limits (see feasible condition Equation (5.16), presented in Section 5.3.2);
- in case of late arrival, greater than a given delay δ , the vehicle is still accepted, but the requested final SoC cannot be guaranteed; and
- the departure time d_j is fixed by the EV owner request, and is considered as a deterministic variable (see Figure 5.2b).

In this context, the arrival time is considered as a random variable uniformly distributed within a given time range around the scheduled time. The arrival SoC is

taken into account as a random variable uniformly distributed between zero and the SoC at the request SOC_{j,r_j} . This distribution is applied not only due to the lack of real data (for feeding the model), but also because it ensures the random value between the defined range.

The aim is to dispatch the J requests to the I chargers, via an allocation algorithm. This algorithm provides two output data sets: (i) the ID_i of the assigned charger (if any), sent to the user, and (ii) a binary state signal $\xi_{i,k}$, sent to the aggregator. This signal indicates the schedule of the i th charger, i.e., if at the k th time slot, an EV is plugged into it. Hence, at time slot k , it holds:

$$\xi_{i,k} = \begin{cases} 1, & \text{if the charger } i \text{ has a plugged-in EV,} \\ 0, & \text{if the charger } i \text{ does not have a plugged-in EV.} \end{cases} \quad (5.3)$$

The decision variables used for the energy dispatch design are the power signals $P_{i,k}$ describing the power delivered by each charger i to the EV connected to it at the time step k . This power can be adjusted for each time slot, in a way consistent with the "Smart charging" concept defined in (Colmenar-Santos et al., 2019) as *charge speed changes in order to match with a control signal or frequency regulation and vehicle parameters. In a smart grid environment, smart charging provides flexibility to the grid, allowing demand response services*. Smart charging strategies have been used in (Wenzel et al., 2018) by comparing different strategies with the aim of providing frequency regulation services, in (del Razo et al., 2015) in conjunction with the provision of vehicle-originating signals to minimise the variability of the aggregate power pattern with respect to a predefined reference, in (Naharudinsyah and Limmer, 2018) to minimise the cost of the charging schedule by taking into account the trading on the intraday electricity market. From a technical point of view, the implementation of dynamic EV charging is discussed in (Mouli et al., 2016) considering different solutions for AC charging, Chademo and Combined Charging System (CCS)/COMBO. Moreover, the Open Charge Alliance has issued the Open Charge Point Protocol (Open Charge Alliance, 2015), in which, *while charging is in progress, the connector will continuously adapt the maximum current or power according to the charging profile*. Further recent developments on EV charging have been presented in (Amjad et al., 2018).

Therefore, the instant power extracted from the grid, at each time slot k , is:

$$P_{T,k} = \sum_{i=1}^I P_{i,k} \quad \forall k = 1, 2, \dots, K. \quad (5.4)$$

As a matter of fact, the aim of the aggregator is to define the load profiles $P_{i,k}$ by maximising the operation benefits. To this aim, the EV chargers are considered as flexible loads, in terms of power consumption, which can provide some ancillary services to the electrical grid.

5.1.2 The Charger Dynamics Model

The SoC dynamics of a vehicle j connected to the charger i , namely, the evolution of the energy stored in the EV battery, can be modeled as:

$$SoC_{j,k+1} = SoC_{j,k} + \Delta t P_{i,k}, \quad (5.5)$$

where Δt is the sampling time, and $SoC_{j,k}$ is the accumulated energy in the EV battery through the integration of the charging power $P_{i,k}$. No efficiency losses or nonlinearities are considered. Likewise, battery degradation estimation (Hoke et al., 2014) is not considered because the time steps used in the analysis are relatively short (i.e., tens of minutes, for a period of analysis of one day).

Letting $x_{i,k}$ be the state variable representing the SoC of the EV connected to the i th charger, it holds:

$$x_{i,k+1} = \xi_{i,k} x_{i,k} + \xi_{i,k} \Delta t P_{i,k}. \quad (5.6)$$

Hence, when a vehicle is plugged in, namely $\xi_{i,k} = 1$, the charger dynamics matches Equation (5.5), i.e., $x_{i,k} = SoC_{j,k}$. Note that, over the course of a day, a charger can charge several EVs. Thus, it is convenient to use the charger SoC as the state variable in the model. As a result, $x_{i,k}$ has a switching behaviour, depending on $\xi_{i,k}$, and characterised by jumps either from 0 to \widetilde{SoC}_{j,a_j} , at each EV arrival, or from SoC_{j,d_j} to 0, at the EV departure. Therefore, the chargers dynamics $x_{i,k+1}$ can have three different conditions:

$$x_{i,k+1} = \begin{cases} x_{i,k} + \Delta t P_{i,k} & \text{if } \tilde{a}_j < k < d_j, \\ \widetilde{SoC}_{j,a_j} & \text{if } k = \tilde{a}_j, \\ 0 & \text{if } \xi_{i,k} = 0 \quad \vee \quad k = d_j. \end{cases} \quad (5.7)$$

The first condition in Equation (5.7) must hold until the vehicle SoC reaches a value between the minimum SoC desired by the owner and the maximum allowed one. Moreover, considering the third condition in Equation (5.7), the duration Δt of the time slot k is assumed to be consistent with the time required for an EV finishing the charging process to go away and for another EV to arrive to the same charger.

5.2 Flexibility Evaluation

Considering smart grids, it is possible to provide a service within the energy system by varying the power consumption at the demand side, without affecting significantly the overall service provided by the load. This is known as flexibility (Ottesen et al., 2018). As a matter of fact, a certain degree of flexibility is allowed because there are different ways to charge EV batteries, fulfilling the departure state of charge \widetilde{SoC}_{j,d_j} constraint and maximum power limits.

Generally speaking, flexibility enhances electrical grid security. For example, when a renewable energy source is connected to the grid, fluctuations can imbalance the grid itself. In these cases, a flexible load management system can favourably counteract these effects. Provided that a certain degree of flexibility is available, the system operator can adopt different ancillary services to avoid system instabilities, depending on the component that unbalances the system (Hao et al., 2015a)

In Subsection 2.2, demand response and ancillary services are presented. From this perspective, the current EV charger technology allows adjusting the power supply within a second, then, EV chargers could provide both frequency regulation and reserve services to the grid. However, given that a centralized infrastructure is considered, the communication between the system operator and the EVCS is limited by a few-minute response (Quinn et al., 2010; Kirby and Hirst, 2000). This implies that, among the many North American ancillary services, an EVCS can provide spinning or non-spinning reserve, and replacement reserve. Likewise, regarding Colombian ancillary services, an EVCS can provide secondary and tertiary regulation reserves. In turn, this work will focus on spinning reserve, being the most economically valuable one (Kirby et al., 2008). With the spinning reserve service, a charging station restores the generation and load balance, in the event of a contingency, in a matter of minutes (González et al., 2014). Then, in order to provide spinning reserve services through an aggregator that takes advantage of the EV flexibility, the concept of flexibility must be evaluated.

Availability of a specific definition of the flexibility of EV battery chargers may help improving the EV schedule and the ancillary services an EVCS can offer. Therefore, a novel definition of flexibility for EV battery chargers is provided as follows.

Definition 1. Given a nominal charging profile $P_{i,k}$ for $k = 1, \dots, K$, the flexibility F_k of an EVCS, for each time slot k , is defined as:

$$F_k = \sum_{i=1}^I F_{i,k} = \sum_{i=1}^I (U_{i,k}^F + L_{i,k}^F), \quad \forall k=1,2,\dots,K, \quad (5.8)$$

where

$$U_{i,k}^F = \begin{cases} P_{i,\max} - P_{i,k} & \text{if } \xi_{i,k} = 1 \wedge k < d_m, \\ 0 & \text{if } x_{i,k} = x_{i,\max} \vee x_{i,k} = 0 \vee k \geq d_m, \end{cases} \quad (5.9a)$$

$$L_{i,k}^F = \begin{cases} P_{i,k} & \text{if } \xi_{i,k} = 1 \wedge k < d_m, \\ 0 & \text{if } x_{i,k} = x_{i,\max} \vee x_{i,k} = 0 \vee k \geq d_m. \end{cases} \quad (5.9b)$$

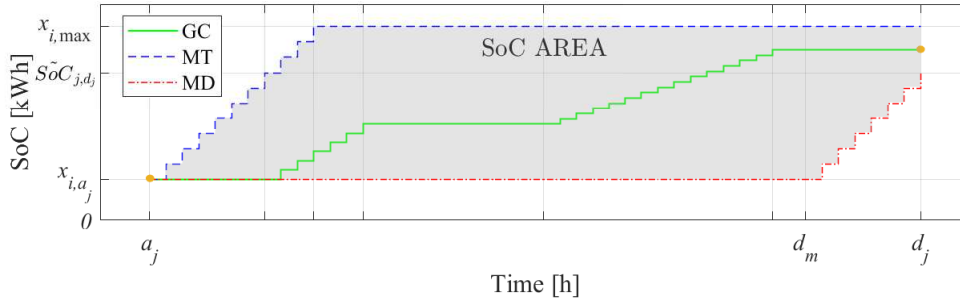
Note that the flexibility is the maximum power deviation that the profile can reach either upward or downward.

Therefore, a charger is said to be upward-flexible ($U_{i,k}^F > 0$), when it can increase the power injected to the connected EV. It happens whenever the power delivered by the charger is lower than $P_{i,\max}$, and the $SoC_{j,k} < x_{i,\max}$. On the other hand, a charger is downward-flexible ($L_{i,k}^F > 0$) if it can decrease the power injected to the connected EV (see Equation (5.9b)). Since the V2G concept is not considered, the charging station problem works only in a unidirectional system, thus $P_{i,k} \geq 0$.

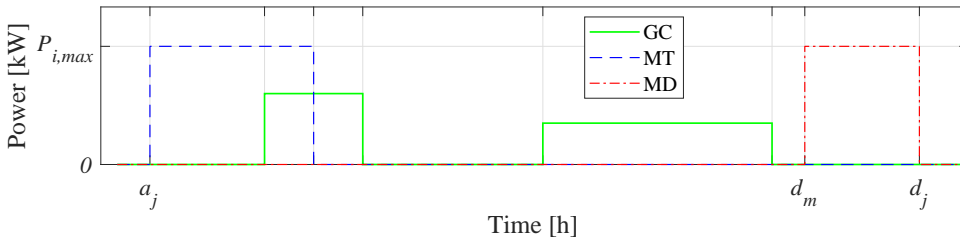
A detailed view of EV battery charger flexibility is presented in Figure 5.3. The structure of the figure is consistent with the framework presented in (Mills and Macgill, 2018) for EVs, which considers SoC on the vertical axis, while the operational flexibility framework introduced in (Ulbig and Andersson, 2015) (not referring to EVs) has a similar representation, but the vertical axis is expressed in MW for power system studies. In particular, Figure 5.3a shows the EV SoC behaviour during the charging time. The continuous green line is an example of an EV Generic Charging (GC) profile, and the dashed-blue and the dash-dotted red lines represent the limits of the SoC area. These limits are described by two charging profiles. First, of all, the Minimum Time (MT) strategy (dashed blue line), obtained by injecting the maximum power $P_{i,\max}$, immediately at the EV arrival time, until the full charge.

Secondly, the Most Delayed (MD) strategy (dash-dot red line) suggests that, starting from time d_m , only the maximum allowed power $P_{i,\max}$ lets the SoC reach the (minimum) desired departure value \widetilde{SoC}_{j,d_j} (in this case, no flexibility is possible from d_m to d_j). Figure 5.3b depicts the power injected by strategies GC, MT, and MD for creating the SoC area. Note that there are no idle losses due to the short time horizon,

and no negative power flows are considered as this work does not take into account V2G applications.



(A) SoC area with an example of a SoC profile (continuous green line).



(B) Charging power profile.

FIGURE 5.3: SoC area in an EV charger.

In short, the upward flexibility is the capacity of increasing the charging power up to $P_{i,max}$, while the downward flexibility is the capacity of charging with lower power or renounce to charge. Finally, the EV should depart with a charge level $x_{i,d_j} \in [\widetilde{SoC}_{j,d_j}, x_{i,max}]$, where $x_{i,max}$ corresponds to the full charge condition.

In addition, in Figure 5.4, the flexibility areas for the three strategies are shown, highlighting the upward (U) and the downward (L) flexibility. Although the downward (L) flexibility is positive, for better representation, it is plotted as a negative value to indicate a power reduction, i.e., $-L$ is depicted. In the MT case (Figure 5.4a), it is possible to achieve downward flexibility ($-L_{MT}$) only, due to the possibility of reducing power (up to $P_{i,max}$). However, after fully charging the EV, no flexibility is allowed. In the MD case (Figure 5.4b), it is possible to achieve upward flexibility (U_{MD}) only, due to the possibility of increasing power to $P_{i,max}$. However, after d_m , charging at maximum power $P_{i,max}$ is needed to reach \widetilde{SoC}_{j,d_j} . Consequently, no charging flexibility is allowed after that instant. In the GC case (Figure 5.4c), the upward (U_{GC}) and the downward ($-L_{GC}$) flexibilities are shown. The filled parts indicate the area where the power charging profiles can be adjusted, following profiles of $P_{i,k} \in [0, P_{i,max}]$ that guarantee not to violate the constraints. It is noteworthy that the SoC might also remain constant for a certain period, e.g., when the EV is not charged, according to the

aggregator needs.

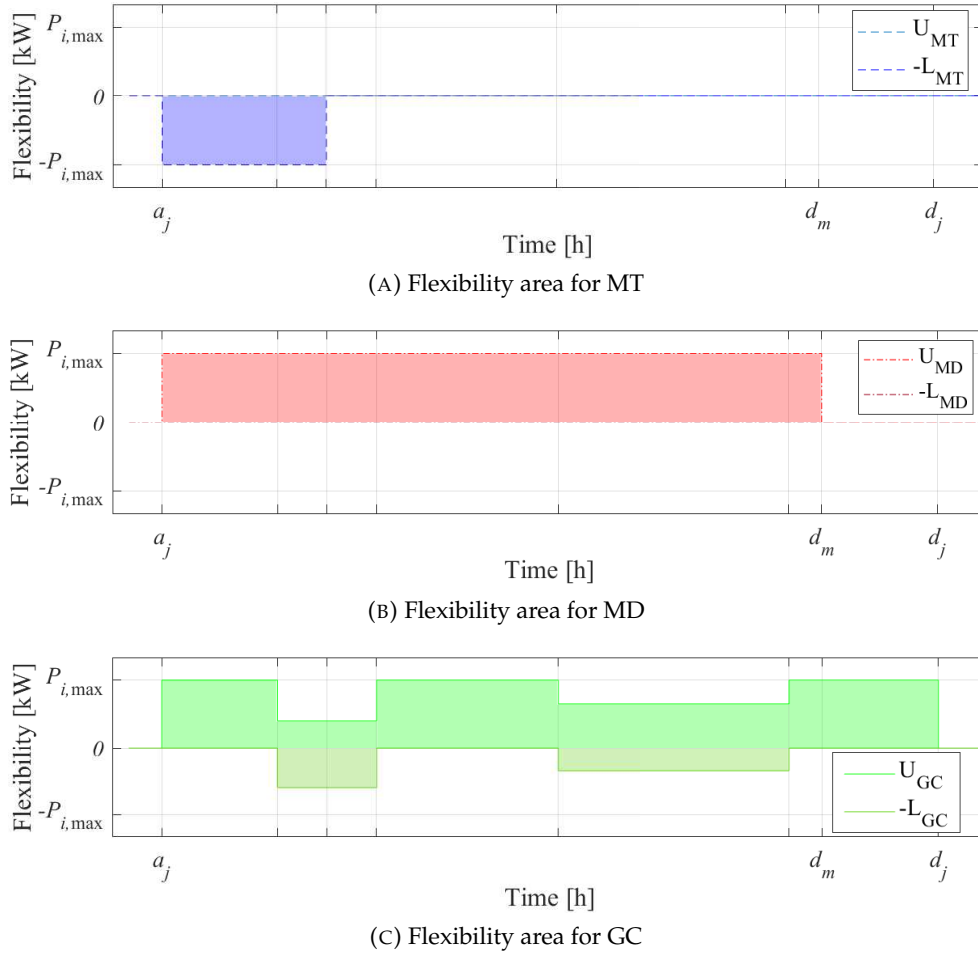


FIGURE 5.4: Flexibility in an EV charger.

As a result, the flexibility assessment turns out to be crucial to maintaining the electrical grid balance. Consequently, the aggregator can provide a balancing service, restricted by the defined GC profiles, admitting the possibility of having zero flexibility capacity in some time slots. Note that, with the defined GC power exemplified in Figure 5.3b, it is possible to achieve a flexibility $F_{i,k} = P_{i,k}$ at all plugged-in time, i.e., all time steps (see Figure 5.4c).

Therefore, the charging station problem, given the power design variables (namely, the power supply sequence $P_{i,k}$ and the flexibility capacities $U_{i,k}^F$ and $L_{i,k}^F$), consists of selecting the optimal power load profile $P_{i,k}^*$ for each charger i , for all the time slots up to the total operation time of the charging station β . Interestingly, the aggregation decision might also be based on the electricity price c_k and reserve prices, assumed to be known from bilateral contracts (with the aggregator that manages the charging

station) and variable hourly. As such, no uncertainty is considered for these prices. In this framework, the optimisation problem formulation will aim at guaranteeing a flexibility capacity, while minimising operational costs, and ensuring a departure SoC within the requested limits for each EV.

5.3 Solution Strategies

In this section, three strategies to attack the EVs charging station problem are discussed:

1. *Minimum Time (MT)*, as a standard approach, here adopted as a benchmark;
2. *economic Model Predictive Control (eMPC)*, a novel formulation whose basics have been published in (Diaz et al., 2018a,b);
3. *Optimal Control with minimum Cost and maximum Flexibility (OCCF)*, a novel strategy based on the Definition 1 presented in subsection 5.2, and published in (Diaz-Londono et al., 2019a)

In the eMPC and OCCF strategies, uncertain parameters such as EVs' initial SoC at the arrival and their arrival times are considered. Both strategies are based on MPC formulations. The MPC strategy (also known as Receding Horizon Control) makes explicit use of a plant model to obtain the optimal control signal by minimising an objective function. MPC exploits forecast values together with new information to establish the future evolution of the system, handling the constraints in an efficient way. The main advantages of the MPC strategy are: (i) it introduces feed-forward control implicitly, to compensate disturbances and measurement noise rejection; (ii) it is not conceptually complex to treat the constraints over inputs, states, outputs and slew-rate variables; (iii) single-variable and multi-variable cases are easily treated; and (iv) it is appropriate to address single-objective and multi-objective control, and signal following.

5.3.1 Minimum Time as a Benchmark

A straightforward strategy to charge EVs in an EVCS is based on the charging time minimisation. In short, each vehicle is charged at the maximum allowed power $P_{i,\max}$, until it reaches its full capacity $SoC_{i,\max}$. However, this strategy does not take into account the time-varying energy price, nor the possibility to provide ancillary services

to the electrical grid. To sum up, the charging power $P_{i,k}$ is determined as:

$$P_{i,k} = \begin{cases} P_{i,\max} & \text{if } 0 < x_{i,k} < x_{i,\max} \\ 0 & \text{otherwise} \end{cases}, \quad (5.10)$$

where $x_{i,\max}$ is the maximum admissible SoC in the EV_{*j*}. For example, by considering an EVCS with charging power levels 2 (semi-fast) and 3 (fast), and an EV with a battery capacity of 50 kWh, the charging time is expected to be around six hours for level 2 and one hour for level 3 (Yilmaz and Krein, 2013), depending on the SoC at the arrival. Note that, for achieving the minimum SoC \widetilde{SoC}_{j,d_j} (full SoC capacity with this strategy) at the departure time, only the EV_{*j*} charging feasibility in a time-span from a_j to d_j is required. This is clarified below.

5.3.2 Economic Model Predictive Control

A novel formulation for the cost minimisation strategy is presented in this section and it is based on a Model Predictive Control (MPC) strategy.

The MPC strategy emerged in the late seventies (Richalet et al., 1976, 1978). It is also known as Model-based Predictive Control (MBPC) or Receding Horizon Control (RHC). MPC is not a specific control technique, but a family of time-domain strategies. These strategies make explicit use of a plant model to obtain the control signal by minimizing an objective function. MPC exploits forecast values together with new information to establish the future evolution of the system, handling the constraints in an efficient way (Camacho and Bordons, 2007).

The main advantages of the MPC strategy are:

- it is applicable to a wide variety of processes, from very simple to complex dynamics;
- it can be developed with linear and non-linear models.
- single-variable and multi-variable cases are easily treated;
- it is appropriate to address single-objective and multi-objective control, and signal following;
- it has inherent compensation of dead-time and time-delay phenomena;
- it introduces feed-forward control implicitly, to compensate disturbances and measurement noise rejection;

- it is not conceptually complex to treat the constraints over inputs, states, outputs and slew-rate variables; and,
- it is very useful for processes where future patterns are known, e.g., with reference trajectory available.

However, some disadvantages of the MPC strategy are:

- the dependency on an appropriate model of the process;
- the control law derivation is more complex than in classical controllers; and,
- the process dynamics must be considered at each step.

Therefore, the MPC path to the solution of the charging station problem looks for adjustments in the injected power $P_{i,k}$, at every time slot k , in each charger i , considering the time-variant energy prices c_k , the uncertainty in the EV arrival time and SoC at the arrival time, i.e., a_j and \widetilde{SoC}_{j,a_j} . Hence, the optimality here refers to a charging profile that minimises the EVCS operation costs, while guaranteeing for all EV _{j} the minimum \widetilde{SoC}_{j,d_j} at the departure time d_j . Thus, by recalling Equation (5.3), Equation (5.4) and Equation (5.7), it holds:

$$\min_{P_{i,k}} \quad \Delta t \sum_{k=0}^{H-1} \left(c_k \sum_{i=1}^I P_{i,k} \right) \quad (5.11a)$$

$$\text{s.t.} \quad x_{i,k+1} = \begin{cases} x_{i,k} + \Delta t P_{i,k} & \text{if } \tilde{a}_j < k < d_j, \\ \widetilde{SoC}_{j,a_j} & \text{if } k = \tilde{a}_j, \\ 0 & \text{if } \xi_{i,k} = 0 \quad \vee \quad k = d_j, \end{cases} \quad (5.11b)$$

$$\widetilde{SoC}_{j,d_j} \leq x_{i,d_j} \leq \widehat{SoC}_{j,d_j},$$

$$0 \leq P_{i,k} \leq P_{i,\max},$$

$$0 \leq x_{i,k} \leq x_{i,\max},$$

$$\forall k = 1, 2, \dots, H, \quad i = 1, 2, \dots, I, \quad j = 1, 2, \dots, J.$$

Notice that the dynamic constraint considers the reported arrival time \tilde{a}_j in the request, and a random initial state \widetilde{SoC}_{j,a_j} given with a uniform distribution between the minimum \widetilde{SoC}_{j,r_j} and the SoC at the request time \widehat{SoC}_{j,r_j} . Therefore, the actual arrival SoC is lower than the one at the request, i.e., $SoC_{j,a_j} < \widehat{SoC}_{j,r_j}$. In addition, the actual arrival time a_j is known within the time interval previous to the connection of the EV to the charger.

In Equation (5.11), the aggregator problem is an optimal control strategy in open loop. Specifically, for the k th time slot, $x_{i,k}$ is the state variable corresponding to the i th charger SoC, while $P_{i,k}$ is the commanded variable corresponding to the delivered power profile. It is worthwhile to notice that the problem parameters in Equation (5.11) are affected by uncertainties on arrival time and SoC of the EVs. An open loop strategy cannot consider the future unknown behaviours, leading to possible unfeasibilities in the optimal solution. Therefore, the solution strategy should take these uncertain behaviours into account, and possibly recompute the control signal, even at each time step if needed. For this reason, a model predictive control strategy is proposed, following the receding horizon principle. In a nutshell, the idea is to compute, at time k , an optimal control sequence, over the complete time-interval, e.g., $[k, k + H - 1]$, taking into account the current and future constraints. Nevertheless, only the first step in the resulting optimal control sequence is applied. Then, in the next time slot $k + 1$, once the chargers' information is updated with the new measures, the aggregator recomputes the sequences, thus iterating the process.

Thereupon, in the eMPC problem framework, finding the problem solution requires to analyse, at each time slot, the system dynamics, and the future energy prices, while taking into account the current SoC and the arrival and departure times for each vehicle, as per Equation (5.11). Notice that both uncertain parameters (the arrival time and the initial SoC) are revealed when the EV arrives at EVCS and is plugged in. After this, there is no more uncertainty in the EV state, leading to an appropriate power profile schedule. Then, using time slots of the order of minutes, the possible variations with respect to the scheduled values are compensated in the first time slot of the MPC algorithm.

The parameters (price sequence c_k , reported arrival time \tilde{a}_j , and SoC at the request \widehat{SoC}_{j,r_j}) are assumed to be known, while $P_{i,\max}$ depends on the maximum power that either the charger can deliver, or the EV can accept. Moreover, the actual SoC_{a_j} is known when the EV connects to the charger; then, the prediction model is developed considering the expected value \tilde{a}_j for each EV (see Figure 5.2a). Regarding $\xi_{i,k}$, it is determined by using the requested times \tilde{a}_j and d_j . Notice that both the arrival time and arrival SoC of each EV can be different at the actual connection time step.

The eMPC strategy looks for input sequences minimising the total cost of the EVCS, as per Equation (5.11), in a time window of H hours, for each EV. To this aim, the dynamic constraint Equation (5.11b), i.e., when $\xi_{i,k} = 1$ while $\tilde{a}_j < k < d_j$, can be

expressed in an extended form as:

$$\hat{\mathbf{x}}_{k+1} = \underbrace{\text{diag}(\xi_{i,k})}_{A_k} \hat{\mathbf{x}}_k + \underbrace{\text{diag}(\xi_{i,k} \Delta t)}_{B_k} \hat{\mathbf{P}}_k, \quad (5.12)$$

where

$$\hat{\mathbf{x}}_k = [x_{1,k} \ x_{2,k} \ \dots \ x_{I,k}]^T, \quad \hat{\mathbf{P}}_k = [P_{1,k} \ P_{2,k} \ \dots \ P_{I,k}]^T. \quad (5.13)$$

Hence, the evolution of all x_i , throughout the prediction horizon H , reads:

$$\mathbf{x} = \mathbb{A} \hat{\mathbf{x}}_k + \mathbb{G} \mathbf{P}, \quad (5.14)$$

where

$$\mathbf{x} = \begin{bmatrix} \hat{\mathbf{x}}_{k+1} \\ \hat{\mathbf{x}}_{k+2} \\ \vdots \\ \hat{\mathbf{x}}_{k+H} \end{bmatrix}, \quad \mathbf{P} = \begin{bmatrix} \hat{\mathbf{P}}_k \\ \hat{\mathbf{P}}_{k+1} \\ \vdots \\ \hat{\mathbf{P}}_{k+H-1} \end{bmatrix}, \quad \mathbb{A} = \begin{bmatrix} A_k \\ A_k A_{k+1} \\ \vdots \\ A_k \cdots A_{k+H-1} \end{bmatrix}, \quad (5.15)$$

$$\mathbb{G} = \begin{bmatrix} B_k & 0 & 0 & 0 \\ A_{k+1} B_k & B_{k+1} & 0 & 0 \\ \vdots & \vdots & \ddots & 0 \\ A_{k+1} \cdots A_{k+H-1} B_k & A_{k+2} \cdots A_{k+H-1} B_{k+1} & \cdots & B_{k+H-1} \end{bmatrix}.$$

Notably, the system in Equation (5.14) is time variant, since $x_{i,k+1}$ in the prediction horizon has a switching behaviour. In addition, $\hat{\mathbf{x}}_k$ is the initial condition, it contains the current EV SoC when $\xi_{i,k}=1$ and zero when $\xi_{i,k}=0$. Moreover, the cost function in Equation (5.11a) is linear in $P_{i,k}$, and the dynamic equation Equation (5.14) is a linear equality constraint in $P_{i,k}$. Furthermore, the other constraints in Equation (5.11) are linear inequalities that bind the feasible region described as a polytope. Then, the aggregator deals with a Linear Programming (LP) convex problem, which can be efficiently solved by Simplex or interior point methods.

Furthermore, it is noteworthy that the devised eMPC strategy might be affected by feasibility issues related to the charging time. As a matter of fact, it is assumed that the resulting charging time, when the eMPC formulation is employed, must be greater or equal than in the Minimum Time charging case. Thereby, the optimal control problem Equation (5.11) is said to be feasible if and only if:

$$(d_j - a_j) P_{i,\max} > \widetilde{\text{SoC}}_{j,d_j} - \text{SoC}_{j,a_j}. \quad (5.16)$$

In short, Equation (5.16) implies that the time an EV spends plugged-in (from a_j to d_j) is at least enough to charge it with maximum power $P_{i,\max}$. From the feasibility condition Equation (5.16), how the economic MPC strategy will generally increase the time spent at the charging station premises appears, although a certain reduction of the recharge operating costs is guaranteed. Regarding the uncertain parameters, they must be inside the feasible region; otherwise, the problem is not feasible and the EV cannot be charged up to the minimum state $\widetilde{\text{SoC}}_{j,d_j}$. However, an EV that arrives too late with respect to the request is still allowed to be charged, without guaranteeing that the minimum $\widetilde{\text{SoC}}_{j,d_j}$ will be reached.

In order to assess the complexity of the problem, it can be noticed that:

- the size of the decision and the state variables, $P_{i,k}$ and $x_{i,k}$ respectively, is $I \cdot H$;
- the number of constraints in $P_{i,k}$ is $2 \cdot I \cdot H$, for each time slot, half for the lower bounds, and half for the upper bounds;
- the number of constraints in $x_{i,k}$ is $3 \cdot I \cdot H$, for each time slot; equally allocated among the lower and the upper bounds, and the charger dynamics;
- the number of constraints in x_{i,d_j} , related to the minimum SoC requirement $\widetilde{\text{SoC}}_{j,d_j}$ at the departure, is I .

It is evident that the problem complexity grows linearly with H . This implies that, by scaling up the number of chargers, the number of constraints and decision variables would also increase accordingly, possibly impinging on the optimisation solution efficiency.

5.3.3 Optimal Control with Minimum Cost and Maximum Flexibility

In this subsection, a novel strategy for the charging station problem solution, based on flexibility maximisation, is proposed. The aim of this novel strategy is to offer a power flexibility capacity to the electrical grid, while guaranteeing the minimum SoC requirement $\widetilde{\text{SoC}}_{j,d_j}$ at the departure time. The uncertainty in the EV arrival time and SoC at the arrival time are considered as in Section 5.3.2.

According to Definition 1, the concept of (upward or downward) flexibility F_k is determined with respect to a nominal charging profile $P_{i,k}$, whereas $F_k = 0$ implies that no ancillary service may be offered to the grid. Hence, it could be crucial to set-up a charging strategy that always guarantees a certain amount of flexibility capacity. To pursue such an objective, two parallel paths can be developed, involving the flexibility as either an optimisation constraint or part of the cost function.

In fact, on the one hand, the optimisation constraints in Equation (5.11b) can be properly rephrased, in order to impose a minimum flexibility capacity to the chargers. Specifically, such an approach envisages two possible strategies for the constraint reformulation. In the first strategy, Equation (5.11b) binding the vehicle charging power $P_{i,k}$ is adapted to guarantee a certain degree of flexibility $F_{i,k}$,

$$F_{i,k} \leq P_{i,k} \leq P_{i,\max} - F_{i,k}, \quad \text{where} \quad F_{i,k} = \frac{F_k}{\sum_{i=1}^I \xi_{i,k}}, \quad (5.17)$$

$F_{i,k}$ being a parameter defining the flexibility requested to charger i at time slot k , while F_k is the overall flexibility offered by the EVCS, at the k time slot. It is worth noting that the constraint Equation (5.17) implies the same upward and downward flexibility, achievable for $\sum_{i=1}^I \xi_{i,k} \geq 1$. Moreover, all the I chargers provide the same flexibility level at each time slot.

The second strategy for the constraints reformulation mainly consists of adding a new constraint to Equation (5.11b), binding the aggregated power $P_{T,k}$, yet leaving unmodified the single-vehicle power limits. Such a further constraint reads:

$$F_k \leq P_{T,k} \leq \sum_{i=1}^I (\xi_{i,k} \cdot P_{i,\max}) - F_k, \quad \forall k=1, 2, \dots, K. \quad (5.18)$$

Note that, by introducing Equation (5.18), the flexibility of each charger can be different. Indeed, the idea is to impose a gap in the power requested to the grid.

Finally, in spite of its capability to grant some level of flexibility, and, in turn, some extra energy service to the grid, a solution of the EVCS optimisation problem including the constraints Equation (5.17) or Equation (5.18) might result in being infeasible. In fact, the maximum flexibility $F_{C_{T,k}}$ achievable by the EVCS is not known in advance. Indeed, this capacity depends on the state behaviour.

On the other hand, in a second path to approach the charging problem improving the flexibility capacity, the optimisation problem formulation is re-framed according to an optimal control strategy, aimed to simultaneously maximise the charging flexibility and minimise the operational cost of the EVCS. This formulation assumes that remuneration factors π_k^U (upward) and π_k^L (downward) for the flexibility offered by the station are driven by prices.

To sum up, the aggregator deals with an optimal control problem, i.e.:

$$\min_{P_{i,k}, U_{i,k}^F, L_{i,k}^F} \Delta t \sum_{k=0}^{H-1} \left(c_k \sum_{i=1}^I P_{i,k} - \pi_k^U \sum_{i=1}^I U_{i,k}^F - \pi_k^L \sum_{i=1}^I L_{i,k}^F \right) \quad (5.19a)$$

$$\text{s.t.} \quad x_{i,k+1} = \begin{cases} x_{i,k} + \Delta t P_{i,k} & \text{if } \tilde{a}_j < k < d_j, \\ \widehat{\text{SoC}}_{j,d_j} & \text{if } k = \tilde{a}_j, \\ 0 & \text{if } \zeta_{i,k} = 0 \quad \vee \quad k = d_j, \end{cases} \quad (5.19b)$$

$$\widehat{\text{SoC}}_{j,d_j} \leq x_{i,d_j} \leq \widehat{\text{SoC}}_{j,d_j}, \quad (5.19c)$$

$$L_{i,k}^F \leq P_{i,k} \leq \zeta_{i,k} (P_{i,\max} - U_{i,k}^F), \quad (5.19d)$$

$$0 \leq U_{i,k}^F \leq P_{i,\max}, \quad (5.19e)$$

$$0 \leq L_{i,k}^F \leq P_{i,\max}, \quad (5.19f)$$

$$0 \leq x_{i,k} \leq x_{i,\max}, \quad (5.19g)$$

$$\forall k = 1, 2, \dots, H, \quad i = 1, 2, \dots, I \quad j = 1, 2, \dots, J.$$

In this case, the aggregator decision variables are the optimal profile $P_{i,k}$ and the flexibilities $U_{i,k}^F$ and $L_{i,k}^F$ of the i th charger. Concerning $U_{i,k}^F$ and $L_{i,k}^F$, in Equation (5.19), two new constraints are introduced. Indeed, $U_{i,k}^F$ and $L_{i,k}^F$ are considered as lower-bounded by zero and upper-bounded by $P_{i,\max}$. Then, the charging power $P_{i,k}$ is always positive.

This formulation allows for finding solutions that maximise both upward $U_{i,k}^F$ and downward $L_{i,k}^F$ flexibilities. Furthermore, the resulting charging strategy may lead to non-symmetric flexibility capacities, consistently with Definition 1.

Finally, the dynamic constraint for the SoC in $x_{i,k}$ being in line with Equation (5.11b), its evolution can be again consistently expressed as per Equation (5.14). Taking into account the discussion after Equation (5.15) about linearity in the problem Equation (5.11), note also that the cost function in Equation (5.19a) is a linear function of $P_{i,k}$ as Equation (5.11a) and the new constraints are linear as well. Then, like for the eMPC case, the aggregator faces an LP convex problem. Similarly, the feasibility condition presented in Equation (5.16) also holds for the problem formulation Equation (5.19). From this perspective, it can be noticed how the approach Equation (5.19), in the worst-case scenario, would not allow any flexibility, thus reducing to the same outcome of the eMPC model in Equation (5.11).

To conclude, it is expected that this innovative OCCF strategy, with flexibility maximisation, generates higher expenses for the EVCS with respect to the eMPC one because the energy value is not the only element of the cost function. Nonetheless, it

can provide to the grid a significant flexibility capacity. In turn, such additional flexibility would allow the generation of relevant extra revenues for the EVCS, due to the aggregator service in maintaining the electrical grid balance.

5.4 Case Study and Results

In this section, a case study with several simulation results is presented, with the aim of evaluating the performance of the three charging strategies:

1. Minimum time (MT).
2. Economic MPC (eMPC).
3. MPC with minimum cost and flexibility maximisation (OCCF).

For this purpose, the EV charging profiles $P_{i,k}$, the charger SoC $x_{i,k}$, the flexibility capacities $L_{T,k}^F$ and $U_{T,k}^F$, and the resulting operation costs for each strategy are compared. An EVCS sampling time of $\Delta t = 10$ minutes is employed in order to provide spinning reserve service. The solution of the resulting optimization problems is obtained with the CVX package (Grant and Boyd, 2014)—specifically, the convex LPs in Equation (5.11) and Equation (5.19), with a one-day simulation length, thus $\beta = 24$ h (144 time steps).

The EVs considered in the case study are the electric taxis that circulate in Bogotá, Colombia. In fact, all the EVs have the same characteristics, namely, they are BYD e6 cars with a battery capacity of 80 kWh and a nominal charging rate of 8 kW. They can also support a fast charging rate of 50 kW (Yilmaz and Krein, 2013). Concerning the minimum desired SoC at the departure, a full charge condition is requested in all the simulations ($\widehat{SoC}_{j,d_j} = \widehat{SoC}_{j,d_j}$), in order to make a meaningful comparison with the MT strategy, in which the EVs are fully charged at the end of the period. Regarding the uncertain parameters, the actual arrival time a_j for each EV is generated as a sample of a random variable with uniform distribution, mean value given by the declared arrival time \tilde{a}_j , and support between $\tilde{a}_j \pm \delta$, with $\delta = 20$ min. This variability leads to a feasible problem, considering that the minimum interval an EV owner can book a charger is 2 h (see Equation (5.16)). Then, in the worst case, a charging time of 1 h and 40 min is enough time for charging an EV with the given characteristics, by injecting the maximum feasible power. Moreover, the actual EV_j arrival state of charge SoC_{j,a_j} is generated as a sample of a uniform distribution with support between the reported SoC at the request \widehat{SoC}_{j,r_j} and \widehat{SoC}_{j,r_j} , where, without loss of generality, \widehat{SoC}_{j,r_j} is a

random number between 15% and 40% of the EV capacity, and $\widetilde{SoC}_{j,r_j} > 0$. In addition, for the MPC algorithm, the expected value \widetilde{SoC}_{j,d_j} is considered as a random value lower than \widehat{SoC}_{j,r_j} and higher than zero.

The adopted simulation parameters, characterising the optimisation models, are reported in Table 5.2. Concerning the optimisation scenario configuration, a prediction horizon of $H = 6$ h (36 time steps) is assumed as the maximum time an EV can spend at the charging station premises. Furthermore, in these tests, two different energy price sequences are considered. They are hourly sampled time-variable prices, named $c_{1,k}$ (Figure 5.5a) and $c_{2,k}$ (Figure 5.11), corresponding to real data taken from the Colombian stock market. They allow for assessing the potential diversity in the aggregator responses. Moreover, in line with the Colombian energy market regulation and without loss of generality, the benefit price granted to the EVCS for its flexibility capacity is assumed to have the same price as the traded energy (CREG, 2015), i.e., $\pi_k^U = \pi_k^L = c_k$. The simulation is performed in MATLAB® R2019a on a computer with a Intel® Core i7-7700HQ, CPU 2.80 GHz, 16 GB of RAM, and running Windows® 10 64-bit operating system.

TABLE 5.2: Case study simulation parameters.

Name	Symbol	Value	Notes
EVCS sample time	Δt	10 min	-
Operation time of the station	β	24 h	(144 iterations)
Maximum arrival delay	δ	20 min	-
Prediction horizon	H	6 h	(36 iterations)
Battery capacity in EV _j	C_j	80 kWh	-
Charging power (time slot k)	$P_{i,k}$	8 kW	Semi-fast (Level 2)
Charging power (time slot k)	$\widetilde{P}_{i,k}$	50 kW	Fast (Level 3)
Minimum SoC in EV _j (at departure)	\widetilde{SoC}_{j,d_j}	80 kWh	$x_{i,d_j} = C_j$
Energy price 1 (time slot k)	$c_{1,k}$	0.0577 \$/kWh	Mean value
		0.0252 \$/kWh	Std dev.
Energy price 2 (time slot k)	$c_{2,k}$	0.0614 \$/kWh	Mean value
		0.0115 \$/kWh	Std dev.
Remuneration price (time slot k)	π_k^U, π_k^L	$c_{1,k}$ or $c_{2,k}$	-

5.4.1 Charger Flexibility Analysis

In order to perform a worthwhile analysis of the proposed charging strategies, a simulation campaign is set up, considering first a deterministic scenario and then a setting with uncertainty. The simulated charging station considers three chargers, and 11 EV re-charge requests, with the energy price sequence $c_{1,k}$, as per Table 5.2. Specifically,

Table 5.3 lists the 11 electric taxis requests, with their request arrival time \tilde{a}_j and departure time d_j , their SoC at the request $\widehat{SoC}_{r,j}$, and the identification number ID_i of the charger assigned by the scheduler. The actual information on the arrival time a_j and arrival state of charge $SoC_{a,j}$ is also reported.

Let us notice that the taxi EV₈ could not be served (i.e., its request was not accepted), all the three chargers already being in use at the EV₈ requested time; for that reason, the charger ID of the taxi EV₈ is marked as not available (n/a), and the variables corresponding to its arrival are marked as not defined (n/d).

TABLE 5.3: EV charger schedule.

EV _j	EV ₁	EV ₂	EV ₃	EV ₄	EV ₅	EV ₆	EV ₇	EV ₈	EV ₉	EV ₁₀	EV ₁₁
$\widehat{SoC}_{r,j}$	28.0	23.0	32.0	13.0	23.0	17.0	22.0	26.0	24.0	18.0	30.0
$SoC_{j,a,j}$	8.4	21.7	17.1	7.6	6.9	3.2	3.4	n/d	6.6	16.3	21.5
\tilde{a}_j	3:30	5:30	5:30	7:30	10:30	10:30	11:30	13:30	15:30	16:30	20:30
a_j	3:40	5:20	5:40	7:20	10:10	10:20	11:20	n/d	15:30	16:30	20:20
d_j	5:30	8:30	9:30	10:30	15:30	15:30	14:50	n/d	19:30	19:30	23:30
ID_i	1	2	3	1	2	3	1	n/a	1	2	1

In the following subsection, the behaviour of charger number 1 is analysed to benchmark the tested solution strategies, due to its high activity in this simulation (five electric vehicles served: EV₁, EV₄, EV₇, EV₉, and EV₁₁).

Deterministic Performance

In order to perform a deterministic analysis of the proposed charging strategies, the first simulation campaign takes into account a full information approach. It is assumed that: (i) an Oracle informs the aggregator about the actual arrival SoC of each EV, i.e., it knows the information since the moment when a request is performed, that is, at least H hours in advance; and (ii) the EV arrival time is the one reported in the request.

In Figure 5.5, the most relevant aspects of the three charging strategies are shown and compared. Figure 5.5a depicts the simulated time-variable energy price sequence $c_{1,k}$ adopted in this simulation, as reported in Table 5.2. Figure 5.5b shows the power profile delivered by charger 1, namely $P_{1,k}$, to the 5 EVs it serves. As expected, the $P_{1,k}$ profiles are always positive or equal to zero. By definition, the MT strategy (red line) charges the vehicles with a constant power $P_{\max} = 50$ kW, until the battery SoC reaches a full condition, i.e., $x_{1,d_j} = 80$ kWh (100%). Conversely, the eMPC solution (dashed-green line) envisages different power levels taking into account the energy prices, while ensuring the 100% SoC target at the departure time. Finally, in the OCCF

strategy (dash-dot blue line), the charging power is continuously adjusted while the algorithm tries to achieve the same upward and downward flexibility, by keeping $P_{1,k}$ close to a medium level, roughly 25 kW. Nevertheless, for EV₁, in Figure 5.5b, between the arrival time $a_1 = 3:30$ a.m. and the departure time $d_1 = 5:30$ a.m., a medium power level cannot be maintained, due to the shorter charging time (2 h) given by the EV owner request. In the last 30 min, the energy price increases, and the OCCF strategy takes into account this fact to schedule lower power in that period. Figure 5.5c shows the resulting SoC evolution, $x_{1,k}$, of the EVs served by the charger. As expected, the MT strategy reaches a full charge condition faster. On the other side, by comparing Figure 5.5a and Figure 5.5c, it is worthwhile to notice how the eMPC strategy strives to limit as much as possible its charging level at high price hours. Conversely, the OCCF solution, which depends on both flexibility and economic aspects, achieves a trade-off between energy cost reduction and flexibility generation.

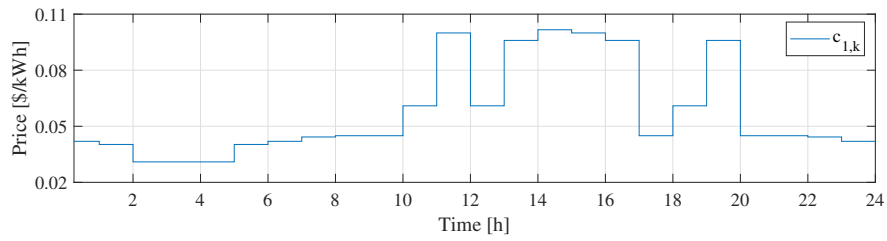
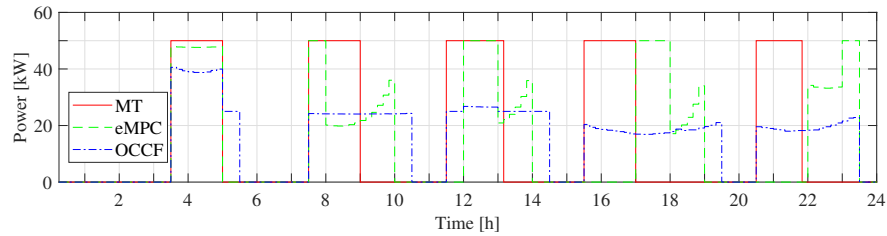
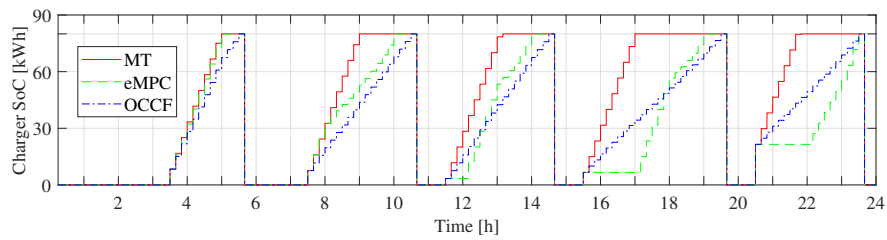
(A) Energy price sequence $c_{1,k}$.(B) Power profiles $P_{1,k}$ with the different strategies.(C) Charger SoC $x_{1,k}$ with the different strategies.

FIGURE 5.5: The behaviour of the three charging strategies in charger 1, considering only request parameters.

Figure 5.6 depicts the charger 1 flexibility level, referring to the three strategies.

The MT strategy cannot offer any upward flexibility capacity (U_{MT}), but it can offer a downward one ($-L_{MT}$). Conversely, the eMPC strategy has the possibility to offer an amount of upward (U_{eMPC}) and downward ($-L_{eMPC}$) flexibility, but it cannot provide both flexibilities at the same time for the majority of the time slots. However, the OCCF strategy according to the problem formulation (see Equation (5.19a) and Equation (5.19b)), which includes the flexibility in the cost function, offers both upward (U_{OCCF}) and downward ($-L_{OCCF}$) flexibilities at almost all the time steps when there is a connected EV.

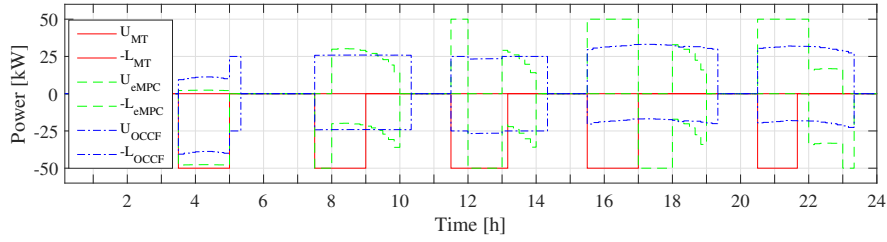


FIGURE 5.6: Flexibility capacity provided by charger 1.

From the results shown in Figure 5.6, it is clear that charger 1 can provide ancillary services to the grid, e.g., a spinning reserve service, for a relevant amount of time. The best option to offer this service is with the OCCF charging strategy. For example, by comparing the trends in Figure 5.6 and Figure 5.5b, let us notice that, between hours 13:10 and 14:20, the charger can offer its maximum flexibility capacity ($F_{1,k} = 25$ kW). Indeed, in that interval, the delivered charging power is roughly in the middle of the maximum one $P_{1,max} = 50$ kW. In different time intervals, no flexibility might exist (see Definition 1), for instance between hours 5:20 and 5:30 or 23:20 and 23:30.

To conclude, the overall results of this simulation campaign are summarised in Table 5.4—specifically, the total aggregator cost, the savings of the two MPC strategies with respect to the MT solution and both upper and downward flexibilities capacities. It can be seen how the OCCF solution, maximising the flexibility levels, is an attractive solution for the aggregator.

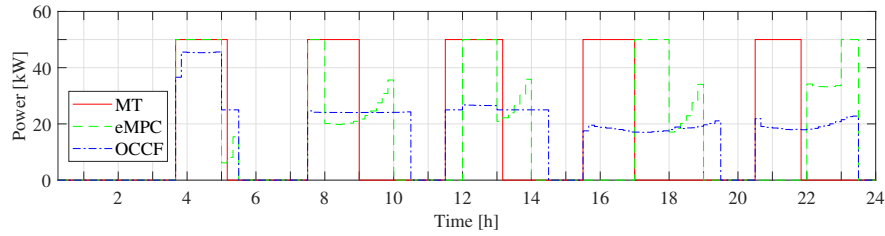
TABLE 5.4: Three strategies' overall simulation results (three chargers, 11 EV requests)

Strategy	Charging Cost [\$]	Cost Savings [%]	$U_{T,k}^F$ Capacity [kWh]	$L_{T,k}^F$ Capacity [kWh]
MT	272.55	—	0.00	4,300.00
eMPC	216.98	20.39	3,226.06	4,073.94
OCCF	257.34	5.55	6,097.77	3,902.23

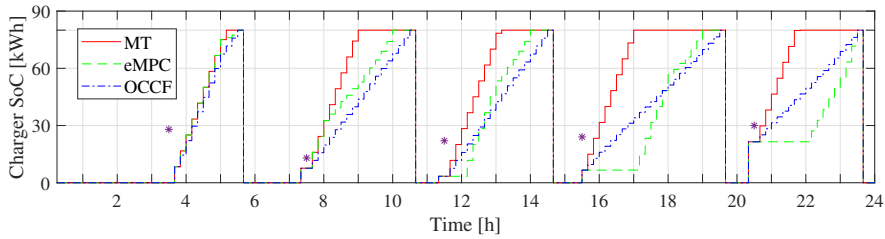
Results with Uncertainty in Arrival SoC and Arrival Time

In the second set of simulations, the same conditions of the previous subsection are maintained, considering the set up presented in Table 5.2. There is no oracle providing the exact EV information about arrival time a_j , departure time d_j , and initial SoC SoC_{j,a_j} . These parameters are generated randomly as described at the beginning of the section. Then, the eMPC and OCCF strategies can, in the prediction step, over or underestimate the time required to fully charge an EV. However, the feedback structure of the MPC solution is able to overcome the uncertainty as shown in the following.

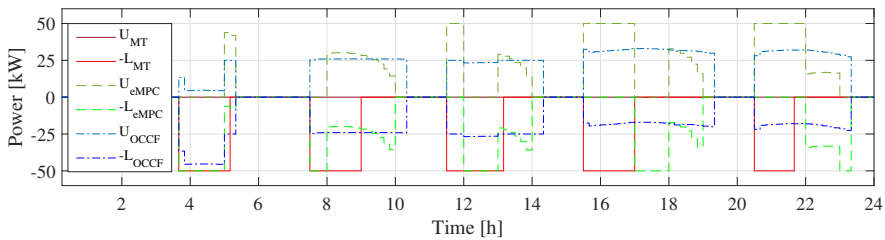
Figure 5.7 shows the performance of the three charging strategies. Figure 5.7a shows the power trajectories $P_{1,k}$. Figure 5.7b shows the SoC $x_{1,k}$ of charger 1, where the purple asterisks (*) indicate the reported arrival time \tilde{a}_j and EV SoC (\widehat{SoC}_{j,r_j}) at the request time, i.e., the expected arrival time with the maximum expected SoC at the arrival.



(A) Power profiles $P_{1,k}$ with the different strategies.



(B) Charger SoC $x_{1,k}$ with the different strategies.



(C) Flexibility capacity provided by charger 1.

FIGURE 5.7: The behaviour of the three charging strategies in charger 1, with arrival SoC and time uncertainties.

Comparing the power consumptions in Figure 5.5b with the ones presented in Figure 5.7a, for strategies eMPC and OCCF, it can be seen that they have similar behaviours, especially when the prediction error is small, as for EVs 4, 7 and 11. However, for EVs 1 and 9, the prediction is far from the actual arrival SoC and the arrival time is also different. Note that the aggregator assumes that EV₁ ($a_1=3:40$, $d_1=5:30$) and EV₉ ($a_9=15:30$, $d_9=19:30$) were arriving with a high SoC. Then, the power curves show a peak during the first sample times, while the MPC strategies correct the mismatch; then, they follow an optimal charging profile, similar to the exact information case. Interestingly, the flexibility offered by charger 1, shown in Figure 5.7c, is just marginally affected by the prediction error. There is always a symmetric capacity, with a small deviation during the first sample times.

The results of the complete simulation (EVCS with all its chargers) are summarised in Table 5.5. The aggregator operation cost with different strategies is shown. In addition, the savings of the eMPC and OCCF strategies are calculated in comparison with the MT strategy. As expected, the OCCF strategy maximises the flexibility capacities. Furthermore, there is no relevant difference for the eMPC and OCCF strategies between knowing or not in advance the EV arrival SoC. Indeed, for this case, the charging cost for the eMPC strategy increases by just 0.17%, while, for the OCCF, it increases by 0.06%. Therefore, this suggests that the MPC strategies are robust in front of the EV arrival time and initial SoC information.

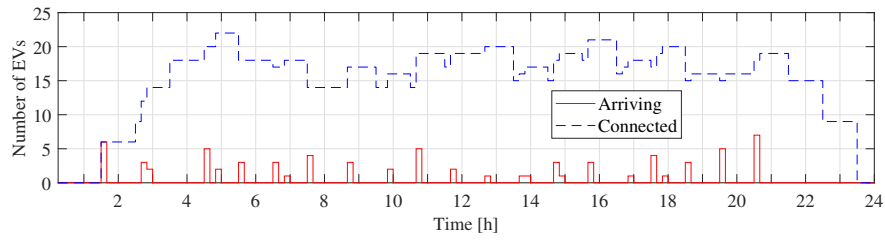
TABLE 5.5: Strategies' overall simulation results, with uncertainty in the arrival time and initial SoC (three chargers, 11 EV requests).

Strategy	Charging Cost [\$]	Cost Savings [%]	U_T^F Capacity [kWh]	L_T^F Capacity [kWh]
MT	272.63	—	0.00	4,300.00
eMPC	217.34	20.27	3,241.46	4,058.54
OCCF	257.50	5.54	5,997.95	3,902.05

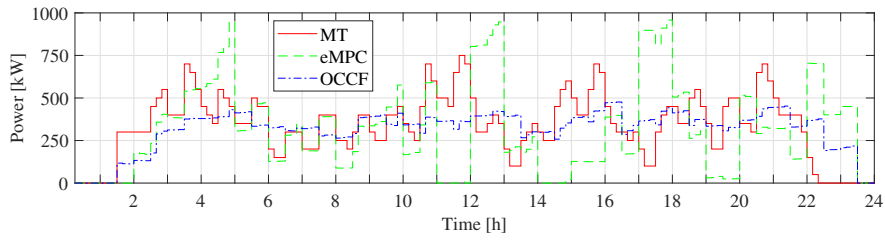
5.4.2 Savings, Benefits, and Flexibility in the EVCS

Now that the main characteristics of the proposed strategies have been highlighted in a small example, an extensive simulation campaign is presented, reproducing an EVCS with 25 chargers and 110 EV re-charge requests to be fulfilled in one day. These simulations are developed considering uncertainty in the arrival SoC and arrival time. The simulation run time for the MT solution is 10 ms, for the eMPC and the OCCF strategies is 3 s per station operation hour. The main results are shown in Figure 5.8.

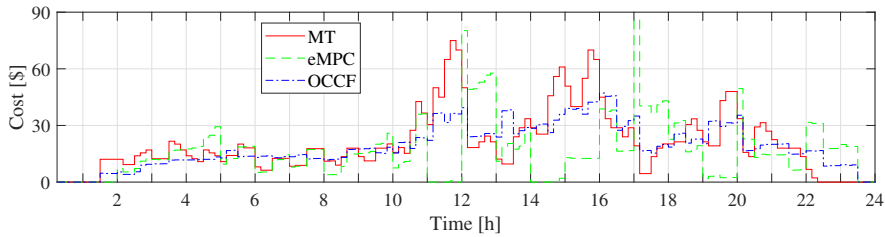
In Figure 5.8a, the number of EVs arriving at the station (red line) and the number of EVs connected (dashed-blue line) at each time slot are shown. In Figure 5.8b, the time history of the delivered charging power is shown for the three solution strategies. Consistently with the preliminary case, the OCCF solution generates the smoothest behaviour. Then, Figure 5.8c focuses on the overall station operational cost at each time slot. Specifically, it provides further evidence that, although the eMPC strategy might be the more expensive one at certain time intervals, by considering the overall daily operations, it is the cheapest solution. This is in line with the preliminary results listed in Table 5.5.



(A) EV arrival and EVs connected in the operational time.



(B) Power delivered.



(C) EVCS cost.

FIGURE 5.8: The behaviour of the three charging strategies in the EVCS.

Figure 5.9 shows the flexibility capacity that the EVCS can offer to the system operator at each time slot k , with the three strategies, along the operation time of the station. As already mentioned, the upward and the downward flexibilities in the OCCF strategy are maximised, according to the optimal problem formulation. Interestingly, by comparing this simulated result with the outcome in Figure 5.7c, the OCCF strategy

offers a certain level of flexibility at every time interval, allowing for providing spinning reserve service to the grid all day long. This evidence suggests that the more EVs are connected, the higher is the algorithm capability to achieve charging flexibility.

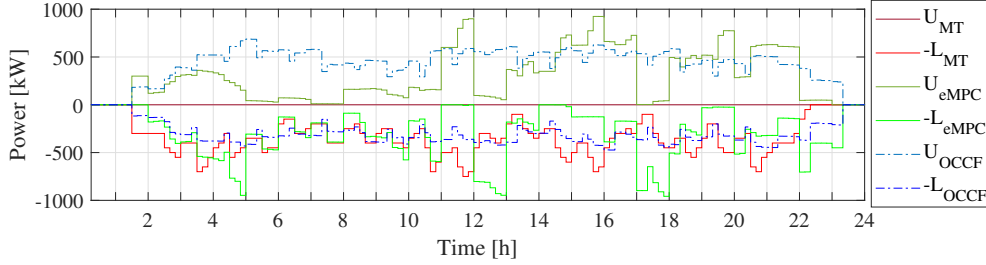


FIGURE 5.9: EVCS flexibility capacity.

To sum up, Table 5.6 lists the overall results of this second simulation scenario. Once again, it is shown that the higher flexibility capacity levels are achieved by the OCCF solution. Concerning the savings of the MPC solutions with respect to the MT strategy, the values are of the same order of magnitude of the preliminary case in Table 5.4. This might imply that those savings are independent of the amount of plugged-in EVs, yet dictated by the chosen solution strategy and energy price evolution.

TABLE 5.6: Three strategies' overall simulation results, considering uncertainties (25 chargers, 110 EV requests)

Strategy	Charging Cost [\$]	Cost Savings [%]	$U_{T,k}^F$ Capacity [kWh]	$L_{T,k}^F$ Capacity [kWh]
MT	2,913.13	—	0.0	47,600.00
eMPC	2,322.36	20.28	40,979.68	42,620.32
OCCF	2,706.40	7.10	61,059.26	42,240.74

5.4.3 Monte Carlo Analysis

The performance of the proposed EVCS operation strategies is evaluated through a Monte Carlo simulation, where the EVs SoC, arrival and departure times are randomised, and the resulting overall savings with respect to the outcomes of the MT strategy are analysed. To this aim, the optimal decision problem for an EVCS with 25 chargers and 110 EV requests is solved for 500 realisations of random EV arrival and departure times, a_j and d_j . In more detail, the EV arrival flow is assumed to be a random variable with uniform distribution during the day, considering that electric taxis

operate 24 hours and can be charged at any time. Then, in the simulation, \tilde{a}_j is generated as a random variable, with uniform distribution between hour 1:30 a.m. and hour 20:30. Note that, for another type of user, it would be possible to identify the distribution that better represents it (Flammini et al., 2019), for example, analysing historical data (Bascetta et al., 2018). Moreover, d_j is also randomly generated, constrained to guarantee a charging time between $2 \div 6$ h; 2 h is the minimum interval guaranteeing a feasible charging procedure, and 6 h as a reasonable time for resting between work shifts. Two price sequences, $c_{1,k}$ and $c_{2,k}$ as per Table 5.2, are considered, allowing for evaluating the sensitivity of the strategies to the energy cost.

In the MT and eMPC strategies, no remuneration factor is considered. In particular, the results of the eMPC strategy are to avoid or reduce the consumption at high energy prices, thus increasing the upward capacity available and reducing the downward capacity available. This available capacity is calculated from a purely technical point of view. Conversely, the OCCF algorithm, as per the formulation Equation (5.19), finds a trade-off between energy cost and flexibility capacity, thus distributing the energy consumption throughout all the time-slots. In turn, this leads to a schedule with the EV charging station operating during high-cost hours, thus making the overall charging process more expensive but guaranteeing an almost symmetrical flexibility at all times.

In the OCCF strategy, the remuneration is given to provide flexibility. The remuneration factor is assumed to be higher when the energy price is high because, without an appropriate incentive, nobody would provide flexibility in the higher energy price periods. Thereby, it is reasonable that the trend of the remuneration factor follows the energy price sequence.

A comparison is introduced here in the form of parametric analysis, in which the remuneration factor is chosen at different percentages of the energy prices. In this way, the overall cost savings of providing flexibility with respect to the MT strategy are quantified. When the price sequence $c_{1,k}$ (see Figure 5.5a) is considered in the Monte Carlo simulation, the probability density function (PDF) of the overall savings is shown in Figure 5.10. The other cases for the OCCF strategy are formulated with remuneration factors of 10%, 20%, and 30% of the energy price (the further case with 100% is not shown but is included in Table 5.7). By definition, with null remuneration factor, the solution is the same as in the eMPC. By introducing remuneration, the energy costs of the different solutions increase, but the benefits due to remuneration are higher, and the solutions become more profitable. Indeed, when the remuneration is equal to the energy price, the overall savings are very high (even though these savings

refer to the MT strategy, such values higher than 100% are conceptually feasible).

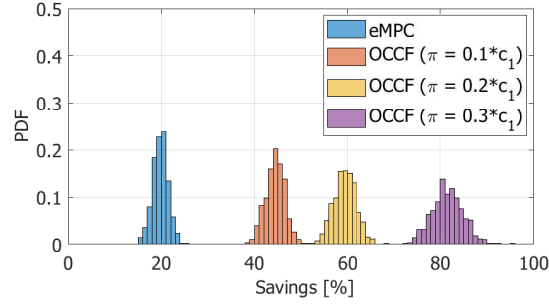


FIGURE 5.10: Overall savings for different strategies and remuneration factors based on c_1 .

When the energy price sequence $c_{2,k}$ is used (Figure 5.11), the most relevant outcomes of the Monte Carlo trials are shown in Figure 5.12.

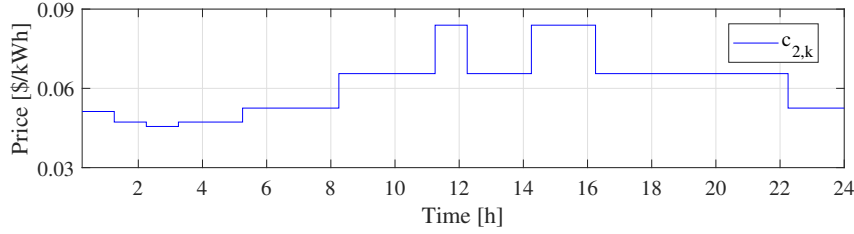


FIGURE 5.11: Energy price sequence $c_{2,k}$.

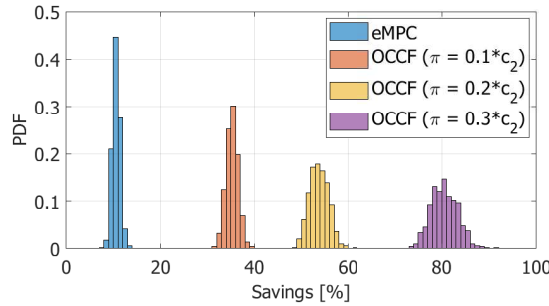


FIGURE 5.12: Overall savings for different strategies and remuneration factors based on c_2 .

The results summarised in Table 5.7 show that the average savings for the set-up with price $c_{1,k}$ are higher than for the price $c_{2,k}$. This can be explained by the difference in the ratio between the standard deviation and the mean value of the energy prices, 0.44 for $c_{1,k}$ and 0.19 for $c_{2,k}$ (see Table 5.2). Hence, the higher the variability of the energy cost profile, the higher the capability of the MPC strategies to achieve more convenient schedules on a daily basis, charging the vehicles principally at the cheapest

time slots. When the remuneration factor increases, the mean overall savings increase, and the standard deviation of the overall savings also increases. Furthermore, the overall savings found starting from the two different energy price sequences tend to be similar when the remuneration factor increases. This is due to the fact that, with high remuneration factors, the power profiles tend to be more constant (see Figure 5.7a and Figure 5.8b). This happens already when the remuneration factor is 30% of the energy price for the two energy price sequences, and, for this reason, the results shown in Figure 5.10 and Figure 5.12 are shown up to 30%.

TABLE 5.7: Mean value and standard deviation of the overall savings with respect to the MT strategy.

Strategy and Remuneration Factor	Overall Savings		Strategy and Remuneration Factor	Overall Savings	
	Mean [%]	Std [%]		mean [%]	std [%]
eMPC, $\pi = 0$	19.8	1.6	eMPC, $\pi = 0$	10.6	0.8
OCCF, $\pi = 0.1 * c_1$	44.5	2.1	OCCF, $\pi = 0.1 * c_2$	35.3	1.3
OCCF, $\pi = 0.2 * c_1$	59.5	2.4	OCCF, $\pi = 0.2 * c_2$	53.9	2.2
OCCF, $\pi = 0.3 * c_1$	81.6	3.4	OCCF, $\pi = 0.3 * c_2$	80.6	3.0
OCCF, $\pi = c_1$	257.9	10.2	OCCF, $\pi = c_2$	257.9	10.1

5.5 Findings

In this Chapter two novel strategies that can be used by the aggregators for Electric Vehicle Charging Station (EVCS) have been proposed. The first strategy looks for minimizing the EVCS operation costs, via an economic Model Predictive Control (eMPC). The second strategy starts from a formal definition of EV charger flexibility and develops an Optimal Control with minimum Cost and maximum Flexibility (OCCF) formulation. In both strategies, the effect of uncertainty on the arrival time and on the EV state of charge at the arrival are taken into account. Interestingly, this charging strategy was found not only to reduce the station operating costs but also to maximise the possibility of offering ancillary services to the grid, like spinning reserve, through the power flexibility capacity given at each time slot.

A dynamic model of an EVCS charger as a flexible load was developed. The model has a switching behaviour, according to whether there is an EV plugged-in to the charger or not. Also, the charger flexibility capacity was defined, with respect to a

given nominal charging trajectory, considering the power deviations attainable by the trajectory itself.

The two proposed charging strategies were benchmarked against the simple Minimum Time (MT) charging strategy. Specifically, a wide range of numerical simulations based on the electric taxi service used in *Bogotá, Colombia* is performed, assuming two real electric energy price sequences. In addition, the two strategies are evaluated with and without knowledge of the EVs arrival SoC, achieving a difference in average savings lower than 0.6%. Therefore, this suggests that the MPC strategy is robust in front of the EV arrival SoC information.

As future work, the response of the aggregators with uncertainty in the price sequences will be explored. The strategies used by the aggregator will be improved by considering the use of real data on EV usage. In addition, the EV battery degradation cost will be included in the optimization cost function. However, these future features do not modify the proposed formulation of the flexibility.

Chapter 6

Strategy for EVCS participation in RT and DA Markets

In this Chapter, Day-Ahead (DA) and Real-Time (RT) strategies are developed for the EVCS considering the availability of a local renewable generation source. First, the DA controller is based on a renewable source forecast and on an EVs schedule. This approach aims to define the electrical grid energy to be purchased for the next day. Second, the RT controller aims to manage the DA forecast grid energy, taking into account the fluctuations of the actual renewable generation and EVs behaviour. Then, for both approaches, the aggregator is responsible for deciding the injected power of the electrical grid and renewable source, considering the EV owners preferences. Moreover, these strategies consider a Photo-Voltaic (PV) generation source.

In order to assess the PV generation forecast, the DA and RT controllers, this chapter is divided into three main topics:

- *PV generation model*, a solar radiation forecast, based on real data of Bogotá, Colombia;
- *DA controller*, a formulation based on the eMPC strategy that considers the PV generation forecast;
- *RT controller*, a strategy whose aim is to follow the power purchased to the electrical grid in the DA strategy.

The rest of the Chapter is organized as follows: Section 6.1 describes how the EVCS operates taking into account the participation of a local renewable generation source. In Section 6.2, a Photo-Voltaic (PV) generation model is presented, considering Bogotá whether conditions. In Section 6.3, the DA formulation is proposed. Section 6.4 introduces the RT strategy. Finally, in Section 6.5 case study is shown, along with the

related numerical results. The results of this Chapter were derived in the publications (Giordano et al., 2020; Diaz-Londono et al., 2020b).

6.1 EVCS Operation with RES generation

In this section, two controllers are proposed, one for an EVCS Day-Ahead (DA) and another for an EVCS Real-Time (RT). In these strategies, a solar radiation forecast is considered for calculating the Renewable Energy Source (RES) production. The EVCS goal and operation is the same as the one presented in Subsection 5.1. However, in this case study, the total power delivered by the station P_T is composed of a traditional generation P_p and a RES P_w one, as,

$$P_{T,k} = P_{p,k} + P_{w,k}. \quad (6.1)$$

Therefore, some additional variables are used in this chapter. Table 6.1 shows the additional variables notation.

TABLE 6.1: Additional variables notation of the EVCS with PV generation.

Symbol	Variable	Units
P_p	Power delivered by the power grid	kW
P_w	Power delivered by the PV generator	kW
w	PV information	{set}
G_{PV}	Solar radiation	W/m ²
T_{amb}	Ambient Temperature	°C
G_{STC}	Radiation standard test conditions	W/m ²
P_{nom}	Nominal power of a PV plant	kW
γ_p	Power thermal coefficient	A/K
ΔT	Temperature difference	°C

Figure 6.1 shows the EVCS operation. This station is as the one presented in Figure 5.1. However, in this case, a Photo-Voltaic (PV) generation and bilateral communication with the System Operator (SO) are considered. It is assumed that the PV generator has a smart meter that informs the aggregator about the solar radiation G_{PV} and the ambient temperature T_{amb} , this information is collected as $w = \{G_{PV}, T_{amb}\}$. In addition, the communication between the aggregator and SO aims to report the energy for consuming the next day by the EVCS, this is the DA controller output. The RT controller looks for minimizing the error between the DA purchased power and the actual EVCS consumption, taking into account the solar radiation fluctuations.

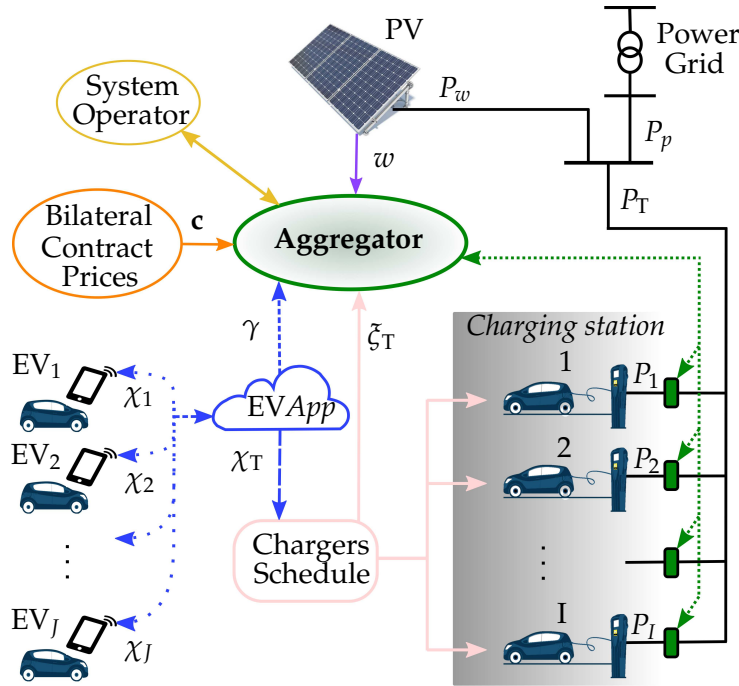


FIGURE 6.1: EVCS operation with Photo-Voltaic generation.

6.2 Bogotá, Colombia Photo-Voltaic generation model

In this subsection, a renewable generation model is developed for the solar radiation in Bogotá, Colombia. Considering 5 years of hourly registered solar radiation data, the model is estimated. Both, the data pre-processing and the model are carried out in MATLAB[®] software. The model comprises three elements:

1. an expected value;
2. a Non-linear AutoRegressive eXogenous (NARX) model;
3. an error Gaussian model.

First, due to the fact that data are acquired from real measurements, there are outliers across the measures. These data holes are detected and replaced by applying quadratic polynomial curves. Then, three profiles based on the Colombian seasons are generated from the expected values, as:

- *Profile 1*: the same hourly values in a day for all years;
- *Profile 2*: four different hourly values, one per each season (2 dry and 2 rainy);
- *Profile 3*: two different hourly values, one for dry seasons and one the rainy ones.

Profile 2 is selected to develop the model because of its lower standard deviation and mean value.

Second, the residue between the original data and the expected values are analysed through the autocorrelation, obtaining one day of correlation. Hence, an Artificial Neural Network (ANN) is used for identifying the residue dynamics. It is carried out a NARX with sigmoidal neurons.

Finally, the residue between the original data and estimated model, i.e., the expected values and the NARX model is assessed, detecting a Gaussian behaviour.

Pre-processing data

In this work, the hourly solar radiation measurements of *Centro de alto rendimiento* in Bogotá, Colombia are evaluated. It is analysed for 5 years, from 2011 to 2015. Then, the length of the data is 43,824 (2012, leap year) in 1826 days, or 8,760 data per year (24 hours in 365 days). Considering that Bogotá has almost the same sunlight time in a whole year, this is from 6:00 to 18:00, data are evaluated for these 13 hours.

Given that data are acquired from a real sensor, some information becomes outliers or does not exist, probably because of particular damage or maintenance of the equipment. Therefore, to fill data outliers, two processes are developed. First, when a complete day data is missed, the average of the nearest days is generated to complete that day; then, this is developed for each missing day. Otherwise, when there are missed few data during a day, a quadratic polynomial curve is calculated with the available information of the specific day and is evaluated in the missing points; this is developed for each day with missing data. Table 6.2 shows the total amount of missing data per year and the number of days where there is no solar radiation information through a whole day.

TABLE 6.2: Lack of data in the solar radiation information.

Year	Lack of data	
	total	whole day
2011	308 (3.52%)	6
2012	280 (3.19%)	3
2013	75 (0.85%)	2
2014	389 (4.44%)	12
2015	32 (0.37%)	1

Therefore, it can be seen that 2014 is the year with the highest lack of data. However, the percentage is lower than the 10% required for analysing the radiation data (Huang et al., 2014).

6.2.1 Profiles based on expected values

Taking into account 5 years data, this is without holes, the first element of the model is calculated. Then, three profiles based on the expected value are generated and compared.

The profiles are calculated for the 13 hours of sunlight between 6:00 and 18:00; between 19:00 and 5:00 the radiation is zero for the whole year. Figure 6.2 shows the estimated profiles. *Profile 1* is the expected value of each hour considering the mean value of the 5 years data (one sequence). This profile achieves the highest radiation at 545 W/m^2 at 12:00. Moreover, to estimate the *Profile 2*, it is considered the Colombian seasons, there are: a first dry season (Dry 1), from December to February; a first rainy season (Rainy 1), from March to May; a second dry season (Dry 2), from June to August; and a second rainy season (Rainy 2), from September to November. Hence, *Profile 2* has 4 sequences calculated as the expected value of each hour at each season. It is noticed that the dry seasons 1 and 2 achieve higher peak radiation than rainy ones, obtaining 614 W/m^2 for Dry 1 and 547 W/m^2 for Dry 2 at 12:00, while in the rainy ones, the peak is reached at 11:00. Finally, *Profile 3* is the expected value of each season, i.e., one for dry and other for rainy (two sequences). As in *Profile 2*, it is shown that dry season achieves a higher radiation at 12:00 while the rainy one at 11:00. Moreover, in the dry season, the radiation remains slightly more time, and also its area is greater than the rainy season.

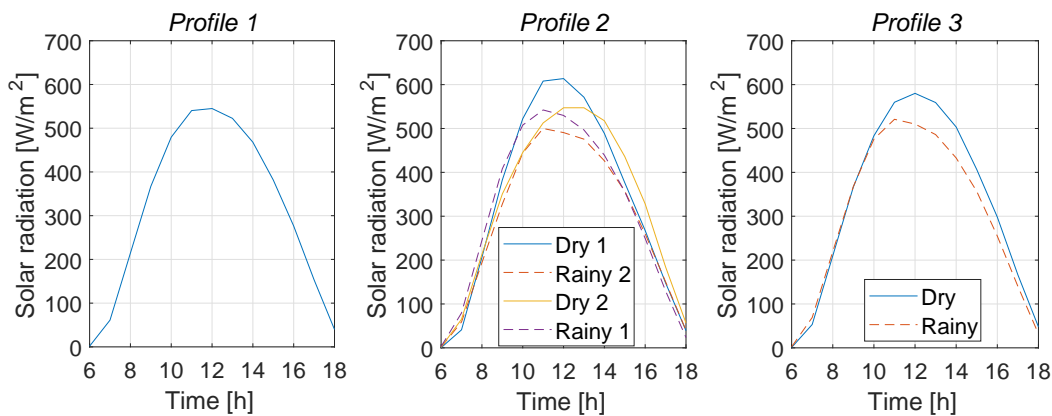


FIGURE 6.2: Solar radiation *Profiles 1, 2 and 3*, based on the expected values.

Figure 6.3, 6.4 and 6.5 depict the *Profiles 1, 2 and 3*, respectively. In these figures, the mean value (blue line), the standard deviation (error blue line), the minimum value

(purple asterisk), and the maximum value (green asterisk) are calculated for each profile. It is noticeable that there are few changes among them.

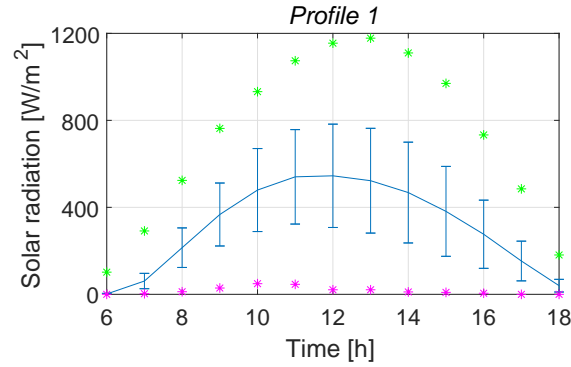


FIGURE 6.3: Profile 1.

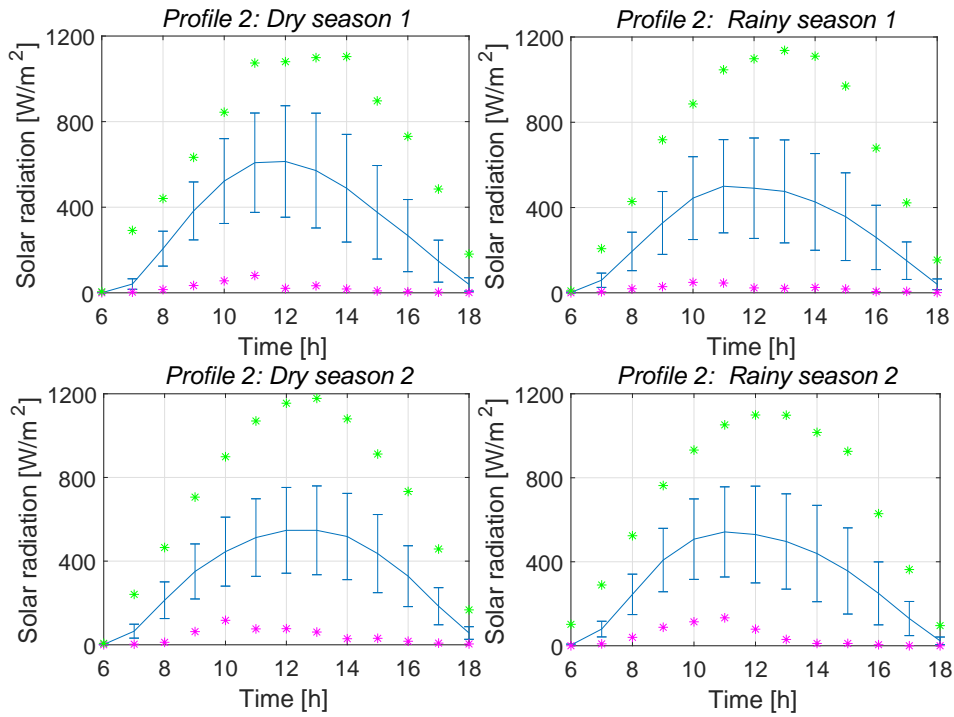


FIGURE 6.4: Profile 2.

The profiles are compared considering the percentage of the output variations that are reproduced by the model, this is called the FIT (see Eq. 4.18). Then, in Table 6.3, the FIT of each profile compared with the complete real data is obtained. It is observed that *Profile 2* achieve the best FIT, which is the expected result due to the 4 sequences that illustrate the solar radiation data. However, *Profile 1* and *3* are not that bad, it

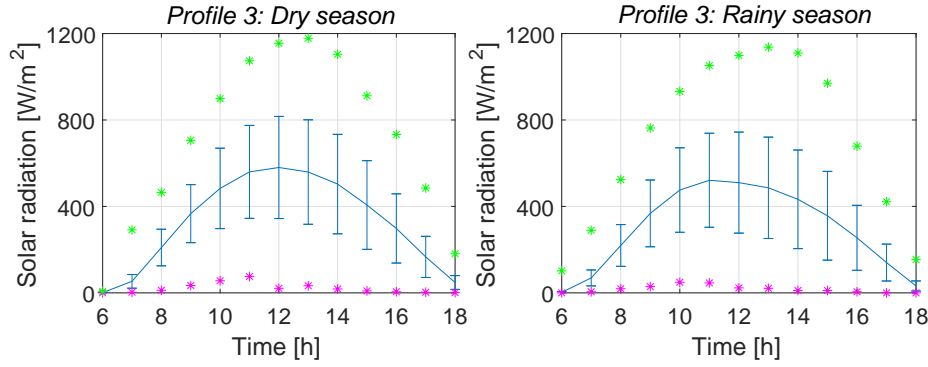


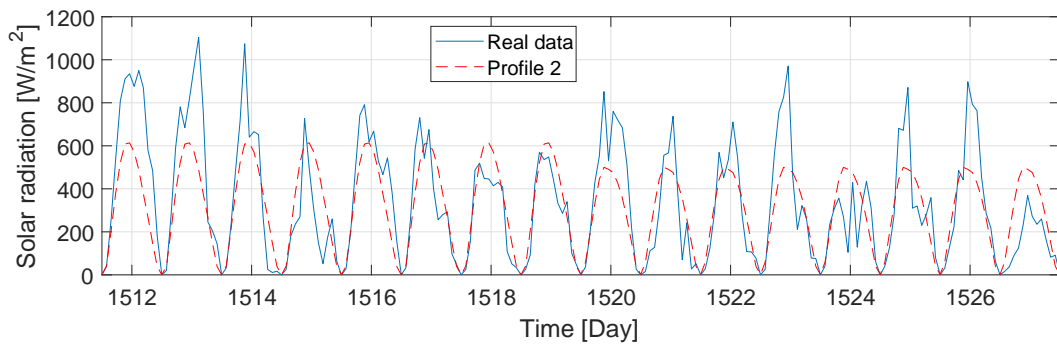
FIGURE 6.5: Profile 3.

is shown that the greater percentage difference is 0.67%, between *Profile 1* and 2, i.e., taking into account 1 or 4 sequences.

TABLE 6.3: Similitude of the profiles with the real data

Profile	FIT [%]
1	58.69
2	59.36
3	59.00

Therefore, for the second elements of the model, the *Profile 2* is considered. Figure 6.6 shows the real data in a blue line and the model with the *Profile 2* in a red line. It is shown the radiation between the day 1512 (20/2/2015) and 1527 (7/03/2015). Note that, there is a season change in 1520 (1/03/2015), from Dry 1 to Rainy 1.

FIGURE 6.6: Real data and *Profile 2* behaviour.

6.2.2 Non-linear auto-regressive model

For the purpose of acquiring the second element of the model, the residues between the original data and each profile are assessed. Table 6.4 depicts the mean value (which

can be assumed as zero), the variance, and the standard deviation of the residue with each profile. As expected the best result is with *Profile 2*.

TABLE 6.4: Residues between the original data and each profile statistics.

<i>Profile</i>	Mean [W/m ²]	Variance	Standard deviation [W/m ²]
1	2.63×10^{-13}	$2.76 * 10^4$	166.07
2	2.68×10^{-13}	$2.70 * 10^4$	163.40
3	1.58×10^{-13}	$2.72 * 10^4$	164.85

To develop an ANN it is required to determine the residue autocorrelation, which is present in Figure 6.7. It is noticed that this residual is 19.2% autocorrelated for the previous 13 hours (one day in this case).

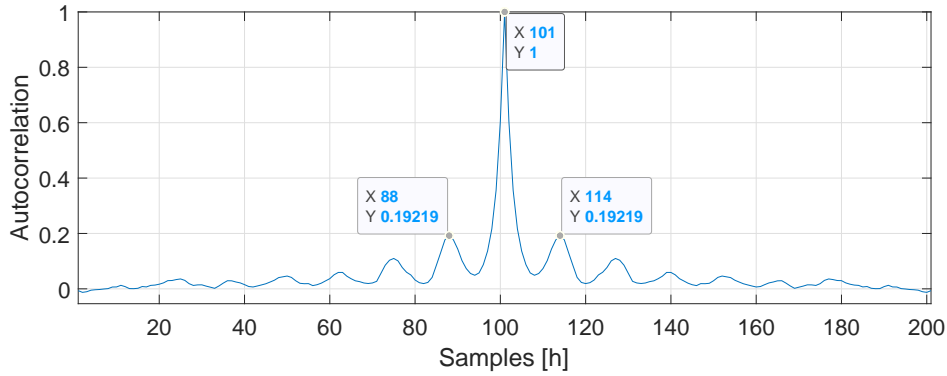


FIGURE 6.7: Residue autocorrelation.

In this work, an ANN is developed considering synchronous and discrete networks in which the dynamics are non-linear. It is developed by estimating the parameters of a non-linear ARX model. Then, 70% of the residue data is used for the estimation, while the last 30% is used for validation. The order of the model, i.e., the number of steps for performing the prediction, and the number of the predicted steps (prediction horizon) are assessed in Table 6.5. It can be seen that the best order of the model is 13, as found in the autocorrelation (see Figure 6.7); while in the prediction horizon, the best solution is 1 step. Therefore, for predicting the one value (next value), it is needed the 13 nearest past values. Notice that it is considered only 13 values of the sunlight in a day, then, the actual order of the model is one day i.e., 24 hours. Hence, it is possible to predict the radiation of the next hour with a FIT of 21.59%. However, comparing the FIT of predicting one step ahead when considering a model order of one and another of 13, it can be seen that the difference is 1.34%, which is not quite significant; by contrast, increasing the prediction horizon (steps) considering the same

model order, the FIT reduces notably. In addition, the estimator is carried out with a sigmoid network.

TABLE 6.5: Similitude of the residue validation with different model orders and prediction steps.

Model orders	FIT [%]		
	Prediction steps 1	2	13
1	20.25	6.79	1.05
13	21.59	8.77	2.57
26	21.57	8.92	3.42
39	21.58	8.80	3.17

Hence, the performance of the NARX model is shown in Figure 6.8. The validation is analysed in the same time interval of Figure 6.6.

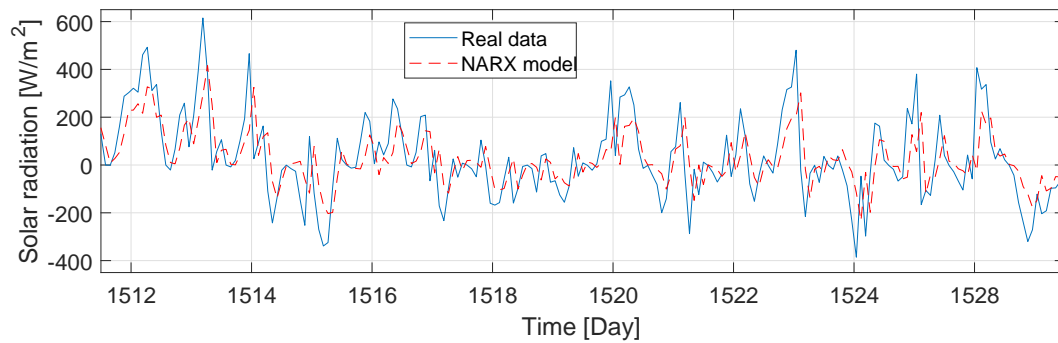


FIGURE 6.8: Validation between real data and NARX model.

In order to analyse the estimated model with the two elements, the expected value of *Profile 2* and NARX model, a validation is carried out. Then, both models are added and compared with the real data, obtaining a FIT equal to **68.97%**. This represents an increase of 9.61% in comparison with the first model element, see Table 6.3. Figure 6.9 shows in a blue line the real data and in a red line the estimated model.

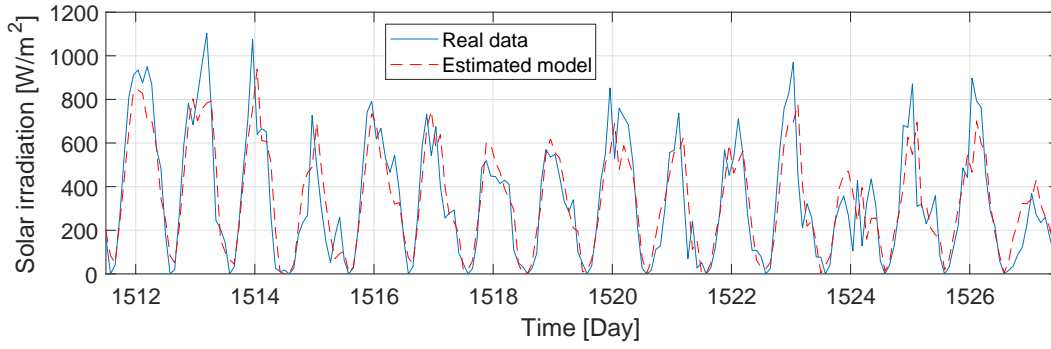


FIGURE 6.9: Validation of the estimated model (expected value and NARX model).

6.2.3 Residue analysis

In order to determine the third element of the model, the residue between the original radiation and the model estimated in the previews section (with the first and second elements) are evaluated.

Then, the autocorrelation of this second residue is shown in Figure 6.10. It is shown that there is no correlation between the samples.

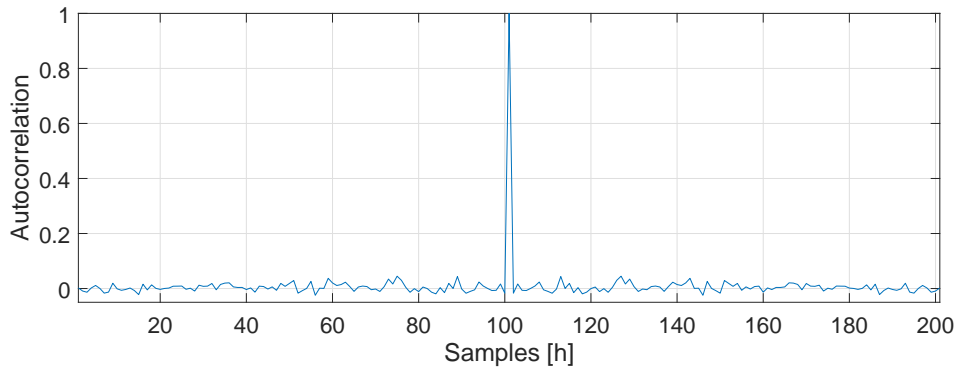


FIGURE 6.10: Second residue autocorrelation.

Therefore, the second residue is plotted in a histogram with the purpose of knowing its distribution, achieving a Gaussian behaviour as shown in Figure 6.11. There are shown both histograms the one for the estimation set and one for validation set. Moreover, statistical parameters are calculated, obtaining,

- Mean value: -1.77 W/m^2
- Standard deviation: 126.27 W/m^2

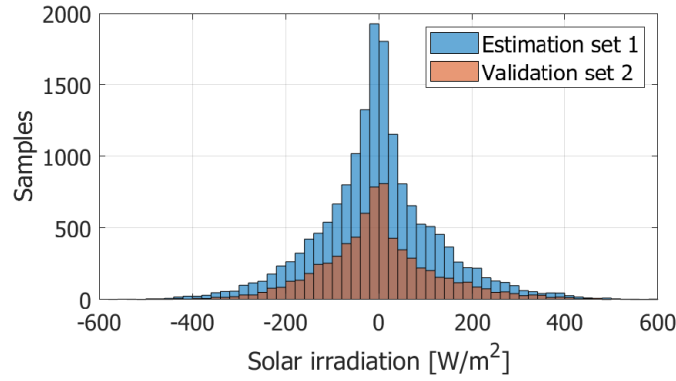


FIGURE 6.11: Histogram. Gaussian distribution

6.2.4 Solar Power Forecast

Considering the solar radiation model previously developed and the ambient temperature data of the same analysed period, the generated solar power can be expressed as (Tascikaraoglu et al., 2016),

$$P_w = \frac{G_{PV}}{G_{STC}} P_{nom} (1 + \gamma_p \Delta T) \quad (6.2)$$

where, G_{PV} is the solar radiation either real or predicted, this variable is the output of the solar radiation model, G_{STC} is the solar radiation at Standard Test Conditions (STC) given by $G_{STC}=1000\text{W/m}^2$, P_{nom} is the nominal power of the PV plant, γ_p is the short circuit current thermal coefficient, usually $\gamma_p=0.004\text{A K}^{-1}$, and ΔT is a temperature difference defined as,

$$\Delta T = \left(T_{amb} + \frac{NOCT - 20}{800} G_{PV} \right) - 25, \quad (6.3)$$

where, T_{amb} is the ambient temperature, and the parameter $NOCT$ is defined between 42°C and 50°C and depends on how is the PV array physically installed. Typically, $NOCT=45^\circ\text{C}$ corresponding to a cell temperature of 25°C , an ambient temperature of 20°C , and a STC solar radiance of 800W/m^2 .

6.3 Day-Ahead Formulation

A formulation for the Day-Ahead (DA) strategy for planning the energy purchase an EVCS needs for the next day is presented in this subsection. This solution looks for

minimizing the operation costs as in the eMPC strategy (see subsection 5.3.2). However, in this DA strategy, a PV plant is involved, therefore, a PV generation forecast is considered. Likewise, the optimality here refers to a charging profile planning that minimizes the EVCS operation costs, while guaranteeing for all EV_j the minimum \widetilde{SoC}_{j,d_j} at the departure time d_j . Thus, the optimal problem is defined as,

$$\min_{P_{p,i,k}, P_{w,i,k}} \Delta t \sum_{k=0}^{\beta-1} \left(c_k \sum_{i=1}^I P_{p,i,k} \right) \quad (6.4a)$$

$$\text{s.t.} \quad x_{i,k+1} = \begin{cases} x_{i,k} + \Delta t (P_{p,i,k} + P_{w,i,k}) & \text{if } a_j < k < d_j \\ \widetilde{SoC}_{j,a_j} & \text{if } k = a_j \\ 0 & \text{if } \zeta_{i,k} = 0 \vee k = d_j \end{cases} \quad (6.4b)$$

$$\widetilde{SoC}_{j,d_j} \leq x_{i,d_j} \leq x_{i,\max} \quad (6.4c)$$

$$\sum_{k=0}^{\Delta k-1} \sum_{i=1}^I P_{w,i,k} \leq \widetilde{P}_{w,\delta k} \quad (6.4d)$$

$$P_{p,i,k} + P_{w,i,k} \leq P_{i,\max} \quad (6.4e)$$

$$0 \leq P_{p,i,k} \leq P_{i,\max} \quad (6.4f)$$

$$0 \leq P_{w,i,k} \leq P_{i,\max} \quad (6.4g)$$

$$0 \leq x_{i,k} \leq x_{i,\max} \quad (6.4h)$$

$$\forall k = 1, 2, \dots, \beta, \quad i = 1, 2, \dots, I, \quad j = 1, 2, \dots, J.$$

In this strategy, each charger has two decision variable at each time step i.e., the optimal trajectories $P_{p,i,k}$ and $P_{w,i,k}$ that create the power injected by the charger, expressed as,

$$P_{i,k} = P_{p,i,k} + P_{w,i,k}. \quad (6.5)$$

Therefore, this aggregator has two decision variables sets. On one hand, the power that will be purchased to the electrical grid $P_{p,k}$ at each time step, defined as the sum of the optimal grid power $P_{p,i,k}$ in each charger. On the other hand, the locally RES power that can be dispatched at each time step, which is based on the PV generation prediction (see Section 6.2) and is defined as the sum of the optimal $P_{w,i,k}$ power in each charger.

Notice that the cost function considers only the energy price for the grid power $P_{p,i,k}$, while, the renewable power $P_{w,i,k}$ is dispatched with zero energy cost. Concerning the constraints, the same of the eMPC strategy are considered and three new constraints are introduced. First, Eq. (6.4d) bounds the dispatch of the predicted RES

power $\tilde{P}_{w,\delta k}$ that is distributed into all chargers that have an EV connected. Besides, the RES predicted power data is given by a discrete time slot $\delta k = 1, \dots, \delta K$, lasting Δk hours. Second, in Eq. (6.4e) the maximum injected power $P_{i,\max}$ is considered with the summation of the grid power and RES. Third, in Eq. (6.4g) the lower and upper bounds for $P_{w,i,k}$ are considered.

Taking into account the discussion after Eq. (5.15) about linearity in the problem Eq. (5.11), this new aggregator faces an LP convex problem. Similarly, also the feasibility condition presented in Eq. (5.16) holds for the problem formulation Eq. (6.4).

In order to solve the DA strategy, the controller assumes the PV generation model $\tilde{P}_{w,\delta k}$ as an input for the EV chargers (see Eq. (6.4b)). Then, one simulation of the PV generation model is developed for the next day (24 hours).

Finally, this formulation is an open-loop optimal control problem that allows finding the power grid trajectory to purchase in a DA market. Then, this power is calculated considering all $P_{p,i,k}^*$ defined as,

$$P_{p,DA,k} = \sum_{i=1}^I P_{p,i,k}^*. \quad (6.6)$$

To sum up, it is expected that this strategy minimize the EVCS operating costs considering a PV generation forecast.

6.4 Real-Time Formulation

In this subsection, a Real-Time (RT) controller is proposed. The aim of the RT dispatch is to deliver a proper grid power $P_{p,i,k}$ at each time slot to each charger, by following the DA power scheduling sequence $P_{p,DA,k}$. Then, an MPC strategy is adopted to achieve this goal, adjusting the injected power to compensate fluctuations of the RES power $P_{w,i,k}$, while guaranteeing for all EV_j the minimum \widetilde{SoC}_{j,d_j} at the departure time d_j . Then, the EVCS deals with the following optimal control problem,

$$\begin{aligned} \min_{P_{p,i,k}, P_{w,i,k}} \quad & \Delta t \sum_{k=0}^{H-1} \left(\phi_k \left(\sum_{i=1}^I P_{p,i,k} - P_{p-DA,k} \right)^2 \right) \\ \text{s.t.} \quad & \text{Eq. (6.4b), Eq. (6.4c), Eq. (6.4d), Eq. (6.4e),} \\ & \text{Eq. (6.4f), Eq. (6.4g) and Eq. (6.4h)} \end{aligned} \quad (6.7a)$$

The cost function in Eq. (6.7a) looks to minimize the error between the schedule DA grid power $P_{p,DA,k}$ and the power decided by the MPC strategy to be delivered to all chargers at each time slot. Note that in the cost function, the error is penalized by an energy price sequence ϕ_k . This MPC formulation has the advantage of recalculating the optimal injected power considering the RES fluctuations every δk .

In this strategy, the aggregator has the same two decision variables $P_{p,i,k}$ and $P_{w,i,k}$ than in the DA aggregator. Likewise, the constraints are the same as in problem Eq. (6.4). However, the cost function is different.

Regarding the PV generation forecast $\tilde{P}_{w,\delta k}$, it is calculated every δk sample and predicts the next H hours. Then, the real PV measured power $P_{w,\delta k}$ is updated every Δk hour and used in the following predictions. Indeed, it is assumed that the RT aggregator knows with high accuracy the PV generation at the current time step.

6.5 Case study and Day-Ahead and Real-Time strategy results

In this case study, the simulation results are presented considering the parameters in Table 5.2. However, the prediction horizon and the battery capacity in EVs are changed as $H=7$ h (42-time steps) and $C=30$ kWh, respectively (these changes are considered with the purpose of carrying out a scenario where the PV production and the EVCS consumption are comparable). In fact, this battery capacity belongs to a Kia Soul EV[®] car, which is one of the EVs circulating in Bogotá, Colombia. The level 2 (semi-fast) charging power is selected for the station chargers, i.e., $P_{max}=8$ kW. Furthermore, hourly solar radiation data of *Centro de alto rendimiento* in Bogotá are used for forecasting the PV production. To assess the PV generation forecast and the DA and RT controllers, a simulation campaign is set up considering the EVCS *El Salitre* located in Bogotá. It has 13 chargers ($n=13$) and it is possible to implement a PV plant of 50 kW ($P_{nom}=50$ kW). Besides, $\Delta k=1$ h (6-time steps), taking into account that the solar radiation data are given hourly. The penalization energy price ϕ_k is assumed the same as the second time-variant energy cost, i.e., $\phi_k=c_{2,k}$. The rest of the simulation is set as in the first case study presented in Subsection 5.4.

Furthermore, the hourly PV generation data used in the DA controller are predicted with the PV generation model developed in Section 6.2, by feeding it with the solar radiation data of the day before (24 hours). In order to solve the problem of Eq. (6.7), the predicted hourly data for the next H hours are computed in the PV generation model considering the previous 24 hours of solar radiation. Notice that the

data entering the model is updated every hour with the actual generation information. Moreover, for simulating the actual EVCS, a PV generation model with high-frequency variations is employed. Therefore, the real hourly solar radiation data are preprocessed with a linear polynomial model for obtaining data every 10 min. However, these new data do not consider the solar radiation variability in a 10 min sample time. Then, real solar radiation data acquired between June 5 and June 10 of 2014 at the *Pontificia Universidad Javeriana* are used for adding variability to the 10 min data. This Javeriana solar radiation data has 6 days of information with a 2 s sample time (518400 data) and is presented in Figure 6.12. The variability is calculated with the difference between the hourly mean values and the 10 min mean values of the Javeriana data. The results show that the variability can be generated randomly with normal distribution considering the mean value as $2.14 \times 10^{-14} \approx 0 \text{ W/m}^2$ and the standard deviation as 90.29 W/m^2 . Therefore, the RT 10 min solar generation is computed as the sum of the linear polynomial model and a random variable generated as white noise with Gaussian distribution, zero mean and standard deviation 90.29 W/m^2 .

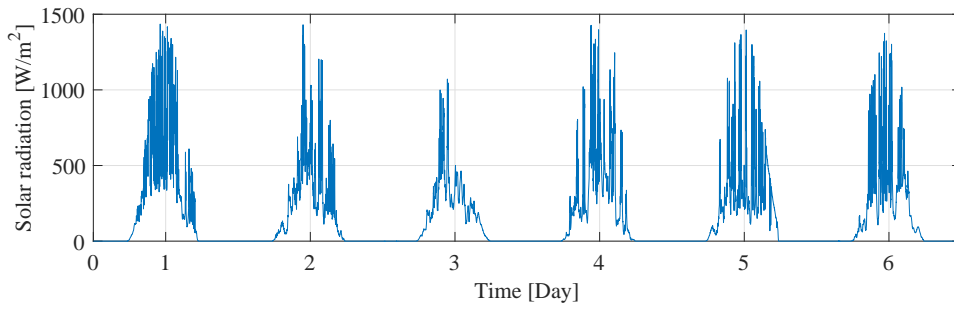


FIGURE 6.12: Solar radiation data at *Pontificia Universidad Javeriana*.

In order to analyse the DA and RT controllers, a simulation campaign is set up, considering 13 chargers, 34 EVs re-charge request (all EVs are scheduled for been charged), and energy price sequence $c_{2,k}$. All chargers are scheduled for charging two, three or four EVs in the day, however, charger number 3 is selected for assessing the controllers, due to the high activity by charging four EVs in the simulation, let us say EV_1 , EV_2 , EV_3 , and EV_4 . Table 6.6 presents the EV schedule for charger 3, with their arrival and departure times, and the minimum battery state at the departure \widetilde{SoC}_{j,d_j} . This SoC is generated randomly with a uniformly distributed pseudo-random between 24 kWh (80%) and 30 kWh (100%).

In the following analysis, only charger 3 is considered. In Figure 6.13, the behaviour of the DA and RT controllers are presented. Indeed, Figure 6.13a shows the

TABLE 6.6: EV Schedule for Charger 3.

$\mathbf{EV_j}$	$\mathbf{EV_1}$	$\mathbf{EV_2}$	$\mathbf{EV_3}$	$\mathbf{EV_4}$
a_j	2:00	7:00	13:00	18:00
d_j	6:00	12:00	17:00	23:00
\widetilde{SoC}_{j,d_j}	29kWh (97%)	25 kWh (83%)	24 kWh (80%)	25 kWh (83%)

trajectories of the predicted DA and the actual RT power $P_{3,k}$ to charge the 4 EVs, considering the grid and solar power sources. These trajectories are always positive or equal to zero and ensure the state \widetilde{SoC}_{j,d_j} at the departure. Notice that trajectories in some periods are not the same neither when there is no PV generation, for example for EV_1 . This is due to the global optimal solution in each charger; however, the total power demanded in RT by the EVCS follows the DA schedule (as presented later). In Figure 6.13b the trajectories of the EV SoC are reported. It can be seen that the \widetilde{SoC}_{j,d_j} constraint in the 4 EVs is fulfilled in both controllers DA and RT. The DA controller charges the EVs up to the minimum possible value (\widetilde{SoC}_{j,d_j}) due to the aim of minimizing cost. In particular, the EV_1 in RT departs with a slightly different value (29.8 kWh) of the DA scheduled, but the constraint is respected.

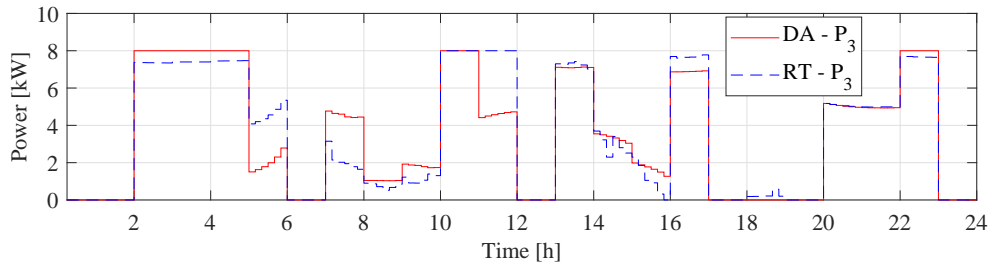
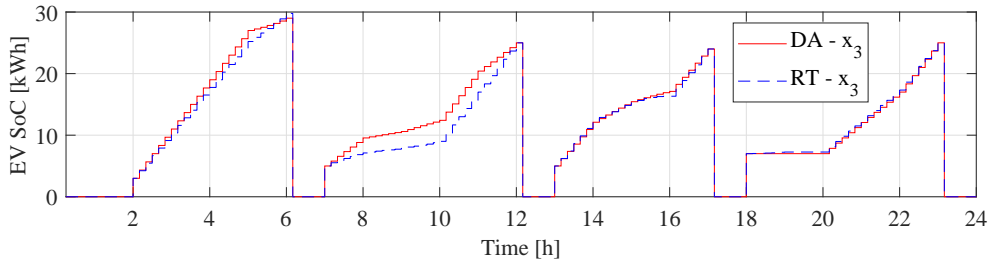
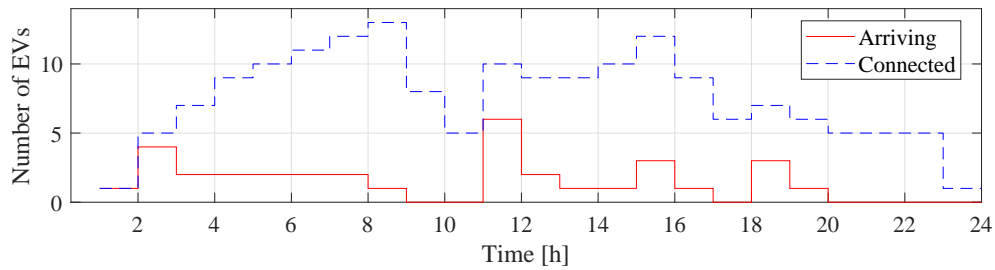
(A) Power trajectories $P_{3,k}$.(B) Charger SoC $x_{3,k}$.

FIGURE 6.13: The behavior of the Day-Ahead and Real-Time controllers in charger 3.

The overall results of this EVCS simulation campaign are presented below and summarized in Figure 6.14. Figure 6.14a depicts the amount of EVs arriving at the station (red line) and the number of EVs connected (dashed-blue line) at each time slot,

for example, at 8:00 all chargers have an EV connected. In Figure 6.14b, the predicted solar power in DA is shown in the red line, the dispatched solar power in RT is depicted in the blue dashed line, and the power produced by the PV plan is presented in green dashed dot line. Notice that not always the PV production was injected to the EVs, for example, at 12:00 the injected PV power is lower than the available PV power. This is due to the RT cost function, which is to follow the DA power scheduled. Then, in Figure 6.14c, the station delivered grid power is shown, for the DA and RT controllers. In contrast to the individual charger power that has significant deviations between the DA and RT controllers (see Figure 6.13b), the grid power consumed by the EVCS has small variations between the controllers.



(A) EVs arrival and EVs connected to the EVCS.

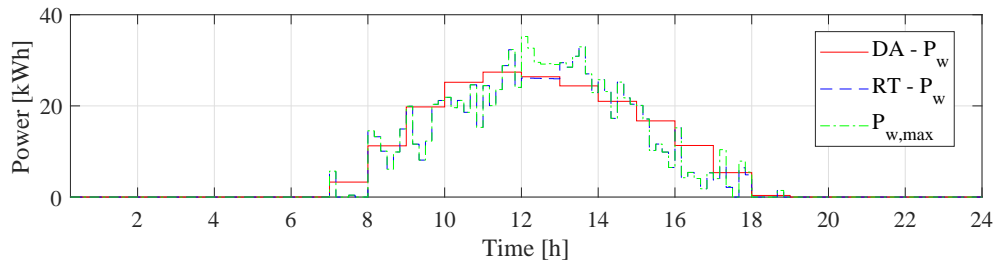
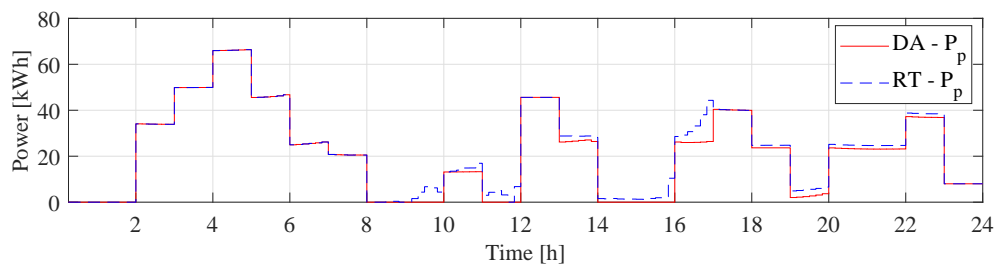
(B) Forecasted and delivered PV power trajectories P_w .(C) Grid power trajectories P_p .

FIGURE 6.14: EVCS behavior in the Day-Ahead and Real-Time controllers.

To sum up, the RMSE between the purchased power P_p in DA and the consumed power in RT is 7.37 kW, obtaining a maximum error of 17.9 kW at 16:50. In fact,

514.26 kWh is the purchased energy in DA, which has a cost of US\$152.18. This is only considering the grid power due to solar power dispatched at zero cost. On the other hand, the consumed grid energy in RT deviates 5.9% (32.23 kWh) from the DA. This produces consumption of 546.49 kWh, generating a penalization cost to the EVCS of US\$15.37. Regarding the solar power P_w , the RMSE between the DA and RT strategies is 10.17 kW, the maximum positive error is 8.6 kW at 13:30, while the maximum negative error is -11.67 kW at 9:20. Indeed, the DA forecasts solar production of 192.41 kWh, however, in RT it is consumed 173.48 kWh, 11.1% (18.93 kWh) less. Finally, it is highlighted that the real PV production is not dispatched completely, missing 5.88 kWh. In Table 6.7, the energy and cost of the DA and RT are reported.

TABLE 6.7: Energy and cost for the Day-Ahead schedule and Real-Time controller.

Step	Energy [kWh]	Cost [US\$]
DA	514.26 (Grid purchased)	152.18
	192.41 (PV estimated)	N.A.
RT	546.49 (Grid consumed)	15.37 (Penalization)
	173.48 (PV consumed)	N.A.
	179.36 (PV available)	N.A.

6.6 Remarks

In this chapter two novel strategies were proposed, a Day-Ahead schedule (DA) and a Real-Time (RT) dispatch. The DA strategy aims to minimize the operation cost, while the RT strategy looks for minimizing the error on following the DA schedule. In these strategies, the EVCS considers power from the electrical grid and a Photo-Voltaic (PV) plant. Therefore, a PV generation model is proposed based on five-years data of solar radiation in *Bogotá*, achieving a prediction model explaining 69% of the signal. Then, the RT strategy is able to follow the DA schedule with a similitude of 91%, considering the real-time fluctuations of the solar radiation.

There are several future directions of interest. The use of a range of renewable energy sources, such as wind power will be assessed, considering the weather features of different countries. Moreover, strategies to bid in the electricity markets will be evaluated.

Chapter 7

Hierarchical Architecture Structure for European Balancing Services

In this chapter, a unified Hierarchical Architecture Structure (HAS) is presented for a Balancing Service Provider (BSP) able to provide European balancing services (see Section 2.2). The HAS is presented as a centralized algorithm capable of aggregating and coordinating distributed flexible loads, considering not only adjustable but also deferrable loads. As shown in previous chapters, flexibility from WBPS, TER, and EVCS has an enormous potential to provide various balancing services to a smart grid. The challenge of the HAS is how to integrate various aggregators (AGGs) with different loads and response times. Therefore, a two-hierarchy structure is proposed, i) a coordinator level (high level), and ii) an AGGs level (low level). The coordination logic is developed considering the SO requirements and the availability of the AGGs; while, AGGs level considers the WBPS-AGG (see Section 3.3), the TER-AGG (see Section 4.2.2), and the EVCS with minimum cost and maximum flexibility (see Section 5.3.3). The simulation results evidence that the HAS can provide FCR, aFRR, mFRR, and RR services to the electrical grid operator by guiding the AGGs consumption.

The sections of this chapter are organized as follows. Section 7.1 presents the considerations of a unified structure for providing European Balancing services with different aggregators. In Section 7.2, the hierarchical structure operation is illustrated through several simulations results.

7.1 Unified Aggregation Framework

In this section, the balancing services considerations are presented. Then, the flexible loads' aggregator (low level) with its set of equivalent load models is considered in

order to propose the coordinator logic (high level).

The balancing services are managed by the SO of the electrical grid with the purpose of ensuring that demand equals the supply in the real time dispatch. The balancing market normally considers the SO, the BSP, and the Balance Responsible Party (BRP) (see Figure 2.3), and consist of two phases:

1. *Balancing planning phase*: performed in a Day-Ahead (DA) market. The main actions are:
 - The BRP reports the scheduled demand and generation per step time (not analysed in this work). In addition, the BRP computes the energy imbalances and sends them to the SO.
 - The BSP informs the SO about the power demand baseline, which is defined as the sum of all the AGGs power demand. This could be based on a forecast or on historical data.
 - The BSP offers to the SO an upward and downward flexibility. This is based on the sum of all the AGGs flexibility.
 - * Notice that each AGG is responsible for its own flexibility forecast and baseline.
2. *Balance settlement phase*: performed in a Real-Time (RT) market. The main actions are:
 - The SO guides the BSP for activating the balancing service based on the BRP imbalances information.
 - The High Logic Coordinator (HLC) allocates the SO energy request among its AGGs.
 - Each AGG manages its loads with the purpose to providing upward or downward power variations for following the HLC request.

7.1.1 Hierarchical Coordination

In this subsection, the HAS is presented considering the two levels. Figure 7.1 depicts the interaction between the levels. Notice that the communication between the HAS and the SO considers few parameters as well as the internally HAS interaction between the HLC and the AGGs. In fact, the exchanged information is the power, the flexibility of the AGGs, and the balancing services requests. The dispatching is guided by the HLC and carried out by the AGGs.

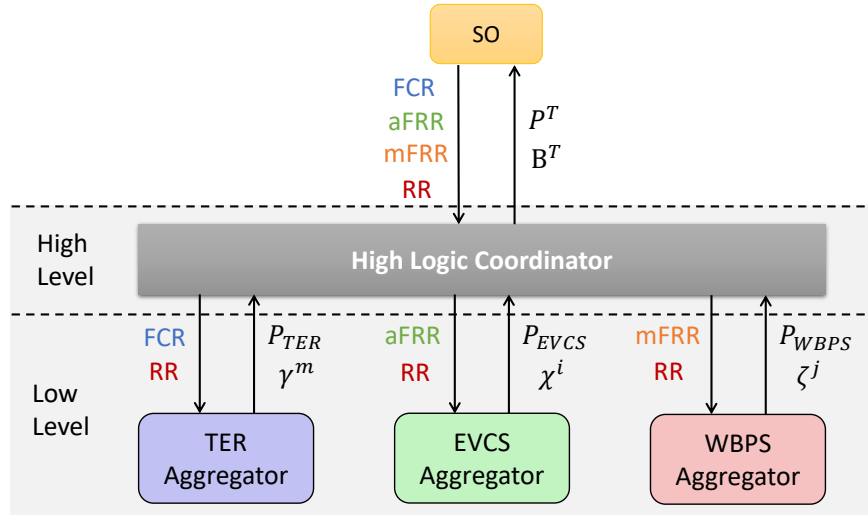


FIGURE 7.1: Hierarchical Architecture Structure.

Notice that the HAS is scalable in the AGGs, i.e., the number of AGGs could be higher; in fact, if more AGGs participate in the HAS, better performance of the balancing service can be reached.

The main responsibilities of the HLC are:

- Understand the capacity and the time response of the AGGs.
- Assign the balancing services that each AGG can provide.
- Offer the complete flexibility of the HAS to the SO.
- Manage the SO requests, i.e., if some AGG has variations following its requested power, the HLC can compensate the overall power with another AGG.

The HLC manages the European balancing services (FCR, aFRR, and mFRR) provision by assigning them among the AGGs considering the time response of each one, as,

- the TER-AGG can provide FCR as presented in Section 4.2.2;
- the EVCS-AGG due to the response time (few-minutes, see Section 5.2) can provide aFRR (5 min activation time);
- the WBPS-AGG due to the response time (power stabilization of 12 min after the SO call, see Section 3.3.1) can provide mFRR (12.5 min activation time); and,
- the RR service can be provided by all the AGGs.

7.1.2 Flexible Loads Aggregators

In this subsection, the flexible load aggregators considered in the low level are presented. In fact, the aggregators presented in the previous chapters are used for this integration assessing continuous and discrete systems. Therefore, the estimated dynamic responses of the WBPS-AGG and TER-AGG are considered, this is because of the lower computational time. Whereas, the EVCS is taken into account with the original MPC strategy. Moreover, modifications on the originals aggregators are taken into account for integrating it in the HAS.

TER-AGG

The TER-AGG can offer upward and downward flexibility. In the present approach, the estimated models presented in Eq. (4.16) and Eq. (4.17) of a TER set in transfer function are used. The models are:

$$G_{TER-up}(s) = \frac{25.95s^2 + 0.017s + 9.3e^{-6}}{s^2 + 1.1e^{-3}s + 6.8e^{-7}}, \quad (7.1)$$

$$G_{TER-down}(s) = \frac{-17.35s^2 - 0.018s - 3.6e^{-6}}{s^2 + 2.3e^{-3}s + 3.7e^{-7}}. \quad (7.2)$$

Moreover, the TER-AGG presented in 4.2.2, follows a PI controller structure as,

$$C_{TER-AGG}(s) = \frac{-0.012}{s} \quad (7.3)$$

The TER-AGG controller is improved for achieving faster changes when providing different services. This is possible considering the instantaneous response of the TERs. The new controller has the opportunity of changing the k_p and k_i parameters; the aim is to synchronize the power in one second when interacting with other AGGs.

WBPS-AGG

The WBPS-AGG can only offer downward flexibility. Then, as in the TER-AGG, the estimated model presented in Eq. (3.8) of a WBPS set in transfer function is used. The model is:

$$G_{WBPS}(s) = \frac{10.21s + 0.039}{45s + 1}. \quad (7.4)$$

However, considering that the AGG sample time is 3 min, the model is discretized as,

$$G_{WBPS}(z) = \frac{0.2269z + 0.1886}{z + 0.01832}. \quad (7.5)$$

As presented in Eq. (3.10) and Eq. (3.11) the WBPS-AGG is based on a PI Gain-Scheduling controller (see Section 3.3.2), where the controllers are represented as,

$$C_{WBPS-AGG}(z) = k_p + k_i * \frac{2}{T} \frac{z+1}{z-1} \quad (7.6)$$

The values for k_p and k_i depend on the HLC request and are defined in the Table 3.8. Notice that the parameter of the controller varies with the model.

EVCS-AGG

The EVCS-AGG can provide upward and downward flexibility to the SO. This AGG has the opportunity to schedule a DA power demand based on the EV charger request. Then, the DA is considered following the problem presented in Eq. (5.19); however, in this market is assessed as an optimal controller. The problem is,

$$\min_{P_{i,k}, U_{i,k}^F, L_{i,k}^F} \Delta t \sum_{k=0}^{\beta} \left(c_k \sum_{i=1}^I P_{i,k} - \pi_k^U \sum_{i=1}^I U_{i,k}^F - \pi_k^L \sum_{i=1}^I L_{i,k}^F \right) \quad (7.7a)$$

$$\text{s.t.} \quad x_{i,k+1} = \begin{cases} x_{i,k} + \Delta t P_{i,k} & \text{if } \tilde{a}_j < k < d_j, \\ \widetilde{SoC}_{j,a_j} & \text{if } k = \tilde{a}_j, \\ 0 & \text{if } \xi_{i,k} = 0 \quad \vee \quad k = d_j, \end{cases} \quad (7.7b)$$

$$\widetilde{SoC}_{j,d_j} \leq x_{i,d_j} \leq \widehat{SoC}_{j,d_j}, \quad (7.7c)$$

$$L_{i,k}^F \leq P_{i,k} \leq \xi_{i,k} (P_{i,\max} - U_{i,k}^F), \quad (7.7d)$$

$$0 \leq U_{i,k}^F \leq P_{i,\max}, \quad (7.7e)$$

$$0 \leq L_{i,k}^F \leq P_{i,\max}, \quad (7.7f)$$

$$0 \leq x_{i,k} \leq x_{i,\max}, \quad (7.7g)$$

$$\forall k = 1, 2, \dots, \beta, \quad i = 1, 2, \dots, I \quad j = 1, 2, \dots, J.$$

Therefore, the DA power is,

$$P_{p,DA,k} = \sum_{i=1}^I P_{p,i,k}^* \quad (7.8)$$

The reported $P_{p,DA,k}$ is computed as the hourly mean value.

In RT dispatch, the MPC strategy is adopted in order to follow the DA power scheduled. Then, the optimal control problem is,

$$\begin{aligned} \min_{P_{p,i,k}, P_{w,i,k}} \quad & \Delta t \sum_{k=0}^{H-1} \left(\phi_k \left(\sum_{i=1}^I P_{p,i,k} - P_{p-DA,k} \right)^2 \right) \\ \text{s.t.} \quad & \text{Eq. (7.7b), Eq. (7.7c), Eq. (7.7d), Eq. (7.7e), Eq. (7.7f), and Eq. (7.7g)} \end{aligned} \quad (7.9a)$$

7.2 Balancing Service Provider Operation

In this subsection, the operation of the HAS as BSP is proposed. Therefore, simulation campaigns are performed in order to evaluate the HAS provision of FCR, aFRR, mFRR, and RR services.

The AGGs DA power are defined as: i) in the TER-AGG and in the WBPS-AGG is considered as the nominal power presented in sections 3.3.2 and 4.2.2, respectively; and ii) in the EVCS is the day-ahead scheduling as presented in Subsection 7.1.2.

In order to evaluate the HAS performance, two different service provisions are evaluated:

- *Case 1:* Each AGG provides a specific service, except the RR service that can be provided by all the AGG.
- *Case 2:* The services are provided by overlapping the AGG power demand in the services by following the idealized provision case of Figure 2.3.

Both cases are evaluated in Simulink simulations. These cases provide different power capacity due to the maximum power the TER (fast service) can provide to the grid in each case. The HLC defines and reports to the AGGs the power deviation they should follow. Moreover, in the simulations, only reduction power requests by the SO are analysed due to the WBPS response that only considers reduction flexibility.

In Figure 7.2 the HAS operation is depicted, presenting the HLC (low level) and the flexible loads AGGs with their loads (low level). The TER and WBPS sets are implemented as transfer functions, continuous and discrete, respectively. These functions allow the simulation to be computationally lightweight. Besides, the EVCS-AGG runs the MPC in a MATLAB function as well as the EV chargers.

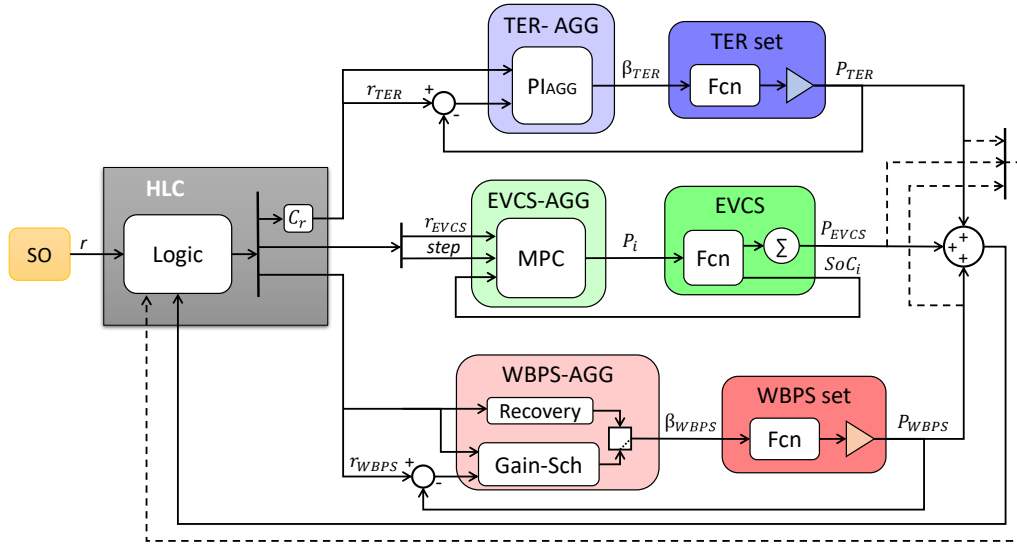


FIGURE 7.2: Balancing service provider operation.

Case 1

The case study evaluates a frequency restoration process where all the aggregators participate in providing balancing services. In this case, the FCR, the aFRR, and the mFRR services are provided by a single AGG considering the time response of each one.

Figure 7.3 depicts how the HAS performs the services when the SO requests a power reduction of $r=40$ kW. The DA power is 305.82 kW, the ideal RT power is 265.82 kW, while the HAS RT power is 265.88 kW, achieving an error of 22.6 W and standard deviation of 0.78 kW.

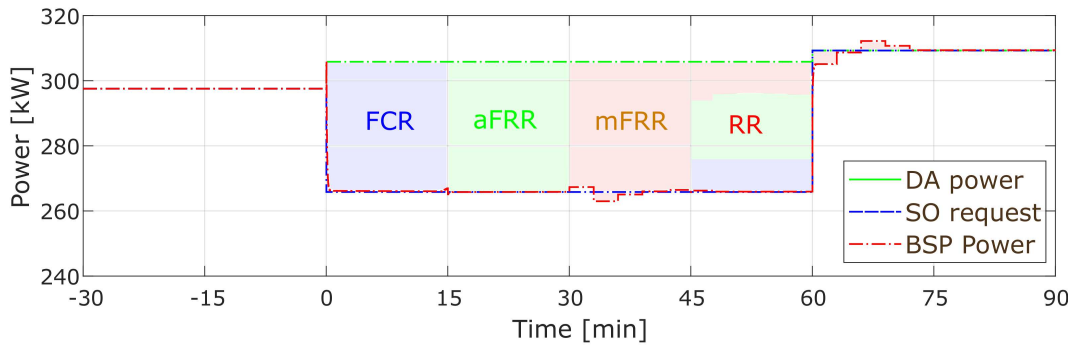


FIGURE 7.3: Hierarchical Architecture Structure perform in balancing services.

In Figure 7.4 the TER-AGG power response is presented, while in Figure 7.5, the percentage of systems changing the set-point to follow the required power is depicted.

Notice that the maximum power deviation of the HAS is computed as the maximum power the TER-AGG can provide, in this case for 15 min.

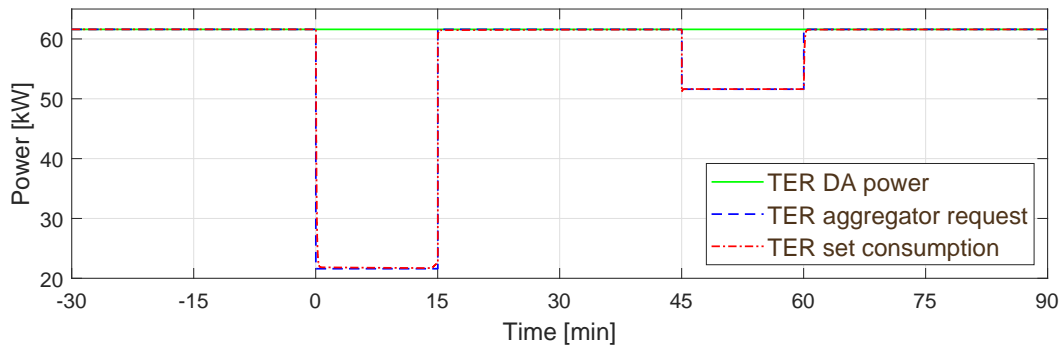


FIGURE 7.4: TER Aggregator power demand.

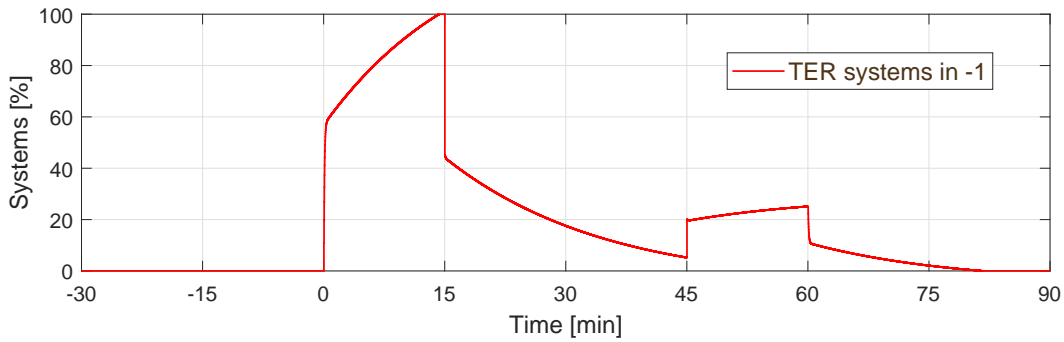


FIGURE 7.5: Percentage of TER systems changing the set-point.

The WBPS-AGG response is presented in Figure 7.6, while in Figure 7.7 the percentage of systems changing the set-point to follow the required power is depicted. In addition, the ramp-down is considered to avoid a rebound effect of the HAS.

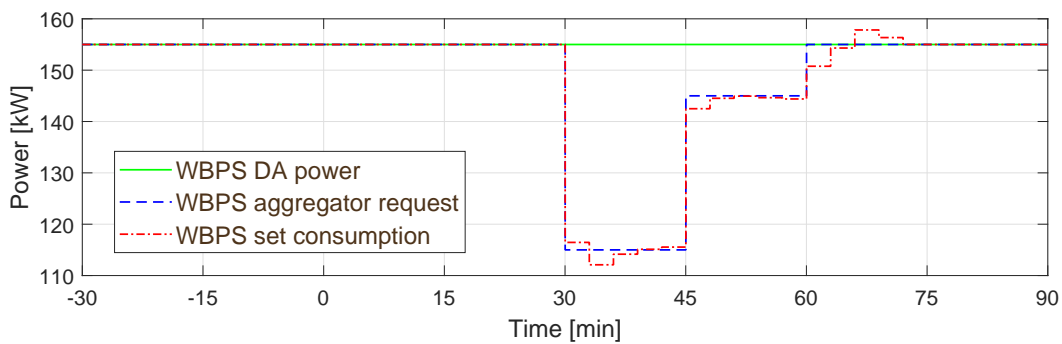


FIGURE 7.6: WBPS Aggregator power demand.

In Figure 7.8 the power demanded by the EVCS-AGG is shown. It can be seen that between the minutes 45 and 60, the power is not constant, this is due to the fact that the

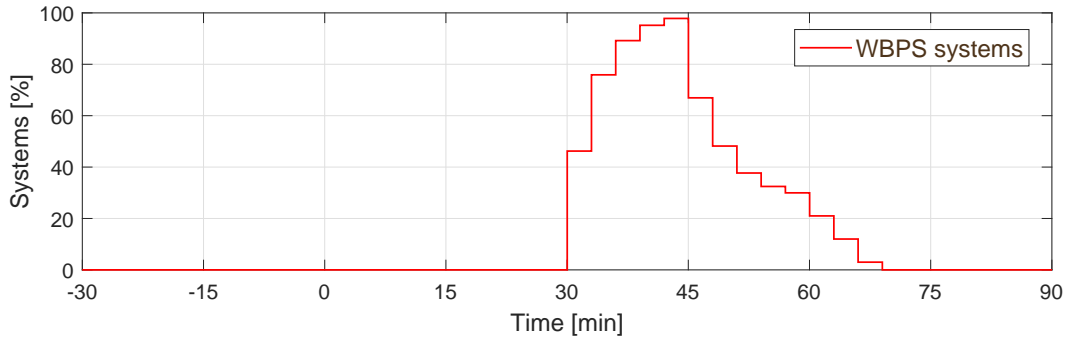


FIGURE 7.7: Percentage of WBPS systems changing the set-point.

HLC modifies the EVCS consumption depending on the others AGG consumption. In particular, the WBPS-AGG has small variations when following its request; then, the EVCS is able to maintain the balance. Notice that at each hour the DA power varies.

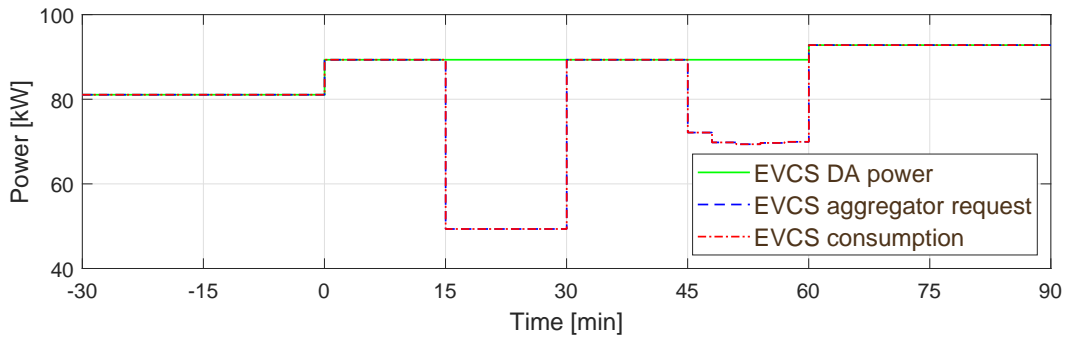


FIGURE 7.8: EVCS Aggregator power demand.

Case 2.

In this case, the aim is that the HCL coordinates the aggregators in a similar performance of the one presented by ENTSO-E (see Figure 2.3), considering ramps rates and times per service.

Figure 7.9 presents the power response of the HAS when aggregating the AGGs power. The SO requests a power reduction of $r=57$ kW, 17 kW higher than in case 1. The DA power is 305.82 kW (the same as Case 1), the ideal RT power is 248.82 kW, while the HAS RT power is 249.00 kW achieving an error of 71.5 W and standard deviation of 0.10 kW (lower than in Case 1).

The TER-AGG is the first AGG to modify its consumption, it is the only one that

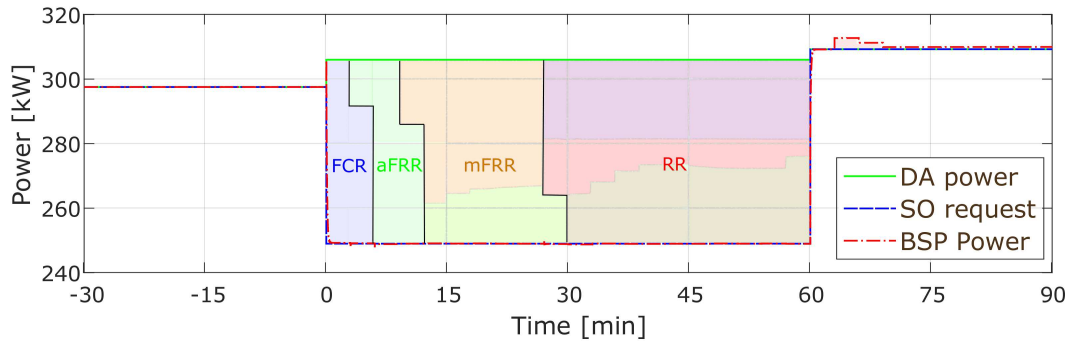


FIGURE 7.9: Aggregation system power in balancing services

can provide this energy service; therefore, the maximum power is defined by the maximum capacity of this AGG in a specific time window (3 min in this case). The TER-AGG performance is shown in Figure 7.10 and the percentage of systems changing the temperature set-point is depicted in Figure 7.11.

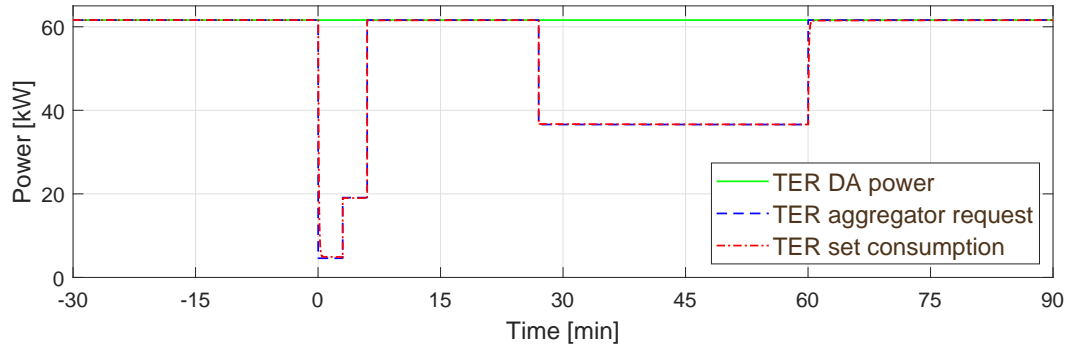


FIGURE 7.10: TER Aggregator power.

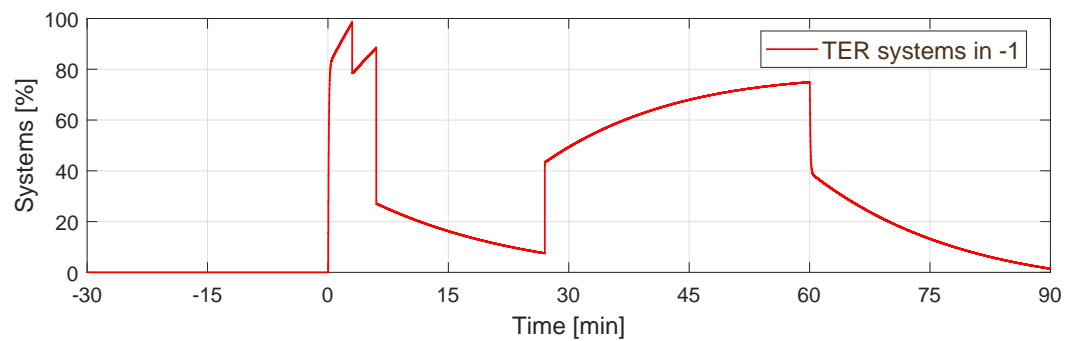


FIGURE 7.11: TER systems.

The WBPS-AGG response is presented in Figure 7.12, while in Figure 7.13 the percentage of systems changing the pressure set-point is depicted. In addition, the ramp-down is considered to avoid a rebound effect at the end of the HAS energy provision.

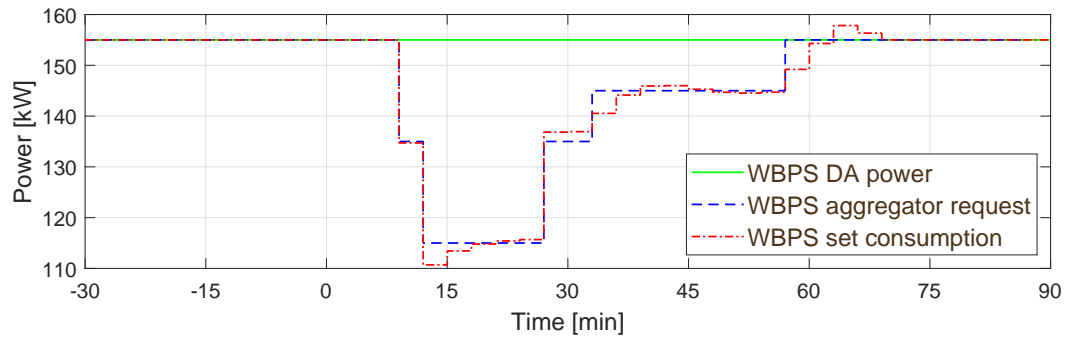


FIGURE 7.12: WBPS Aggregator power.

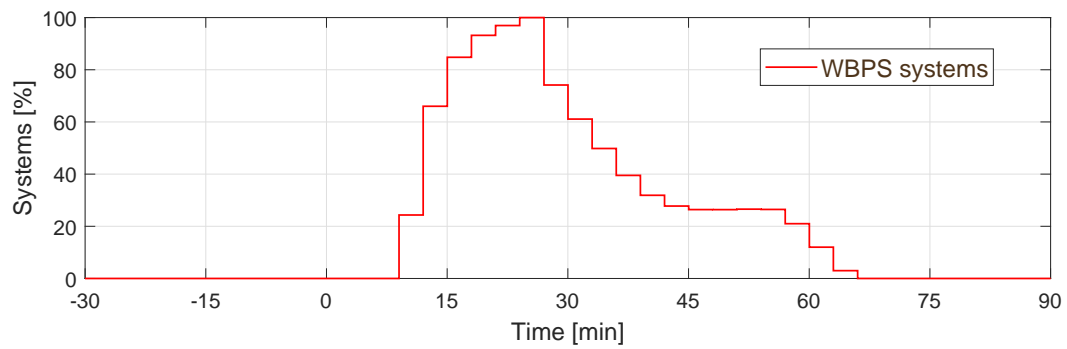


FIGURE 7.13: WBPS systems.

Finally, in Figure 7.14 the power demanded by the EVCS-AGG is shown. It can be seen that the HCL is constantly changing the requested power due to the variations of the WBPS-AGG.

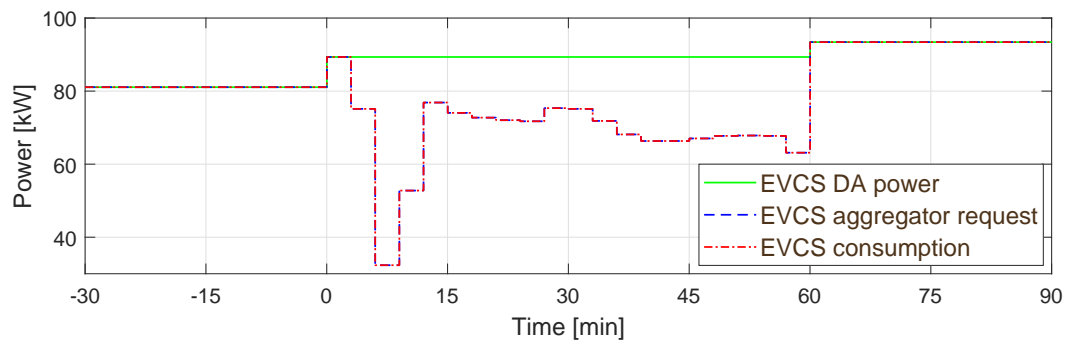


FIGURE 7.14: EVCS Aggregator power.

Chapter 8

Conclusions

In this dissertation, flexible loads aggregators have been proposed to provide different ancillary services to the system operator of a smart grid. This research has covered the topics related to direct load control in Demand Response (DR) services, specifically at the customer level, controlling the power consumption. The achieved contribution can be applied for the implementation of innovative balance strategies that improve the DR programs for contributing to enhancing the operation of a smart grid through the participation of flexible demand in regulation and reserve services.

In the literature, flexible load models and aggregation strategies have been reported. Selected loads that are potentially useful for providing ancillary services have been considered. Therefore, the first part of this work presents a framework defining an aggregator design process and a methodology for the load aggregation. In the framework, the main steps are the flexible load modeling, the flexibility analysis for defining the energy service the load can offer, the aggregation control strategy design, and the solution evaluation. Hence, the framework can be applied to any flexible load.

The aggregator framework is applied to three flexible loads for offering different ancillary services. First, an aggregator for Water Booster Pressure System (WBPS) has been proposed, capable of offering spinning reserve services. A gain-scheduled control system performs the demand response decisions with the aim of tracking a reduction signal sent by the system operator. A dynamic model of the WBPS was estimated and tuned with real data. The system flexibility in power consumption was evaluated by changing the operation pressure set-point.

Second, an aggregator for ThermoElectric Refrigeration (TER) units has been proposed to offer both frequency containment reserve and balancing services by reducing and increasing the power of a set of TERs. Based on a three-state signal (0,1, or-1), the aggregator decides the temperature set-point of each TER for following a signal sent

by the system operator. A dynamic model of a TER unit has been estimated from experimental data and a modified PI controller strategy has been proposed based on a PI controller that is tested in a real TER.

Third, two novel aggregators for Electric Vehicle Charging Station (EVCS) have been proposed. The first strategy looks for minimizing the EVCS operation costs, via an economic Model Predictive Control (MPC). The second strategy develops an Optimal Control with minimum Cost and maximum Flexibility formulation. This charging strategy has the possibility of offering spinning reserve services to the grid. A dynamic model of an EVCS charger as a flexible load is developed. In addition, an evaluation of the sensitivity of the control strategy in front of state of charge uncertainty suggests that the MPC strategy is robust in front of the EV arrival state of charge information.

A specific definition of flexibility for EV chargers has been provided with respect to a given nominal charging trajectory, considering the power deviations attainable by the trajectory itself.

Another two strategies were proposed, a Day-Ahead (DA) schedule and a Real-Time (RT) dispatch. The DA strategy aims to minimize the operation cost, while the RT strategy looks for minimizing the error on following the DA schedule. In these strategies, the EVCS considers power from the electrical grid and a local photo-voltaic plant.

A Hierarchical Architecture Structure (HAS) is proposed in order to integrate the TER, the WBPS, and the EVCS aggregators. The HAS is capable of providing European balancing services to the electrical grid considering a logic coordinator that allocates the system operator energy request among the aggregators.

This research has provided aggregation strategies for improving smart grids management when a high penetration of renewable energy sources is considered, helping to reduce carbon emissions. Economic benefits can be obtained by the stakeholders, reducing operating costs and obtaining profits from the ancillary service provision. Detailed technical solutions have been developed for the implementation of demand response services through direct load control.

Finally, there are still many aspects to be explored for these aggregation strategies. For instance, carry out an experimental evaluation of the flexible loads controllers considering the communication requirements between the aggregator and the loads. Technical requirements of smart meters should be assessed for the large scale implementation. Also, proper contracts should be designed to promote the participation of customers in the demand response programs.

Appendix A

Model Predictive Control

In this Appendix, the Model Predictive Control (MPC) formulation is presented based on (Camacho and Bordons, 2007). It is explained the strategy and structure of an MPC controller, particularly for linear systems. Besides, the unconstrained and constrained cases are analyzed.

A.1 MPC strategy

The methodology of the MPC is characterized by the strategy shown in Fig. A.1. It can be described as follows:

1. A prediction horizon H_p is defined with the purpose of calculating the plant outputs x_{k+r} for the future times $r=1, 2, \dots, H_p$, which depends on the known past and present system behavior (inputs and outputs) and on the future control signals u_{k+r} .
2. The set of future inputs or control signals is obtained by optimizing a certain criterion of a cost function. For example, this can be to follow a reference trajectory. Besides, the set of free variables u_{k+r} is solved for a control horizon H_c , hence, u_{k+r}^* is evaluated for $r=1, 2, \dots, H_c$. Note that, H_c must be $H_p \geq H_c$ and $\hat{u}_{k+r}=0$ for $r \geq H_c$.
3. The first control signal u_k ($r=0$) is applied to the process.

Then, in the next step k the process is repeated, thus, the control sequence \hat{u}_{k+r} is recalculated using the receding horizon concept, i.e., updating the process with the information available, e.g. real disturbances in $r=0$ that cannot be measured in the prediction horizon. Moreover, the MPC strategy can handle constraints not only in the plant output (x_{\min} and x_{\max}) but also in the control signal (u_{\min} and u_{\max}).

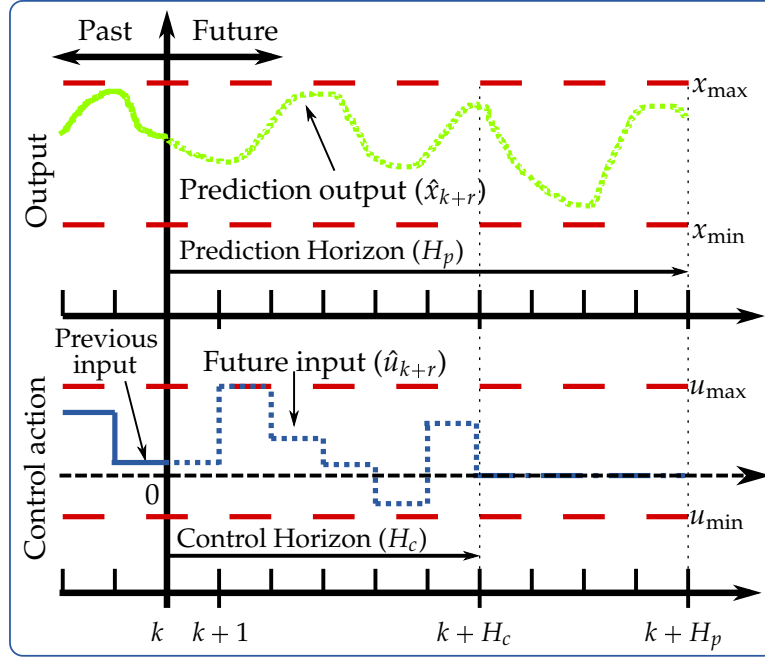


FIGURE A.1: MPC Strategy.

A basic structure to implement the MPC strategy is shown in Fig. A.2. An explicit model is used to predict the future plant outputs, which are based on past, current information and on the optimizer proposed control actions. Therefore, the suitable system model must be accurate enough to capture significant dynamics behaviors, and simple enough for allowing online optimization.

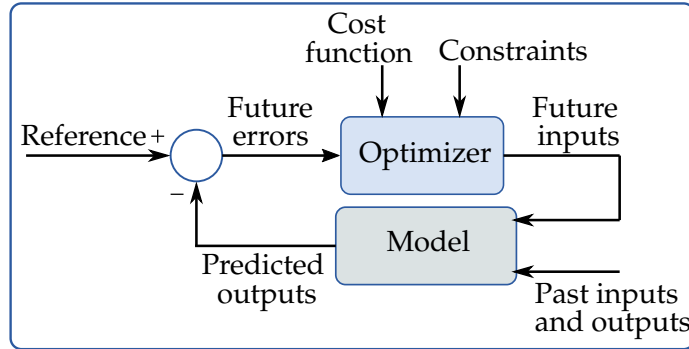


FIGURE A.2: MPC Structure.

Several types of models can be used for the formulation, consequently, there are various types of MPC developments. The State Space Model is one of the most useful as the derivation of the controller is clearer even for a multi-variable case.

Regarding the optimizer, it is in charge of delivering the calculation of a control sequence that minimizes a cost function J that penalizes the evolution of the inputs and system variables. A minimization criterion for the function can be to keep the process as close as possible to a reference trajectory. J usually is expressed by a quadratic function of the errors between the predicted output signal and the predicted reference trajectory, and a quadratic term of the input effort. Then, considering a linear model and no constraints, an explicit solution can be obtained. Otherwise, in the presence of inequality constraints, an iterative optimization method has to be used, and in order to achieve the solution, more computationally demanding algorithms must be applied. In addition, the size of the optimization problem depends on the number of variables, the prediction and control horizon (H_p and H_c) used.

A.2 MPC for linear systems

In this subsection, a prediction model, a cost function and an unconstrained and a constrained case are analyzed. Therefore, with the purpose of developing an understandable formulation, the following assumptions are considered:

1. The plant model is linear and time-invariant.
2. The constraints are linear inequalities.
3. The state measurements and the disturbances are known.

The third assumption allows the knowledge of the states in each step. However, when this information is not available it is required to implement a state estimator, such as an observer. According to the first assumption, a state space model is used in the present work as:

$$\mathbf{x}_{k+1} = \mathbf{A}\mathbf{x}_k + \mathbf{B}\mathbf{u}_k \quad (\text{A.1a})$$

$$\mathbf{y}_k = \mathbf{C}\mathbf{x}_k \quad (\text{A.1b})$$

where, $\mathbf{x} \in \mathbb{R}^n$ is the state vector whose components are as $\mathbf{x}_k = [x_{1,k}, \dots, x_{n,k}]^T$, $\mathbf{u} \in \mathbb{R}^m$ is the input vector whose components are $\mathbf{u}_k = [u_{1,k}, \dots, u_{m,k}]^T$, and $\mathbf{y} \in \mathbb{R}^p$ are the measured outputs whose components are $\mathbf{y}_k = [y_{1,k}, \dots, y_{p,k}]^T$. In addition, $\mathbf{A} \in \mathbb{R}^{n \times n}$, $\mathbf{B} \in \mathbb{R}^{n \times m}$ and $\mathbf{C} \in \mathbb{R}^{p \times n}$ are the system, input and output matrices respectively. To generate the prediction model, it is assumed $\mathbf{C} = \mathbf{I}$ an identity matrix. Then, the future outputs calculation is developed by the following model,

$$\hat{\mathbf{x}} = \mathbf{A}\mathbf{x}_{k_0} + \mathbf{G}\mathbf{u}, \quad (\text{A.2})$$

where,

$$\underbrace{\begin{bmatrix} \hat{x}_{k+1} \\ \hat{x}_{k+2} \\ \vdots \\ \hat{x}_{k+H_c} \\ \hat{x}_{k+H_c+1} \\ \vdots \\ \hat{x}_{k+H_p} \end{bmatrix}}_{\hat{\mathbf{x}}} = \underbrace{\begin{bmatrix} A \\ A^2 \\ \vdots \\ A^{H_c} \\ A^{H_c+1} \\ \vdots \\ A^{H_p} \end{bmatrix}}_{\mathbf{A}} \mathbf{x}_{k_0} + \underbrace{\begin{bmatrix} B & 0 & 0 & 0 \\ AB & B & 0 & 0 \\ \vdots & \vdots & \ddots & \vdots \\ A^{H_c-1}B & A^{H_c-2}B & \dots & B \\ A^{H_c}B & A^{H_c-1}B & \dots & AB \\ \vdots & \vdots & \ddots & \vdots \\ A^{H_p-1}B & A^{H_p-2}B & \dots & A^{H_p-H_c}B \end{bmatrix}}_{\mathbf{G}} \underbrace{\begin{bmatrix} \mathbf{u}_k \\ \hat{\mathbf{u}}_{k+1} \\ \vdots \\ \hat{\mathbf{u}}_{k+H_c-1} \end{bmatrix}}_{\mathbf{u}}, \quad (\text{A.3})$$

where, \hat{x}_{k+r} and \hat{u}_{k+r} are the predicted output and input vectors, respectively; \mathbf{x}_{k_0} is the initial condition of the model. This prediction model allows fulfilling the first step of the MPC methodology.

On the other hand, different cost functions formulation can be used for obtaining the control law. Let us define the reference trajectory as,

$$\mathbf{z} = [z_{1,k+1}, \dots, z_{n,k+1}, \dots, z_{1,k+H_p}, \dots, z_{n,k+H_p}]^T. \quad (\text{A.4})$$

For the second step of the MPC methodology, it is used a quadratic cost function of the form:

$$J(\mathbf{u}) = (\hat{\mathbf{x}} - \mathbf{z})^T \mathbf{Q} (\hat{\mathbf{x}} - \mathbf{z}) + \mathbf{u}^T \mathbf{R} \mathbf{u} \quad (\text{A.5})$$

where, \mathbf{Q} is the output error penalty diagonal matrix, whose components must satisfy $Q_r \geq 0$, for $r=1, \dots, H_p \times n$, and \mathbf{R} is the control move penalty diagonal matrix, whose components must satisfy $R_r \geq 0$, for $r=1, \dots, H_p \times m$. Moreover, the superscript T denotes transposition. Taking into account the matrix and transpose properties, the quadratic cost function of Eq. (A.5) can be written as (Lewis et al., 2012),

$$J(\mathbf{u}) = \hat{\mathbf{x}}^T \mathbf{Q} \hat{\mathbf{x}} - \underline{\hat{\mathbf{x}}^T \mathbf{Q} \mathbf{z}} + \mathbf{z}^T \mathbf{Q} \mathbf{z} - \underline{\mathbf{z}^T \mathbf{Q} \hat{\mathbf{x}}} + \mathbf{u}^T \mathbf{R} \mathbf{u}. \quad (\text{A.6})$$

Considering that \mathbf{Q} is symmetrical, the two terms underlined in Eq.(A.6) became the same, and using Eq. (A.2):

$$J(\mathbf{u}) = (\mathbf{A} \mathbf{x}_{k_0} + \mathbf{G} \mathbf{u})^T \mathbf{Q} (\mathbf{A} \mathbf{x}_{k_0} + \mathbf{G} \mathbf{u}) - 2 \mathbf{z}^T \mathbf{Q} (\mathbf{A} \mathbf{x}_{k_0} + \mathbf{G} \mathbf{u}) + \mathbf{z}^T \mathbf{Q} \mathbf{z} + \mathbf{u}^T \mathbf{R} \mathbf{u} \quad (\text{A.7})$$

that is,

$$\begin{aligned}
 J(\mathbf{u}) = & \underbrace{\mathbf{x}_{k_0}^T \mathbb{A}^T \mathbf{Q} \mathbb{A} \mathbf{x}_{k_0}}_{\text{Cons}} + \underbrace{\mathbf{x}_{k_0}^T \mathbb{A}^T \mathbf{Q} \mathbf{G} \mathbf{u}}_{\text{Cons}} + \underbrace{\mathbf{u}^T \mathbf{G}^T \mathbf{Q} \mathbb{A} \mathbf{x}_{k_0}}_{\text{Cons}} + \\
 & \mathbf{u}^T \mathbf{G}^T \mathbf{Q} \mathbf{G} \mathbf{u} - \underbrace{2\mathbf{z}^T \mathbf{Q} \mathbb{A} \mathbf{x}_{k_0}}_{\text{Cons}} - 2\mathbf{z}^T \mathbf{Q} \mathbf{G} \mathbf{u} + \underbrace{\mathbf{z}^T \mathbf{Q} \mathbf{z}}_{\text{Cons}} + \mathbf{u}^T \mathbb{R} \mathbf{u}.
 \end{aligned} \tag{A.8}$$

The constant terms can be removed because they do not depend on \mathbf{u} , and the two terms underlined in Eq.(A.8) became the same, obtaining the formulation that leads to:

$$J(\mathbf{u}) = 2\mathbb{F}\mathbf{u} + \mathbf{u}^T \mathbb{H} \mathbf{u} \tag{A.9}$$

where,

$$\mathbb{F} = \mathbf{x}_{k_0}^T \mathbb{A}^T \mathbf{Q} \mathbf{G} - \mathbf{z}^T \mathbf{Q} \mathbf{G} \tag{A.10}$$

$$\mathbb{H} = \mathbf{G}^T \mathbf{Q} \mathbf{G} + \mathbb{R} \tag{A.11}$$

The next step is to find the optimal solution u_k^* by minimizing the quadratic objective function. Then, an unconstrained and a constrained case are assessed.

A.2.1 Unconstrained case

The optimization problem of an unconstrained MPC, also know as Generalized Predictive Control (GPC) is:

$$\min_{\mathbf{u}} \quad J(\mathbf{u}) = 2\mathbb{F}\mathbf{u} + \mathbf{u}^T \mathbb{H} \mathbf{u} \tag{A.12}$$

Therefore, to calculate the optimal solution, it is applied the gradient of J , which leads the following optimal control signal:

$$\mathbf{u}^* = -\frac{1}{2} \mathbb{H}^{-1} \mathbb{F} \tag{A.13}$$

A.2.2 Constrained case

The majority of the processes are subject to constraints which are related to the actuators physical limits, i.e., safety limits (see Fig.A.1), also, technical and environmental requirements, or saturation in control actions. In any case, constraints are expressed in terms of the optimization variables, i.e., control signals. Therefore, fulfilling these constraints can cause higher values of the cost or the solution can become unfeasible due to the fact that some constraints can be violated over the H_p . The most common

constraints acting on a process are presented as,

$$1_u u_{\min} \leq \mathbf{u}_k \leq 1_u u_{\max} \quad (\text{A.14a})$$

$$1_u \delta u_{\min} \leq \mathbf{u}_k - \mathbf{u}_{k+1} \leq 1_u \delta u_{\max} \quad (\text{A.14b})$$

$$1_x x_{\min} \leq \mathbf{x}_k \leq 1_x x_{\max} \quad (\text{A.14c})$$

where, 1_u is a vector with $H_c \times m$ components equal to unity and 1_x is a vector with $H_p \times n$ components equal to unity. Eq. (A.14a) represents the limits of the output, Eq. (A.14b) are the limits of the slew rate, and Eq. (A.14c) are the bounds of the states. Moreover, u_{\min} , u_{\max} , δu_{\min} , δu_{\max} , x_{\min} and x_{\max} are scalar values that limits the output and states. Taking into account H_p and H_c , the constraints can be expressed in condensed form as:

$$\Phi \mathbf{u} \leq \gamma. \quad (\text{A.15})$$

Then, considering the constraints of Eq. (A.14a) and Eq. (A.14c), Φ and γ are:

$$\Phi = \begin{bmatrix} \mathbb{I} \\ -\mathbb{I} \\ \mathbf{G} \\ -\mathbf{G} \end{bmatrix}, \quad \gamma = \begin{bmatrix} 1_u u_{\max} \\ -1_u u_{\min} \\ 1_x x_{\max} - \mathbb{A} \mathbf{x}_{k_0} \\ -1_x x_{\min} + \mathbb{A} \mathbf{x}_{k_0} \end{bmatrix} \quad (\text{A.16})$$

where, \mathbb{I} is an identity matrix of size $H_c \times m$. With the purpose of calculating the optimal output, it is needed to solve the Open-loop Optimization Problem (OOP) in each step k . The OOP can be stated as,

$$\begin{aligned} \min_{\mathbf{u}} \quad & J(\mathbf{u}) = 2\mathbf{F}\mathbf{u} + \mathbf{u}^T \mathbb{H} \mathbf{u} \\ \text{s.t.} \quad & \Phi \mathbf{u} \leq \gamma \end{aligned} \quad (\text{A.17})$$

In order to find the \mathbf{u} that minimizes $J(\mathbf{u})$ and fulfill the third step of the methodology, the next pseudo algorithm is presented: this algorithm allows to calculate the optimal \mathbf{u}^* for each step k . Note that, this algorithm generates a closed loop control on account of the state \mathbf{x}_k measured that is used for obtaining the next solution of the OOP.

On the other hand, the cost function J is convex, and the constraints form a convex set. Therefore, computationally, it is possible to find efficiently the global minimum of the OOP.

Algorithm 1 Constrained MPC controller

```

Generate  $\mathbb{A}, \mathbb{G} \wedge \Phi$ 
 $k = 0$ 
 $\bar{x}_k = x_{k_0}$  initial condition
for  $k \leftarrow 1, \beta$  do
     $x_k \Leftarrow \bar{x}_k$ 
    Calculate  $\gamma$  depending on  $x_k$ 
     $\mathbf{u}^* \Leftarrow \text{solve OOP}$ 
    Apply only  $\mathbf{u}_k^*$  to obtain  $\bar{x}_{k+1}$ 
end for

```

Moreover, the problem can become unfeasible due to modeling errors, disturbances or improper MPC tuning. One option to avoid unfeasibilities is by relaxing constraints as soft constraints (Zeilinger et al., 2014). The idea is to relax the constraints limits as $\Phi \mathbf{u} \leq \gamma + \varepsilon$, then the cost function J must include a new term as $\varepsilon^T \mathbb{T} \varepsilon$, where \mathbb{T} is a proper weighting matrix. In this case, the optimization problem considers a new decision variable ε , i.e., $J(\mathbf{u}, \varepsilon)$.

Bibliography

Aghaei, J., Alizadeh, M. I., 2013. Demand response in smart electricity grids equipped with renewable energy sources: A review. *Renewable and Sustainable Energy Reviews* 18, 64–72.

URL <http://dx.doi.org/10.1016/j.rser.2012.09.019>

Albadi, M. H., El-Saadany, E. F., 2008. A summary of demand response in electricity markets. *Electric Power Systems Research* 78 (11), 1989–1996.

Amjad, M., Ahmad, A., Rehmani, M. H., Umer, T., 2018. A review of EVs charging: From the perspective of energy optimization, optimization approaches, and charging techniques. *Transportation Research Part D: Transport and Environment* 62 (March), 386–417.

URL <https://doi.org/10.1016/j.trd.2018.03.006>

Arjun, K. G., Pruthviraj, B. G., Chethan, K. Y., Rashmi, P., 2017. Design and implementation of peltier based solar powered portable refrigeration unit. In: *RTEICT 2017 - 2nd IEEE International Conference on Recent Trends in Electronics, Information and Communication Technology*. pp. 1971–1974.

Arteconi, A., Polonara, F., 2018. Assessing the demand side management potential and the energy flexibility of heat pumps in buildings. *Energies* 11 (7), 1–19.

Arun Shankar, V. K., Umashankar, S., Paramasivam, S., Hanigovszki, N., 2016. A comprehensive review on energy efficiency enhancement initiatives in centrifugal pumping system. *Applied Energy* 181, 495–513.

URL <http://dx.doi.org/10.1016/j.apenergy.2016.08.070>

Astrain, D., Aranguren, P., Martínez, A., Rodríguez, A., Pérez, M. G., 2016. A comparative study of different heat exchange systems in a thermoelectric refrigerator and their influence on the efficiency. *Applied Thermal Engineering* 103, 1289–1298.

URL <http://dx.doi.org/10.1016/j.applthermaleng.2016.04.132>

- Astrain, D., Martínez, A., Gorraiz, J., Rodríguez, A., Pérez, G., 2012. Computational Study on Temperature Control Systems for Thermoelectric Refrigerators. *Journal of Electronic Materials* 41 (6), 1081–1090.
- Azad, P., 2019. Temperature Controlled Voltage Regulated Boost Converter for Thermoelectric Energy Harvesting. *IETE Journal of Research*, 1–8.
URL <https://doi.org/03772063.2019.1651678>
- Baccino, F., Conte, F., Massucco, S., Silvestro, F., Grillo, S., 2014. Frequency Regulation by Management of Building Cooling Systems through Model Predictive Control. In: 18th Power Systems Computation Conference, PSCC. pp. 1–7.
- Bakirtzis, E. A., Simoglou, C. K., Biskas, P. N., Bakirtzis, A. G., 2018. Storage management by rolling stochastic unit commitment for high renewable energy penetration. *Electric Power Systems Research* 158, 240–249.
URL <http://dx.doi.org/10.1016/j.epsr.2017.12.025>
- Bansal, P. K., Martin, A., 2000. Comparative study of vapour compression, thermoelectric and absorption refrigerators. *International Journal of Energy Research* 24 (2), 93–107.
- Bascetta, L., Gruosso, G., Storti Gajani, G., 2018. Analysis of Electrical Vehicle behavior from real world data: a V2I Architecture. In: 2018 International Conference of Electrical and Electronic Technologies for Automotive. AEIT, pp. 1–4.
- Bastidas, D. C., 2009. Caracterización y estimación de consumos de agua de usuarios residenciales. caso de estudio: Bogotá. Ph.D. thesis, Universidad De Los Andes, Departamento De Ingeniería Civil Y Ambiental.
- Bilgin, E., Caramanis, M. C., Paschalidis, I. C., Cassandras, C. G., 2016. Provision of Regulation Service by Smart Buildings. *IEEE Transactions on Smart Grid* 7 (3), 1683–1693.
- Blum, D. H., Norford, L. K., 2014. Dynamic simulation and analysis of ancillary service demand response strategies for variable air volume hvac systems. *HVAC&R Research* 20 (8), 908–921.
URL <http://dx.doi.org/10.1080/10789669.2014.958975>
- Borba, B. S. M., Szklo, A., Schaeffer, R., 2012. Plug-in hybrid electric vehicles as a way to maximize the integration of variable renewable energy in power systems: The

- case of wind generation in northeastern Brazil. *Energy* 37 (1), 469–481.
URL <http://dx.doi.org/10.1016/j.energy.2011.11.008>
- Brickey, P. L., Sanchez, J., 2005. How Potable Water Rises to the Top of Skyscrapers. *Plumbing Standards Magazine*, 1–3.
- Cabrera, E., Gomez, E., Cabrera Jr., E., Soriano, J., Espert, V., 2015. Energy Assessment of Pressurized Water Systems. *Journal of Water Resources Planning and Management* 141 (8), 1–12.
- Camacho, E., Bordons, C., 2007. *Model Predictive Control*, 2nd Edition. London.
- Cao, Y., Wang, T., Kaiwartya, O., Min, G., Ahmad, N., Abdullah, A. H., 2018. An EV Charging Management System Concerning Drivers' Trip Duration and Mobility Uncertainty. *IEEE Transactions on Systems, Man, and Cybernetics: Systems* 48 (4), 596–607.
URL <http://ieeexplore.ieee.org/document/7756376/>
- Carreiro, A. M., Jorge, H. M., Antunes, C. H., 2017. Energy management systems aggregators: A literature survey. *Renewable and Sustainable Energy Reviews* 73 (January), 1160–1172.
URL <http://dx.doi.org/10.1016/j.rser.2017.01.179>
- Clairand, J.-M., Rodríguez-García, J., Álvarez-Bel, C., 2018. Smart Charging for Electric Vehicle Aggregators Considering Users' Preferences. *IEEE Access* 6, 54624–54635.
URL <https://ieeexplore.ieee.org/document/8086068>
- Coccia, G., D'Agaro, P., Cortella, G., Polonara, F., Arteconi, A., 2019. Demand side management analysis of a supermarket integrated HVAC, refrigeration and water loop heat pump system. *Applied Thermal Engineering* 152 (February), 543–550.
URL <https://doi.org/10.1016/j.applthermaleng.2019.02.101>
- Colmenar-Santos, A., Muñoz-Gómez, A. M., Rosales-Asensio, E., López-Rey, Á., 2019. Electric vehicle charging strategy to support renewable energy sources in Europe 2050 low-carbon scenario. *Energy* 183, 61–74.
- CREG, 2015. Resolución Creg 209 de 2015.
URL <http://apolo.creg.gov.co/Publicac.nsf/Documentos-Resoluciones?OpenView{&}Start=4.26{&}Count=30{&}Expand=4{#}4>
- CREG, 2018. Análisis de los Servicios Complementarios para el Sistema Interconectado Nacional (SIN). Tech. rep.

- Cui, W., Ding, Y., Hui, H., Lin, Z., Du, P., Song, Y., Shao, C., 2018. Evaluation and sequential dispatch of operating reserve provided by air conditioners considering lead-lag rebound effect. *IEEE Transactions on Power Systems* 33 (6), 6935–6950.
- del Razo, V., Goebel, C., Jacobsen, H.-A., 2015. Vehicle-Originating-Signals for Real-Time Charging Control of Electric Vehicle Fleets. *IEEE Transactions on Transportation Electrification* 1 (2), 150–167.
URL <https://ieeexplore.ieee.org/document/7122933>
- Deng, R., Yang, Z., Chow, M.-Y., Chen, J., 2015. A Survey on Demand Response in Smart Grids: Mathematical Models and Approaches. *IEEE Transactions on Industrial Informatics* 11 (3), 570 – 582.
URL <http://ieeexplore.ieee.org/lpdocs/epic03/wrapper.htm?arnumber=7063260>
- Diaz, C., Mazza, A., Ruiz, F., Patino, D., Chicco, G., 2018a. Understanding Model Predictive Control for Electric Vehicle Charging Dispatch. In: 2018 53rd International Universities Power Engineering Conference (UPEC). IEEE, pp. 1–6.
URL <https://ieeexplore.ieee.org/document/8542050>
- Diaz, C., Ruiz, F., Patino, D., 2017a. Analysis of Water Booster Pressure Systems as Dispatchable Loads in Smart-Grids. In: 7th IEEE International Conference on Innovative Smart Grid Technologies (ISGT Europe 2017). pp. 1–6.
URL <https://ieeexplore.ieee.org/document/8260168>
- Diaz, C., Ruiz, F., Patino, D., 2017b. Modeling and control of water booster pressure systems as flexible loads for demand response. *Applied Energy* 204, 106–116.
URL <http://dx.doi.org/10.1016/j.apenergy.2017.06.094>
- Diaz, C., Ruiz, F., Patino, D., 2018b. Smart Charge of an Electric Vehicles Station: A Model Predictive Control Approach. In: 2018 IEEE Conference on Control Technology and Applications (CCTA). pp. 54 –59.
URL <https://ieeexplore.ieee.org/document/8511498>
- Diaz, I., Mendaza, D. C., Member, S., Szczesny, I. G., 2015. Flexible Demand Control to Enhance the Dynamic Operation of Low Voltage Networks. *IEEE Transactions on Smart Grid* 6 (2), 705–715.
- Diaz-Londono, C., Colangelo, L., Ruiz, F., Patino, D., Novara, C., Chicco, G., 2019a. Optimal Strategy to Exploit the Flexibility of an Electric Vehicle Charging Station.

- Energies 12 (20), 1–29.
URL <https://doi.org/10.3390/en12203834>
- Diaz-Londono, C., Enescu, D., Mazza, A., Ruiz, F., 2019b. Characterization and Flexibility of a ThermoElectric Refrigeration Unit. In: 2019 54th International Universities Power Engineering Conference (UPEC). pp. 1–6.
- Diaz-Londono, C., Enescu, D., Ruiz, F., Mazza, A., 2020a. Experimental Modeling and Aggregation Strategy for Thermoelectric Refrigeration Units as Flexible Loads. Applied Energy 272 (115065), 1–17.
URL <https://doi.org/10.1016/j.apenergy.2020.115065>
- Diaz-Londono, C., Ruiz, F., Mazza, A., Milano, P., 2020b. Optimal Operation Strategy for Electric Vehicles Charging Stations with Renewable Energy Integration. In: 21st International Federation of Automatic Control (IFAC) World Congress. pp. 1 – 6.
- Du, P., Lu, N., 2011. Appliance Commitment for Household Load Scheduling. IEEE Transactions on Smart Grid 2 (2), 411–419.
- Energy U.S., D., 2006. Benefits of demand response in electricity markets and recommendations for achieving them. Tech. Rep. February.
- Energy U.S., I. A., 2017. International Energy Outlook 2017. Tech. rep.
URL www.eia.gov/ieo
- Enescu, D., Ciocia, A., Mazza, A., Russo, A., 2017. Solutions based on thermoelectric refrigerators in humanitarian contexts. Sustainable Energy Technologies and Assessments 22, 134–149.
URL <http://dx.doi.org/10.1016/j.seta.2017.02.016>
- Enescu, D., Diaz, C., Ciocia, A., Mazza, A., Russo, A., 2018. Experimental Assessment of the Temperature Control System for a Thermoelectric Refrigeration Unit. In: 2018 53rd International Universities Power Engineering Conference (UPEC). pp. 1–6.
URL <https://ieeexplore.ieee.org/document/8542014>
- ENTSO-E, 2018a. All TSOs’ proposal for the implementation framework for a European platform for the exchange of balancing energy from frequency restoration reserves with manual activation in accordance with Article 20 of Commission Regulation (EU) 2017/2195 establishing . Tech. rep.

- ENTSO-E, 2018b. All TSOs' proposal for the implementation framework for the exchange of balancing energy from frequency restoration reserves with automatic activation in accordance with Article 21 of Commission Regulation (EU) 2017/2195 establishing a guideline on electr. Tech. rep.
- ENTSO-E, 2018c. The proposal of all TSO performing the reserve replacement process for the implementation framework for the exchange of balancing energy from Replacement Reserves in accordance with Article 19 of Commission Regulation (EU) 2017/2195. Tech. rep.
- Esmaili, M., Goldoust, A., 2015. Multi-objective optimal charging of plug-in electric vehicles in unbalanced distribution networks. *International Journal of Electrical Power and Energy Systems* 73, 644–652.
URL <https://www.sciencedirect.com/science/article/pii/S0142061515002574>
- European Commission, 2017. Commission Regulation (EU) 2017/1485 establishing a guideline on electricity transmission system operation. *Official Journal of the European Union* L 220, 1–120.
- Flammini, M. G., Prettico, G., Julea, A., Fulli, G., Mazza, A., Chicco, G., 2019. Statistical characterisation of the real transaction data gathered from electric vehicle charging stations. *Electric Power Systems Research* 166, 136–150.
URL <https://doi.org/10.1016/j.epsr.2018.09.022>
- Food Standards Agency (FSA), 2016. Guidance on Temperature Control Legislation in the United Kingdom, 1–17.
- Food Standards Australia New Zealand (FSANZ), 2017. Essential food safety practices. Cool and reheat food safely to the right temperatures.
URL <https://www.foodstandards.gov.au/consumer/safety/faqsafety/Pages/default.aspx>
- Forward Market Operations, 2017. PJM Manual 11: Energy and Ancillary services Market Operations. Tech. rep.
URL <https://www.pjm.com/-/media/documents/manuals/archive/m11/m11v87-energy-and-ancillary-services-market-operations-03-23-2017.ashx>
- García, J., Bermudez, R., Barbosa, J., 2013. Modeling and Simulation of a Centrifugal Pump With Single phase motor in Simulink. *Revista Colombiana de Tecnologías de Avanzada* 2 (22), 78 – 84.

- García-Villalobos, J., Zamora, I., San Martín, J. I., Asensio, F. J., Aperribay, V., 2014. Plug-in electric vehicles in electric distribution networks: A review of smart charging approaches. *Renewable and Sustainable Energy Reviews* 38, 717–731.
URL <http://dx.doi.org/10.1016/j.rser.2014.07.040>
- Gelazanskas, L., Gamage, K. A., 2014. Demand side management in smart grid: A review and proposals for future direction. *Sustainable Cities and Society* 11, 22–30.
URL <http://dx.doi.org/10.1016/j.scs.2013.11.001>
- Gellings, C., 1985. The concept of demand-side management for electric utilities. *Proceedings of the IEEE* 73 (10), 1468–1470.
URL <http://ieeexplore.ieee.org/xpl/articleDetails.jsp?arnumber=1457586{%&}newsearch=true{%&}queryText=Theconceptofdemand-sidemanagementforelectricutilities{%}%5Cnhttp://ieeexplore.ieee.org/lpdocs/epic03/wrapper.htm?arnumber=1457586>
- Gevorkov, L., Vodovozov, V., Lehtla, T., Raud, Z., 2016. Hardware-in-the-loop simulator of a flow control system for centrifugal pumps. In: *Proceedings - 2016 10th International Conference on Compatibility, Power Electronics and Power Engineering, CPE-POWERENG 2016*. pp. 472–477.
- Ghafouri, J., Khayatzaheh, H., 2012. Dynamic Modeling of Variable Speed Centrifugal Pump Utilizing MATLAB/SIMULINK. *International Journal of Science and Engineering Investigations* 1 (5), 1–7.
URL <http://www.ijsei.com/papers/ijsei-10512-09.pdf>
- Giordano, F., Arrigo, F., Diaz-Londono, C., Spertino, F., Ruiz, F., 2020. Forecast-Based V2G Aggregation Model for Day-Ahead and Real-Time Operations. In: *11th Conference on Innovative Smart Grid Technologies*. pp. 1–5.
- Giordano, F., Ciocia, A., Di Leo, P., Spertino, F., Tenconi, A., Vaschetto, S., 2018. Self-Consumption Improvement for a Nanogrid with Photovoltaic and Vehicle-to-Home Technologies. In: *2018 IEEE International Conference on Environment and Electrical Engineering and 2018 IEEE Industrial and Commercial Power Systems Europe (EEEIC / I&CPS Europe)*. IEEE, pp. 1–6.
URL <https://ieeexplore.ieee.org/document/8493708>

- González, P., Villar, J., Díaz, C. A., Campos, F. A., 2014. Joint energy and reserve markets: Current implementations and modeling trends. *Electric Power Systems Research* 109, 101–111.
URL <http://dx.doi.org/10.1016/j.epsr.2013.12.013>
- González Vayá, M., Andersson, G., 2016. Self Scheduling of Plug-In Electric Vehicle Aggregator to Provide Balancing Services for Wind Power. *IEEE Transaction on Sustainable Energy* 7 (2), 886–899.
- Grahn, P., Alvehag, K., Söder, L., 2014. PHEV Utilization Model Considering Type-of-Trip and Recharging Flexibility. *IEEE Transactions on Smart Grid* 5 (1), 139–148.
URL <https://ieeexplore.ieee.org/document/6623210>
- Grant, M., Boyd, S., 2014. CVX: Matlab software for disciplined convex programming, version 2.1.
- Haeri, H., Schaefer, F., Aiona, J., Jayaweera, T., Walker, T., 2014. Comprehensive Assessment of Demand-Side Resource Potentials (2014–2033). Tech. rep., The Cadmus Group, Inc. / Energy Services, United States.
- Haidar, A. M. A., Muttaqi, K. M., Haque, M. H., 2015. Multistage time-variant electric vehicle load modelling for capturing accurate electric vehicle behaviour and electric vehicle impact on electricity distribution grids. *IET Generation, Transmission & Distribution* 9 (16), 2705–2716.
URL <https://ieeexplore.ieee.org/document/7337593>
- Hao, H., Chen, W., 2014. Characterizing flexibility of an aggregation of deferrable loads. *Proceedings of the IEEE Conference on Decision and Control* 2015-Febru (February), 4059–4064.
- Hao, H., Middelkoop, T., Barooah, P., Meyn, S., 2012. How demand response from commercial buildings will provide the regulation needs of the grid. In: *2012 50th Annual Allerton Conference on Communication, Control, and Computing*, Allerton 2012. pp. 1908–1913.
- Hao, H., Sanandaji, B. M., Poolla, K., Vincent, T. L., 2015a. Aggregate Flexibility of Thermostatically Controlled Loads. *IEEE Transactions on Power Systems* 30 (1), 189–198.
URL <https://ieeexplore.ieee.org/document/6832599>

- Hao, H., Somani, A., Lian, J., Carroll, T. E., 2015b. Generalized aggregation and co-ordination of residential loads in a smart community. In: 2015 IEEE International Conference on Smart Grid Communications, SmartGridComm 2015. pp. 67–72.
- He, R. R., Zhong, H. Y., Cai, Y., Liu, D., Zhao, F. Y., 2017. Theoretical and Experimental Investigations of Thermoelectric Refrigeration Box Used for Medical Service. *Procedia Engineering* 205, 1215–1222.
URL <https://doi.org/10.1016/j.proeng.2017.10.356>
- Hoke, A., Brissette, A., Smith, K., Pratt, A., 2014. Accounting for Lithium-Ion Battery Degradation in Electric Vehicle Charging Optimization. *IEEE Journal of Emerging and Selected Topics in Power Electronics* 2 (3), 691–700.
- Holttinen, H., Tuohy, A., Milligan, M., Silva, V., Müller, S., Söder, L., 2013. The Flexibility Workout: Managing Variable Resources and Assessing the Need for Power System Modification. *IEEE Power and Energy Magazine* 11 (6), 53–62.
URL <https://ieeexplore.ieee.org/document/6634499>
- Hsiao, Y. Y., Chang, W. C., Chen, S. L., 2010. A mathematic model of thermoelectric module with applications on waste heat recovery from automobile engine. *Energy* 35 (3), 1447–1454.
URL <http://dx.doi.org/10.1016/j.energy.2009.11.030>
- Hu, J., Cao, J., Chen, M. Z., Yu, J., Yao, J., Yang, S., Yong, T., 2017a. Load Following of Multiple Heterogeneous TCL Aggregators by Centralized Control. *IEEE Transactions on Power Systems* 32 (4), 3157–3167.
- Hu, J., Cao, J., Yong, T., Guerrero, J. M., Chen, M. Z., Li, Y., 2017b. Demand Response Load Following of Source and Load Systems. *IEEE Transactions on Control Systems Technology* 25 (5), 1586–1598.
- Hu, J., Morais, H., Sousa, T., Lind, M., 2016. Electric vehicle fleet management in smart grids: A review of services, optimization and control aspects. *Renewable and Sustainable Energy Reviews* 56, 1207–1226.
URL <http://dx.doi.org/10.1016/j.rser.2015.12.014>
- Huang, J., Troccoli, A., Coppin, P., 2014. An analytical comparison of four approaches to modelling the daily variability of solar irradiance using meteorological records. *Renewable Energy* 72, 195 – 202.
URL <http://www.sciencedirect.com/science/article/pii/S0960148114004017>

- IHM S.A., 2002. Tanques hidroacumuladores HIDROFLO, manual de usuario.
- Ikäheimo, J., Evens, C., Kärkkäinen, S., 2010. DER Aggregator Business: the Finnish Case. Tech. rep.
URL http://www.ece.hut.fi/enete/DER_{_}Aggregator_{_}Business_{_}Finnish_{_}Case.pdf
- International Code Council, 2008. Virginia Plumbing Code. Appendix E. Sizing of water piping system.
- ISO New England Inc, 2006. Operating reserves white paper.
- Janevska, G., 2013. Mathematical Modeling of Pump System. In: The 2nd Electronic International Interdisciplinary Conference. No. 5. pp. 455–458.
URL <http://www.eiic.cz/archive/?vid=1{&}aid=3{&}kid=20201-50{&}q=f6>
- Janjic, A., Velimirovic, L., Stankovic, M., Petrusic, A., 2017. Commercial electric vehicle fleet scheduling for secondary frequency control. *Electric Power Systems Research* 147, 31–41.
URL <http://dx.doi.org/10.1016/j.epsr.2017.02.019>
- Jugsujinda, S., Vora-Ud, A., Seetawan, T., 2011. Analyzing of thermoelectric refrigerator performance. In: 2nd International Science, Social-Science, Engineering and Energy Conference 2010: Engineering Science and Management. Vol. 8. pp. 154–159.
URL <http://dx.doi.org/10.1016/j.proeng.2011.03.028>
- Kara, E. C., Bergés, M., Hug, G., Member, S., 2015. Impact of Disturbances on Modeling of Thermostatically Controlled Loads for Demand Response. *IEEE Transactions on Smart Grid* 6 (5), 2560–2568.
- Kara, E. C., Tabone, M. D., MacDonald, J. S., Callaway, D. S., Kiliccote, S., 2014. Quantifying flexibility of residential thermostatically controlled loads for demand response: a data-driven approach. In: *Proceedings of the 1st ACM Conference on Embedded Systems for Energy-Efficient Buildings*. pp. 140–147.
URL <http://dl.acm.org/citation.cfm?id=2674082>
- Khemakhem, S., Rekik, M., Krichen, L., 2017. A flexible control strategy of plug-in electric vehicles operating in seven modes for smoothing load power curves in smart grid. *Energy* 118, 197–208.
URL <https://www.sciencedirect.com/science/article/abs/pii/S0360544216318448>

- Kirby, B., Hirst, E., 2000. Customer-Specific Metrics for the Regulation and Load-Following Ancillary Services. Tech. rep.
URL <https://certs.lbl.gov/publications/customer-specific-metrics-regulation>
- Kirby, B., Kueck, J., Laughner, T., Morris, K., 2008. Spinning Reserve from Hotel Load Response: Initial Progress. No. October.
URL http://www.consultkirby.com/files/TM2008-217_{_}Spin_{_}From_{_}Hotel.pdf
- Kirby, B. J., 2004. Frequency regulation basics and trends. U.S. Department of Energy.
URL <http://www.ferc.gov/CalendarFiles/20100526085937-Kirby,FrequencyRegulationBasicsandTrends.pdf>
- Kirschen, D., Strbac, G., 2004. Fundamentals of Power System Economics. WILEY.
- Latchoomun, L., Sockalingum, T., Poulle, K. V., King, R. T., Busawon, K. K., Barbot, J. P., 2019. Design of a water pressure boosting system for pressure-driven demand in a distribution network. In: Proceedings of the 2018 5th International Symposium on Environment-Friendly Energies and Applications, EFEA 2018. pp. 1–6.
- Lewis, F. L., Vrabie, D., Syrmos, V. L., 2012. Optimal Control, 3rd Edition. Vol. XXXIII. New Jersey.
URL [{%}5Cnhttp://cid.oxfordjournals.org/lookup/doi/10.1093/cid/cir991{%}5Cnhttp://www.scielo.cl/pdf/udecada/v15n26/art06.pdf{%}5Cnhttp://www.scopus.com/inward/record.url?eid=2-s2.0-84861150233{%}&partnerID=tZ0tx3y1](http://www.ncbi.nlm.nih.gov/pubmed/15003161)
- Li, J., Liu, F., Li, Z., Shao, C., Liu, X., 2018. Grid-side flexibility of power systems in integrating large-scale renewable generations: A critical review on concepts, formulations and solution approaches. Renewable and Sustainable Energy Reviews 93, 272–284.
URL <https://doi.org/10.1016/j.rser.2018.04.109>
- Liu, M., Shi, Y., 2015. Optimal control of aggregated heterogeneous thermostatically controlled loads for regulation services. In: Proceedings of the IEEE Conference on Decision and Control. pp. 5871–5876.
- Liu, M., Shi, Y., Liu, X., feb 2016. Distributed MPC of Aggregated Heterogeneous Thermostatically Controlled Loads in Smart Grid. IEEE Transactions on Industrial Electronics 63 (2), 1120–1129.

- Lu, N., Member, S., Zhang, Y., 2013. Design Considerations of a Centralized Load Controller Using Thermostatically Controlled Appliances for Continuous Regulation Reserves. *IEEE Transactions on Smart Grid* 4 (2), 914–921.
- Lund, P. D., Lindgren, J., Mikkola, J., Salpakari, J., 2015. Review of energy system flexibility measures to enable high levels of variable renewable electricity. *Renewable and Sustainable Energy Reviews* 45 (45), 785–807.
URL <http://www.sciencedirect.com/science/article/pii/S1364032115000672>
- Luo, F., Dong, Z. Y., Meng, K., Wen, J., Wang, H., Zhao, J., 2017. An Operational Planning Framework for Large-Scale Thermostatically Controlled Load Dispatch. *IEEE Transactions on Industrial Informatics* 13 (1), 217–227.
- Ma, J., Silva, V., Belhomme, R., Kirschen, D. S., Ochoa, L. F., 2013. Evaluating and Planning Flexibility in Sustainable Power Systems. *IEEE Transactions on Sustainable Energy* 4 (1), 200–209.
URL <https://ieeexplore.ieee.org/document/6313967>
- Mahmoudi, N., Heydarian-Forushani, E., Shafie-khah, M., Saha, T. K., Golshan, M. E., Siano, P., 2017. A bottom-up approach for demand response aggregators' participation in electricity markets. *Electric Power Systems Research* 143, 121–129.
URL <http://dx.doi.org/10.1016/j.epsr.2016.08.038>
- Mai, W., Member, S., Chung, C. Y., Member, S., 2015. Economic MPC of Aggregating Commercial Buildings for Providing Flexible Power Reserve. *IEEE Transactions on Power Systems* 30 (5), 2685–2694.
- Makarov, Y. V., Loutan, C., Ma, J., de Mello, P., 2009. Operational impacts of wind generation on California power systems. *IEEE Transactions on Power Systems* 24 (2), 1039–1050.
- Martínez, A., Astrain, D., Rodríguez, A., 2013a. Dynamic model for simulation of thermoelectric self cooling applications. *Energy* 55, 1114–1126.
URL <http://dx.doi.org/10.1016/j.energy.2013.03.093>
- Martínez, A., Astrain, D., Rodríguez, A., Pérez, G., 2013b. Reduction in the electric power consumption of a thermoelectric refrigerator by experimental optimization of the temperature controller. *Journal of Electronic Materials* 42 (7), 1499–1503.

- Mathieu, J. L., Koch, S., Callaway, D. S., 2012. State Estimation and Control of Electric Loads to Manage Real-Time Energy Imbalance. *Power Systems, IEEE Transactions on PP* (99), 1.
- Menke, R., Abraham, E., Parpas, P., Stoianov, I., 2016. Demonstrating demand response from water distribution system through pump scheduling. *Applied Energy* 170, 377–387.
URL <http://dx.doi.org/10.1016/j.apenergy.2016.02.136>
- Meyn, S., Barooah, P., Buši, A., Chen, Y., Ehren, J., 2015. Ancillary Service to the Grid Using Intelligent Deferrable Loads. *IEEE Transactions on Automatic Control* 60 (11), 2847–2862.
- Mills, G., Macgill, I., 2018. Assessing Electric Vehicle storage , flexibility, and Distributed Energy Resource potential. *Journal of Energy Storage* 17, 357–366.
URL <https://doi.org/10.1016/j.est.2018.01.016>
- Min, G., Rowe, D. M., 2006. Experimental evaluation of prototype thermoelectric domestic-refrigerators. *Applied Energy* 83 (2), 133–152.
- Mitrani, D., Tomé, J., Salazar, J., Turó, A., M.J. García, J., Chávez, A., 2005. Methodology for Extracting Thermoelectric Module Parameters. *IEEE Transaction on Instrumentation and Measurement* 54 (4), 1548–1552.
- Moria, H., Ahmed, M., Alghanmi, A., Mohamad, T. I., Yaakob, Y., 2019. Experimental study of solar based refrigerator using thermoelectric effect. *Energy Procedia* 158, 198–203.
URL <https://doi.org/10.1016/j.egypro.2019.01.074>
- Mouli, G. R. C., Kaptein, J., Bauer, P., Zeman, M., 2016. Implementation of dynamic charging and V2G using Chademo and CCS/Combo DC charging standard. 2016 IEEE Transportation Electrification Conference and Expo, ITEC 2016, 1–6.
- Munshi, A. A., Mohamed, Y., 2018. Extracting and Defining Flexibility of Residential Electrical Vehicle Charging Loads. *IEEE Transactions on Industrial Informatics* 14 (2), 448–461.
URL <https://ieeexplore.ieee.org/document/7972985>
- Naharudinsyah, I., Limmer, S., 2018. Optimal Charging of Electric Vehicles with Trading on the Intraday Electricity Market. *Energies* 11 (6), 1–12.

- Nghitevelekwa, K., Bansal, R. C., 2018. A review of generation dispatch with large-scale photovoltaic systems. *Renewable and Sustainable Energy Reviews* 81, 615–624.
URL <http://dx.doi.org/10.1016/j.rser.2017.08.035>
- Nguyen, Y., Pham, T., Nguyen, T., 2014. Demand Response on Pumping Systems of Tall Buildings with Real-time Pricing. In: 1st International e-Conference on Energies. pp. 1–8.
- Nijhuis, M., Babar, M., Gibescu, M., Cobben, J. F. G., 2016. Demand response: Social welfare maximisation in an unbundled energy market - Case study for the low-voltage networks of a distribution network operator in the Netherlands. *IEEE Transactions on Industry Applications* PP (99).
- Noel, L., Rubens, G. Z. D., Sovacool, B. K., 2018. Optimizing innovation, carbon and health in transport: Assessing socially optimal electric mobility and vehicle-to-grid pathways in Denmark. *Energy* 153, 628–637.
URL <https://www.sciencedirect.com/science/article/abs/pii/S0360544218306832>
- O’Connell, N., Pinson, P., Madsen, H., Omalley, M., 2014. Benefits and challenges of electrical demand response: A critical review. *Renewable and Sustainable Energy Reviews* 39, 686–699.
- Ogunjuyigbe, A., Ayodele, T., Akinola, O., 2017. User satisfaction-induced demand side load management in residential buildings with user budget constraint. *Applied Energy* 187, 352–366.
URL <http://linkinghub.elsevier.com/retrieve/pii/S0306261916317020>
- Oikonomou, K., Parvania, M., Khatami, R., 2018. Optimal Demand Response Scheduling for Water Distribution Systems. *IEEE Transaction on Industrial Informatics* 14 (11), 5112 – 5122.
- Open Charge Alliance, 2015. Open Charge Point Protocol 1.6. Tech. rep.
URL <https://www.openchargealliance.org/>
- Ottesen, S. Ø., Tomasgard, A., Fleten, S. E., 2018. Multi market bidding strategies for demand side flexibility aggregators in electricity markets. *Energy* 149, 120–134.
URL <https://doi.org/10.1016/j.energy.2018.01.187>

- Palensky, P., Dietrich, D., 2011. Demand side management: Demand response, intelligent energy systems, and smart loads. *IEEE Transactions on Industrial Informatics* 7 (3), 381–388.
- Pandurangan, V., Zareipour, H., Malik, O., 2012. Frequency Regulation Services : A Comparative Study of Select North American and European Reserve Markets. In: 2012 North American Power Symposium (NAPS). pp. 1 – 8.
URL <https://ieeexplore.ieee.org/document/6336376>
- Papadaskalopoulos, D., Strbac, G., Mancarella, P., Aunedi, M., Stanojevic, V., 2013. Decentralized Participation of Flexible Demand in Electricity Markets — Part II : Application With Electric Vehicles and Heat Pump Systems. *IEEE Transactions on Power Systems* 28 (4), 3667–3674.
URL <https://ieeexplore.ieee.org/document/6515366>
- Paschalidis, I. C., Li, B., Caramanis, M. C., 2012. Demand-side management for regulation service provisioning through internal pricing. *IEEE Transactions on Power Systems* 27 (3), 1531–1539.
- Pavić, I., Capuder, T., Kuzle, I., 2015. Value of flexible electric vehicles in providing spinning reserve services. *Applied Energy* 157, 60–74.
URL <https://www.sciencedirect.com/science/article/pii/S0306261915009101>
- Perfumo, C., Braslavsky, J. H., Ward, J. K., 2014. Model-Based Estimation of Energy Savings in Load Control Events for Thermostatically Controlled Loads. *IEEE Transactions on Smart Grid* 5 (3), 1410–1420.
- Pertl, M., Carducci, F., Tabone, M., Marinelli, M., Kiliccote, S., Kara, E. C., 2019. An Equivalent Time-Variant Storage Model to Harness EV Flexibility : Forecast and Aggregation. *IEEE Transactions on Industrial Informatics* 15 (4), 1899 – 1910.
URL <https://ieeexplore.ieee.org/document/8438563>
- Ponds, K. T., Arefi, A., Sayigh, A., Ledwich, G., 2018. Aggregator of Demand Response for Renewable Integration and Customer Engagement: Strengths, Weaknesses, Opportunities, and Threats. *Energies* 11 (9), 1 – 20.
- Qi, W., Xu, Z., Shen, Z. J. M., Hu, Z., Song, Y., 2014. Hierarchical coordinated control of plug-in electric vehicles charging in multifamily dwellings. *IEEE Transactions on Smart Grid* 5 (3), 1465–1474.
URL <https://ieeexplore.ieee.org/document/6785970>

- Quinn, C., Zimmerle, D., Bradley, T. H., 2010. The effect of communication architecture on the availability, reliability, and economics of plug-in hybrid electric vehicle-to-grid ancillary services. *Journal of Power Sources* 195 (5), 1500–1509.
URL <https://www.sciencedirect.com/science/article/abs/pii/S0378775309015195>
- Quirós-Tortós, J., Ochoa, L., Butler, T., 2018. How Electric Vehicles and the Grid Work Together: Lessons Learned from One of the Largest Electric Vehicle Trials in the World. *IEEE Power and Energy Magazine* 16 (6), 64–76.
URL <https://ieeexplore.ieee.org/document/8501603>
- Rahman, B. M., Wagner, J. R., 2016. Energy efficient refrigeration - Improvement of compact thermoelectric units through modeling, testing, and control. In: *American Control Conference*. American Automatic Control Council (AACC), pp. 1311–1316.
- Richalet, J., Rault, A., Testud, J., Papon, J., 1978. Model predictive heuristic control: Applications to industrial processes. *Automatica* 14 (5), 413–428.
- Richalet, J., Rault, A., Testud, J. L., Papon, J., 1976. Algorithmic control of industrial processes. In: *The 4th IFAC symposium on identification and system parameter estimation*. pp. 1119–1167.
- Rodriguez Martinez, A., Garduno Ramirez, R., Valdes Vela, L. G., 2011. PI fuzzy gain-scheduling speed control of a gas turbine power plant. *Transactions on Energy Conversion* 26 (1), 310–317.
- Sadeghianpourhamami, N., Refa, N., Strobbe, M., Develder, C., 2018. Quantitative analysis of electric vehicle flexibility : A data-driven approach. *International Journal of Electrical Power and Energy Systems* 95, 451–462.
URL <https://doi.org/10.1016/j.ijepes.2017.09.007>
- Saidur, R., Masjuki, H. H., Hasanuzzaman, M., Mahlia, T. M. I., Tan, C. Y., Ooi, J. K., Yoon, P. H., 2008. Performance investigation of a solar powered thermoelectric refrigerator. *International Journal of Mechanical and Materials Engineering* 3 (1), 7–16.
- Saifizi, M., Zakaria, M. S., Yaacob, S., Wan, K., 2018. Development and Analysis of Hybrid Thermoelectric Refrigerator Systems. In: *IOP Conference Series: Materials Science and Engineering*. Vol. 318. pp. 1 – 13.

- Sajjad, I. A., Chicco, G., Napoli, R., 2016. Definitions of Demand Flexibility for Aggregate Residential Loads. *IEEE Transactions on Smart Grid* 7 (6), 2633–2643.
URL <https://ieeexplore.ieee.org/document/7457676>
- Schuller, A., Flath, C. M., Gottwalt, S., 2015. Quantifying load flexibility of electric vehicles for renewable energy integration. *Applied Energy* 151, 335–344.
URL <http://dx.doi.org/10.1016/j.apenergy.2015.04.004>
- Shen, L., Zhang, W., Liu, G., Tu, Z., Lu, Q., Chen, H., Huang, Q., 2020. Performance enhancement investigation of thermoelectric cooler with segmented configuration. *Applied Thermal Engineering* 168 (December 2019), 1–10.
URL <https://doi.org/10.1016/j.applthermaleng.2019.114852>
- Siano, P., 2014. Demand response and smart grids - A survey. *Renewable and Sustainable Energy Reviews* 30, 461–478.
URL <http://dx.doi.org/10.1016/j.rser.2013.10.022>
- Škugor, B., Deur, J., 2015. Dynamic programming-based optimisation of charging an electric vehicle fleet system represented by an aggregate battery model. *Energy* 92, 456–465.
URL <https://www.sciencedirect.com/science/article/abs/pii/S036054421500362X>
- Sortomme, E., El-Sharkawi, M. A., 2011. Optimal charging strategies for unidirectional vehicle-to-grid. *IEEE Transactions on Smart Grid* 2 (1), 119–126.
- Söylemez, E., Alpman, E., Onat, A., 2018. Experimental analysis of hybrid household refrigerators including thermoelectric and vapour compression cooling systems. *International Journal of Refrigeration* 95, 93–107.
- Sun, B., Tan, X., Tsang, D. H. K., 2018. Eliciting Multi-dimensional Flexibilities from Electric Vehicles: A Mechanism Design Approach. *IEEE Transactions on Power Systems*, In press.
URL <https://ieeexplore.ieee.org/document/8411183>
- Sundström, O., Binding, C., 2012. Flexible charging optimization for electric vehicles considering distribution grid constraints. *IEEE Transactions on Smart Grid* 3 (1), 26–37.
URL <https://ieeexplore.ieee.org/document/6112699>

- Tascikaraoglu, A., Sanandaji, B. M., Chicco, G., Cocina, V., Spertino, F., Erdinc, O., Paterakis, N. G., Catalão, J. P. S., July 2016. Compressive spatio-temporal forecasting of meteorological quantities and photovoltaic power. *IEEE Transactions on Sustainable Energy* 7 (3), 1295–1305.
- The European Commission, 2017. Commission Regulation (EU) 2017/2195 of 23 November 2017 establishing a guideline on electricity balancing. *Official Journal of the European Union* 2017 (November), 312/6 – 312/53.
URL https://eur-lex.europa.eu/legal-content/EN/TXT/?uri=uriserv:OJ.L_{_}.2017.312.01.0006.01.ENG{&}toc=OJ:L:2017:312:TOC{#}d1e2376-6-1
- The European Parliament and the Council of the European Union, 2004. Regulation (EC) No 852/2004 of the European Parliament and of the Council of 29 April 2004 on the hygiene of foodstuffs. *Official Journal of the European Union* (L 139/1), 1–54.
URL <https://eur-lex.europa.eu/legal-content/EN/TXT/?uri=CELEX{%}3A32004R0852>
- Tindemans, S. H., Trovato, V., Member, S., Strbac, G., 2015. Decentralized Control of Thermostatic Loads for Flexible Demand Response. *IEEE Transactions on Control Systems Technology* 23 (5), 1685–1700.
- Tsai, H. L., Lin, J. M., 2010. Model building and simulation of thermoelectric module using Matlab/Simulink. *Journal of Electronic Materials* 39 (9), 2105–2111.
- UKERC, 2007. The Rebound Effect: an assessment of the evidence for economy-wide energy savings from improved energy efficiency. Vol. 42.
URL <http://www.ncbi.nlm.nih.gov/pubmed/24690348>
- Ulbig, A., Andersson, G., 2015. Analyzing operational flexibility of electric power systems. *International Journal of Electrical Power and Energy Systems* 72, 155–164.
URL <http://dx.doi.org/10.1016/j.ijepes.2015.02.028>
- Vardakas, J. S., Zorba, N., Verikoukis, C. V., 2015. A Survey on Demand Response Programs in Smart Grids: Pricing Methods and Optimization Algorithms. *IEEE Communication Surveys & Tutorials* 17 (1), 152 – 178.
URL <http://ieeexplore.ieee.org/lpdocs/epic03/wrapper.htm?arnumber=7063260>

- Venkataraman, B., Godsey, B., Premerlani, W., Shulman, E., Thakur, M., Midence, R., 2005. Fundamentals of a Motor Thermal Model and its Applications in Motor Protection, 41–55.
- Veselý, V., Ilka, A., 2013. Gain-scheduled PID controller design. *Journal of Process Control* 23 (8), 1141–1148.
- Vuelvas, J., Ruiz, F., 2017. Rational consumer decisions in a peak time rebate program. *Electric Power Systems Research* 143, 533 – 543.
- Wang, R., Xiao, G., Wang, P., 2017. Hybrid Centralized-Decentralized (HCD) Charging Control of Electric Vehicles. *IEEE Transactions on Vehicular Technology* 66 (8), 6728–6741.
URL <https://ieeexplore.ieee.org/document/7852525>
- Warren, P., 2014. A review of demand-side management policy in the UK. *Renewable and Sustainable Energy Reviews* 29, 941–951.
URL <http://dx.doi.org/10.1016/j.rser.2013.09.009>
- Wenzel, G., Negrete-pincetic, M., Olivares, D. E., Macdonald, J., Callaway, D. S., 2018. Real-Time Charging Strategies for an Electric Vehicle Aggregator to Provide Ancillary Services. *IEEE Transactions on Smart Grid* 9 (5), 5141–5151.
URL <https://ieeexplore.ieee.org/document/7876762>
- Xu, W., Wei, D., Lei, C., 2016. Control for the Centrifugal Pump in the Simulation Platform of Power Plants. In: *International Conference on Industrial Informatics - Computing Technology*, pp. 263 – 267.
URL <http://www.lucelec.com/content/power-plants>
- Yang, L., Zhang, J., Poor, H. V., 2014. Risk-aware day-ahead scheduling and real-time dispatch for electric vehicle charging. *IEEE Transactions on Smart Grid* 5 (2), 693–702.
URL <https://ieeexplore.ieee.org/document/6740918>
- Yilmaz, M., Krein, P. T., 2013. Review of charging power levels and infrastructure for plug-in electric and hybrid vehicles. *IEEE Transactions on Power Electronics* 28 (5), 2151–2169.
URL <https://ieeexplore.ieee.org/document/6183208>
- Yin, R., Kara, E. C., Li, Y., DeForest, N., Wang, K., Yong, T., Stadler, M., 2016. Quantifying flexibility of commercial and residential loads for demand response using

- setpoint changes. *Applied Energy* 177, 149–164.
URL [//www.sciencedirect.com/science/article/pii/S0306261916306870](http://www.sciencedirect.com/science/article/pii/S0306261916306870)
- You, P., Yang, Z., Chow, M. Y., Sun, Y., 2016. Optimal Cooperative Charging Strategy for a Smart Charging Station of Electric Vehicles. *IEEE Transactions on Power Systems* 31 (4), 2946–2956.
- Zeilinger, M. N., Morari, M., Jones, C. N., 2014. Soft constrained model predictive control with robust stability guarantees. *IEEE Trans. on Automatic Control* 59 (5), 1190–1202.
- Zhao, D., Tan, G., 2014. Experimental evaluation of a prototype thermoelectric system integrated with PCM (phase change material) for space cooling. *Energy* 68, 658–666.
URL <http://dx.doi.org/10.1016/j.energy.2014.01.090>
- Zhao, L., Zhang, W., 2017. A Geometric Approach to Aggregate Flexibility Modeling of Thermostatically Controlled Loads. *IEEE Transactions on Power Systems* 32 (6), 4721–4731.
URL <https://ieeexplore.ieee.org/document/7864461>
- Zhou, B., Yao, F., Littler, T., Zhang, H., 2016. An electric vehicle dispatch module for demand-side energy participation. *Applied Energy* 177, 464–474.
URL [//www.sciencedirect.com/science/article/pii/S0306261916307255](http://www.sciencedirect.com/science/article/pii/S0306261916307255)
- Zhou, Y., Wang, C., Wu, J., Wang, J., Cheng, M., Li, G., 2017. Optimal scheduling of aggregated thermostatically controlled loads with renewable generation in the intraday electricity market. *Applied Energy* 188, 456–465.
URL [//www.sciencedirect.com/science/article/pii/S0306261916317718](http://www.sciencedirect.com/science/article/pii/S0306261916317718)